Computational Studies Across Catalysis

Carine Michel

HABILITATION À DIRIGER DES RECHERCHES

Présentée le 8 juin 2016

En vue d'obtenir l'Habilitation à diriger des Recherches
de l'Ecole Normale Supérieure de Lyon

Par Carine MICHEL

Computational Studies Across Catalysis

Les Membres du Jury sont :

Pr. Núria López	*Rapporteur*
Pr. Anastassia Alexandrova	*Rapporteur*
Dr. Dorothée Berthomieux	*Rapporteur*
Pr. Anne Milet	*Membre*
Pr. Christophe Coutanceau	*Membre*
Dr. Philippe Marion	*Membre*
Dr. Philippe Sautet	*Membre*

ABSTRACT

My research activities focus on the theoretical study of chemical reactivity catalysis and green chemistry. Based on models and simulations and strong collaborations with experimentalists, this research aims at establishing structure/catalytic activity relationships to promote a rational and efficient development of new catalysts in homogeneous catalysis, heterogeneous catalysis and electrocatalysis. My main ambition is to improve the models and methodologies beyond their limits to provide a better understanding. For instance, with a simple microsolvation effect, I could rationalize the impact of the water solvent on the activity of metallic catalysts for the levulinic acid conversion into γ-valerolactone. Solvent effects are even more crucial in electrocatalysis as shown recently on the CO_2 electroactivation. Thus, developing solvatation models for heterogeneous interfaces is a clear milestone for the coming years. Another challenge will be the constant improvement of the quality of the model of the catalyst in its steady state.

MERCI ! THANKS!

Mes recherches se sont construites au grès de rencontres marquantes qui m'ont fait progressée aussi bien scientifiquement qu'humainement.

Première rencontre fondamentale, celle qui restera toujours ma chef, Pr. Anne Milet qui m'a initié à la recherche, à la chimie théorique, à l'art de la collaboration et aux arcanes du monde universitaire. Deuxième rencontre, Pr. Evert Jan Baerends, qui m'a fait confiance en me laissant 'trouver un nouveau sujet' et monter une collaboration. Je pense à lui à chaque article que j'écris, lui qui m'a appris à écrire pour "mes" lecteurs. Enfin, mes derniers guides, Françoise Delbecq et Philippe Sautet, qui m'ont accueillie au Laboratoire de Chimie et surtout qui m'ont accompagnée dans le monde fascinant de la Catalyse. Merci à eux deux pour leur patience, leur bienveillance, pour les échanges riches et passionnés, pour tout.

Je ne sais pas travailler seule, ces travaux de recherche sont tous le fruit de collaborations, que ce soit avec d'autres théoriciens aux compétences complémentaires ou avec des expérimentateurs de différents domaines. A chaque collaboration, de belles rencontres, des amitiés qui se construisent. Rassembler autour d'un projet commun des collaborateurs est pour moi un moteur fort, et je suis très heureuse que cela se concrétise à travers le projet **Tanopol**. A tous mes collaborateurs, passés, présents et même futurs, merci!

Et surtout, cette habilitation s'est construite grâce aux étudiants qui m'ont fait confiance et ils sont nombreux. De ma première stagiaire, Lise Morlet à Stephan Steinmann, post-doc recruté au CNRS, j'ai une pensée pour chacun, que chacun trouve sa voie! Tous m'ont appris

à leur manière à accompagner, encadrer, guider sur le chemin de la Recherche. J'essaie à mon tour d'être une "bonne chef" et c'est un apprentissage de chaque jour! Merci à tous pour votre confiance et surtout . . . votre patience!

Le travail de recherche ne peut se faire sans le groupe de Chimie Théorique, membres passés et présents, le Laboratoire et tous ceux en "soutien à la recherche", du pôle de gestion aux informaticiens, du Laboratoire de Chimie aux services de l'ENS de Lyon et du CNRS, merci à tous pour votre soutien!

Pour finir, mon infinie reconnaissance à mes proches, amis, famille. Nicolas, Mathilde, Romane, merci!

CONTENTS

INTRODUCTION

My research activities focus on the *theoretical study of chemical reactivity* catalysis and green chemistry. Based on models and simulations and strong collaborations with experimentalists, this research aims at establishing structure/catalytic activity relationships to promote a rational and efficient development of new catalysts. Nowadays, this approach is essential to ensure an efficient development of novel catalysts that are more efficient and less polluting. I applied it in homogeneous catalysis, in heterogeneous catalysis and electrocatalysis, as reported in the three corresponding chapters.

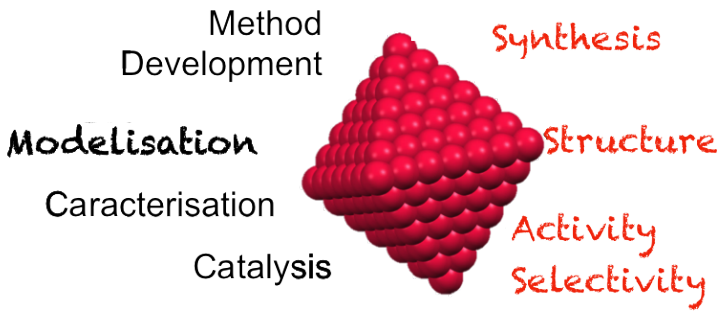

My main interest is the development of novel catalysts in the ever-growing domain of the conversion of biomass into platform molecules needed to advance the sustainable production of fuels and base chemicals. In this domain, solvent effects can manifest in numerous ways, such as explicit participation in the mechanism (e.g., water-mediated proton transfer) and the reaction rate constant (e.g., via electrostatics due to solvent re-organization). Solvent effects are even more crucial in electrocatalysis. This account pushed us to propose to include solvent effects based on micro-solvation and more recently on a force-field development and free energy perturbation (**Music** project).

This manuscript is divided into chapters dedicated to Methodology and then to different kinds of catalysis (homogeneous and single site catalysts, supported metallic catalysts, electrocatalysts). Each chapter dedicated to catalysis includes a summary of my research activities and a short selection of my articles. I have co-authored the references indicated in blue and red, the latter being also including at the end of the chapter. The last chapter is a synthesis of my research perspectives. In appendix, my curriculum vitae and a list of my peer-reviewed publications.

1

METHODOLOGY

My research is focused on the modeling of catalytic cycles of various systems. The first step is to evaluate the energetic and the structures of the plausible intermediate and transition states along the catalytic cycle but also along potential side routes that could deactivate the catalyst. The evaluation of these reaction pathways require to make several choices: (i) choice of the model (ii) choice of the methodology to compute the energies. Those choices are intrinsically interconnected since the most accurate methods are generally not affordable for the most accurate models. I mostly use the Density Functional Theory (DFT) as a good trade-off between cost and accuracy. At the crossing point between molecular chemistry and solid state physics, the study of molecules adsorbed at metallic surfaces are challenging to describe accurately and still highly rely on the use of the Generalized Gradient Approximation (GGA), now often including dispersion correction (Grimme D3[2], dDsC[7,8] or non-local functionals[3]). A recent benchmark on the adsorption of insaturated molecules on Pt(111) against single crystal adsorption calorimetry SCAC experiments demonstrates that optPBE and PBE-DdSc are the best approaches we can afford nowdays for this kind of system.[11] In metallic heterogeneous catalysis, the metallic nanoparticles are described using a periodic finite slab of the most compact facet (typically a p(3x3) cell of a four layers slab). The solvent is generally modeled as a continuum model[9] when available[1,5] and by including few water molecules in a simple micro-solvation ap-

proach. More advanced models for describing the metal/water interface require methodological development. I have also collaborated with R. Bulo who is developing adaptive QM/MM approaches.[10] However, those methods are not mature yet to tackle complex catalytic systems, especially for heterogeneous metallic systems. We are currently working on development of novel strategies based on free energy perturbation to obtain solvation free energies, combined with the development of better force field for water/platinum interface (**Music** project).

Once the Gibbs free energy profiles are computed, we need efficient tools to extract the predicted variations in activity or selectivity. The data could be input to a micro-kinetics model to include the effect of concentration and get the turn-over frequency and the selectivity.[6] The reaction profile of a catalytic reaction can also be easily interpreted using the energetic span framework that relates the energetic span of a profile to the turn over frequency (TOF) of the catalyst.[4] In short, the rate-determining transition state is not necessarily the highest in energy of the reaction profile since this is not invariant with the choice of the starting point in the cycle. It is neither the one corresponding to the elementary step with the highest activation energy. To determine the rate determining transition state, one has to first compute the energy difference δE between each intermediate **I** and transition state **TS** in the forward direction:

$$\begin{aligned} \delta E &= E(TS) - E(I) \quad \text{if } \mathbf{TS} \text{ appears after } \mathbf{I} \\ \delta E &= E(TS) - E(I) + \Delta G_r \quad \text{if } \mathbf{TS} \text{ appears before } \mathbf{I} \end{aligned}$$

The rate determining transition state and the rate determining intermediate are the ones that maximize δE. And the corresponding δE is the energetic span of the catalytic cycle. Those concepts are illustrated in Figure 1.1 and Figure 1.2.

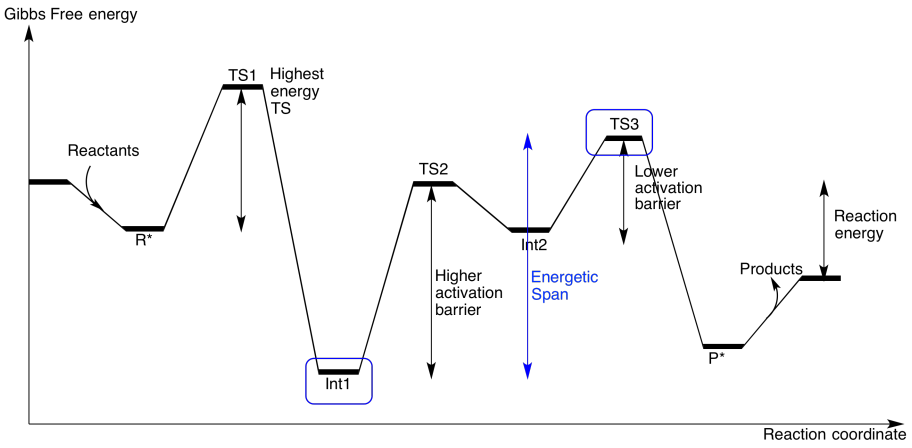

Figure 1.1: A typical Gibbs energy profile for the conversion of reactants into products catalyzed by a heterogeneous catalyst with an exothermic Gibbs free energy. In this typical case, the adsorption of the reactants (**R***) is followed by the highest transition state in energy. This step is exergonic, yielding to the intermediate **Int1** that is strongly stabilized by the surface. The stability of this intermediate clearly controls the overall kinetics. This first step is followed by the step with the higher activation energy of the profile. The subsequent intermediate **Int2** is weakly stabilized by the surface and is quickly converted into the product **P*** through the rate determining transition state.

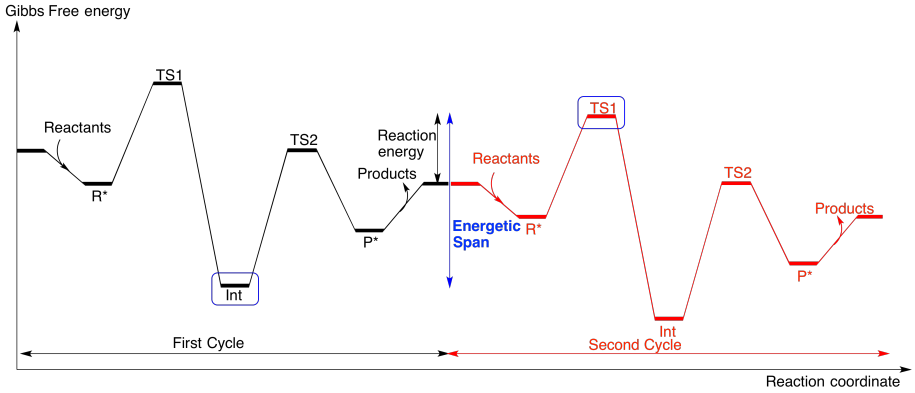

Figure 1.2: A typical Gibbs energy profile for the catalytic conversion of reactants into products catalyzed by a heterogeneous catalyst with an exothermic Gibbs free energy. In this typical case, the rate determining intermediate is **Int**, the rate determining transition state is **TS1** and the energetic span is given by $\delta E = E(TS1) - E(Int) + \Delta G_r$

Bibliography

[1] Fishman, M.; Zhuang, H. L.; Mathew, K.; Dirschka, W.; Hennig, R. G. *Phys. Rev. B* **2013**, *87*, 245402.

[2] Grimme, S.; Antony, J.; Ehrlich, S.; Krieg, H. *J. Chem. Phys.* **2010**, *132*.

[3] Klimeš, J. c. v.; Bowler, D. R.; Michaelides, A. *Phys. Rev. B: Condens. Matter* **2011**, *83*, 195131.

[4] Kozuch, S.; Shaik, S. *Acc. Chem. Res.* **2011**, *44*, 101–110, PMID: 21067215.

[5] Mathew, K.; Sundararaman, R.; Letchworth-Weaver, K.; Arias, T. A.; Hennig, R. G. *J. Chem. Phys.* **2014**, *140*.

[6] Medford, A. J.; Shi, C.; Hoffmann, M. J.; Lausche, A. C.; Fitzgibbon, S. R.; Bligaard, T.; Nørskov, J. K. *Catal. Lett.* **2015**, *145*, 794–807.

[7] Steinmann, S. N.; Corminboeuf, C. *J. Chem. Theory Comput.* **2011**, *7*, 3567.

[8] Steinmann, S. N.; Corminboeuf, C. *J. Chem. Phys.* **2011**, *134*.

[9] Tomasi, J.; Mennucci, B.; Cammi, R. *Chem. Rev.* **2005**, *105*, 2999–3094, PMID: 16092826.

[10] Bulo, R. E.; Michel, C.; Fleurat-Lessard, P.; Sautet, P. *Journal of Chemical Theory and Computation* **2013**, *9*, 5567–5577.

[11] Gautier, S.; Steinmann, S. N.; Michel, C.; Fleurat-Lessard, P.; Sautet, P. *Physical Chemistry Chemical Physics* **2015**, *17*, 28921–28930.

2

SINGLE SITE CATALYSIS

Introduction

After a PhD dedicated to mechanistic studies of molecular systems, I have chosen to work on homogeneous catalysts under the supervision of Pr.Evert Jan Baerends in Amsterdam. There, I focused on C−H oxidation, working on two different systems, leading to the publication of three articles.[24,22,25]

Since then, I keep a research activity in this domain, in particular in collaboration with Rhodia and then Solvay (which tookover Rhodia few years ago). Thanks to the support of Solvay, Prokopis Andrikopoulos was hired for 18 months as a postdoc to work on the screening of homogeneous catalysts for the alkane oxidation.[21] Later, Wenping Guo was hired as a postdoc to work in collaboration with the E2P2L, a join laboratory between Solvay and the CNRS set in Shanghai, China. He focused on two reactions: (i) the CO_2/ethylene reductive coupling[23] (ii) the amination of alcohols. Those reactions were also considered in heterogeneous catalysis, see later.

More recently, I have also started to work on the catalytic cleavage of C−C bond in lignin models in collaboration with T. Baker (uOttawa) and P. Fleurat-Lessard (Université de Bourgogne) in the context of the LIA Funcat. Last, I have been recently involved in the long-term collaboration between Philippe Sautet and Christophe Copéret (ETH Zurich) on the understanding of single site heterogeneous catalysts for metathe-

sis reaction, at the cross-section between homogeneous and heterogeneous catalysis.

2.1 Oxidation of alkanes

The activation of C−H bonds in alkanes is central to several important industrial processes to upgrade petroleum derivatives into alcohols, alkenes and carbonyls. A typical example is the oxidation of the cyclohexane into cyclohexanol, the first step to nylon-6. This major industrial reaction is also one of the less efficient ones: in most cases, O_2 from air is used as a final oxidant and the oxidation is catalyzed by cobalt or manganese derivatives at high temperature (160°C) in the K-A process.[10,13]

In fine chemistry, most of the oxidant are still based on chromium or manganese used in stoichiometric quantities and thus leading to the production of large quantities of toxic salt. The development of novel catalysts based preferentially on transition metals opens the road to greener processes that are less demanding in energy and less polluting regarding the production of toxic salts. Two majors challenges have to be faced in this domain: (i) ensure the stability of the catalyst in those highly oxidative conditions (ii) avoid the over-oxidation when this is needed while it is generally favored. oxidant The C−H activation can be performed using either homogeneous or heterogeneous catalysts based on transition metals. In both cases, a better comprehension of the mechanism is essential to a rational development of novel modern catalysts. Those reactions involve the transfer of electron from the target to the catalyst and then from the reduced catalyst to the final oxidant.

The oxidation reactions catalyzed by transition metals are mostly believed to follow a radical mechanism.[11] However, experimental studies of the Fenton reaction have questioned this dogma and demonstrated the crucial role of the high spin Fe(IV)=O moiety.[4] Those studies were at the origin of a long-term project on this reaction lead

by Pr. E.J. Baerends. The C−H oxidation in alkane can be catalyzed by the Fe(IV)=O entity following a rebound mechanism in two steps, as show in Figure 2.1. The C−H bond is activated by the electrophilic Fe(IV)=O, leading to a carbon radical intermediate together with Fe(III)−OH. Then a rebound step results in the oxidized product (alcohol) and the reduced catalyst (Fe(II)).

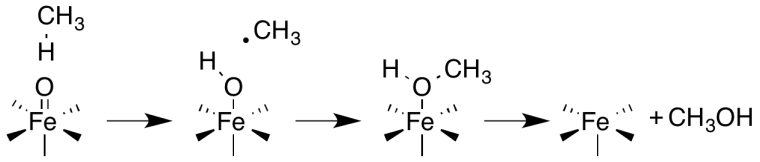

Figure 2.1: Main steps involved in the oxidation of C−H bond by the Fe(IV)=O moiety.

Since the catalyst acts as an electrophile, its oxidative ability lies in its lower active acceptor molecular orbital. To establish which orbital controls the activity, one of the key aspects is the spin state of the Fe(IV)=O. Two spin sates are generally accessible: the triplet state and the quintet state. The spin gap varies with the ligand field. Weaker ligands such as water favors the high spin state while stronger ligands such as ammonia destabilizes more the $\delta_{x^2+y^2}$ orbital and favors the triplet state (see Figure 2.2). The change in the spin state results in a reduction of the exchange stabilization of the α spin-orbitals. In the quintet state, the lowest acceptor orbital is the $\sigma*(\alpha)$. It is pushed up in energy upon the replacement of weak ligands by stronger ligands as a result of two phenomena: the destabilizing stronger field *and* the reduction of the exchange. Then, in the triplet state, the lowest acceptor orbital is not any more the $\sigma*(\alpha)$ but the $\pi*(\beta)$.

In a nutshell, depending on the ligand, two different spin states are accessible, with two different electronic configurations. They lead to two different reactive channels for the C−H bond cleavage. The corresponding transition states are represented in Figure 2.3. The quintet spin state opens the σ channel, where the C−H points towards the Fe(IV)=O

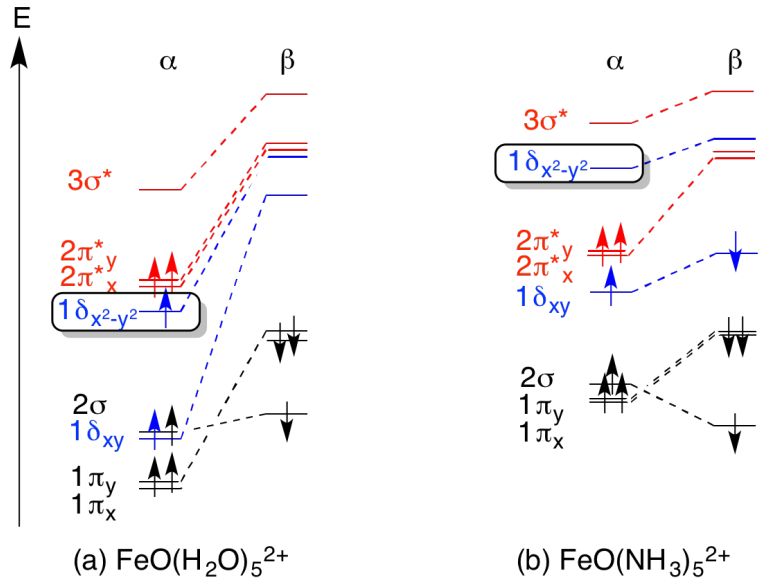

Figure 2.2: Main molecular orbitals of Fe(IV)=O in two environments (a) with weak ligands (water), in a quintet spin state (b) with donor ligands (ammonia), in a triplet spin state.

with an angle of 180°. The overlap is optimal and the steric hindrance between the substrate and the ligand sphere is minimized. On the triplet state, this channel is generally not accessible since the $\sigma*$ is strongly destabilized. However, the oxidation can still take place through the π channel, where the C−H points towards the Fe(IV)=O with an angle of 120°, as a compromise between the overlap (optimal at 90°) and the steric hindrance (minimal at 180°).

This system has been extensively studied with a large variety of ligands, both experimentally[12,14,15,19] and theoretically[2,6,8,18]. To enable a efficient design *in silico*, we built a data base of potential ligands (over 50 complexes).[21] We demonstrated that the activation energy for the C-H abstraction on the high spin state can be correlated with the energy of the lowest lying active orbital, namely the $\sigma*$. This correlation validates the usage of the electronic structure as a tool for understanding and design this type of catalyst. As expected, we had to separate the set

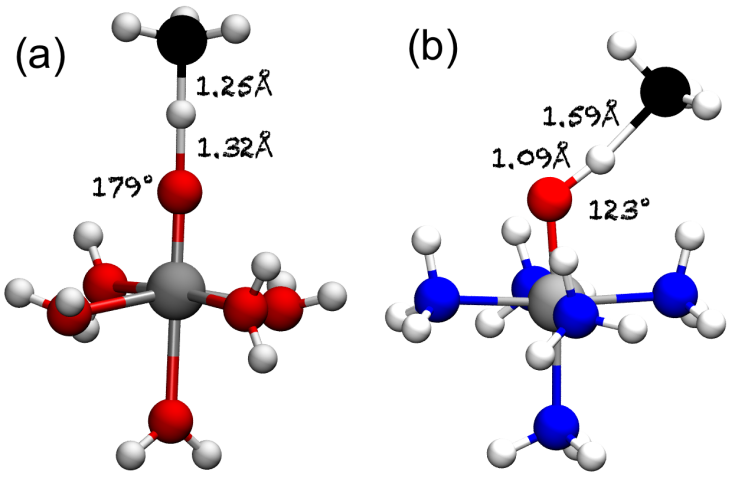

Figure 2.3: Transition state structures for the C−H cleavage as promoted by the Fe(IV)=O moiety in two different environments (a) with water ligands, in a quintet spin state (b) with ammonia ligands, in a triplet spin state.

according to the total charge of the complex since the orbital energies vary considerably with the electric field. In addition, we had to separate the monodentate ligands from the multidentate ones: for a given $\sigma*$ orbital energy, the Fe(IV)=O is more active when coordinated by a multidentate ligand than with several monodentates. The solvent can also tune the activity, a too high dielectric constant being detrimental. As a result of this study, we were able to propose to use (i) non-polar solvent (the target alkane), (ii) polydentate ligands with weak coordination sites (oxygen based) to ensure a high spin state, to our experimental partners in Solvay. [21]

This Fe(IV)=O moiety is wide-spread. It can also be found in several enzymes such as P450[3] and TauD[16] and is postulated being the active center in some zeolites.[7] The screening *in silico* of the activity of $M(H_2O)_n^{2+}$, M=V,...,Cu, shows that Fe is indeed special. Its appears that the number of 3d electrons in Fe(IV) is optimal to ensure that the π^* and σ^* are low lying in energy but not filled up yet with electrons,

that would increase the repulsion with the electrons of the σ(C-H). [24]

2.2 Oxidation of alcohols

The team of Pr. Reedijk has proposed a simple system based on $CuBr_2$(Bipy)−TEMPO catalyst that is efficient and selective: while the secondary alcohols are not oxidized, primary alcohols are converted selectively into the corresponding aldehyde.[5] After a detailed study of the solvent effect, the counter-ions, etc, they have proposed a reaction mechanism involving a copper (II) center, coordinated by the TEMPO radical, the alcoholate and the bipyridine. In this case, the substrate is postulated to be oxidized by a Cu-coordinated TEMPO· radical. However, in the oxidation of alcohols, others postulate that the substrate is oxidized by uncoordinated $TEMPO^+$.[17]

In collaboration with the group of Pr. Reedijk, we have performed a theoretical study of this catalytic cycle in collaboration with P. Belanzoni et E.J. Baerends that refined this initial proposition.[22,25] In the key step, the copper (II) activates the TEMPO radical by a partial oxidation, favoring the proton transfer from the primary alcoholate to the nitrogen of the TEMPO as shown in Figure 2.4. Based on a careful analysis of the electronic structure, we claimed that this Cu(bipy)2+/TEMPO cocatalyst system can be best viewed as electrophilic attack on the alcohol C−Hα bond by coordinated $TEMPO^+$. This mechanism combines elements of the Semmelhack mechanism (oxidation of TEMPO to $TEMPO^+$) and the Sheldon proposal (in the coordination sphere of Cu). The chemio-selectivity is ensured by the four methyl groups that surround the nitrogen. Those results open the door to a rational design of novel ligands that link the bipyridine and the TEMPO, for a catalyst that could be more efficient and easier to graft.

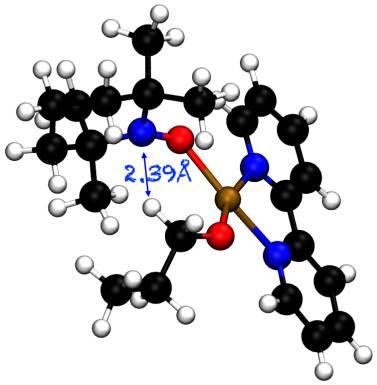

Figure 2.4: Key structure for the selective oxidation of CH_3CH_2OH into CH_3CHO as catalyzed by TEMPO - Cu(II)(bipy) system.

2.3 Coupling of CO_2 and ethylene using Ni-Based systems

CO_2 is a inert molecule, with a completely oxidized carbon. Its utilization as a C1 fragment, for instance to be coupled with an unsaturated molecule such as ethylene, requires strongly reducing conditions. In collaboration with Solvay, we focused on two strategies: (i) electrochemical activation (ii) using strong reductants such as complexed based on Ni(0). In the later case, the major difficulty is to turn this stœchiometric process into a catalytic one. The product is a very stable nickel lactone. By addition of methyl iodide as an electrophile in large excess, the methylacrylate can then be recovered and the yield was tuned with different amine and phosphine ligands [1,9] Based on an hybrid approach in collaboration with Pr. X. Xu, Shanghai, we demonstrated that the choice of ligand has little effect on the main productive pathway. However, it has a significant influence on side reactions, which compete with the productive pathway and are detrimental to methyl acrylate formation. Finally, the need for a very large overstoichiometry of MeI for a good yield of methyl acrylate is explained by the lower polarity

of MeI, which avoids the stabilization of nonproductive intermediates. The nature of the limiting intermediates has been validated by comparing calculated and experimental vibrational spectra.[23]

2.4 Amination of alcohols

Wenping Guo worked also on the amination of alcohols catalyzed by aluminium triflate salts in collaboration with experimentalists from the E2P2L laboratory in Shanghai, China. The reaction mechanism is simple. It is based on the nucleophilic substitution of the alcohol by the amine, catalyzed by the Lewis acid to favor the C−O rupture. The typical benchmark reaction in the domain is the amination of benzyl alcohol by aniline. Our DFT study demonstrated that the catalyst has a highly labile coordination sphere that is completed by both reactants and products. Once the structure of the catalyst assessed, we focused on the impact of the solvent and the nature of the alcohol and the amine, the main target being the amination of aliphatic alcohol by ammonia.

2.5 What's next?

My research activities in the understanding of single sites catalysts will continue along two lines of research, both in collaboration with reknown experimental groups: (i) the lignin valorization with Pr. Tom Baker, uOttawa in the context of the LIA **Funcat** (ii) characterization of tungsten supported catalysts for metathesis with Pr. Christophe Copéret, ETH Zurich, and Pr. Olga Safonova, Paul Scherrer Institute, Zurich, in the context of the SNF-ANR **Mascat**.

2.5.1 Lignin valorization

The controlled depolymerization of the lignin part is currently highly challenging and limits the potential of this feedstock as a source of

aromatics. The complexity lies in the high structural heterogeneity of lignin. This polymer is based on several monomers that are linked through various types of bonds. This is illustrated in 2.5. The ratio of monomers and the occurrence of a given type of link depends on the source (softwood, hardwood, etc.).[20]

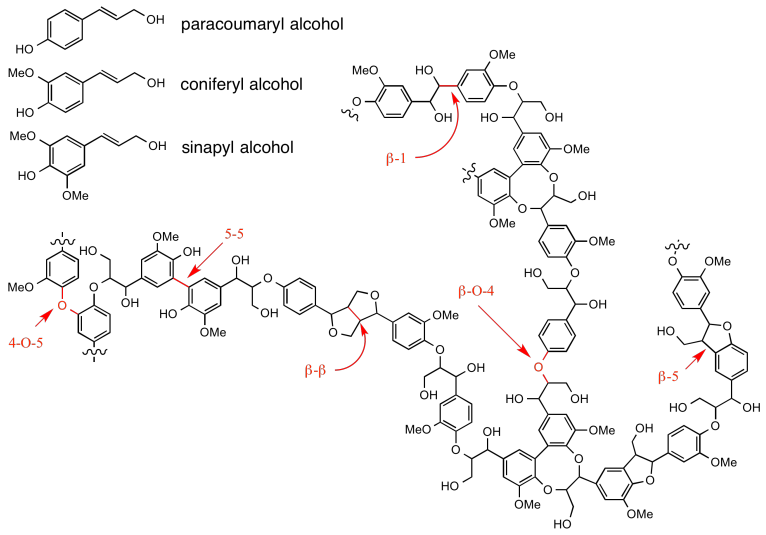

Figure 2.5: A typical lignin polymer and the three common monolignols

The main idea is to design homogeneous catalysts that would selectively perform the oxidative cleavage of the C−C bond in the β-O-4 linkage, the most abundant in lignin. In the group of Tom Baker, they characterize the catalytic activity of vanadium-oxo complexes to selectively cleave the C−C bond (and not the ether bond) in model molecules. The mechanism is still rather speculative and a better understanding would favor a rational design of those catalysts. In line with our previous studies in the domain, we hope to provide guidelines in a near future.

2.5.2 Metathesis

Industrial heterogeneous alkene metathesis catalysts are based on supported Mo and W oxides and contain very low concentrations of active sites (typically below 1%). These sites are presumably formed under operating conditions from dispersed metal oxo species, and they have been proposed to correspond to oxo alkylidene species. Despite their industrial use, the low activity in these catalysts – by comparison to their homogeneous homologues –raise several important questions: what is the structure of the active sites, how are they formed, what are the necessary structural features for surface sites to become active, and finally how to tune catalysts preparation to increase the density of active sites in order to increase the efficiency of the process.

To address these questions we suggest an original approach based on the in situ characterization of the surface (active) sites at the molecular level at the precursor stage and during the catalytic event (in situ/operando), using in particular X-ray absorption fine structure (XAFS) and Raman spectroscopies combined with first principle density functional theory (DFT) calculation.

Bibliography

[1] Bruckmeier, C.; Lehenmeier, M. W.; Reichardt, R.; Vagin, S.; Rieger, B. *Organometallics* **2010**, *29*, 2199–2202.

[2] Cho, K.-B.; Kim, E. J.; Seo, M. S.; Shaik, S.; Nam, W. *Chem. Eur. J.* **2012**, *18*, 10444–10453.

[3] Denisov, I. G.; Makris, T. M.; Sligar, S. G.; Schlichting, I. *Chem. Rev.* **2005**, *105*, 2253–2277.

[4] Ensing, B.; Buda, F.; Blöchl, P.; Baerends, E. J. *Angew. Chem. Int. Ed.* **2001**, *40*, 2893–2895.

[5] Gamez, P.; Arends, I. W.; Reedijk, J.; Sheldon, R. A. *Chem. Commun.* **2003**, 2414–2415.

[6] Geng, C. Y.; Ye, S. F.; Neese, F. *Angew. Chem. Int. Ed.* **2010**, *49*, 5717–5720.

[7] Gonzalez-Olmos, R.; Holzer, F.; Kopinke, F. D.; Georgi, A. *Appl. Catal., A* **2011**, *398*, 44–53.

[8] Kazaryan, A.; Baerends, E. J. *ACS Catal.* **2015**, *5*, 1475–1488.

[9] Lee, S. Y. T.; Cokoja, M.; Drees, M.; Li, Y.; Mink, J.; Herrmann, W. A.; KÃ¼hn, F. E. *ChemSusChem* **2011**, *4*, 1275–1279.

[10] Li, H.; She, Y.; Wang, T. *Frontiers of Chemical Science and Engineering* **2012**, *6*, 356–368.

[11] Limberg, C. *Angew. Chem. Int. Ed.* **2003**, *42*, 5932–5954.

[12] McDonald, A. R.; Guo, Y.; Vu, V. V.; Bominaar, E. L.; Munck, E.; Que, L. *Chem. Sci.* **2012**, *3*, 1680–1693.

[13] Musser, M. T. *Ullmann's Encyclopedia of Industrial Chemistry*; Wiley-VCH Verlag GmbH & Co. KGaA, 2000.

[14] Nam, W. *Acc. Chem. Res.* **2015**, *48*, 2415–2423, PMID: 26203519.

[15] Nam, W.; Lee, Y.-M.; Fukuzumi, S. *Acc. Chem. Res.* **2014**, *47*, 1146–1154, PMID: 24524675.

[16] Price, J. C.; Barr, E. W.; Tirupati, B.; Bollinger, J. M.; Krebs, C. *Biochemistry (Mosc.)* **2003**, *42*, 7497–7508.

[17] Semmelhack, M.; Schmid, C. R.; Cortes, D. A.; Chou, C. S. *J. Am. Chem. Soc.* **1984**, *106*, 3374–3376.

[18] de Visser, S. P.; Rohde, J.-U.; Lee, Y.-M.; Cho, J.; Nam, W. *Coord Chem Rev* **2013**, *257*, 381 – 393, A Tribute to Edward I. Solomon on his 65th Birthday: Part 2.

[19] Wang, D.; Ray, K.; Collins, M. J.; Farquhar, E. R.; Frisch, J. R.; Gomez, L.; Jackson, T. A.; Kerscher, M.; Waleska, A.; Comba, P.; Costas, M.; Que, L. *Chem. Sci.* **2013**, *4*, 282–291.

[20] Zakzeski, J.; Bruijnincx, P. C. A.; Jongerius, A. L.; Weckhuysen, B. M. *Chem. Rev.* **2010**, *110*, 3552–3599.

[21] Andrikopoulos, P. C.; Michel, C.; Chouzier, S.; Sautet, P. *ACS Catalysis* **2015**, *5*, 2490–2499 .

[22] Belanzoni, P.; Michel, C.; Baerends, E. J. *Inorganic Chemistry* **2011**, *50*, 11896–11904 .

[23] Guo, W.; Michel, C.; Schwiedernoch, R.; Wischert, R.; Xu, X.; Sautet, P. *Organometallics* **2014**, *33*, 6369–6380, .

[24] Michel, C.; Baerends, E. J. *Inorganic Chemistry* **2009**, *48*, 3628–3638 .

[25] Michel, C.; Belanzoni, P.; Gamez, P.; Reedijk, J.; Baerends, E. J. *Inorganic Chemistry* **2009**, *48*, 11909–11920 .

Inorg. Chem. **2009**, *48*, 3628−3638

Inorganic Chemistry
Article

What Singles out the FeO^{2+} Moiety? A Density-Functional Theory Study of the Methane-to-Methanol Reaction Catalyzed by the First Row Transition-Metal Oxide Dications $MO(H_2O)_p^{2+}$, M = V−Cu

Carine Michel and Evert Jan Baerends*

Theoretische Chemie, Vrije Universiteit Amsterdam, De Boelelaan 1083, 1081 HV Amsterdam, The Netherlands

Received November 1, 2008

Metaloxo species are often postulated as key active species in oxidative catalysis. Among all, the quintet FeO^{2+} moiety is particularly widespread and active: aliphatic C−H bonds undergo hydroxylation easily through a H-abstraction/O-rebound mechanism. The high electrophilicity of quintet FeO^{2+} originates from its electronic structure: a low lying vacant σ^* can accept electronic density from the aliphatic C−H bond. What singles out this quintet FeO^{2+}? Its lowest vacant acceptor orbital energy? its shape (σ^* vs π^*)? or has its biological importance more simply arisen from the high iron abundance? To answer those questions, we have performed density-functional theory calculations to study systematically the methane-to-methanol reaction catalyzed by $MO(H_2O)_p^{2+}$ complexes (M = V, Cr, Mn, Fe, Co, $p = 5$ and M = Ni, Cu, $p = 4$) in gas phase. We show here that the lower the MO^{2+} acceptor orbital lies in energy, the lower the H-abstraction barrier is in general. However, a σ^* acceptor orbital is much more efficient than a π^* acceptor orbital for a given energy. Finally, we found that indeed, the FeO^{2+} moiety is particularly efficient but also CoO^{2+} and MnO^{2+} could be good candidates to perform C−H hydroxylation.

Introduction

Homogeneous catalytic oxidation processes have attracted much attention for years for several reasons:[1] (1) they are one of the most challenging processes to bring to satisfactory peformance (yield, selectivities, sustainability, etc.); (2) the existing processes often leave room for considerable improvement; (3) involved mechanisms are quite complex (multiple pathways, multiple spin states); (4) they have extensive applications in various areas from fine chemical production[2] to waste degradation or bleaching.[3]

Currently, the main challenge is the development of green oxidative processes. To reach this goal, the stoichiometric oxidant has to be efficient, benign, and easily accessible. Dioxygen from air or hydrogen peroxide are the favorite ones, but they cannot oxidize directly and selectively alkanes into more valuable functionalized products such as alcohols, esters, aldehydes, ketones, and others.[1,4] Among all, the selective conversion of methane into various oxidized products, such as methanol and acetic acid, is particularly challenging: methane is the most abundant and unreactive hydrocarbon, a cheap raw material, and a greenhouse gas. New mild green selective routes to convert methane into valuable products could contribute to sustainable routes to methanol or other oxidized products and also to methods to lower its present concentration in the atmosphere. A widely used strategy in this field is to use transition metal complexes as catalysts together with a stoichiometric oxidant, such as dioxygen or peroxides. For instance, iron derivatives are used in Fenton-like processes in bleaching.[5,6] Manganese is a well-known key ingredient of the Jacobsen−Katsuki catalyst to perform alkene epoxidation.[7] And now, (salen)manganese complexes can also perform asymmetric oxidation of the σ C−H bond.[8] Last but not least, vanadium complexes such

* To whom correspondence should be addressed. E-mail: ej.baerends@few.vu.nl.

(1) Barton, D.; Martell, A.; Sawyer, D.; Sheldon, R.; van Santen, R. *Catalytic Oxidation: Principles and Applications*; World Scientific: Singapore, 1995.
(2) Caron, S.; Dugger, R. W.; Gut Ruggeri, S.; Ragan, J. A.; Brown Ripin, D. H. *Chem. Rev.* **2006**, *106*, 2943–2989.
(3) Hage, R.; Lienke, A. *Angew. Chem., Int. Ed.* **2006**, *45*, 206–222.
(4) Simandi, L. *Catalytic Activation of Dioxygen by Metal Complexes*; Kluwer Academic Publishers: Dordrecht, 1992.
(5) Fenton, H. J. H. *Chem. News* **1876**, 190.
(6) Pignatello, J. J.; Oliveros, E.; MacKay, A. *Crit. Rev. Environ. Sci. Technol.* **2006**, *36*, 1–84.
(7) Katsuki, T. *Coord. Chem. Rev.* **1995**, *140*, 189–214.
(8) Katsuki, T. *Synlett* **2003**, *3*, 281–297.

10.1021/ic802095m CCC: $40.75
Published on Web 03/20/2009

What Singles out the FeO^{2+} Moiety?

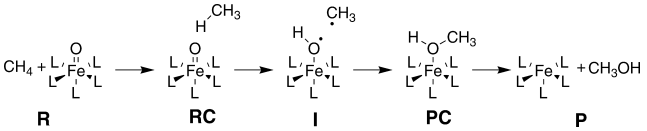

Figure 1. H-abstraction/O-rebound mechanism scheme. **R** is the reactants. **RC** is the reactants complex. **I** is the intermediate. **PC** is the products complex. **P** is the products.

as amadavine derivatives can perform a single-pot conversion of methane into acetic acid in the presence of potassium peroxodisulphate ($K_2S_2O_8$).[9−11] In all those examples, the postulated active species is the MO^{n+} moiety: FeO^{2+} in Fenton-like processes, MnO^{3+} in Jacobsen−Katsuki epoxidation,[12] VO^{2+} in amadavine derivatives.

The most widely spread MO^{n+} moiety is the oxoiron(IV) (ferryl ion) FeO^{2+}, well established in hydroxylating aliphatic C−H bonds.[13] A well-known example is the active center in heme iron enzymes such as cytochrome P450.[14−17] There is also evidence of such a reactive moiety for some non-heme enzymes,[18,19] for iron containing zeolites,[20,21] for biomimetic complexes,[22] or for the Fenton reaction.[23−25] This noticeable wide range of use, from enzymes to zeolite catalysts, leads us to the following question: What singles out FeO^{2+}?

First of all, iron is the most abundant transition metal in the Earth's crust, easily accessible and cheap.[26] This may explain why it is the most widespread co-factor of enzymes involved in oxidative processes for instance. But the main reason may lie also in the reactivity of the FeO^{2+} moiety. The C−H hydroxylation by the FeO^{2+} moiety is generally described by an H-abstraction/O-rebound mechanism, as proposed about 30 years ago by Groves and co-workers.[27,28] The scheme of this mechanism is given Figure 1: in the first step, one hydrogen atom is abstracted from the alkyl species by the FeO^{2+} species, yielding an $FeOH^{2+}$ moiety together with a carbon radical (intermediate **I**); in the second step, this latter species collapses onto the hydroxyl oxygen. This rebound step is almost a barrierless process.[25] Consequently, the kinetics of the reaction is controlled by the first step **RC** → **I**, namely the H-abstraction step.

Table 1. Ligand Environment Influence on the FeO^{2+} Moiety As Illustrated on the $FeO(H_2O)_n(NH_3)_{5-n}^{2+}$, n = 5,4,1,0 Complexes by Bernasconi et al.[30] [a]

ligand		spin	lowest vacant acceptor orbital		
equatorial	axial	$(2S+1)$	label	energy (eV)	energy barrier (kJ/mol)
H_2O	H_2O	5	$3\sigma^*(\alpha)$	−13.6	23
H_2O	NH_3	5	$3\sigma^*(\alpha)$	−13.3	54
NH_3	H_2O	3	$2\pi_x^*(\beta)$	−11.9	111
NH_3	NH_3	3	$2\pi_x^*(\beta)$	−11.9	103

[a] Those data refer to BLYP calculations as detailed in this work.[30] Note the strong influence of the strength of the equatorial ligand field on the spin state, the nature and energy (in eV) of the lowest vacant orbital and as a consequence on the H-abstraction energy barrier (in kJ/mol). Note also the influence of the axial ligand in the high spin state on the $3\sigma^*$ energy: an increase in the ligand donation (from H_2O to NH_3) pushes up the $3\sigma^*$ and as a consequence, leads to a higher energy barrier (kJ/mol) for the H-abstraction step.

Let us then focus on the H-abstraction from an alkyl C−H bond by a FeO^{2+} species. The first issue is the presence and the role of different spin states of the oxidoiron species.[29] To investigate the FeO^{2+} reactivity as a function of the spin state, Bernasconi et al. have studied the electronic structure and the reactivity of $[FeO(H_2O)_n(NH_3)_{5-n}]^{2+}$, n = 5,4,1,0 (see Table 1).[30] From those results, one can notice that the triplet state is stabilized by a strong equatorial ligand field, such as created by NH_3, whereas the quintet state is stabilized by a weak equatorial ligand field such as created by H_2O. The reason is simple and lies in the orbital pattern depicted in Figure 2 in the H_2O versus NH_3 equatorial environment case. The ligands lying in the equatorial plane affect the energy of the orbitals lying in this plane, namely the $1\delta_{xy}$ and the $1\delta_{x^2-y^2}$. The stronger the ligand field is, the more destabilized those δ orbitals are. The destabilization shift depends on the orbital shape: the $1\delta_{x^2-y^2}$ orbital is more strongly destabilized than the $1\delta_{xy}$ orbital because of its lobes

(9) Reis, P.; Silva, J.; Palavra, A.; Da Silva, J.; Kitamura, T.; Fujiwara, Y.; Pombeiro, A. *Angew. Chem., Int. Ed.* **2003**, *42*, 821–823.
(10) Kirillova, M. V.; Kuznetsov, M. L.; Reis, P. M.; Da Silva, J. A. L.; Da Silva, J. J. R. F.; Pombeiro, A. J. L. *J. Am. Chem. Soc.* **2007**, *129*, 10531–10545.
(11) Kirillova, M. V.; Kuznetsov, M. L.; Da Silva, J. A. L.; Guedes Da Silva, M. F. C.; Da Silva, J. J. R. F.; Pombeiro, A. J. L. *Chem.−Eur. J.* **2008**, *14*, 1828–1842.
(12) Mardani, H. R.; Golchoubian, H. *J. Mol. Catal. A: Chem.* **2006**, *259*, 197–200.
(13) Groves, J. T. *J. Inorg. Biochem.* **2006**, *100*, 434–447.
(14) de Visser, S. P.; Shaik, S.; Sharma, P. K.; Kumar, D.; Thiel, W. *J. Am. Chem. Soc.* **2003**, *125*, 15779–15788.
(15) Shaik, S.; Kumar, D.; de Visser, S. P.; Altun, A.; Thiel, W. *Chem. Rev.* **2005**, *105*, 2279–2328.
(16) Altun, A.; Shaik, S.; Thiel, W. *J. Am. Chem. Soc.* **2007**, *129*, 8978–8987.
(17) Schöneboom, J. C.; Neese, F.; Thiel, W. *J. Am. Chem. Soc.* **2005**, *127*, 5840–5853.
(18) Bassan, A.; Blomberg, M. R. A.; Borowski, T.; Siegbahn, P. E. M. *J. Inorg. Biochem.* **2006**, *100*, 727–743.
(19) Krebs, C.; Fujimori, D. G.; Walsh, C. T.; Bollinger, J. M. *Acc. Chem. Res.* **2007**, *40*, 484–492.
(20) Yoshizawa, K.; Yumura, T.; Shiota, Y.; Yamabe, T. *Bull. Chem. Soc. Jpn.* **2000**, *73*, 29–36.
(21) Yang, G.; Zhou, D.; Liu, X.; Han, X.; Bao, X. *J. Mol. Struct.* **2006**, *797*, 131–139.
(22) Nam, W. *Acc. Chem. Res.* **2007**, *40*, 522–531.
(23) Buda, F.; Ensing, B.; Gribnau, M.; Baerends, E. J. *Chem.−Eur. J.* **2001**, *7*, 2775–2783.
(24) Ensing, B.; Buda, F.; Blöchl, P.; Baerends, E. J. *Angew. Chem., Int. Ed.* **2001**, *40*, 2893–2895.
(25) Ensing, B.; Buda, F.; Gribnau, M. C. M.; Baerends, E. J. *J. Am. Chem. Soc.* **2004**, *126*, 4355–4365.
(26) Earnshaw, A.; Greenwood, N. *Chemistry of the elements*; Butterworth-Heinemann: Woburn, MA, 1997.
(27) Groves, J. T.; McClusky, G. A. *J. Am. Chem. Soc.* **1976**, *98*, 859–861.
(28) Groves, J. T.; Vanderpuy, M. *J. Am. Chem. Soc.* **1976**, *98*, 5290–5297.
(29) Neese, F. *J. Inorg. Biochem.* **2006**, *100*, 716–726.
(30) Bernasconi, L.; Louwerse, M. J.; Baerends, E. J. *Eur. J. Inorg. Chem.* **2007**, 3023–3033.

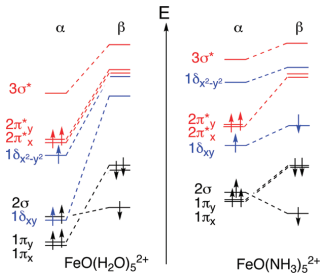

Figure 2. Simplified molecular orbital diagram for FeO^{2+} moiety in two different ligand environments: a weak equatorial ligand field environment (H_2O; left panel) favors the quintet spin state; a strong equatorial ligand field (NH_3; right panel) favors the triplet spin state. The most important orbitals are in color. The spin state is mainly controlled by the δ orbitals (in blue) whereas the reactivity is mainly controlled by the σ^* orbital (high spin configuration) or the π^* orbitals (low spin configuration) (in red).

pointing toward the ligands. When the destabilization is large enough, the $1\delta_{x^2-y^2}(\alpha)$ becomes then so high-lying that it loses its electron in favor of the $1\delta_{xy}(\beta)$, the complex switches from a high spin state (quintet) to a low spin state (triplet).

Thus, the spin state is essentially controlled by the strength of the equatorial field through the differential δ orbital destabilization. What about the reactivity? It has already been emphasized that the capability of the FeO^{2+} moiety to promote H-abstraction is directly connected to its electrophilicity: the C−H bond breaking is induced by electron donation from this C−H bond into a low lying empty molecular orbital of the FeO^{2+} species. This low lying empty orbital which accepts electronic density from the substrate is the *lowest acceptor molecular orbital*. It can be different from the lowest unoccupied molecular orbital (LUMO). Indeed, because of the hindrance of equatorial ligands, $1\delta_{x^2-y^2}$ and $1\delta_{xy}$ orbitals cannot accept density from the substrate C−H bond, but they can be the LUMO. The nature and the energy level of the lowest acceptor orbital depends on the spin state of this electrophilic species as illustrated by the $[FeO(H_2O)_n(NH_3)_{5-n}]^{2+}$, $n = 5, 4, 1, 0$ cases (see Table 1 and Figure 2). In a high spin configuration, the LUMO is the $1\delta_{xy}(\beta)$ orbital. The strong exchange field of the four unpaired α electrons stabilizes significantly the α orbitals. As a consequence, the $\sigma^*(\alpha)$ orbital is lying below the $2\pi^*(\beta)$ orbitals. It is the lowest acceptor orbital: it will accept electron donation from the C−H bond during the H-abstraction step. In the low spin configuration, the exchange field stabilization is weaker; hence, the $2\pi_x^*(\beta)$ orbital is both the LUMO and the lowest acceptor orbital. As seen previously, the strength of the equatorial ligand field controls the relative position of the 1δ energy levels—from which follow the spin state and the nature of the lowest acceptor orbital. It also controls the global position of the energy levels of the π and σ orbitals. Indeed, donating ligands such as NH_3 induce a global stronger destabilization of those orbitals and as a consequence they reduce the FeO^{2+} electrophilicity. To conclude, the choice of the equatorial ligands is crucial. A weak ligand field strongly enhances the electrophilicty of the FeO^{2+} moiety: (1) orbitals are relatively low lying in energy, (2) the high spin state stabilizes the lowest lying vacant orbital ($3\sigma^*(\alpha)$) by the strong exchange field.

Last but not least, what about the influence of the axial ligand field? The axial ligand may affect the molecular orbitals lying along the z axis, namely the σ and π orbital. Indeed, according to Bernasconi et al.,[30] a stronger σ-donating ligand pushes up the $3\sigma^*$. Thus, the electrophilicity of the FeO^2 is reduced, the H-abstraction energy barrier is higher. For instance, replacing H_2O by NH_3 in axial position of the $FeO(H_2O)_5^{2+}$ complex leads to a higher lying $3\sigma^*(\alpha)$ (from −13.6 eV to −13.3 eV) and a higher energy barrier (from 23 to 54 kJ/mol) (see Table 1). This effect can be used to tune the reactivity of a FeO^{2+} complex in high spin configuration.[30,31]

In summary: (1) a wide range of transition metals can be used to perform oxidation reactions; (2) the FeO^{2+} moiety is a widespread active species in alkyl hydroxylation, from zeolites to enzymes; (3) the strong reactivity of the high spin FeO^{2+} moiety results from its electronic structure: the low lying $3\sigma^*(\alpha)$ vacant orbital is responsible for its strong electrophilicity, making it accept electrons even from poor donating entities such as aliphatic C−H bonds. We thus understand the role of the ligand environment on the reactivity of the FeO^{2+} species. In this article, we will focus on the role of the metal. We present here an extensive study in gas phase of the methane-to-methanol reaction catalyzed by the first row transition-metal oxide-dications $MO(H_2O)_p^{2+}$ (M = V, Cr, Mn, Fe, Co, $p = 5$ and M = Ni, Cu, $p = 4$). The electronic structure analysis together with the reactive scheme for each complex allow us to discuss the relative importance of the vacant $3\sigma^*$ compared with the vacant $2\pi^*$ and to highlight the great importance of the "d count" on the reactivity of those complexes.

Method

Level of Theory. All the calculations have been performed using the ADF (Amsterdam Density Functional) package,[32−35] using the OPBE density functional.[36,37] This functional has been chosen for its performance in describing close-lying spin states, in particular in iron complexes.[38] In the ADF code, the electronic orbitals are written in terms of Slater-type orbitals (STO). We use a triple-ζ basis set with two polarization functions for the C, O, and H atoms and a quadruple zeta basis set with three polarization functions for the transition metal atoms, as available in the ADF library of standard basis sets. Additionally, the calculations were corrected for relativistic effects using the zero-order regular approximation (ZORA) approach.[39,40] When needed, the frequencies are computed

(31) Bernasconi, L.; Baerends, E. J. *Eur. J. Inorg. Chem.* **2008**, 1672–1681.
(32) Bickelhaupt, F.; Baerends, E. *Rev. Comp. Chem.* **2000**, *15*, 1–86.
(33) Baerends, E. J.; Ellis, D. E.; Ros, P. *Chem. Phys.* **1973**, *2*, 41–51.
(34) Velde, G. T.; Bickelhaupt, F. M.; Baerends, E. J.; Guerra, C. F.; Van Gisbergen, S. J. A.; Snijders, J. G.; Ziegler, T. *J. Comput. Chem.* **2001**, *22*, 931–967.
(35) *SCM, ADF2006.01*; Theoretical Chemistry,Vrije Universiteit Amsterdam: The Netherlands, 2006; http://www.scm.com/.
(36) Perdew, J. P.; Burke, K.; Ernzerhof, M. *Phys. Rev. Lett.* **1997**, *78*, 1396.
(37) Cohen, A. J.; Handy, N. C. *Mol. Phys.* **2001**, *99*, 607–615.
(38) Swart, M.; Ehlers, A.; Lammertsma, K. *Mol. Phys.* **2004**, *102*, 2467–2474.
(39) van Lenthe, E.; Baerends, E. J.; Snijders, J. G. *J. Chem. Phys.* **1994**, *101*, 9783–9792.
(40) van Lenthe, E.; Ehlers, A.; Baerends, E. J. *J. Chem. Phys.* **1999**, *110*, 8943–8953.

What Singles out the FeO^{2+} Moiety?

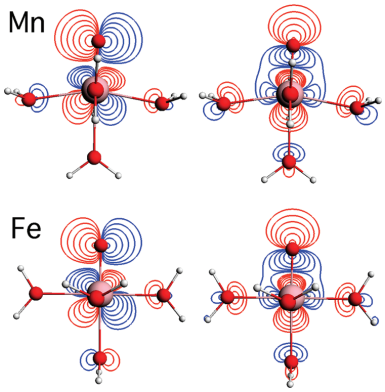

Figure 3. $2\pi_x^*(\alpha)$ (left side) and $3\sigma(\alpha)^*$ (right side) molecular orbitals of the $MnO(H_2O)_5^{2+}$ (top) and $FeO(H_2O)_5^{2+}$ (bottom) in the ground state.

analytically. All the transition state structures have been characterized by the presence of an imaginary frequency.

Chosen Systems. To better understand the reactivity of the MO^{2+} moiety toward aliphatic C−H bonds, it is crucial to take into account its ligand environment. Indeed, as seen in the Introduction, it influences the electronic structure and the spin state of the MO^{2+} moiety, hence its reactivity toward a C−H bond. To study the influence of the metal, we have chosen to study a hydrated MO^{2+} moiety.

First, the presence of ligands prevents methane from interacting directly with the transition metal. For the bare oxo MO^+ in gas phase, Shiota and Yoshizawa propose for instance a reactant complex OM-CH_4^+ where the methane interacts directly with the metal and an intermediate HOM-CH_3^+, which exhibits a metal−carbon bond.[41] Such a mechanism is strongly disadvantaged if the metal is surrounded by ligands.[25]

In our study of the influence of the "d count" on the reactivity of the MO^{2+} moiety, we have chosen to focus on the first row transition metal series, from vanadium to copper. The chosen systems are then the $MO(H_2O)_p^{2+}$ complexes (M = V, Cr, Mn, Fe, Co, Ni, Cu). They can be divided into two groups according to the number p of water molecules in the first solvation shell of the MO^{2+} moiety.

• $p = 5$: for M = V, Cr, Mn, Fe, Co, the $MO(H_2O)_5^{2+}$ complex is pseudo-octahedral, keeping almost the same geometry along the series. The M=O distance is slightly increasing from 1.54 Å to 1.59 Å when going from V to Co. The metal-water distances are between 2.05 Å and 2.15 Å in general (see the iron case in Figure 4 and Table 2).

• $p = 4$: for M = Ni, Cu, the $MO(H_2O)_4^{2+}$ complex presents a strongly distorted trigonal bipyramid geometry coordination, the oxo group lying in the trigonal plane (see Figure 5 and Table 2). Some species along the reaction path can afford an extra water molecule such as $NiO(H_2O)_4^{2+}$ in high spin state ($2S + 1 = 5$). However, most of the species along the reaction path cannot afford an extra water molecule in their coordination sphere: all attempts to optimize the geometry of $NiO(H_2O)_4^{2+}$ in low spin state or $CuO(H_2O)_4^{2+}$ in both spin states result in the dissociation of one metal-water bond. We therefore keep in all cases the coordination shell constant at four water molecules along the entire reaction path.

(41) Shiota, Y.; Yoshizawa, K. *J. Am. Chem. Soc.* **2000**, *122*, 12317–12326.

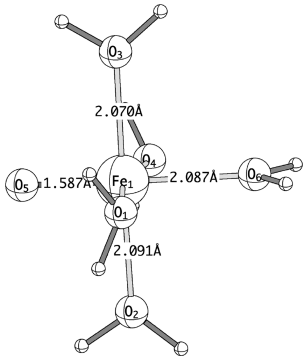

Figure 4. Structure of $FeO(H_2O)_5^{2+}$, high spin state. Distances are given in angstrom. See Table 2 for data on angles.

Table 2. Geometrical Data for $MO(H_2O)_p^{2+}$, M = Fe and $p = 5$, M = Ni, Cu and $p = 4$ in Their Ground State[a]

angle	Fe	Ni	Cu
O1−M−O2	87.8	93.0	107.7
O1−M−O3	92.7	87.8	94.6
O1−M−O4	168.5	129.4	91.1
O1−M−O5	95.0	110.3	108.0
O1−M−O6	85.0		
O2−M−O3	178.9	165.8	157.1
O2−M−O4	87.2	85.9	87.2
O2−M−O5	90.6	97.4	88.3
O2−M−O6	90.3		
O3−M−O4	91.9	82.6	87.6
O3−M−O5	90.3	95.6	89.2
O3−M−O6	88.8		
O4−M−O5	95.5	119.9	160.7
O4−M−O6	84.5		
O4−M−O5	179.1		

[a] Angles are in degree. See Figure 4 and Figure 5 for notations.

Results and Discussion

First, we will focus on the electronic structure of the MO^{2+} moiety in the $MO(H_2O)_p^{2+}$ complexes. Then, we will expose the reaction scheme of the methane hydroxylation catalyzed by those complexes. Those results will provide us some clues to answer the questions raised in the introduction: what is the relative importance of the vacant $3\sigma^*$ compared with the vacant $2\pi^*$ orbital? what is the importance of the "d count" on the reactivity of the MO^{2+} species? what singles out FeO^{2+}?

Electronic Structure of the MO^{2+} Moiety. The electronic structure of the $MO(H_2O)_p^{2+}$ complex is reported in Table 3. All along the series, the M−O bonding results from the filling of the 1π and 2σ orbitals, which are $M_{3d}-O_{2p}$ bonding orbitals. From V to Fe, each added electron occupies an extra α orbital, stabilized by the exchange field: $1\delta_{x^2-y^2}(\alpha)$ in the chromium complex, $2\pi_x^*(\alpha)$ in the manganese complex, $2\pi_y^*(\alpha)$ in the iron complex. As a consequence, the spin state increases regularly from doublet to quintet. Then, the next step is cobalt. Whereas the spin state of the bare oxo complex CoO^{2+} is a sextet, the extra electron occupies a β orbital ($1\delta_{xy}(\beta)$) in the $CoO(H_2O)_5^{2+}$ complex, leading to a quartet

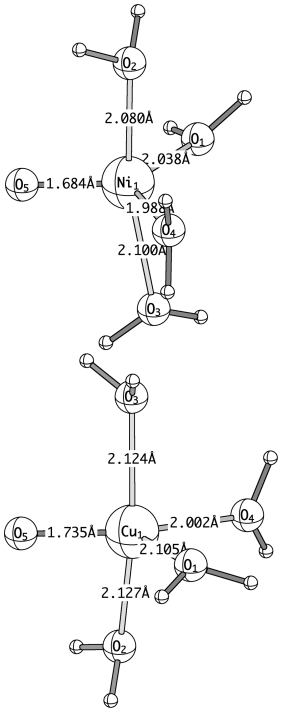

Figure 5. Structures of $MO(H_2O)_4^{2+}$, M = Ni, Cu, high spin state. Distances are given in angstrom. See Table 2 for data on angles.

Table 3. Spin State ($2S + 1$) and Electronic Configuration of the Ground State of $MO(H_2O)_p^{2+}$ (for M = V, Cr, Mn, Fe, Co, $p = 5$; for M = Ni, Cu, $p = 4$)

metal	spin ($2S + 1$)	configuration
V	2	$(2\sigma)^2\,(1\pi_x)^2\,(1\pi_y)^2\,1\delta_{xy}$
Cr	3	$(2\sigma)^2\,(1\pi_x)^2\,(1\pi_y)^2\,1\delta_{xy}\,1\delta_{x^2-y^2}$
Mn	4	$(2\sigma)^2\,(1\pi_x)^2\,(1\pi_y)^2\,1\delta_{xy}\,1\delta_{x^2-y^2}\,2\pi_x^*$
Fe	5	$(2\sigma)^2\,(1\pi_x)^2\,(1\pi_y)^2\,1\delta_{xy}\,1\delta_{x^2-y^2}\,2\pi_x^*\,2\pi_y^*$
Co	4	$(2\sigma)^2\,(1\pi_x)^2\,(1\pi_y)^2\,(1\delta_{xy})^2\,1\delta_{x^2-y^2}\,2\pi_x^*\,2\pi_y^*$
Ni	5	$(2\sigma)^2\,(1\pi_x)^2\,(1\pi_y)^2\,(1\delta_{xy})^2\,1\delta_{x^2-y^2}\,2\pi_x^*\,2\pi_y^*\,3\sigma^*$
Cu	4	$(2\sigma)^2\,(1\pi_x)^2\,(1\pi_y)^2\,(1\delta_{xy})^2\,(1\delta_{x^2-y^2})^2\,2\pi_x^*\,2\pi_y^*\,3\sigma^*$

spin state for the ground state. Then, in nickel and copper, the extra electron occupies successively the $3\sigma^*(\alpha)$ and the $1\delta_{x^2-y^2}(\beta)$, leading to two complexes with all 3d α orbitals filled.

We have already emphasized in the Introduction the importance of the *lowest lying acceptor orbital* for the electrophilic properties of the FeO^{2+} moiety. Along this series, it can be either a σ^* orbital or a π^* orbital. These orbitals are illustrated with plots of the $3\sigma^*(\alpha)$ and the $2\pi^*(\alpha)$ for Mn and Fe complexes in Figure 3.

Table 4 gives some properties of the lowest vacant $3\sigma^*$, the lowest vacant $2\pi^*$, and the LUMO (which may or may not be the $2\pi^*$ or $3\sigma^*$): energy, spin, composition in terms of d metal and p oxygen percentage ($\%d_M$ and $\%p_O$). In Figure 6, we plot the most important molecular orbital energies as a function of the metal: $2\pi^*(\alpha)$, $3\sigma^*(\alpha)$, $1\delta_{xy}(\beta)$, $1\delta_{x^2-y^2}(\beta)$, $2\pi^*(\beta)$, and $3\sigma^*(\beta)$ (in order of increasing energy). From this table and Figure 6, the first striking fact is that the molecular orbital energy decreases when the atomic number of M increases: it is due to the higher nuclear charge along the series. A closer analysis of those results leads us to divide the studied complexes into three groups according to the lowest vacant orbital:

Table 4. Selected Vacant Molecular Orbitals (Energy in eV) for the Ground State of $MO(H_2O)_p^{2+}$ (for M = V, Cr, Mn, Fe, Co, $p = 5$; for M = Ni, Cu, $p = 4$)[a]

	LUMO		lowest vacant $3\sigma^*$				lowest vacant $2\pi^*$			
metal	label	E	spin	$\%d_M$	$\%p_O$	E	spin	$\%d_M$	$\%p_O$	E
V	$2\pi^*(\alpha)$	−12.2	α	45	20	−10.1	α	64	29	−12.2
Cr	$2\pi^*(\alpha)$	−13.8	α	44	25	−12.0	α	44	32	−13.8
Mn	$2\pi^*(\alpha)$	−14.8	α	43	32	−13.2	α	34	59	−14.8
Fe	$\delta_{xy}(\beta)$	−14.3	α	40	36	−13.9	β	50	35	−13.2
Co	$3\sigma^*(\alpha)$	−14.5	α	42	30	−14.5	β	47	47	−14.1
Ni	$1\delta_{x^2-y^2}(\beta)$	−15.7	β	26	18	−14.8	β	63	18	−15.4
Cu	$2\pi^*(\beta)$	−16.3	β	36	18	−15.8	β	16	58	−16.3

[a] The molecular orbital spin is provided together with its composition in terms of d metal orbitals percentage ($\%d_M$) and p oxygen orbitals ($\%p_O$) percentage.

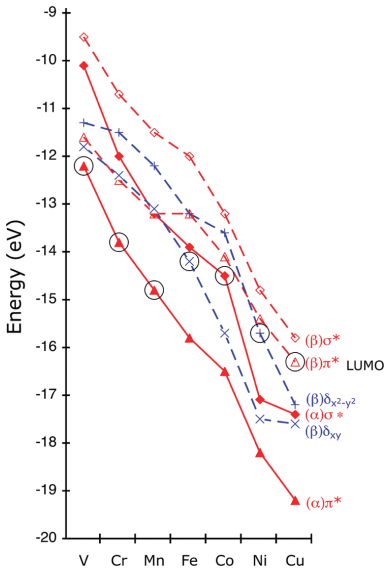

Figure 6. Energies of molecular orbitals of interest (in eV) for the studied complexes $(MO(H_2O)_p^{2+}$, M = V, Cr, Mn, Fe, Co, $p = 5$; for M = Ni, Cu, $p = 4$). As a guide to the eye, we connect the same orbitals with a line that is solid for α orbitals and dashed for β orbitals. For the sake of simplicity, π_x and π_y are not distinguished. The LUMO orbital is highlighted by a black circle.

M = V, Ce, Mn. In this group, the lowest acceptor orbital is a $2\pi^*(\alpha)$ orbital. It is also the LUMO.

M = Fe, Co. In this group, the lowest acceptor orbital is the $3\sigma^*(\alpha)$ orbital. In the iron case, it differs from the LUMO ($1\delta_{xy}(\beta)$), for Co, it is the LUMO.

M = Cu, Ni. In this group, the lowest acceptor orbital is a $2\pi^*(\beta)^*$ orbital. In the nickel case, it differs from the LUMO ($1\delta_{x^2-y^2}(\beta)$), for Cu, it is the LUMO.

What Singles out the FeO^{2+} Moiety?

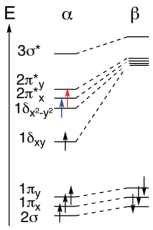

Figure 7. Simplified molecular orbital diagram of $MO(H_2O)_5^{2+}$, M = V, Cr, Mn. The black spins represent the occupation in the vanadium case. For the chromium complex, the supplementary spin (here in blue) occupies the $1\delta_{x^2-y^2}(\alpha)$ orbital. Then, for the manganese complex, the second extra electron (here in red) occupies the $2\pi_x^*(\alpha)$ orbital. For the sake of simplicity, we have not shown here the crossing between $2\pi_x^*(\alpha)$ and the $\delta_{x^2-y^2}$ when switching from the vanadium to the chromium complex. The main consequence of the energy levels crossing is that the LUMO in both complexes is the $2\pi_x^*(\alpha)$ molecular orbital.

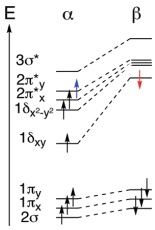

Figure 8. Simplified molecular orbital diagram of $MO(H_2O)_5^{2+}$, M = Fe, Co. The black spins represent the occupation in the manganese case. For the iron complex, the supplementary spin (here in blue) occupies the $2\pi_y^*(\alpha)$ orbital. Then, for the cobalt complex, the second extra electron (here in red) occupies the $1\delta_{xy}(\beta)$ orbital.

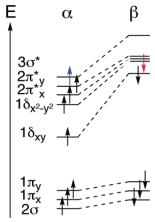

Figure 9. Simplified molecular orbital diagram of $MO(H_2O)_4^{2+}$, M = Ni, Cu. The black spins represent the occupation in the cobalt case. For the nickel complex, the supplementary spin (here in blue) occupies the $3\sigma^*(\alpha)$ orbital. Then, for the copper complex, the second extra electron (here in red) occupies the $1\delta_{x^2-y^2}(\beta)$ orbital.

Let us consider the electronic structure within each group.

V, Cr, Mn. A schematic orbital energy diagram of this group is given Figure 7. From V to Mn, each added electron occupies an extra α orbital, stabilized by the exchange field: $1\delta_{x^2-y^2}(\alpha)$ in Cr complex, $2\pi_x^*(\alpha)$ in Mn complex. The spin state increases from doublet to quartet.

Along this group, very few crossings of energy levels occur. The most noticeable one is the crossing of the $2\pi_x^*(\alpha)$ level from below the $1\delta_{x^2-y^2}(\alpha)$ level in the vanadium complex to above the $1\delta_{x^2-y^2}(\alpha)$ level in the chromium complex. For the sake of simplicity, we only represent the orbital ordering for the Cr and Mn cases in the simplified orbital energy diagram of Figure 7. The consequence of this swap is that even with one more α electron in the chromium complex, the lowest acceptor orbital is the same ($2\pi_x^*(\alpha)$) in both the V and Cr complexes.

Thus, in this group, the lowest vacant acceptor orbital, which is also the LUMO, is a $2\pi^*(\alpha)$ orbital, namely the $2\pi_x^*(\alpha)$ orbital for V and Cr and the $2\pi_y^*(\alpha)$ for Mn. Two factors have to be taken into account to predict the electrophilicity of the MO^{2+} moiety: the energy of the lowest vacant orbital, $\varepsilon_{2\pi^*(\alpha)}$, and its oxygen p orbital contribution, $\%p_O$. Generally speaking, the lower the acceptor orbital lies in energy and the higher the $\%p_O$ is, the more electrophilic the MO^{2+} will be: they are both in favor of a large electronic donation from the C−H bond into the MO^{2+} acceptor orbital. Within the series (V, Cr, Mn), $\varepsilon_{2\pi^*(\alpha)}$ is strongly decreasing (from −12.2 eV to −14.8 eV) while $\%p_O$ is strongly increasing (from 29% to 59%), see Figure 6 and Table 4. So, from V to Mn, the $MO(H_2O)_5^{2+}$ complex should be more and more efficient in performing H-abstraction from methane.

Previous studies have demonstrated the high reactivity of the $FeO(H_2O)_5^{2+}$ complex. The lowest acceptor orbital of this complex is the $3\sigma^*(\alpha)$, lying at −13.9 eV. Thus, on the basis of the energy level of the lowest acceptor orbital, one should expect the Mn complex to be even more efficient than the Fe complex. However, the nature of the lowest acceptor orbital differs ($2\pi^*(\alpha)$ versus $3\sigma^*(\alpha)$). In the $2\pi^*$ case, the overlap efficiency requires sideways approach, leading to steric hindrance of the incoming organic substrate molecule (e.g., CH_4) with the equatorial water ligands. This competition may reduce the Mn complex oxidative activity.

Fe, Co. A schematic orbital energy diagram is given in Figure 8. From Mn to Fe, the extra electron goes into the $2\pi_y^*(\alpha)$, leading to the expected high spin configuration (quintet) for the $FeO(H_2O)_5^{2+}$ complex. In the $CoO(H_2O)_5^{2+}$ complex case, the extra electron occupies a β orbital, leading to a quartet spin state for the ground state.[42] Thus, for both iron and cobalt, the $2\pi^*(\alpha)$ is doubly occupied and the lowest acceptor orbital is the $3\sigma^*(\alpha)$ orbital. We have already pointed out that the two main parameters which can control the electrophilicity of the complex are the energy and the $2p_O$ contribution of the lowest lying vacant orbital. The $3\sigma^*(\alpha)$ energy and the $2p_O$ contribution are similar in both complexes: the cobalt complex $3\sigma^*(\alpha)$ lies 0.6 eV below the iron complex $3\sigma^*(\alpha)$ (see Figure 6), but its p_O contribution is slightly less favorable (30% vs 36%), see Table 4. Previous studies have demonstrated the high reactivity of $FeO(H_2O)_5^{2+}$ complex. Even if cobalt has been used much less than iron in oxidative processes, it is clear that cobalt complexes should be as reactive as iron complexes, if not more so.

Ni, Cu. A schematic molecular diagram is given in Figure 9. We have already set apart those two complexes because of a reduced number of water ligands in the coordination shell. They can also be distinguished through their electronic structure. All the α orbitals of interest are occupied: from

(42) Cobalt is the only case where the spin state of the complex $MO(H_2O)_p^{2+}$ differs from the spin state of the bare oxo MO^{2+}.

Table 5. Studied Reaction: $MO(H_2O)_p^{2+} + CH_4 \rightarrow M(H_2O)_p^{2+} + CH_3OH$, i.e., **R** → **P**[a]

	spin ($2S+1$)		
metal	**R**	**P**	ΔE (kJ/mol)
V	2	4	149.1
Cr	3	5	−46.0
Mn	4	6	−206.8
Fe	5	5	−119.1
Co	4	4	−153.8
Ni	5	3	−218.8
Cu	4	2	−302.4

[a] For each metal, this table gives the spin state of the reactant **R** and product **P** ground state and ΔE, the energetic cost of the reaction (in kJ/mol).

cobalt to nickel complex, the extra electron occupies the $3\sigma^*(\alpha)$ leading to a quintet spin state. Then, from nickel to copper, the extra electron is added into the $1\delta_{x^2-y^2}$ orbital. Thus, in both complexes, the lowest lying acceptor orbital is a $2\pi^*(\beta)$. As seen previously, the energy and the composition of this $2\pi^*(\beta)$ orbital determine the electrophilicity of the complex. In the copper complex, the $2\pi^*(\beta)$ lies at a lower energy (−16. eV vs −15.4 eV) and its $2p_O$ contribution is larger (58% vs 18%) than in the nickel complex. So, we can assume that this complex may be more reactive than the Ni complex to perform alkyl hydroxylation.

Anyway, both Ni and Cu complexes seem very promising to promote C−H oxidation based on the lowest vacant orbital energy level (at least 1 eV lower than the iron one). The nature of the lowest acceptor orbital ($2\pi^*(\beta)$) may reduce the efficiency of those complexes because of the overlap/steric hindrance of the water ligands upon the sideways approach of a substrate molecule, which is required for optimal overlap with $2\pi^*$ orbitals. The lower number of water molecules should however reduce the impact of this competition. However, very little is known about the stability of those complexes as active intermediates in oxidative catalysis.

Along the Series. The energy of the lowest acceptor orbital and its $2p_O$ orbital contribution are a bit less favorable in Fe and Co complex than in the Mn or Cu complex. However, for iron and cobalt, the lowest acceptor orbital is the $3\sigma^*(\alpha)$, not a $2\pi^*$ orbital. As noted, the overlap between the acceptor orbital and the C−H bonding orbital may be lower with a $2\pi^*$ orbital than with a $3\sigma^*$ orbital because of the steric hindrance of the ligands. Thus, no conclusion can be drawn yet concerning the H-abstraction capability of all these complexes. To investigate further the $MO(H_2O)_p^{2+}$ reactivity toward the C−H bond, we have made an extensive study of the intermediates and transition states involved in the $CH_4 + MO(H_2O)_p^{2+} \rightarrow M(H_2O)_p^{2+} + CH_3OH$ reaction.

Mechanism. Overview. In Table 5, data concerning the **R** → **P** reaction are collected: energetic cost $\Delta E = E(P) - E(R)$, spin state of the reactants **R**, spin state of the products **P**. Except in the vanadium case, this reaction is exoenergetic. The energetic cost decreases from V (149.1 kJ/mol) to Cu (−302.4 kJ/mol) and is particularly low in the Mn case (−206.8 kJ/mol). Moreover, this reaction implies a spin crossing, except for iron and cobalt.

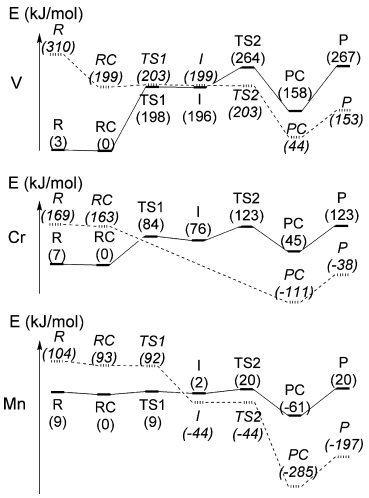

Figure 10. Energy profile (in kJ/mol) for the methane to methanol conversion catalyzed by $MO(H_2O)_5^{2+}$, M = V, Cr, Mn. Dashed line stands for the high spin mechanism and continuous line for the low spin mechanism. Along the reaction coordinate, the following species have been characterized: the reactants $MO(H_2O)_5^{2+}$ and CH_4 (**R**); the reactant complex $[MO(H_2O)_5^{2+}, CH_4]$ (**RC**); the transition state corresponding to the H-abstraction step (**TS1**); the intermediate $[MOH(H_2O)_5^{2+}\cdots{}^{\bullet}CH_3]$, (**I**); the transition state corresponding to the rebound step (**TS2**); the product complex $MCH_3OH(H_2O)_5^{2+}$ (**PC**); the products $M(H_2O)_5^{2+}$ and CH_3OH (**P**).

This reaction follows a rebound mechanism (see Figure 1).[25] First, one hydrogen atom is abstracted from the substrate, here CH_4. This yields intermediate **I** ($MOH(H_2O)_p^{2+} + {}^{\bullet}CH_3$. Then, the carbon radical ${}^{\bullet}CH_3$ can collapse onto the hydroxo group to yield the product complex **PC** ($M(OHCH_3)(H_2O)_p^{2+}$). The energy profile of those steps is given in Figure 10 for the V, Cr and Mn complexes, in Figure 11 for the Fe and Co complexes, and in Figure 12 for the Ni and Cu complexes.

The rebound step is relatively uninteresting, being very smooth. Data concerning this step are collected in Table 6: spin evolution, energetic cost $\Delta E_2 = E(P) - E(I)$, energy barrier $\Delta E^{\ddagger}_{TS2}$, C−O distance and MOC angle in the transition state structure. This step is highly exoenergetic in all cases. It is a non-activated process or with very low activation barrier $\Delta E^{\ddagger}_{TS2}$. Thus, we will mainly focus on the H-abstraction step, which controls the reaction kinetics. We will put in evidence the strong link between the activation energy $\Delta E^{\ddagger}_{TS1}$, and the transition state structure (**TS1**) on one hand and the lowest lying acceptor orbital of the $MO(H_2O)_p^{2+}$ complex on the other hand. In the previous section, we have discussed the electronic structure of the $MO(H_2O)_p^{2+}$ complexes. To supplement this, we have also performed a detailed study of the electronic structure of the H-abstraction transition state structures (**TS1**) thanks to a fragment interaction analysis. We have chosen to focus on the interaction between two fragments[43] in the transition state geometry: (i) the fragment $MO(H_2O)_p^{2+}$ (ii) the fragment CH_4. The

What Singles out the FeO^{2+} Moiety?

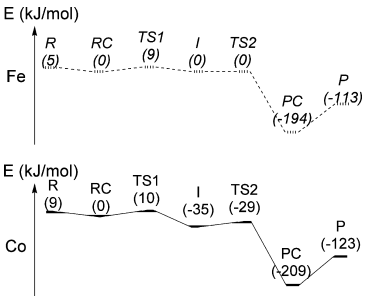

Figure 11. Energy profile (in kJ/mol) for the methane to methanol conversion catalyzed by $MO(H_2O)_5^{2+}$, M = Fe, Co. Dashed line stands for the high spin mechanism and continuous line for the low spin mechanism. Along the reaction coordinate, the following species have been characterized: the reactants $MO(H_2O)_5^{2+}$ and CH_4 (**R**); the reactant complex $[MO(H_2O)_5^{2+}, CH_4]$ (**RC**); the transition state corresponding to the H-abstraction step (**TS1**); the intermediate $[MOH(H_2O)_5^{2+}\cdots CH_3]$ (**I**); the transition state corresponding to the rebound step (**TS2**); the product complex $MCH_3OH(H_2O)_5^{2+}$ (**PC**); the products $M(H_2O)_5^{2+}$ and CH_3OH (**P**).

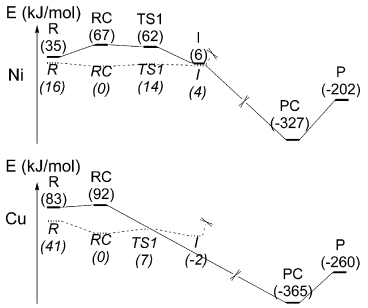

Figure 12. Energy profile (in kJ/mol) for the methane to methanol conversion catalyzed by $MO(H_2O)_4^{2+}$, M = Ni, Cu. Dashed line stands for the high spin mechanism and continuous line for the low spin mechanism. Along the reaction coordinate, the following species have been characterized: the reactants $MO(H_2O)_4^{2+}$ and CH_4 (**R**); the reactant complex $[MO(H_2O)_4^{2+}, CH_4]$ (**RC**); the transition state corresponding to the H-abstraction step (**TS1**); the intermediate $[MOH(H_2O)_5^{2+}\cdots CH_3]$ (**I**); the transition state corresponding to the rebound step (**TS2**); the product complex $MCH_3OH(H_2O)_4^{2+}$ (**PC**); the products $M(H_2O)_4^{2+}$ and CH_3OH (**P**).

Table 6. Data for the Rebound Step: **I** → **PC**[a]

	spin state					
metal	**I**	**PC**	ΔE_2 (kJ/mol)	$\Delta E^{\ddagger}_{TS2}$ (kJ/mol)	C−O (Å)	MOC (deg)
V	2	4	−37.3	7.5	2.12	140
Cr	3	6	−187.5			
Mn	6	6	−249.5	0	3.33	173
Fe	5	5	−194.9	0	2.59	135
Co	4	4	−173.1	6.6	3.00	159
Ni	3	3	−331.1			
Cu	2	2	−363.2			

[a] For each metal, this table gives the spin state ($2S+1$) of **I** and **PC** ground state and the energetic cost of the reaction $\Delta E_2 = E(PC) - E(I)$ (in kJ/mol). It provides also the activation energy $\Delta E^{\ddagger}_{TS2}$ (kJ/mol), the CO distance (in Å), and the MOC angle (in degree) in the transition state structure **TS2**.

gross population of the interesting fragment molecular orbitals in the transition state structure **TS1** are given in Table 8. The overlaps between the σ_{C-H} orbital of the stretched C−H bond and the $2\pi^*$ and $3\sigma^*$ orbitals of the complexes are given in Table 9.

Table 7. Studied Reaction: **RC** → **I**[a]

	spin state							lowest vacant acceptor MO	
metal	**RC**	**I**	ΔE_1 (kJ/mol)	$\Delta E^{\ddagger}_{TS1}$ (kJ/mol)	C−H (Å)	O−H (Å)	MOH (deg)	label	energy (eV)
V	2	2	196.3	198.9	1.76	1.04	128	$2\pi^*(\alpha)$	−12.2
Cr	3	3	76.3	84.9	1.39	1.17	125	$2\pi^*(\alpha)$	−13.8
Mn	4	6	−44.7	9.7	1.34	1.20	126	$2\pi^*(\alpha)$	−14.8
Fe	5	5	0.7	9.2	1.25	1.32	179	$3\sigma^*(\alpha)$	−13.9
Co	4	4	−35.0	11.7	1.34	1.19	177	$3\sigma^*(\alpha)$	−14.5
Ni	5	5	4.1	14.5	1.38	1.20	123	$2\pi^*(\beta)$	−15.4
Cu	4	4	−2.5	6.8	1.30	1.28	125	$2\pi^*(\beta)$	−16.3

[a] For each metal, this table gives the spin state ($2S+1$) of **RC** and **I** (ground states) and the energetic cost ΔE_1 of the reaction (in kJ/mol). It provides also the activation energy $\Delta E^{\ddagger}_{TS1}$, the OH distance (in Å) and the MOH angle (in degree) in the transition state structure **TS1**. The last two columns are a reminder of the key data concerning the lowest vacant acceptor molecular orbital: label and energy (in eV).

Table 8. Fragment Analysis of the Transition State Structure **TS1** for Each Complex $MO(H_2O)_p^{2+}$ (M = V, Cr, Mn, Fe, Co, $p = 5$; for M = Ni, Cu, $p = 4$)[a]

	α				β			
metal	$2\pi^*_x$	$2\pi^*_y$	$3\sigma^*$	σ_{C-H}	$2\pi^*_x$	$2\pi^*_y$	$3\sigma^*$	σ_{C-H}
V	0.43	0.40	0.02	0.28	0.05	0.05	0.02	0.89
	+0.43	*+0.40*	*+0.02*	*−0.72*	*+0.05*	*+0.05*	*+0.02*	*−0.11*
Cr	0.99	0.67	0.02	0.46	0.03	0.06	0.02	0.91
	+0.99	*+0.67*	*+0.02*	*−0.54*	*+0.03*	*+0.06*	*+0.02*	*−0.09*
Mn	0.74	0.96	0.04	0.43	0.09	0.03	0.03	0.91
	+0.74	*−0.04*	*+0.04*	*−0.57*	*+0.09*	*+0.03*	*+0.03*	*−0.09*
Fe	0.97	0.97	0.51	0.63	0.01	0.01	0.14	0.87
	−0.03	*−0.03*	*+0.51*	*−0.37*	*+0.01*	*+0.01*	*+0.14*	*−0.13*
Co	0.99	0.99	0.67	0.43	0.04	0.04	0.10	0.88
	−0.01	*−0.01*	*+0.67*	*−0.57*	*+0.04*	*+0.04*	*+0.10*	*−0.12*
Ni	0.97	0.97	0.98	0.94	0.29	0.34	0.09	0.37
	−0.03	*−0.03*	*−0.02*	*−0.06*	*+0.29*	*+0.34*	*+0.09*	*−0.63*
Cu	0.97	0.98	0.99	0.96	0.48	0.16	0.07	0.41
	−0.03	*−0.02*	*−0.01*	*−0.04*	*+0.48*	*+0.16*	*+0.07*	*−0.59*

[a] The two fragments are $MO(H_2O)_p^{2+}$ and CH_4. In this table, the gross populations of the relevant fragment molecular orbitals are given: the $2\pi^*$ and $3\sigma^*$ of the complex and the σ_{C-H} of the methane. In italic, the difference between the integer gross population in the isolated fragment and the gross population in the transition state. The orbitals have been defined in spin restricted calculations on the isolated fragments in the geometry they have in **TS1**.

Data related to the H-abstraction step are collected in Table 7: spin state evolution, energetic cost (ΔE_1), and activation energy barriers ($\Delta E^{\ddagger}_{TS1}$), selected geometrical data of the transition state structures (**TS1**). We have also added some key features of the electronic structure of the reactant $MO(H_2O)_p^{2+}$.

As we already noticed, this series can be divided into three groups according to the lowest acceptor orbital of the $MO(H_2O)_p^{2+}$ complex. We keep this subdivision to discuss the mechanism of the reaction $CH_4 + MO(H_2O)_p^{2+} \rightarrow M(H_2O)_p^{2+} + CH_3OH$. Before entering the discussion of the three groups we note that the calculated transition barriers are for gas phase reactions, and therefore much lower than

(43) The orbitals of the fragments are obtained in spin restricted calculations on the fragments with the geometries they have in the transition state. The orbital occupations have been enforced to yield electronic structures for the fragments that conform to the situation in the complex.

Table 9. Overlaps between the Highest σ Molecular Orbital of the CH_4 Fragment and the Molecular Orbitals of Interest of the Metal Complex Are Given for the Transition State Structure **TS1** of Each Complex $MO(H_2O)_p^{2+}$ (M = V, Cr, Mn, Fe, Co, $p = 5$; for M = Ni, Cu, $p = 4$)[a]

metal	$2\pi_x^*$	$2\pi_y^*$	$3\sigma^*$
V	0.0783	0.093	0.0583
Cr	0.0035	0.1147	0.05605
Mn	0.1171	0.0334	0.05317
Fe	0.0031	0.0021	0.1200
Co	0.0088	0.0063	0.1378
Ni	0.1029	0.1207	0.0891
Cu	0.1359	0.0813	0.0770

[a] The fragments are $MO(H_2O)_p^{2+}$ and CH_4.

what would be obtained in water solvent. This difference between gas phase and solvent has been observed in Car−Parrinello MD simulations on the FeO^{2+} catalyzed oxidation of methane to methanol in water solution.[25] It was found that the solvent effect raises the barrier by more than 80 kJ/mol. This explains that the methane to methanol conversion is not readily effected by ironoxo based catalysts or enzymes, even though the barrier in the gas phase is quite low. The solvent effect has also been studied with polarizable continuum models and a full explanation has been given[44] based on the very electronic structure characteristics of this reaction we are discussing in this work. The solvent effects will affect all the reactions similarly, and we therefore can use the present gas phase studies to obtain insight in the differences between the various metaloxo species.

V, Cr, Mn. For the earlier metal complexes (V, Cr, Mn), the high spin state surface lies above the low spin state surface in the entrance channel (before **TS1**) of the considered reaction (see Figure 10). In the vanadium case, the spin crossing occurs in the entrance channel of the second step (the rebound step). For the chromium complex, the high spin surface does not exhibit any intermediate **I** such as $[CrOH(H_2O)_5^{2+}, {}^{\bullet}CH_3]$. Thus, it is hard to predict when the spin crossing is likely to occur. In the manganese case, the spin crossing is likely to occur in the exit channel of the first step (the H-abstraction step).

Whereas the rebound step is, as observed before, an almost barrierless process in each case (see Table 6), the H-abstraction can exhibit quite a high barrier $\Delta E_{TS1}^{\ddagger}$, depending on the metal used (up to 198.9 kJ/mol in the vanadium case, see Table 7). For the H-abstraction step, the energetic cost ΔE_1 *and* the energy barrier $\Delta E_{TS1}^{\ddagger}$ decrease along the series V, Cr, Mn. As one could expect, the lower the activation energy barrier is, the longer the O−H bond is (from 1.04 Å to 1.20 Å) and the shorter the C−H bond is (from 1.76 Å to 1.34 Å). The manganese complex is particularly efficient with a low energy barrier of 9.7 kJ/mol.

Let us then focus on the correlation between the electronic structure and the H-abstraction step efficiency. As we noticed previously, the $2\pi^*(\alpha)$ orbital is the lowest vacant acceptor orbital in this first group (V, Cr, Mn). According to the fragment analysis, the $\sigma(\alpha)_{C-H}$ donates electronic density to the $2\pi^*(\alpha)(MO^{2+})$ during the H-abstraction step (see Table 8). Indeed, in the transition state **TS1**, the $\sigma(\alpha)$(C−H) gross population has dropped from 1.00 in free CH_4 to 0.28 in **TS1**(V), 0.46 in **TS1**(Cr), 0.43 in **TS1**(Mn). Meanwhile, the $2\pi^*(\alpha)(MO^{2+})$ gross population has increased: from 0 in the free vanadium complex to 0.83 (0.40 + 0.43) in the transition state; from 0 in the free chromium complex to 1.66 (0.99 + 0.67) in the transition state; from 0 in the free Mn complex to 0.70 (0.74 − 0.04) in the transition state. In the Cr case, the transfer of 1.66 el. to the two $2\pi^*(\alpha)$ orbitals gives the impression of a two-electron transfer. However, this is not consistent with the decrease in population of the $\sigma(\alpha)_{C-H}$ orbital of −0.54. This apparent inconsistency is resolved if one takes into account that there is an electronic configuration change of the metal complex when going to the transition state: the $\delta_{x^2-y^2}(\alpha)$ is emptied in favor of the $2\pi^*(\alpha)$ orbital.

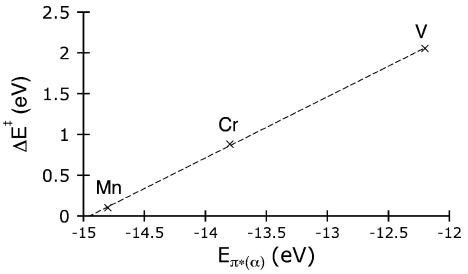

Figure 13. Activation energy of the H-abstraction step $\Delta E^{\ddagger}$ is linearly correlated to the energy of the lowest vacant molecular orbital ($E_{\pi^*(\alpha)}$) along the series $MO(H_2O)_5^{2+}$, M = V, Cr, Mn.

This electronic donation clearly controls the transition state geometry and the activation energy $\Delta E_{TS1}^{\ddagger}$. First, the transition state geometry presents an MOH angle of around 125° (see Table 7) which results from the balance between the orbital interaction (maximized for a 90° MOH angle) and the Pauli repulsion resulting from the equatorial water ligands, which increases when this angle approaches 90°. Then, at these angles of about 125° the activation energy $\Delta E_{TS1}^{\ddagger}$ is linearly correlated to the $2\pi^*(\alpha)$ orbital energy $\varepsilon_{\pi^*(\alpha)}$: $\Delta E_{TS1}^{\ddagger} = 0.75 \times \varepsilon_{\pi^*(\alpha)} + 11.212$ (in eV), with $R^2 = 0.9997$ (see Figure 13). So, the lower the $2\pi^*(\alpha)$ (MO^{2+}) lies in energy ($\varepsilon_{\pi^*(\alpha)}$), the lower the H-abstraction energy barrier ($\Delta E_{TS1}^{\ddagger}$) is.

Fe, Co. No spin crossing occurs during the C−H bond hydroxylation within this group. The reaction occurs on the high spin surface when catalyzed by $FeO(H_2O)_5^{2+}$ complex whereas it occurs on the low spin surface when catalyzed by $CoO(H_2O)_5^{2+}$ complex (see Figure 11).

This second group (Fe, Co) exhibits a $\sigma^*(\alpha)$ orbital as the lowest vacant acceptor orbital. From the fragment analysis, there is clearly an electronic donation from the $\sigma(\alpha)_{C-H}$ molecular orbital to the lowest $\sigma^*(\alpha)_{complex}$ molecular orbital during the H-abstraction (see Table 8): in the transition state structure, about half-electron has been donated from the $\sigma(\alpha)_{C-H}$ to the $\sigma^*(\alpha)_{complex}$. There is also a smaller donation from the $\sigma(\beta)_{C-H}$ molecular orbital to the lowest $\sigma^*(\beta)_{complex}$ molecular orbital (about 0.1 electron).

This donation clearly controls the transition state geometry: Pauli repulsion and orbital interaction are both in favor of a linear transition state (MOH angle around 180°). The $3\sigma^*(\alpha)$

(44) Louwerse, M.; Baerends, E. J. *Phys. Chem. Chem. Phys.* **2007**, 156.

What Singles out the FeO^{2+} Moiety?

lies lower in energy in the cobalt case than in the iron case (−14.5 eV vs −13.9 eV). The energy barriers ($\Delta E^{\ddagger}_{TS1}$) are close (11.7 kJ/mol vs 9.2 kJ/mol). Furthermore, if one compares with the first group (V, Cr, Mn), the energy barrier $\Delta E^{\ddagger}_{TS1}$ is particularly low given that the lowest acceptor orbital energies for, for example, the Cr and Mn complexes, are close to those of the Fe and Co complexes. For instance, the iron complex lowest vacant acceptor orbital energy (−13.9) is very close to the chromium complex one (−13.8 eV) whereas the energy barrier $\Delta E^{\ddagger}_{TS1}$ is much lower: 9.2 kJ/mol versus 84.9 kJ/mol. This huge difference in oxidative capability for a given lowest vacant orbital energy results from the difference in the nature of the lowest vacant orbital. In the chromium case, it is a $2\pi^*$ orbital whereas in the iron case, it is a $3\sigma^*$. During the electronic donation from the C−H bond into this lowest vacant acceptor orbital, the orbital interaction competes with the Pauli repulsion resulting from the water ligands. In both cases, the Pauli repulsion is minimized for an 180° angle whereas the orbital interaction stabilization is optimal for an angle of 90° in the chromium case and 180° in the iron case. The synergy between the strong orbital interaction stabilization and a reduced Pauli repulsion leads to an highly efficient iron complex whereas the disfavorable competition between those two terms leads to a less efficient chromium complex. So, the efficiency of the high spin FeO^{2+} arises from the energy and the orientation of the acceptor orbital, the $3\sigma^*(\alpha)$. According to this study, the high spin CoO^{2+} should be as efficient as the high spin FeO^{2+}, exhibiting the same acceptor orbital.

Ni, Cu. For these late metal complexes, the high spin surface lies below the low spin surface in the entrance channel of the oxidative process (see Figure 12). Then, this high spin state is highly destabilized once the H-abstraction has been carried out: no structure could be optimized for the intermediate species **PC** ($MCH_3OH(H_2O)_4^{2+}$). On the other hand, the low spin surface is highly reactive in both cases. It lies much higher in energy than the high spin surface. The reactant complex **RC** is even higher in energy than the isolated molecules. However, once the CH_4−O distance is small enough (<3 Å), the oxidation of the C−H bond occurs without any barrier, yielding the very stable species $MCH_3OH(H_2O)_4^{2+}$. As a consequence, the spin crossing occurs necessarily before the rebound step, but it is hard to say when exactly.

Let us focus now on the high spin surface reactivity. Let us remember that this last group (Ni, Cu) is characterized first by a different coordination environment, four water molecules instead of five, and second by a $\pi^*(\beta)$ orbital as the lowest vacant acceptor orbital. Once again, the fragment analysis demonstrates that the lowest acceptor orbitals, namely, here the $\pi^*(\beta)$ orbitals, accept electronic density from the $\sigma_{C-H}\beta$ orbital (around 0.6 electron, see Table 8). In this group, the donation from the $\sigma(\alpha)_{C-H}$ orbital to some acceptor molecular orbital of the complex is not feasible: all the α acceptor molecular orbitals are occupied.

The $\sigma_{C-H}\beta \rightarrow 2\pi^*_{x,y}\beta$ donation clearly controls the transition state geometry. Similarly to the V, Cr, Mn group, where also donation into $2\pi^*$ prevails, the **TS1** geometry presents an MOH angle of around 125° (see Table 7), resulting from the balance between orbital interaction (optimal for 90°) and Pauli repulsion (mimimal for 180°). Furthermore, this donation also controls the H-abstraction energy barrier ($\Delta E^{\ddagger}_{TS1}$): the lower the $2\pi^*(\beta)$ lies in energy, the lower $\Delta E^{\ddagger}_{TS1}$ is. But given the very low energy of the acceptor orbitals in this group, particularly in the Cu complex (−16.3 eV), one might have expected an even lower barrier than the low one we have obtained (14.5 kJ/mol for Ni, 6.8 kJ/mol for Cu), or even a barrierless process. An explanation may be the larger Pauli repulsion due to all the occupied α orbitals of the metal complex. Nevertheless, if such species could be generated, they would be highly reactive.

Summary: π^* versus σ^* Control along the Series. The MO^{2+} electrophilicity can be quantified through the H-abstraction energy barrier: the lower $\Delta E^{\ddagger}_{TS1}$ is, the more electrophilic the MO^{2+} moiety is. We have seen previously that the H-abstraction step can be controlled by the electron donation from the σ_{C-H} orbital into the lowest vacant acceptor orbital, namely, the lowest $2\pi^*$ or the $3\sigma^*(\alpha)$. In the first and the last group (V, Cr, Mn and Ni, Cu), the MO^{2+} electrophilicity is under $2\pi^*$ control whereas in the Fe and Co cases, the MO^{2+} electrophilicity is under $3\sigma^*(\alpha)$ control. Let us analyze further the differences between $2\pi^*$ and $3\sigma^*(\alpha)$ control.

Under the $2\pi^*$ control, the lower the $2\pi^*$ orbital lies in energy, the more electrophilic the MO^{2+} moiety is. In the first group, $\varepsilon_{2\pi^*(\alpha)}$ and $\Delta E^{\ddagger}_{TS1}$ are even linearly correlated (see Figure 13). In the last group, the MO^{2+} electrophilicity is controlled by the $2\pi^*(\beta)$: the lower it is, the lower the H-abstraction barrier is. Given the low $2\pi^*(\beta)$ energy $\varepsilon_{2\pi^*(\beta)}$ for the Ni and Cu complexes, the H-abstraction energy barrier $\Delta E^{\ddagger}_{TS1}$ is higher than one might have expected. However, as we have already seen, the α orbitals are fully occupied. Hence, the donation from the $\sigma(\alpha)_{C-H}$ orbital to some 3d-based α acceptor molecular orbital of the complex is not feasible. Futhermore, we can divide the Pauli repulsion into two terms: (1) the Pauli repulsion generated by the interaction of occupied substrate orbitals with MO^{2+} occupied molecular orbitals, and (2) the Pauli repulsion with the ligands. From the first group (V, Cr, Mn) to the last one (Ni, Cu), the first term is increased by the greater number of electrons on MO^{2+} whereas the second term is decreased (only 4 ligands instead of 5). From the energy barriers $\Delta E^{\ddagger}_{TS1}$ one would infer that the larger Pauli repulsion with the MO^{2+} electrons in the last group than in the first one outweighs the reduced Pauli repulsion with the ligands. To conclude, under $2\pi^*$ control, the electrophilicity is directly correlated to the $2\pi^*$ energy only for a given Pauli repulsion.

Under $3\sigma^*(\alpha)$ control, which applies in the case of the Fe and Co complexes, the low energy barrier (around 10 kJ/mol) is striking. The orbital energy of the lowest vacant acceptor orbital of the iron complex is pretty close to the one of the chromium complex, whereas the energy barrier

is quite different: 9.2 kJ/mol in the iron case versus 84.9 kJ/mol in the chromium case. If we would apply the correlation between activation energy $\Delta E^{\ddagger}_{TS1}$ and the controlling orbital energy as obtained in the first group (Figure 13), we would obtain an activation barrier of 75.8 kJ/mol instead of 9.2 kJ/mol in the iron case. This is also true for the cobalt complex: for the H-abstraction step we would obtain an activation barrier of 32.3 kJ/mol instead of 11.7 kJ/mol. Obviously, when the reaction is performed under $3\sigma^*(\alpha)$ control it is much more efficient. The σ^* controlled reactions present lower barriers than the π^* controlled reactions for a given orbital energy thanks to the combination of two effects: (1) the Pauli repulsion with the ligands is lower in the linear geometry, and (2) the orbital overlap is larger (see Table 9).

Conclusions

In this work, we have systematically studied the methane-to-methanol reaction catalyzed by the first row transition-metal complexes $MO(H_2O)_p^{2+}$. This reaction follows a rebound mechanism in two steps: (1) H-abstraction leading to a MOH^{2+} species, and (2) carbon radical collapse onto this species. The first step is the kinetic controlling step for all the studied complexes. The activation barrier and the transition state geometry of this H-abstraction step are directly correlated to the nature of lowest acceptor orbital. The main results are as follows: (1) the σ^* controlled H-abstraction reactions present linear transition states and π^* controlled H-abstraction reactions present bent transition states, (2) the σ^* controlled reactions present lower activation barriers than the π^* controlled reactions for a given lowest acceptor orbital energy, and (3) the activation barrier is directly correlated to the lowest vacant orbital energy provided the Pauli repulsion remains the same (same number of ligands, similar number of electrons) and provided the lowest acceptor orbital remains of the same type (σ^* or π^*). So, now we can answer the question raised in the Introduction. Iron is so special because of the nature of its lowest acceptor orbital: a low lying $3\sigma^*(\alpha)$, which is particularly efficient in promoting the H-abstraction step according to our results. However, the Fe complex does not emerge from this study as the only one. According to our results, the cobalt complex should be as efficient as iron for the Fenton chemistry under the proper experimental conditions. Indeed, cobalt-based compounds have already been used successfully in oxidation of cyclohexane[45−47] and even in decomposition of organic dyes.[48]

Finally, this study leads on to other questions. For instance, what is the ligand environment effect in the cobalt complex? We have seen in the introduction that a nitrogen equatorial environment induces a less favorable low spin state and less reactive species in the iron case. Preliminary tests on the cobalt system indicate the effect to be in the same direction, but Cobalt seems to be less sensitive to those environmental effects. The $CoO(NH_3)_5^{2+}$ complex is high spin (quartet). Its lowest acceptor orbital is still the $3\sigma^*(\alpha)$($\varepsilon_{3\sigma^*(\alpha)} = -12.4$ eV). The H-abstraction step energy barrier is still quite low ($\Delta E_1^{\dagger} = 77.1$ kJ/mol), though much higher than for $CoO(H_2O)_5^{2+}$ (11.7 kJ/mol).

Another question concerns the charge effect. Let us take two isoelectronic complexes: $FeO(H_2O)_5^{2+}$ and $MnO(H_2O)_5^{+}$. The electronic structures of those two complexes are very similar: same spin state (quintet), same lowest acceptor orbital ($3\ \sigma^*(\alpha)$). However, the charge decrease from the Fe to the Mn complex induces orbitals lying higher in energy: $\varepsilon_{3\sigma^*(\alpha)}$ ($FeO(H_2O)_5^{2+}$) $= -13.9$ eV and $\varepsilon_{3\sigma^*(\alpha)}$ ($MnO(H_2O)_5^{+}$) $= -6.7$ eV. As expected, the activation barrier of the H-abstraction step catalyzed by $MnO(H_2O)_5^{+}$ is much higher than the one catalyzed by $FeO(H_2O)_5^{2+}$ ($\Delta E_1^{\dagger}$ (Mn) $= 105.3$ kJ/mol vs $\Delta E_1^{\dagger}$ (Fe) $= 9.2$ kJ/mol. The late transition metal complexes should be less sensitive to this charge effect. Indeed, with a lowest acceptor orbital lying at -9.7 eV, the $CuO(H_2O)_3^{+}$ complex seems to be a promising active species. CuO^{+} has already been postulated in some enzymes and biologically relevant systems as an possible intermediate.[49,50] These and other points will be the subject of further investigations.

Acknowledgment. Support by the National Research School Combination "Catalysis by Design" is gratefully acknowledged.

IC802095M

(45) Pokutsa, A. P.; Sheparovich, R. B.; Zaborovskii, A. B.; Kopylets, V. I. *Kinet. Catal.* **2002**, *43*, 691–697.
(46) Pokutsa, A. P.; Zaborovskii, A. B.; Sheparovich, R. B.; Kopylets, V. I.; Maksim-Lutsik, D. S. *Kinet. Catal.* **2003**, *44*, 121–128.
(47) Tong, J.; Zhen, L.; Xia, C. *J. Mol. Catal. A: Chem.* **2005**, *231*, 197–203.
(48) Chen, W. X.; Lu, W. Y.; Yao, Y. Y.; Xu, M. H. *Environ. Sci. Technol.* **2007**, *41*, 6240–6245.
(49) Kamachi, T.; Kihara, N.; Shiota, Y.; Yoshizawa, K. *Inorg. Chem.* **2005**, *44*, 4226–4236.
(50) Pitié, M.; Boldron, C.; Pratviel, G. *Adv. Inorg. Chem.* **2006**, *58*, 77–1330.

ACS Catalysis

Research Article

pubs.acs.org/acscatalysis

In Silico Screening of Iron-Oxo Catalysts for CH Bond Cleavage

Prokopis C. Andrikopoulos,[†] Carine Michel,[†] Sandra Chouzier,[‡] and Philippe Sautet*[,†]

[†]University of Lyon, CNRS, Laboratoire de Chimie, UMR5182, ENS de Lyon, 69364 Lyon, France

[‡]Research and Innovation Centre Lyon, Solvay Polyamide and Intermediates, 69192 Saint-Fons, France

Supporting Information

ABSTRACT: Inspired by oxidation enzymes such as P450 and TauD, several groups have based their research on the iron−oxo moiety in the field of alkanes partial oxidation. Still, the controlled cleavage and oxidation of the aliphatic C−H bond remains a prized goal in chemistry. We present here a computational methodology to predict the comparative reactivity of iron−oxo complexes for this process from linear relations based on the sole electronic structure of the reactant state. The efficient correlation of the C−H activation barrier to a simple but intuitive molecular orbital descriptor enables the design of ligands that permit low barrier C−H abstraction steps and the fast screening of novel potential complexes. The activation of the catalyst by a multidentate effect is also evidenced. We anticipate this study to improve the rational design of hydrocarbon oxidation catalysts.

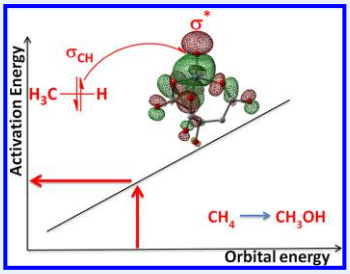

KEYWORDS: *alkane partial oxidation, methane, iron-oxo complex, activation energy, molecular orbital descriptor*

INTRODUCTION

Iron complexes are gradually moving to the forefront of the field of alkane activation.[1−5] These have been inspired by analogue processes in biological systems,[6] where Fe^{IV}=O active sites are responsible for the activity such as the cytochrome-P450 compound-I[7] or the intermediate J of taurine dioxygenase (TauD).[8] In order for iron complexes to cross over to useful applications in industry, an effort in documenting and predicting their properties in a consistent manner has to be implemented—a task that is undertaken here by theoretical means.

The high spin Fe^{IV}=O intermediate is a strong electrophile that can abstract a hydrogen atom from an alkane. A rebound step follows, that forms the C−O bond and leads to the corresponding alcohol.[9] Certain patterns have emerged from the number of iron−oxo complexes that have been recently examined. The C−H abstraction step is expected to be crucial in the full oxidation cycle, the overall kinetics being correlated to the strength of the C−H bond of various substrates.[10] The pK_a of the Fe^{IV}−OH intermediate is also essential to the overall activity as demonstrated recently in cytochrome P450.[11] In other words, the driving force for the C−H activation by the Fe^{IV}=O moiety is given by the difference between the energy of the C−H bond to be broken (BDE_{CH}) and the energy of the O−H bond to be formed (BDE_{OH}). De Visser has rationalized those trends on a family of seven Fe-oxo complexes using DFT calculations: the height of the hydrogen abstraction barrier of propene is linearly correlated to the reaction energy, $\Delta H = BDE_{CH} - BDE_{OH}$.[12] This approach has been generalized recently in a meta-analysis of 13 computational studies on hydrogen abstraction by iron and manganese oxo complexes demonstrating the importance of the reaction driving force.[13] This correlation between the barrier height and the reaction energy is known as the Bell−Evans−Polanyi principle.[14]

Since the pioneering works of K. Fukui[15] and R. Hoffmann,[16] the importance of the interactions between the molecular orbitals of the reagents, and mainly between the frontier orbitals, is well-known as a key parameter governing reactivity. In the CH abstraction step, the proton transfer to the oxo-oxygen is coupled to an electron transfer from the σ(CH) of the alkane substrate to the lowest vacant acceptor orbital of the electrophilic Fe^{IV}=O group.[17,18] The qualitative role of several parameters was underlined for this interaction from the electronic structure calculations of octahedral Fe^{IV}=O complexes.[19−23] Shaik and co-workers stressed the influence of the overlap between the alkane σ(CH) and the acceptor orbitals on the complex to determine the structure of the transition state. Baerends and co-workers noted the crucial importance of the energy of the acceptor orbital. On a set of four model complexes with water as equatorial ligands, they were able to modulate the energy of the acceptor orbital by the nature of the axial ligand and modify the calculated barriers. However, to the best of our knowledge, those qualitative analyses were not transformed into a detailed and predictive correlation between the C−H abstraction barrier and a well-defined electronic structure parameter of the initial complex. Such a correlation would supplement the existing ones derived from the BEP principle providing a fundamental and easy descriptor of the Fe^{IV}=O activity.

Received: July 12, 2014
Revised: March 10, 2015
Published: March 10, 2015

DOI: 10.1021/cs500996k
ACS Catal. 2015, 5, 2490−2499

The possible spin states of d^4 Fe^{IV}═O intermediates are S = 0, 1, or 2 depending on the ligand field. The singlet state (S = 0) is generally very unstable and will not be considered here, the ground state of the complexes being either the triplet (S = 1, called here low spin (LS) for simplicity) or quintet state (S = 2, called here high spin (HS)). In the presence of strong enough donor ligands, (typically nitrogen based), octahedral Fe^{IV}═O intermediates have a triplet low spin (LS) state, the lowest acceptor orbital being generally the so-called $\beta-\pi^*$ (antibonding combination of d_{xz}(Fe)/d_{yz}(Fe) and p_x(O)/p_y(O) in the β manifold; see Figure 1a). The corresponding

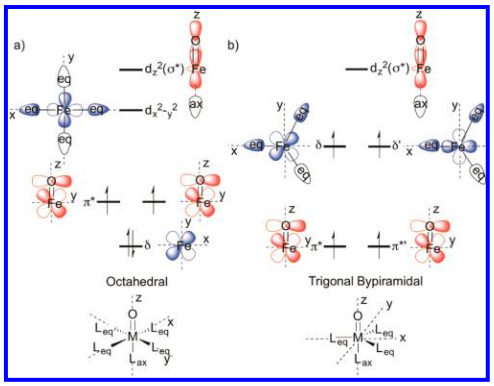

Figure 1. Frontier molecular orbitals of (a) an octahedral Fe-oxo complex in a low spin configuration including the interaction with the equatorial (in the x, y plane) and axial (along the z axis) ligands. In the high spin configuration, the down-spin electron from the δ orbital is promoted to the $d_{x^2-y^2}$ orbital, resulting to a total of four unpaired electrons and (b) a trigonal bipyramidal Fe−oxo complex in a high spin configuration. In this simplified representation up and down spin orbitals are shown with the same energy.

reaction channel is the LS-π path. The proton transfer is coupled to the electron transfer from the σ(CH) of the alkane to the π^*(Fe^{IV}═O). This electronic interaction requires a perpendicular orientation between the CH bond and the Fe^{IV}═O bond, leading to a bended transition state.[24] In the HS state, two types of possible acceptor orbitals are competing, defining two reaction channels: the $\beta-\pi^*$ and the so-called $\alpha-\sigma^*$ (antibonding combination of d_{z^2}(Fe) and p_z(O) in the α spin manifold of molecular orbitals).[25] The $\beta-\pi^*$ opens a HS-π path, similar to the LS-π path. The $\alpha-\sigma^*$ orbital is generally the lowest acceptor orbital on the Fe^{IV}═O fragment due to the considerable electron exchange stabilization of the α molecular orbitals manifold in the S = 2 configuration.[26] This $\alpha-\sigma^*$ acceptor orbital opens a HS-σ path, where the electronic interactions lead to a linear transition state, the CH and the Fe═O bonds being collinear. This alignment favors the frontier orbital overlap[27] and reduces the Pauli repulsion between the alkane and the ligands.[23] These reaction channels have been described in more details in recent reviews.[18,28,29] Later in the text, the $\alpha-\sigma^*$ will be noted simply as σ^* and the $\beta-\pi^*$, simply as π^*.

This active HS-σ path can be reached by weakening the ligand field and a common strategy is to reduce the number of donor ligands in the equatorial plane. One approach is to create a trigonal bipyramidal configuration at the iron with the oxo-oxygen along the axis of the pyramid and three nitrogen type ligands in the equatorial plane, while one N atom holds the other axial position.[30,31] This configuration ensures a high spin ground state (Figure 1b) that is preserved along the hydrogen abstraction step. Another strategy to reach the most active state is the spin crossover from a low spin (S = 1) ground state to a high spin (S = 2) excited state in a two-state reactivity mechanism popularized by Schröder, Shaik, and Schwarz.[32] An indication of its energetic cost is provided by the HS−LS adiabatic gap. The lowest energy path for the reaction is then determined by a comparison of the barrier of the LS-π path against the sum of the HS-σ path barrier and the spin gap.

The working hypothesis of the present paper asserts that the C−H abstraction barrier and the lowest acceptor orbital energy of the initial Fe═O complex are correlated: the lower the acceptor orbital energy, the lower the energy barrier would be. For a high spin ground state complex, the barrier will be related to the energy of the σ^* acceptor orbital (HS-σ path). For a low spin ground state, the barrier will be related to the energy of the π^* orbital (LS-π path). In this latter case, the high spin S = 2 excited state will also be considered. Its σ^* energy will be related to the corresponding HS barrier to compare the multistate reactivity with the LS-π path. These basic qualitative effects were outlined in the original works by Baerends[19−21,27,33] and Shaik.[18,26,32] The work presented here will demonstrate how these can be expanded into a valuable tool for catalyst prediction employing an extensive set combining model and realistic catalysts to establish a correlation between the activation energy and the energy of the lowest acceptor orbital (σ^* for the HS path and π^* for the LS path).

RESULTS

In order to test this hypothesis and demonstrate the correlation, a large data set of iron-oxo complexes was chosen, shown in Figures 2 and 3 (see also the *XYZ* coordinates in the Supporting Information (SI)). The choice of systems was made from popular ligands from the literature,[5] porphyrin complexes,[3] iron ligands from chemical databases, and simple model systems, while methane was the chosen substrate. Since the focus of the paper is on the influence of the ligand, the substrate was not changed. A conscious effort was made to obtain a diverse set of ligands that span the whole range of lowest acceptor orbital energies. The first set, shown in Figure 2, is comprised of complexes with a total charge of 2+. This set mixes model complexes designed to rationalize trends (**1**−**12**, **23**−**28**) and also complexes selected from the literature (**13**−**22**, **19**−**38**)[5] to provide a direct comparison with experiments. This set includes a variety of complexes with mainly N donors: cyclams (TMC **34**−**36**),[34,35] bicyclic bispidine ligands (**32**, **33**),[36] tripodal ligands motifs with pyridyl (TPA **17**), guanidine (TMG3tren **18**), amino (Me6-TREN **22**), or benzimidazole (Me3NTB **37**) groups,[37,38] EDTA (**38**), etc. Those complexes are included, as is customary, without the counterions that would balance the total charge and in some cases, complete the metal coordination.[30]

The second set (Figure 3) covers neutral complexes, selected from the literature[5] or derived from commercially available ligands and Fe complexes. Complexes belonging to the first group can be shifted to the second group by including the omitted counterions. The influence of those counterions can be quite complex[39] and will not be covered extensively in this study. The division in two sets is required since the energy range of the acceptor orbitals differs according to the charge

DOI: 10.1021/cs500996k
ACS Catal. 2015, 5, 2490−2499

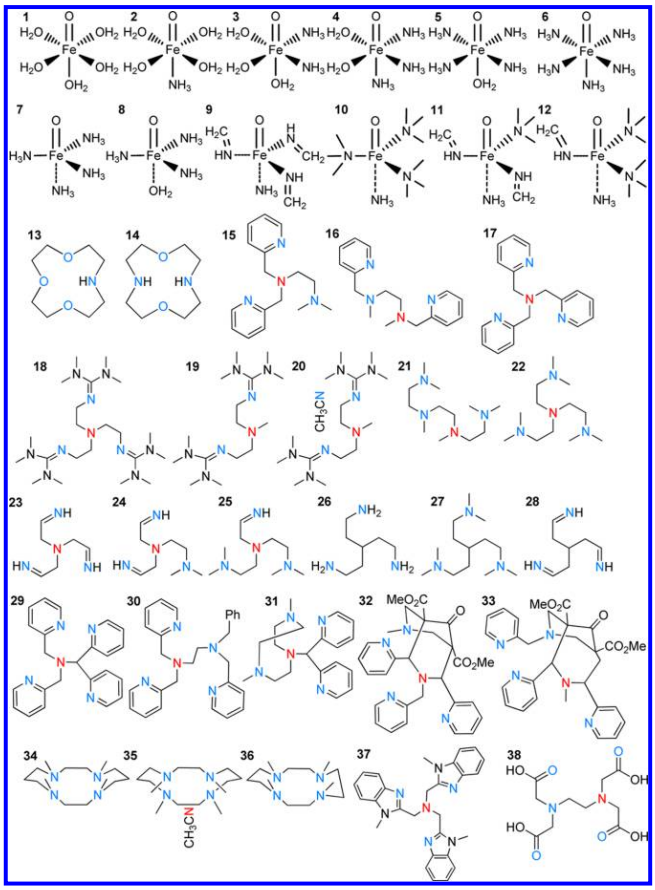

Figure 2. Structure of the complexes with an overall positive charge of 2 included in the first correlation plot. **1**−**12** is the subset of complexes with monodentate ligands, and the drawing includes the position of the Fe═O moiety. **13**−**38** is the subset of polydentate ligands. The position of the Fe═O group is not included for clarity. Atoms coordinated to Fe in the equatorial position are shown in blue, while those in the axial position are in red.

(−14 to −8 eV and −6 to −2 eV for 2+ charged and neutral complexes, respectively). Other popular ligands could be incorporated, such as the negatively charged pyrrolide or urea ones,[40,41] provided an extensive complex set is constructed for their respective charge group, similarly to the 2+ and neutral sets presented here.

The "reactant complex" state, where methane is loosely oriented toward the oxo oxygen (typically 2−3 Å apart) and the transition state structures were then determined to compute the activation barriers E^{ACT}(LS-π path) and E^{ACT}(HS-σ path). In order to accurately compare HS-σ and LS-π paths, reliable predicted spin gaps are required (E^{GAP}). The chosen combination of OPTX (exchange) and PBEc (correlation) functionals with the Dunning's correlation consistent basis sets employed here is known to perform well in this respect.[42] For example, in comparison to CCSD(T) calculations performed by Shaik and co-workers on penta-ammoniated iron oxo (complex **6** here),[43] the quintet-triplet spin gap is estimated accurately (1.3 kcal·mol^{-1}) while the LS-π and HS-σ barriers are not as underestimated as with the popular hybrid B3LYP functional.

A clear correlation was obtained for the first group (**1**−**38**, charge 2+) for the HS-σ path between the activation energy for CH bond dissociation on the HS oxo complexes and the energy of the lowest acceptor σ*(Fe═O) orbital (HS-σ path, black and blue symbols in Figure 4). Crosses and diamonds signify whether the HS-σ path is associated with a ground or excited state of the initial complex, respectively. From the presence of the 2+ charge, the energy of the σ*(Fe═O) orbital can be quite low, lower than the HOMO energy of methane in gas phase. However, the HOMO of methane is markedly stabilized in the reactant complex, where it is in the field of the dication, and its energy is again below that of the σ* acceptor orbital. Evidently, the correlation can be directly applied in order to

DOI: 10.1021/cs500996k
ACS Catal. 2015, 5, 2490−2499

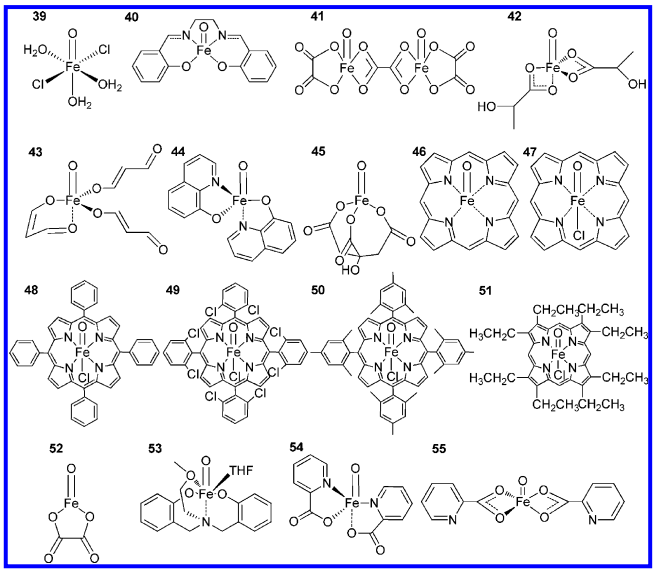

Figure 3. Neutral complexes included in the second correlation plot. All drawings here include the approximate position of the Fe═O moiety.

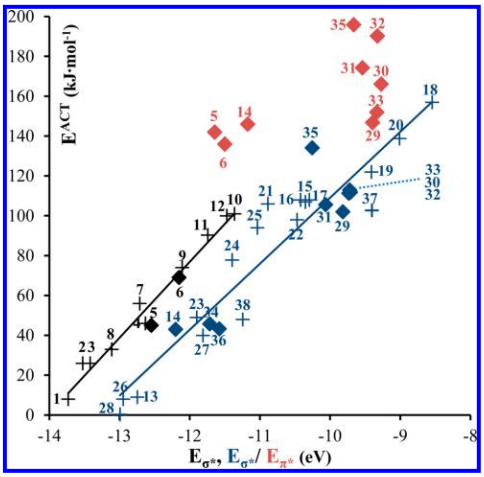

Figure 4. Correlation between the energy of the σ^* orbital of the Fe−oxo complex in electronvolts (x-axis) and the barrier height of the C−H abstraction step in kilojoules per mole (y-axis) for models **1**−**38** (HS-σ path). Two subsets are distinguished: (**1**−**12**) in black and (**13**−**38**) in blue. Crosses indicate complexes with a high spin ground state (quintet), while diamonds indicate those with a low spin (triplet). In addition, for the Fe═O complexes with a LS ground state, the activation energy for C−H abstraction along the LS-π path is also plotted as a function of the energy of the π^* orbital (red diamonds) even if in this case no correlation appears.

obtain the total barrier when dealing with HS ground states, which constitute the majority on this set, or combined with the LS-HS gap, (ideally, with a calculated minimum energy crossing point (MECP)), when dealing with LS ground states. Two subsets of linear relations clearly emerge, and they correspond to different types of ligands.

The first subset (black, **1**−**12**) shows an R^2 value of 0.97, a slope of 38, and a mean absolute deviation (MAD) of 4 kJ·mol^{-1}. In this set, all ligands are monodentate. Models **13**−**38** in Figure 4 (blue) form the second trend-line which is almost parallel to the previous one with a slope of 33, an R^2 value of 0.90, and an MAD of 11 kJ·mol^{-1}. All ligands are here polydentate with three to six coordination sites. In particular, **15**−**18**, **20**−**25**, and **37** are forming with the Fe═O moiety a complex of trigonal bipyramidal geometry.

Overall, the two trend lines reveal a close-fitting linear relation between the energy of the acceptor σ^* orbital and the activation energy. The activation energy of the LS-π path points are also included as a function of the energy of the π^* for the low spin ground state complexes **5**, **6**, **14**, and **29**−**36** (red diamonds). A meaningful correlation cannot be obtained here between the activation energy on the LS-π path and the π^* acceptor orbital energy. The typical bended transition state probably induces a larger variation in the steric hindrance contribution to the activation barrier. For instance, in the TMC−CH_3CN (**35**) complex, the cyclam scaffold hinders the methane approach, leading to a FeOH angle 132° while in the N4Py (**29**), the FeOH angle is smaller (121°), indicating a lower steric hindrance. Despite a similar π^* energy, their activation energy differs by 49 kJ·mol^{-1}.

For the second group of neutral complexes (**39**−**55**), a correlation of the same nature is obtained for the HS-σ path, shown in Figure 5 with black symbols and line. The complexes in this set are less uniform than those of the previous group and show a narrower orbital energy range than for the **1**−**38** group (~3 eV).

The heme Fe−oxo complexes with a Cl axial ligand included here (models **47**−**51**) that originate from a Fe^{III} bare site

DOI: 10.1021/cs500996k
ACS Catal. 2015, 5, 2490−2499

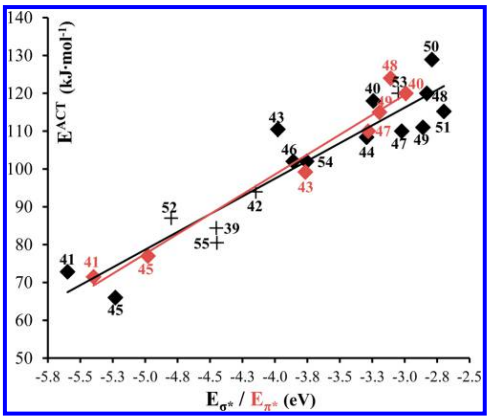

Figure 5. Correlation between the energy of the σ^* orbital of the Fe−oxo complex in electronvolts (x-axis) and the barrier height of the C−H abstraction step in kilojoules per mole (y-axis) for models **39**−**55**, shown in black with all complexes considered in the high spin state (HS-σ path). Crosses indicate complexes with a high spin ground state (sextet/quintet), while diamonds those with a low spin (quartet/triplet). The correlation between the barrier height of the C−H abstraction step (on the low spin surface) and the energy of the π^* of certain low spin ground state models is also included with red diamonds and line (LS-π path).

display the typical ligand radical configuration O═Fe^{IV}($Por^{\bullet+}$)-(Cl^-) and hence correspond to a quartet ground state (called low spin here) and a sextet high spin excited state. Remarkably, the nonheme complexes **43** and **45** that also originate from a Fe^{III} bare site attain a similar configuration O═Fe^{IV}($L^{\bullet+}$). While in heme containing systems the LUMO is typically located mainly on the heme, and in **43**−**45** it is located on the ligand, the C−H abstraction will be initiated normally through the acceptor orbital Fe^{IV}═O(π^*) or Fe^{IV}═O(σ^*).[26] This allows heme containing systems to be included in the correlation.The transition state structures of this neutral group display Fe−O−H angles much lower than 150° (see SI Table S2) typical of a π-path motif. However, the orbital analysis of those transition state structures reveals that the forming bonding orbitals are of substantial σ^* character (e.g., 35% σ^* for the HOMO the transition state structure of **46** with a Fe−O−H angle of 137.5°) which explains their correlation preference with the σ^* energy levels.

No distinct monodentate/polydentate lines are established in this correlation since only one model is exclusively monodentate (**39**). Despite the high heterogeneity of the set, the quality of the correlation is also of high standard with an R^2 value of 0.87 and an MAD of 5 kJ·mol^{-1}.

For several of the low spin ground state models, the relation between the energy of their respective π^* orbital and the activation energy along the low spin PES (LS-π path) is also included in the neutral correlation plot (Figure 5, red). In contrast with the case of the charge 2+ complexes, a good correlation is also obtained here. As mentioned before, to predict the minimum energy pathway, one would only have to compute the spin gap between the two spin variants and then compare the activation barriers obtained from the linear relation on the two spin PESs, simply from the calculation of the energies of the HS state σ^* orbital and the LS state π^* orbital. In the case of the LS path, although most of the complexes show large activation energy in the right part of Figure 5, some of them counterintuitively yield a small barrier (**41**, **45**, and even **43**). This shows that, if the π^* orbital is low enough, the LS-π pathway in the case of neutral systems can also provide efficient systems for CH activation (we again stress that by LS we mean quartet/triplet cases).

The correlations in Figures 4 and 5 illustrate that not only high spin ground state complexes (shown as crosses) can be expected to lie along the linear relation but also high spin excited states (shown as diamonds), isomers, regardless of their relative stability (**54** and **55**), bimetallic complexes (**41**), heme-containing systems, inferring that iron-oxo orbitals facilitate the electron transfer to the porphyrin ring (**46**−**51**), and, as mentioned before, complexes with radical ligands (**43**, **45**, **47**−**51**; see Tables S1, S2, and S3 in the SI for details).

DISCUSSION

These correlations provide, on both sets of ligands, a fast prediction of the H-abstraction activation energy E^{ACT}(HS-σ path) on the S = 2 potential energy surface and in the case of the neutral molecules also for E^{ACT}(LS-π path) on the S = 1 potential energy surface. The MAD for the activation energy ranges between 4 and 11 kJ·mol^{-1}, which is reasonably low for a first screening of a large potential set of ligands, provided that they correspond to the same charge for the (L)Fe^{IV}═O complex. This translates into a deviation of ∼0.3 eV for the characteristic orbital energy (σ^* or π^*) of the Fe−oxo complex, and hence the approach cannot discriminate cases where acceptor orbital energies are too close.

For the +2 charge complexes, the correlation provides the C−H activation barrier in the quintet (HS) spin manifold, but this is the overall barrier only if the reactant complex is a spin quintet. For triplet complexes (diamonds in Figure 4), the spin gap should be added, since spin−orbit coupling should yield a high probability for spin inversion and open the two state reactivity mechanism.[32] The correlation provides the activity order between two complexes only if the change in HS barriers dominates the variations in spin-gap. In the opposite case where the spin-gap variation dominates, reactivity prediction is out of reach of our correlations.

The division of the charge 2+ catalysts in two correlation subsets (monodentate/multidentate) is remarkable and was not underlined before. It shows that the energy of the σ^* orbital is not the only criterion governing the CH dissociation energy. For a given value of the σ^* energy, the presence of the multidentate scaffold tends to lower the activation energy by ∼25 kJ·mol^{-1}. In the case of independent monodentate ligands, Fe is close to the plane of the equatorial ligands, in a rather perfect geometry. This is not the case for the multidentate ligands where the constraint imposed by the scaffold prevents the coordinating atoms to occupy their optimal position in the equatorial plane (see the SI). As a result the Fe and equatorial ligand show a pyramid shape, the ligands being bent away from the oxo group, and this distortion is often stronger in the TS than in the reactant state (see Table S1, S2, and S3 in the SI). In other words, the Fe^{IV}═O unit is pulled out above this plane (see also SI Figure S2). The correlations presented stem from the dominating two electron interaction between the C−H occupied orbital and the Fe-oxo acceptor orbital. The four-electron interaction between occupied states on methane and on the ligands is however non-negligible. Upon its approach,

DOI: 10.1021/cs500996k
ACS Catal. 2015, 5, 2490−2499

methane feels less Pauli repulsion from the pyramidal Fe═O with multidentate ligands than from complexes with monodentate ligands and this leads to a more favorable transition state energy at a given σ^* energy. This effect will depend on the multidentate ligand which gives more scatter in the multidentate line (**13**−**38**) than in the case of the model complexes (**1**−**12**). The use of a multidentate ligand is also known to increase the catalyst stability by reduction of the ligand lability. Thus, using a multidentate scaffold is essential to improve the design of Fe^{IV}═O catalysts as it provides gains in stability *and* activity at once.

These correlations have been established with the OPBE exchange correlation functional and in the gas phase. It is important to assess their general character. For practical reasons this has been performed on the subset of complexes **1**−**12** and on the HS surface. A second functional has been tested, B3LYP-D, and it also provides a clear linear relation. However, if the existence of a correlation between acceptor orbital energy and activation energy is general, the slope and offset are dependent on the chosen functional (see SI Figure S4). The second method-related question concerns the influence of solvent. The implicit PCM method has been considered for three different solvents (cyclohexane, acetonitrile, and water), and the resulting activation energy/acceptor orbital energy relations are shown in Figure 6. A linear relation of high quality

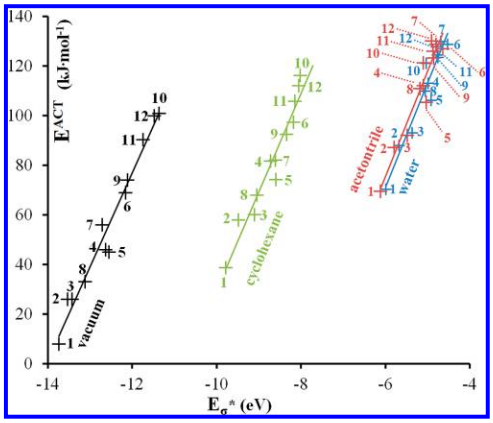

Figure 6. Correlation between the energy of the σ^* orbital of the reactant in electronvolts (*x*-axis) and the barrier height of the C−H abstraction step in kilojoules per mole (*y*-axis) for models **1**−**12** (HS-σ path), demonstrating the solvation effect. Green crosses and line refer to cyclohexane (ε = 2.02), red to acetonitrile (ε = 35.69), and blue to water (ε = 78.36) implicit solvent calculations. The gas phase calculations are recalled for comparison with black crosses and line.

holds for each choice of solvent. The solvent simply shields the positive charge, so that the σ^* orbital energy is less stabilized, the effect being smaller with cyclohexane with low dielectric constant and saturating for acetonitrile/water. The proposed linear relation hence still holds in the presence of a solvent, and the slope is unchanged within error bars. At the same time, the solvent increases the C−H activation barrier for a given ligand, and the effect is stronger for highly polar solvents. This explains the preference for a low polarity solvent, like the alkane itself, for alkane partial oxidation with Fe−oxo complexes. This effect is however dependent on the choice of ligand, since this choice affects the electrostatic properties of the complex, the barrier for **10** being increased by only 20 kJ·mol^{-1} between vacuum and water, while that of **7** is increased by 77 kJ·mol^{-1}. Hence the reactivity order between various ligands is dependent on the choice of solvent, e.g. **7** is more reactive than **9** and **10** in cycloxexane but less reactive in acetonitrile.

Therefore, once calibrated with a few points, such relations represent a practical way to evaluate the activation barrier on the HS surface, with several exchange correlation functionals and solvent polarities, since it only requires to calculate the energy of the σ^* orbital in the Fe−oxo complex. It has also a strong potential to be extended to other catalytic reactions.

Beyond this numerical aspect, the linear relation also provides simple chemical insight since it allows us to link the CH bond dissociation activation energy for a given spin state with a simple quantity, the energy of the lower lying acceptor orbital of the Fe^{IV}═O catalyst, for which we have many guidelines from molecular orbital theory. The energy of this orbital is simply related with the electronic character of the ligands, electron donating ligands pushing it to higher energy and electron withdrawing ones in contrast lowering its energy, and hence yielding a lower barrier for CH activation. This can give simple and powerful design ideas to the chemists.

This effect is clearly illustrated on the first subgroup of the first set (models **1**−**12**, black line). Weakly donating H_2O ligands are progressively substituted by stronger amine type donors (**1**−**8**), shifting up the σ^*(Fe═O) orbital. From the shape of the d_{z^2}(Fe) orbital, the substitution of the axial ligand is more effective than that of the equatorial ones as already discussed in the literature[44] and nicely illustrated experimentally on a cyclam series.[45]

As indicated in the introduction, a BEP type linear relation has been proposed earlier on a set of Fe and Mn oxo complexes, linking the H abstraction barrier to the reaction energy ΔE.[12,13] In the present paper, the reactivity descriptor is not the total reaction energy, but an electronic structure parameter: the energy of the (initially vacant) acceptor orbital of the Fe−oxo complex. Although both types of relations are potentially interesting, one advantage of the present approach is that as said just above, molecular orbital theory gives us qualitative tools to predict the variation of the σ^* energy as a function of the type of ligands.

These correlations have been established with GGA exchange correlation functionals (OPBE mainly, and B3LYP-D in one case) that have already proven a reasonable accuracy for the electronic structure and catalytic reactivity of coordination complexes. To the best they would reproduce the DFT energy and hence cannot perform better than these for the comparison with experimental results. In addition, the intrinsic error forbids distinguishing ligands that yield similar energy for the acceptor orbital, in a window of 0.3 eV, and cases where the complex is not high spin add the complication of the spin-gap. Some of the mentioned complexes are comprised of model ligands and this type of ligand searches should ideally be performed in tandem with experimental work. Hence, we will now discuss how the results from the linear relations compare with experimental data on the reactivity of iron oxo complexes. Such a comparison should optimally be performed by comparing to measured reaction rates.

The guanidyl ligand series (**18**−**20**) nicely demonstrates how the modulation of the donor properties of the ligand enables to tune the reactivity, in the case of complexes with charge +2 and

DOI: 10.1021/cs500996k
ACS Catal. 2015, 5, 2490−2499

with a HS quintet ground state. From TMG3tren (**18**) to TMG2dien−CH_3CN (**20**), one arm of the ligand is removed and a solvent molecule CH_3CN occupies the vacant equatorial coordination site. The change for a weaker donor ligand pulls down the energy of the σ^* orbital by 0.47 eV and activates the Fe^{IV}═O core. The HS barrier is here the global C−H activation barrier and is reduced by 18 kJ·mol^{-1}, in agreement with the experimental gain in the kinetic constant, by a factor of 630 for 9,10-dihydroanthracene.[37] A further activation can be realized by the removal of CH_3CN solvent molecule (**19**). Again, the σ^* orbital is stabilized (by 0.4 eV) and the activation barrier is reduced by an extra 17 kJ·mol^{-1}.

The reactivity of the Fe-oxo complex with benzimidazol **37** has been evaluated in the same conditions as **18** and **20**, and it was found to be 100 to 3000 times more reactive than **18**.[38] The Fe−oxo complex initially coordinates a solvent CH_3CN and is low spin (S = 1), but it is likely that the solvent molecule departs to form the reactive trigonal bipyramidal high spin (S = 2) complex. Compared to **18**, **37** reduces the donor capacity of the equatorial N groups, which move the σ^* orbital 0.9 eV to lower energy. As a result the barrier on the HS surface is markedly reduced, in relation with the experimental result.

The cyclam family (**34**−**36**) remains on the charge 2+ case but shows a LS triplet ground state. The contraction of the scaffold with one carbon less in TMC-13 (**36**) than in TMC-14 (**34**) has little influence on the energy of the σ^* orbital, nor on the spin-gap (see SI Table S1). Experiment however shows that, if acetonitrile is used as solvent, the iron−oxo complex with **34** accepts a solvent molecule in axial position (noted **35**).[46] The strong effect of a donor ligand in axial discussed above pushes the σ^* orbital to higher energy by 1.5 eV and hence, following the linear relation, strongly increases the C−H dissociation barrier on the HS surface. In principle the spin-gap from triplet to quintet in the reactant complex should be added to obtain the global barrier, but the effect is large enough (90 kJ·mol^{-1}) here to allow a direct conclusion. The contracted ring of **36** is too narrow to allow the coordination of acetonitrile and the axial position remains vacant, hence keeping a low σ^* orbital and a high reactivity. This is in good agreement with experiment where the complex TMC-13 (**36**) is much more reactive than that with TMC-14 (**34**) in acetonitrile. From our linear relations one can suggest a further modification in the cyclam family **34**−**36**. In addition to the ring contraction to remove the acetonitrile, one can also play on the nature of the donor atom, replacing nitrogen by oxygen hence leading to aza-crown ether (**13**, **14**).

The comparison of the reactivity of a low spin and a high spin complex should be done with care. **20** and **29** have been experimentally studied in similar conditions, and **20** is 15−30 times more active than **29**, depending on the substrate. Figure 4 indicates that **20** presents a σ^* orbital 0.8 eV higher in energy and, following the linear relation, a barrier of 139 kJ·mol^{-1} on the HS surface, 37 kJ·mol^{-1} larger than that of **29**. This could seem in disagreement with the experiment, but disregards the fact that **29** is a low spin complex. The barrier on the LS surface is calculated at 147 kJ·mol^{-1}, and the promotion from the LS to the HS state for the reactant costs 52 kJ·mol^{-1}, which puts the global barrier through the HS TS at 154 kJ·mol^{-1}. Hence **29** is calculated to be less active than **20**, well in line with the measured reactivity.

Recently, the oxidative properties of a series of N5 ligands have been investigated experimentally by varying the N-donor groups (pyridyl, bispidine, or amino, **29**−**33**).[47] Charge 2+ octahedral Fe-oxo complexes are obtained and their ground state is a triplet. The five points fall very close to the linear fit of Figure 4, but the corresponding σ^* energies only differ by a maximum of 0.25 eV (less than the error related uncertainty for the σ^* energies of 0.3 eV) and points **30**, **32**, and **33** almost overlap. The range in calculated activation energies on the HS surface is hence also small (E^{ACT} = 102−113 kJ·mol^{-1}). In addition since the complex are low-spin, the spin gap should be added to the HS activation energy to obtain the global activation energy. In fact, the variation of the triplet-quintet energy gaps is much larger than that of the HS barriers and controls the relative activity (E^{GAP} = 26−52 kJ·mol^{-1}). Hence, we are here clearly at the limit of applicability of the method. For instance, the two bicyclic bispidine (**32**, **33**) have almost the same HS barrier around 110 kJ·mol^{-1}. The observed greater activity of **33** lies in the spin gap, 15 kJ·mol^{-1} smaller than that of **32**. Similarly, **31** is 10 times more active than **29**, while the HS barriers are 106 and 102 kJ·mol^{-1}, respectively. The correct order in barriers is retrieved after addition of the spin gaps to obtain the global barriers, respectively 142 and 154 kJ·mol^{-1}. For this family of low spin complexes, the reactivity is not controlled by the energy of the σ^* orbital (since changes are small) but rather by variations in the spin gaps and possible influence of the second coordination sphere.[48]

The last comparison with experiment will focus on the set of neutral complexes. Synthetic porphyrins were among the first complexes to be involved in the biomimetic C−H oxidation effort.[3] First generation iron porphyrins (Fe^{III}TPPCl, **48**) perform well for various partial oxidation reactions, such as the cyclohexane to cyclohexanol conversion.[49] Our approach (Figure 5) fittingly predicts the superiority of the TPP (tetraphenylporphyrin) and TDCPP (tetrakis (2, 6-dichlorophenyl)porphyrin) (**48** and **49**, respectively) over the TMP (tetramesitylporphyrin) type (**50**).[50−52] The axial ligand effect in porphyrins is known to differ from the nonheme complexes: a stronger donor leads to a greater activity.[53] The induced variations of reactivity have been shown to correlate mainly with the stability of the intermediate and the ease of the rebound step.[49] Those effects are out of reach of our simple screening approach based on the electronic structure of the Fe═O complex.

In final, it is important to underline that comparisons with experiments have to be considered carefully as a relevant article by Nam and co-workers demonstrates,[54] since yields and alcohol to ketone ratios depend profoundly on the respective conditions, such as the type of solvent used, the amount and kind of oxidant, and the manner the various counterions interact with the metal center. Nevertheless, if one keeps in mind the limited accuracy in acceptor orbital energy (0.3 eV) and the fact that these correlations mainly apply to the HS energy surface, the above comparisons validate our approach.

As a consequence, these correlations have a potential for the design of optimal ligands, specifically tuned to minimize the C−H activation energy using Fe−oxo complexes. A strategy to lower the reaction barrier can be, for example, to replace strongly electron donor trimethylamine ligands by imine ligands in the equatorial plane as illustrated on simple model systems (**22** → **24** → **23**). An even more efficient approach is to act on the axial ligand and to replace it by a noncoordinating carbon atom (i.e., **22** → **27**). This switches from a tetradentate to a tridentate ligand and blocks the axial position of the complex, yielding a strong reduction of both the σ^* energy and the CH activation barrier. These two strategies can be

DOI: 10.1021/cs500996k
ACS Catal. 2015, 5, 2490−2499

combined and this leads to an optimal model complex with a predicted barrierless C−H abstraction in vacuum (**28**, E^{ACT}: 0.3 kJ·mol^{-1}) and hence a low barrier in cyclohexane. Hence, from the analysis of the first set of complexes (2+ charge), several guidelines can be extracted to design efficient nonheme oxidation catalysts based on the Fe^{IV}=O moiety. One should try to reach a high-spin Fe^{IV}=O active species with a low lying σ^* orbital combining (i) a weak equatorial ligand field, using in particular a tridentate ligand, and (ii) the weakest possible axial ligand field, blocking the axial site with noncoordinating carbon, for instance.

To propose potential efficient oxidation catalysts, one can also target the neutral oxo complexes of the second set (Figure 3) extracted from literature such as heme-complexes[50−52] or derived from commercially available Fe complexes. Such a choice of neutral complexes avoids spurious effects of counterions. The porphyrin complexes included in this work are found in the right section of the correlation plot (Figure 5, **46**−**51**) with computed barriers for the C−H dissociation step of over 100 kJ·mol^{-1}. The computational screening and the proposed σ^* energy descriptor however underlines much more efficient systems and predicts the complexes found well to the left on the correlation line (e.g., **41**, **42**, **45**, **52**) as prime candidates for the task. Following the strategies extracted from the model systems analysis, they exhibit a weak equatorial ligand field, no ligand in the axial position and a first coordination sphere replete by the multidentate ligand. The high activity of these complexes is a prediction from our study since to our knowledge they have not yet been tested for alkane partial oxidation yet. A potential limitation is that these complexes also correspond often to weak metal ligand interactions (see SI Figures S3a and b) so that their stability might be an issue. They might appear only as short-lived intermediates in the catalytic cycle. However, some possible candidates combine a reasonable stability and good activity. Complex **45** derived from Fe^{III}−citrate, specifically tried because of the resemblance with **26**−**28**, is the most stable of the neutral set by virtue of its strongly donating carboxylate groups. However, it also combines a trigonal equatorial ligand sphere and an axial site being blocked by a noncoordinating carbon in a multidentate ligand. Therefore, its low-spin ground state exhibits a low-lying π^* that opens the LS path with a reasonable activation barrier (E^{ACT} = 77 kJ·mol^{-1}). Interestingly, this path is more active than the two-state scenario (spin crossing and HS-transition state). This potential catalyst demonstrates that design strategies could also target the LS path efficiently using the correlation we have established here. Next, the very simple Fe^{II}−oxalate complex (**52**), provided that no extra strong ligand could coordinate Fe in the reaction media, or the associated dimer (**41**) seem to be other very promising catalysts. The reasonable stability of the Fe^{IV}=O-oxalate is combined with good activity (E^{ACT} = 87 kJ·mol^{-1}), enrooted in an HS ground state and a low-lying σ^*. It would be of great interest to test those candidates experimentally. Then, the potential synthetic modifications of those complexes could be tested primarily in silico using the correlation presented in this article. These potential catalysts have been evaluated in the absence of solvent. Our model study (Figure 6) however indicates that a solvent with low dielectric constant and weak coordinating capabilities, as cyclohexane, is the best choice, while acetonitrile, frequently used in the literature, might not be the optimal solvent due to its ligand capability.

CONCLUSION

Clear linear relations have been demonstrated between the activation energy for C−H dissociation on the HS (sextet/quintet) energy surface and the σ^* acceptor orbital of the initial (L)Fe^{IV}=O complex. In addition for the neutral LS oxo complexes (quartet/triplet) a relation between π^* acceptor orbital and activation energy on the low-spin surface also holds. Although initially established for the OPBE functional, these linear relations have a general character, however the relation parameters (slope and offset) can depend on the choice of functional and on the solvent. Comparison with experiments validate the concept, although these comparisons have to be performed with care due to the uncertainty in acceptor orbital energy, to potential two-state reactivity, and to the influence of the solvent. The correlation trend-lines included here can hence be used as a powerful tool for the rational design of iron−oxo catalysts for C−H activation. The barrier prediction error lies in the 4−11 kJ·mol^{-1} range, an accuracy that is attained by the robustness of the correlation and the wide range of the data set. The approach described has a twofold advantage, assisting the ligand design process in the lab and allowing for very fast screening of potential candidate models that are commercially available. In addition, it links the reactivity with simple molecular orbital concepts that can be applied at no cost for the generation of potential ligand candidates.

Molecular orbital descriptors hence appear to be more than a qualitative analysis tools but they can be transformed in quantitative relations providing key insights for the rational exploration of potentially efficient ligands and catalysts.

METHODS

All calculations were performed using the Gaussian 09 program.[55] Unless stated otherwise, they were performed in the gas-phase and refer to zero Kelvin temperature and ideal gas conditions, which may be different from room temperature experiments in a solution. The DFT functional employed is the OPBE, comprised by the Handy's OPTX modification of Becke's exchange functional (O)[56] and the 1996 correlation functional of Perdew, Burke, and Ernzerhof (PBE).[57] For an additional DFT functional, see the SI Figure S4. Dunning's correlation consistent basis sets where utilized as follows: for the Fe, Cl atoms, the triple-ζ (cc-pVTZ) was employed, while for the C, H, N, and O atoms this was the double-ζ cc-pVDZ.[58] Transition state optimizations were performed using the Berny algorithm[59] and resulted in a structure with a single imaginary frequency that corresponded to the expected methane C−H bond stretch and was followed by intrinsic reaction coordinate calculations (IRC[60]) to verify the link to the expected reactants and products. For many complexes (such as **8**, **15**, and **22**), it was possible to locate both the HS-σ and HS-π path transition states, while for others the σ^*−π^* energy gap was large enough to be prohibitive for locating the energetically disfavored π-path. All barrier values reported are calculated with respect to the "reactant complex" on the same spin surface as the relevant transition state. When a "low spin, LS" complex is mentioned in the text, this indicates a state lying on the triplet/quartet surface, while "high spin, HS" in the quintet/sextet, as per usual. The solvation method utilized is the PCM method as implemented in Gaussian 09.[61−63] It should also be stressed that the work presented here only focuses on the Fe^{IV}=O unstable intermediates of the catalytic cycle. The reported spin gaps (SI Tables S1−S3) should not be confused with, and

DOI: 10.1021/cs500996k
ACS Catal. 2015, 5, 2490−2499

might radically differ, from their respective Fe^{II}/Fe^{III} bare site spin gaps that are reported experimentally.

■ ASSOCIATED CONTENT

Supporting Information

The following file is available free of charge on the ACS Publications website at DOI: 10.1021/cs500996k.

Geometric and energy data, additional correlation plots and counterion effects, Cartesian coordinates of optimized structures, and spin densities (PDF)

■ AUTHOR INFORMATION

Corresponding Author

*E-mail: philippe.sautet@ens-lyon.fr.

Notes

The authors declare no competing financial interest.

■ ACKNOWLEDGMENTS

P.C.A. acknowledges Solvay for the financial support. We also thank the PSMN at ENS de Lyon for computational resources.

■ REFERENCES

(1) Solomon, E. I.; Brunold, T. C.; Davis, M. I.; Kemsley, J. N.; Lee, S.-K.; Lehnert, N.; Neese, F.; Skulan, A. J.; Yang, Y.-S.; Zhou, J. *Chem. Rev.* **2000**, *100* (1), 235−350.
(2) Borovik, A. S. *Chem. Soc. Rev.* **2011**, *40*, 1870−1874.
(3) Costas, M. *Coord. Chem. Rev.* **2011**, *255*, 2912−2932.
(4) Talsi, E. P.; Bryliakov, K. P. *Coord. Chem. Rev.* **2012**, *256*, 1418−1434.
(5) McDonald, A. R.; Que, L., Jr. *Coord. Chem. Rev.* **2013**, *257*, 414−428 and references therein. .
(6) Hohenberger, J.; Ray, K.; Meyer, K. *Nat. Commun.* **2012**, *3*, 720−733.
(7) Rittle, J.; Green, M. T. *Science* **2010**, *330*, 933−937.
(8) Price, J. C.; Barr, E. W.; Tirupati, B.; Bollinger, J. M., Jr.; Krebs, C. *Biochemistry* **2003**, *42*, 7497−7508.
(9) Groves, J. T. *J. Inorg. Biochem.* **2006**, *100*, 434−447.
(10) Cho, K.; Leeladee, P.; McGown, A. J.; DeBeer, S.; Goldberg, D. P. *J. Am. Chem. Soc.* **2012**, *134*, 7392−7399.
(11) Yosca, T.; Rittle, J.; Krest, C. M.; Onderko, E. L.; Silakov, A.; Calixto, J. C.; Behan, R. K.; Green, M. T. *Science* **2013**, *342*, 825−829.
(12) de Visser, S. P. *J. Am. Chem. Soc.* **2010**, *132*, 1087−1097.
(13) Saouma, C. T.; Mayer, J. M. *Chem. Sci.* **2014**, *5*, 21−31.
(14) Evans, M. G.; Polanyi, M. *Trans. Faraday Soc.* **1938**, *34*, 11−24.
(15) Fukui, K.; Yonezawa, T.; Shingu, H. *J. Chem. Phys.* **1952**, *20*, 722−725.
(16) Woodward, R. B.; Hoffmann, R. *Angew. Chem., Int. Ed. Engl.* **1969**, *8*, 781−853.
(17) Mayer, J. M. *Acc. Chem. Res.* **2011**, *44*, 36−46.
(18) Usharani, D.; Janardanan, D.; Li, C.; Shaik, S. *Acc. Chem. Res.* **2013**, *46*, 471−482.
(19) Buda, F.; Ensing, B.; Gribnau, M. C. M.; Baerends, E. J. *Chem. - Eur. J.* **2001**, *7*, 2775−2783.
(20) Buda, F.; Ensing, B.; Gribnau, M. C. M.; Baerends, E. J. *Chem. - Eur. J.* **2003**, *9*, 3436−3444.
(21) Louwerse, M. J.; Baerends, E. J. *Phys. Chem. Chem. Phys.* **2007**, *9*, 156−166.
(22) Decker, A.; Clay, M. D.; Solomon, E. I. *J. Inorg. Biochem.* **2007**, *100*, 697−706.
(23) Ye, S.; Neese, F. *Proc. Natl. Acad. Sci. U. S. A.* **2011**, *108*, 1228−1233.
(24) Decker, A.; Rohde, J.-U.; Klinker, E. J.; Wong, S. D.; Que, L., Jr.; Solomon, E. I. *J. Am. Chem. Soc.* **2007**, *129*, 15983−15996.
(25) Srnec, M.; Wong, S. D.; England, J.; Que, L., Jr.; Solomon, E. I. *Proc. Natl. Acad. Sci. U. S. A.* **2012**, *109*, 14326−14331.
(26) Shaik, S.; Chen, H.; Janardanan, D. *Nat. Chem.* **2011**, *3*, 19−27.
(27) Michel, C.; Baerends, E. J. *Inorg. Chem.* **2009**, *48*, 3628−3638.
(28) Ye, S.; Geng, C.-Y.; Shaik, S.; Neese, F. *Phys. Chem. Chem. Phys.* **2013**, *15*, 8017−830.
(29) Srnec, M.; Dong, S. D.; Solomon, E. I. *Dalton Trans.* **2014**, *43*, 17567−17577.
(30) Britovsek, G. J. P.; England, J.; White, A. J. P. *Inorg. Chem.* **2005**, *44*, 8125−8134.
(31) England, J.; Martinho, M.; Farquhar, E. R.; Frisch, J. R.; Bominaar, E. L.; Münck, E.; Que, L., Jr. *Angew. Chem., Int. Ed.* **2009**, *48*, 3622−3626.
(32) Schröder, D.; Shaik, S.; Schwarz, H. *Acc. Chem. Res.* **2000**, *33*, 139−145.
(33) Bernasconi, L.; Baerends, E. J. *Eur. J. Inorg. Chem.* **2008**, *10*, 1672−1681.
(34) Rohde, J.-U.; In, J.; Lim, M. H.; Brennessel, W. W.; Bukowski, M. R.; Stubna, A.; Münck, E.; Nam, W.; Que, L., Jr. *Science* **2003**, *299*, 1037−1039.
(35) Hong, S.; So, H.; Yoon, H.; Cho, K.-B.; Lee, Y.-M.; Fukuzumi, S.; Nam, W. *Dalton Trans.* **2013**, *42*, 7842−7845.
(36) Wang, D.; Ray, K.; Collins, M. J.; Farquhar, E. R.; Frisch, J. R.; Gomez, L.; Jackson, T. A.; Kerscher, M.; Waleska, A.; Comba, P.; Costas, M.; Que, L., Jr. *Chem. Sci.* **2013**, *4*, 282−291.
(37) England, J.; Guo, Y.; Van Heuvelen, K. M.; Cranswick, M. A.; Rohde, G. T.; Bominaar, E. L.; Münck, E.; Que, L., Jr. *J. Am. Chem. Soc.* **2011**, *133*, 11880−11883.
(38) Seo, M. S.; Kim, N. H.; Cho, K.-B.; So, J. E.; Park, S. K.; Clémancey, M.; Garcia-Serres, R.; Latour, J.-M.; Shaik, S.; Nam, W. *Chem. Sci.* **2011**, *2*, 1039−1045.
(39) Chen, H.; Lai, W.; Shaik, S. *J. Phys. Chem. Lett.* **2010**, *1*, 1533−1540.
(40) Bigi, J. P.; Harman, W. H.; Lassalle-Kaiser, B.; Robles, D. M.; Stich, T. A.; Yano, J.; Britt, R. D.; Chang, C. J. *J. Am. Chem. Soc.* **2012**, *134*, 1536−1542.
(41) Lacy, D. C.; Gupta, R.; Stone, K. L.; Greaves, J.; Ziller, J. W.; Hendrich, M. P.; Borovik, A. S. *J. Am. Chem. Soc.* **2010**, *132*, 12188−12190.
(42) Guell, M.; Luis, J. M.; Sola, M.; Swart, M. *J. Phys. Chem. A* **2008**, *112*, 6384−6391.
(43) Janardanan, D.; Usharani, D.; Chen, H.; Shaik, S. *J. Phys. Chem. Lett.* **2011**, *2*, 2610−2617.
(44) Bernasconi, L.; Louwerse, M. J.; Baerends, E. J. *Eur. J. Inorg. Chem.* **2007**, *19*, 3023−3033.
(45) de Visser, S. P.; Rohde, J.-U.; Lee, Y.-M.; Choc, J.; Nam, W. *Coord. Chem. Rev.* **2013**, *257*, 381−393.
(46) Hong, S.; Hee, S.; Yoon, H.; Cho, K.-B.; Lee, Y.-M.; Fukuzumi, S.; Nam, W. *Dalton Trans.* **2013**, *42*, 7842−7845.
(47) Wang, D.; Ray, K.; Collins, M. J.; Farquhar, E. R.; Frisch, J. R.; Gomez, L.; Jackson, T. A.; Kerscher, M.; Waleska, A.; Comba, P.; Costas, M.; Que, L., Jr. *Chem. Sci.* **2013**, *4*, 282−291.
(48) Sahu, S.; Widger, L. R.; Quesne, M. G.; de Visser, S. P.; Matsumura, H.; Moenne-Loccoz, P.; Siegler, M. A.; Goldberg, D. P. *J. Am. Chem. Soc.* **2013**, *135*, 10590−10593.
(49) Takahashi, A.; Yamaki, D.; Ikemura, K.; Kurahashi, T.; Ogura, T.; Hada, M.; Fujii, H. *Inorg. Chem.* **2012**, *51*, 7296−7305.
(50) Groves, J. T.; Nemo, T. E.; Myers, R. S. *J. Am. Chem. Soc.* **1979**, *101*, 1032−1033.
(51) Khavasi, H. R.; Davarani, S. S. H.; Safari, N. *J. Mol. Catal. A: Chem.* **2002**, *188*, 115−122.
(52) Iamamoto, Y.; Assis, M. D.; Ciuffi, K. J.; Sacco, H. C.; Iwamoto, L.; Melo, A. J. B.; Nascimento, O. R.; Prado, C. M. C. *J. Mol. Catal. A: Chem.* **1996**, *109*, 189−200.
(53) Kang, Y.; Chen, H.; Jeong, Y. J.; Lai, W.; Bae, E. H.; Shaik, S.; Nam, W. *Chem. - Eur. J.* **2009**, *15*, 10039−10046.
(54) Cho, K.; Kim, E. J.; Seo, M. S.; Shaik, S.; Nam, W. *Chem. - Eur. J.* **2012**, *18*, 10444−10453.
(55) Frisch, M. J. *Gaussian 09*, Revision A.02; Gaussian, Inc., Wallingford CT, 2009; full citation in the SI.
(56) Hoe, W. M.; Cohen, A.; Handy, N. C. *Chem. Phys. Lett.* **2001**, *341*, 319−328.

DOI: 10.1021/cs500996k
ACS Catal. 2015, 5, 2490−2499

(57) Perdew, J. P.; Burke, K.; Ernzerhof, M. *Phys. Rev. Lett.* **1996**, *77*, 3865−3868.
(58) Dunning, T. H., Jr. *J. Chem. Phys.* **1989**, *90*, 1007−1023.
(59) Schlegel, H. B. *J. Comput. Chem.* **1982**, *3*, 214−218.
(60) Hratchian, H. P.; Schlegel, H. B. *J. Chem. Theory Comput.* **2005**, *1*, 61−69.
(61) Scalmani, G.; Frisch, M. J. *J. Chem. Phys.* **2010**, *132*, 114110−15.
(62) Improta, R.; Barone, V.; Scalmani, G.; Frisch, M. J. *J. Chem. Phys.* **2006**, *125*, 054103−9.
(63) Improta, R.; Scalmani, G.; Frisch, M. J.; Barone, V. *J. Chem. Phys.* **2007**, *127*, 074504−9.

DOI: 10.1021/cs500996k
ACS Catal. 2015, 5, 2490−2499

3

OXYGENATES CONVERSION BY METALLIC HETEROGENEOUS CATALYSTS

My main research line as a CNRS researcher is dedicated to the conversion of biomass-derived molecules into chemicals by metallic heterogeneous catalysts.

A typical target is the conversion of glycerol into various chemicals of interests such as 1,2-propanediol, 1,3-propanediol, lactic acid etc. This target nicely illustrates the two main challenges that we face to model such systems: (i) complexity of the reaction networks ; (ii) complexity of the catalytic system. I worked on this system for years, in collaboration with experimentalists in catalysis (C. Pinel and M. Besson, Lyon, France). I started working in the domain with F. Auneau, a PhD student who was combining modeling and experiments during his project on the hydrogenolysis of glycerol. This first collaboration was continued with the ANR **Galac** project and the PhD of J. Zaffran, that was mainly dedicated to the design fast methodologies to screen *in silico* the catalytic activity of metals towards polyol dehydrogenation. It opens the door to the efficient screening of the large reaction networks of higher polyols, the target of our current ANR **Music** project (1PhD and 1 post Doc) in collaboration with D. Vlachos, uDelaware, USA and A. Goetz, UCSD, USA.

In most cases, the conversion of biomass derived molecules is done in liquid phase, usually using water as a solvent. This solvent can considerably affects the catalytic activity of metallic supported catalysts[1,14,21] Thus, the inclusion of water is a necessity to properly model and understand the behavior of those catalysts. Based on a simple micro-solvation approach, we were able to interpret the influence of water in two different contexts (i) the oxidation of alcohols on Pt, during the master project of S. Chibani.[27] (ii) the hydrogenation of levulinic acid as a first step toward γ-valerolactone in collaboration with A. Ruppert (Lodz, Poland).[32] Finally, based on this model, we were able to explain why Ruthenium is widely used in biomass valorisation and not in gas phase reactions.[31] Those studies demonstrate the needs for better methods to described the reactivity at metal/liquid water interfaces, an aspect that is central to the ANR **Music** in collaboration with A. Goetz, San Diego.

I have recently enlarged my research to the amination of alcohols by ammonia in collaboration with Solvay and the E2P2 Lab in Shanghai, China. During his PhD, A. Dumon focused on the later. He demonstrated that one of the reactant (ammonia) strongly modify the catalytic relative activity of Ni and Pd metallic catalysts. T. Wang has just started a screening *in silico* based on the combination of scaling relations, BEP relations and micro-kinetics. He is also working on the deactivation processes of Ni under the reactive conditions (**Shapes** project).

Asolventnother important aspect in green chemistry is to avoid to use H_2 and favors the hydrogen transfer from sustainable feedstock. In collaboration with A. Ruppert, Lodz, Poland, we are currenlty working on the hydrogen transfer from formic acid to levulinic acid to generate γ-valerolactone. We first considered the impact of the preparation of Ru-based catalysts on the overall activity[33] We are now considering alloying as a strategy to overcome the intrinsic limitations of monometallic systems.

3.1 Complex reaction networks

Glycerol is a tri-ol that can be directly obtained by vegetable oil transesterification or by transformation of cellulose. It is an interesting platform molecule, not only *per se* but also as a typical model of more complex polyols that are more up-stream in the cellulose valorisation.[8,10,19,23] This small triol is a typical example of the challenges that catalysis has to overcome to produce chemicals for industry with high yield and high selectivity.[15] With three alcohols function, two at the terminal positions and one at the central position of the C3 molecule, the required chemioselectivity is difficult to achieve for a heterogeneous catalyst. In addition, the extension of the reaction network and the reaction conditions impede a deep understanding of the activity at a molecular level, a necessary step for a rational design. Some steps of the reaction network are catalyzed by the metal supported catalyst while others are solution equilibria that are sensitive to the pH, the solvent etc. Even the surface reactions might be impacted by the solution. And neither experiments, neither simulations can provide a complete picture of the reactive events occurring at the water/catalyst interface in those range of pressure and temperature.

Glycerol can be converted in various interesting chemicals depending on the type of catalysts. We focused on hydrogenolysis conditions. In our case, the target polyol is reduced using a pressure of dihydrogene (around 50 bar) at a mid-range temperature (180°C) in alkaline water using a supported Rh catalyst. While the initial target was the 1,3-propanediol (1,3-PDO), our collaborators (F. Auneau, IRCELyon) obtained mainly the 1,2-propanediol (1,2PDO) and the lactic acid (LA). The production of LA came as a surprise and this product became our target as an interesting platform in the biobased chemical industry.[6] In those conditions, the initial step was highly debated, being either a dehydrogenation or a dehydration. Based on our periodic DFT calculations at the GGA level, we were able to propose a reaction mechanism that starts with the dehydrogenation of glycerol on its terminal position,

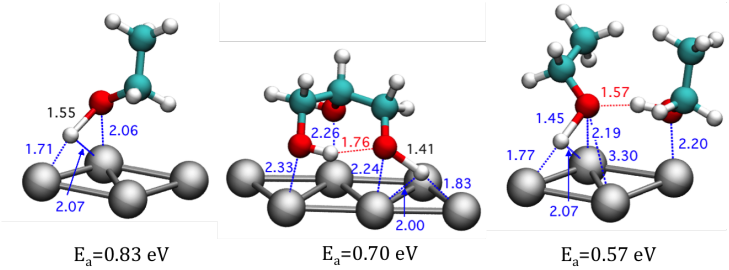

Figure 3.1: Transition state structures and activation barriers obtained at the PW91 level for the O−H scission in (i) ethanol (ii) glycerol (iii) ethanol dimer on Rh(111)

yielding glyceraldehyde (GAL). In addition, according to our mechanism, the two products (lactic acid and 1,2-propanediol) are in equilibrium and this equilibrium can be affected by the pressure of H_2: the lower the pressure, the higher is the yield in LA. Thus, based on our model, decreasing the H_2 partial pressure should fasten the first step and increase the selectivity in LA. Those predictions were confirmed experimentally, demonstrating the validity of our proposition.[25]

During this study, we evidenced the important role of hydrogen bonds on the O−H bond scission. Among the three hydroxyls, it is the one that stands the farther from the catalyst surface that is the most reactive. The corresponding activation barrier is much lower than the O−H bond breaking in ethanol (see Figure 3.1). This reactive O−H in glycerol is not chemisorbed but H-bonded to the other terminal hydroxyl that is chemisorbed on the Rh(111). To provide a deeper understanding, we considered also the dehydrogenation of ethanol when adsorbed as a dimer. The physisorbed, H-bonded ethanol is highly prone to O−H scission, with the lowest barrier among the three systems under consideration. Compared with glycerol, this system is less constrained by the carbon backbone. In a nutshell, physisorbed alcohols that accept a H-bond from a chemisorbed alcohol are more susceptible to overcome an O−H scission than an isolated, chemisorbed alcohol. And if the two alcohol functions under consideration belong to the same polyol

molecule, then, this H-bond assistance is partially compensated by a backbone constraint.[29]

Then, we started to enlarge our scope to other metals such as Iridium.[26] However, to open the door to a screening *in silico*, it was necessary to develop screening tools for dehydrogenation reactions of polyols provided the extensiveness of the corresponding reaction network. We focused on the Bronsdet-Evans-Polyani (BEP) relations for the C−H and O−H bond scissions in (poly)-alcohols on a series of transition metals. BEP relations aim at correlating the kinetics with the thermodynamics of a series of elementary steps. Several choices can be made to represent the kinetics (activation energy, energy of the transition state relative to a reference) and the thermodynamics (reaction energy, energy of the initial or final state relative to the reference). Those relations are classically used to relieve the computational burden of optimizing a high number of transition states. We started assessing the committed error when using various types of Bronsdet-Evans-Polyani (BEP) relations for the C−H and O−H bond scissions in simple alcohols on Rh(111). We demonstrated that the quality of a BEP relation depends on the choices made to cluster the elementary steps and to represent the relation. With an adequate choice, an accurate linear energy relationship is obtained for the O−H and C−H bond breaking on Rh(111). We then show that this relation can then be used for a fast prediction of the reactivity of glycerol on Rh(111) with a systematic deviation of 0.1 eV that can be imputed to intramolecular effects occurring in glycerol.[34]

Upon the extension to a series of transition metals, (Co, Ni, Ru, Rh, Pd, Ir, and Pt), we kept the separation of the elementary steps in two sets: (i) O−H scission (ii) C−H scission. Then, for each set, a single linear relation can be constructed for all metals together on the basis of the original Brønsted-Evans-Polanyi formulation with a mean absolute error smaller than 0.1 eV. In addition, a close statistical analysis demonstrates that errors stemming from such predictive models are not uniform along the set of metals and of chemical reactions that is considered opening the road to a better control of error propagation.[35]

3.2 Effect of water solvent

Once we have evidenced the impact of hydrogen bonds on the O−H scission on Rh(111), a question raises naturally: what is the role of water solvent on the catalytic performance of metal supported catalysts?

To better understand how general is this assistance by hydrogen bond on the O−H breaking, we have systematically analyzed this reactive event in three systems: (i) a single water molecule, chemisorbed on the metallic surface (ii) a physisorbed water molecule, that acceptes a H-bond from a chemisorbed water molecule respectively(iii) a chemisorbed water molecule, that donates a H-bond to a physisorbed water molecule. The last two systems correspond to the two possibilities of O−H scission in a water dimer adsorption on a metallic surface. On a series of transition metals (Ru, Co, Rh, Ir, Ni, Pd, Pt), the scission of the O−H is always easier in the physisorbed water.[30] This bond scission is all the more easy that the metal is oxophilic, the lower barrier being obtained on Ru(0001) and the higher on Pt(111). This assistance can be illustrated plotting the activation energy $\Delta E^{\ddagger}$ in function of the reaction energy ΔE. Since the O−H scission is a very early reaction, this representation is more conclusive based on the reverse reaction, namely the formation of water from OH and H.

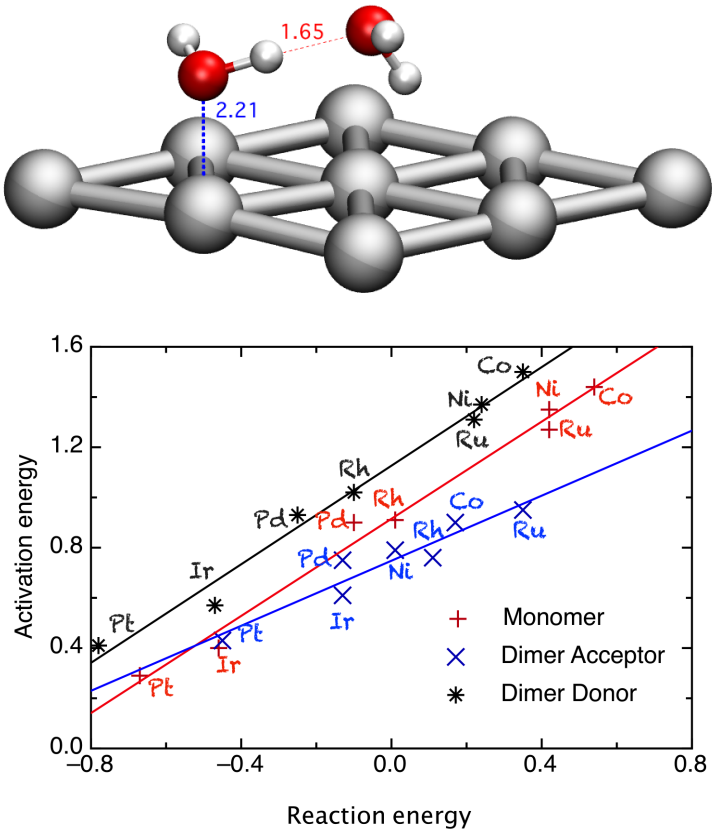

Figure 3.2: Activation energy $\Delta E^{\ddagger}$ of the O−H bond formation in function of the reaction energy ΔE (in eV) on the compact plane of a series of transition metals. +, x, and * display the data points and solid lines the linear regression for (i) a single water molecule, chemisorbed on the metallic surface (ii) a physisorbed water molecule, that acceptes a H-bond from a chemisorbed water molecule respectively(iii) a chemisorbed water molecule, that donates a H-bond to a physisorbed water molecule. Adapted from [30]

We developed a simple model to catch the water solvent influence on the catalytic events, based on a micro-solvation model. A chemisorbed water mimics the hydrated surface. We considered the dehydrogenation of ethanol on two metallic surfaces, the oxophilic Rh(111) and the non-oxophilic Pt(111), and compared their activity with the corresponding hydrated surfaces, H_2O-Rh(111) and H_2O-Pt(111). In each case, two pathways are accessible: (i) the alkyl path, starting with the C−H bond scission that yields a hydroxyalkyl intermediate (ii) the alkoxy path, starting with the O−H bond scission, yielding an alkoxy intermediate. A contrasted picture emerges. The presence of water on Rh(111) drastically changes its activity. With the stabilization of the O−H scission, the reaction path is changed towards the generation of the alkoxy intermediate and the overall process exhibits a lower effective barrier than on Rh(111). On H_2O-Pt(111), the stabilization of the O−H scission transition state is not sufficient to switch to the alkoxy pathway. In addition, the initial C−H bond scission of the productive path is slightly pushed up in energy, reducing the overall catalytic activity. As a conclusion, the dehydrogenation of alcohol is expected to be activated on oxophilic metals and slightly deactivated on non-oxophilic ones.[28]

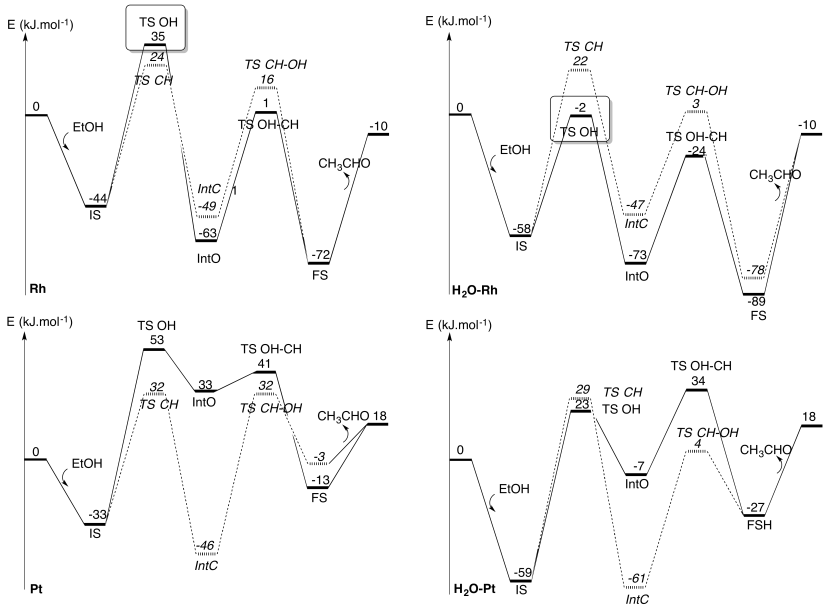

Figure 3.3: Reaction pathways for the dehydrogenation of ethanol to acetaldehyde on Rh(111), H_2O-Rh(111), Pt(111) and H_2O-Pt(111) surfaces. In straight line, the alkoxy path, in dashed line, the alkyl path. The reference energy is the clean slab or the hydrated slab and the ethanol isolated in gas phase. The produced hydrogen is considered as chemisorbed at an infinite distance. Adapted from [28]

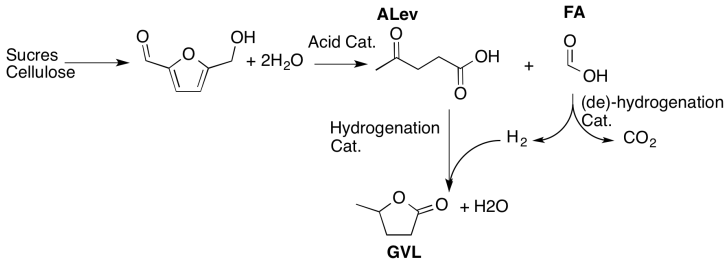

Figure 3.4: Possible route of valorisation of cellulose into γ-valerolactone (GVL) through the production of levulinic acid (LevA) and formic acid (FA).

We applied our solvation model to another reaction in collaboration with the group of A. Ruppert and J. Grams (Poland). Our target reaction was the conversion of levulinic acid (LevA) in γ-valerolactone (GVL). This conversion can be done using Ruthenium supported catalysts at 70°C, 50 bar of H_2. A greener strategy would be to use formic acid (FA) as a hydrogen donor instead of a pressure of H_2. However, the optimisation of the catalyst for the overall reaction is complex since this catalyst should optimally dehydrogenate FA, then hydrogenates the ketone function of LevA, a step that is followed by the cyclic transesterification into GVL.

We have started with the study of the hydrogenation of LevA under a pressure of H_2. Our experimental collaborators demonstrated that the Ruthenium catalyst was active only in presence of water as a solvent while Pt was not affected by the replacement of water by THF as a solvent. Thanks to our simple model of water solvent, we highlighted the key role of the water solvent in ketone hydrogenation in the case of Ruthenium: it stabilizes the initial O−H bond scission and destabilizes the low lying alkoxy intermediate. We have generalized to a series of transition metals (from Ru to Pt). Here again, the less oxophilic metals are poorly affected by chemisorbed water while the more oxophilic are strongly activated.[32] This is key to understand the wide usage of Ruthenium in biomass valorisation while it is barely used in petrochemistry

(gas phase reactions).[31] Building up on this study, we switched to the total reaction. During the hydrogen transfer from FA to LevA, the surface formate is so stable that it blocks at least partially the active sites for the subsequent reaction (LevA hydrogenation).[33]

According to our model, Pt catalysts should be insensitive to the choice of the solvent and exhibit the same activity in absence and in presence of water. However, the addition of water has been shown to increase noticeably the oxidation kinetics of aliphatic alcohols catalyzed by platinum-supported catalyst.[27] To relieve this apparent contradiction, we have to recall that the experimental conditions differ strongly. So far, we worked in the context of hydrogenation/hydrogenolysis, i.e. under a pressure of hydrogen or eventually of an inert gas. Under oxidative conditions, the reaction is performed is presence of O_2, the final oxidant. In those conditions, the splitting of O_2 is the key step impacted by the absence or presence of water. The reaction $O + H_2O \longrightarrow 2\,OH$ is known to occur easily on Pt(111)[5,12], yielding an hydroxylated platinum surface, OH−Pt. The dehydrogenation is greatly facilitated on OH−Pt compared with H_2O−Pt and Pt. In a nutshell, the presence of surface hydroxyls is required to perform the oxidation of alcohols using a Platinum based catalyst and this can be achieved only in presence of O_2 *and* water.[27]

3.3 What's next?

3.3.1 Screening of reaction networks

To tackle the great challenge of screening the extensive reaction networks of polyol transformation, we aimed at developing efficient strategies based on a hierarchy of methods. The complete network is screened based on a combination of scaling relations based on group additivity and BEP relations. Then, both the kinetics and the thermochemistry can be related directly to few descriptors such as the atomic adsorptions of

C, O and H. A sensitivity analysis of the micro-kinetic model build on this extensive network selects the most sensitive steps that need to be refined with more advanced models, including the complete evaluation of the elementary step at the DFT level. This will be achieved on polyol reactivity in collaboration with D. Vlachos, USA, in the project **Music**.

3.3.2 Better solvation models

With a very simple model, we already demonstrated the key role of co-adsorbed water. This micro-solvation can be completed by the inclusion of a continuum model of the bulk water as implemented by Hennig and co-workers in VASPsol for instance.[7] So far, the impact of the continuum is rather limited to few meV on the reaction energies and activation energies we considered so far. The next step is to build more complete models that describe explicitly water molecules. It is the aim of our collaboration with A. Goetz, USA in the project **Music**. This framework will open the door to more advanced simulations that should be able to tackle key questions in the domain of biomass valorisation. For instance, the oxidation of alcohols using O_2 as a final oxidant always require a base in a stoichiometric amount, generating a salt instead of the wanted carboxylic acid. This is a strong limitation of this strategy since the subsequence hydrolysis yields an equivalent of undesired waste.[3,13,18] to better understand the synergetic between the metal (typically Au or Au-Pd, Au-Pt alloys) and the base (NaOH) requires new methodological advances to include the water solvent.

3.3.3 From alcohols to aromatics

The ligno-cellulosic biomass is composed of carbohydrate polymers (cellulose and hemicellulose) and aromatic polymers (lignin). So far, lignin was considered as too recalcitrant to be used as a feedstock, despite its strong content in aromatics. As shown in 2.5, it is a highly heterogeneous polymer, increasing the challenge of a selective produc-

tion of chemical from this feedstock. The conversion of lignin-derived aromatics is one of our next targets in biomass valorization using metallic supported catalysts. In this context, R. Réocreux dedicates his PhD project to the C−C and C−O cleavages in lignin-derived aromatics as a potential source of aromatic compounds in collaboration with J. Giorgi, uOttawa.

3.3.4 Beyond the monometallic supported catalyst

My research was dedicated to supported monometallic catalysts that can be usually nicely modeled using a simple slab model of the most stable facet ((111) or (0001)). To open new directions of design, it is key to probe several manners to tune the catalytic activity. A first possibility is to analyze the alloying of two transition metals.[2,8] This will be our strategy in the amination of alcohols but also in the hydrogen transfert from formic acid to levulinic acid, yielding γ-valerolactone.[22,33] Another possibility to tune a catalyst is to play with the exposed facet.[11,20] We have recently studied how the conditions of preparation of metallic particles can affect the nature of the most exposed facet. Our theoretical approach allows us to predict the influence of the concentration of the shaping agent on the Cobalt nanoparticles shape.[24] An intermediate concentration yields to rods that expose mainly the (10.0) facet, where ternary sites are not present anymore. Being able to control the shape allows us to establish structure/activity relation. This will be address soon in the project **Tanopol**. Another clear way to tune a catalyst activity is to play on co-adsorbant and modifiers.[15] We have shown that the generation of surface hydroxyl is essential in polyols oxidation catalyzed by Pt.[27] Similarly, we are currently focusing on the influence of co-adsorbed ammonia on the amination of alcohol (PhD projet of A. Dumon). The shaping agent used to tune the shape of the nanoparticle may also affect the catalytic activity, as already demonstrated by the group of Medlin[9,17] and others.[4] A better understanding of those co-adsorption effects is still required. In all those ways of modifying a

catalyst, the atomistic simulations can sustain a rational design.[16]

Bibliography

[1] Akpa, B. S.; D'Agostino, C.; Gladden, L. F.; Hindle, K.; Manyar, H.; McGregor, J.; Li, R.; Neurock, M.; Sinha, N.; Stitt, E. H.; Weber, D.; Zeitler, J. A.; Rooney, D. W. *J. Catal.* **2012**, *289*, 30–41, CH, OH.

[2] Alonso, D. M.; Wettstein, S. G.; Dumesic, J. A. *Chem. Soc. Rev.* **2012**, *41*, 8075–8098.

[3] Besson, M.; Gallezot, P.; Pinel, C. *Chem. Rev.* **2014**, *114*, 1827–1870.

[4] Chen, K.; Wu, H. T.; Hua, Q.; Chang, S. J.; Huang, W. X. *Phys. Chem. Chem. Phys.* **2013**, *15*, 2273–2277.

[5] Clay, C.; Haq, S.; Hodgson, A. *Phys. Rev. Lett.* **2004**, *92*, 046102.

[6] Dusselier, M.; Van Wouwe, P.; Dewaele, A.; Makshina, E.; Sels, B. F. *Energy & Environmental Science* **2013**, *6*, 1415–1442.

[7] Fishman, M.; Zhuang, H. L.; Mathew, K.; Dirschka, W.; Hennig, R. G. *Phys. Rev. B* **2013**, *87*, 245402.

[8] Gallezot, P. *Chem. Soc. Rev.* **2012**, *41*, 1538–1558.

[9] Kahsar, K. R.; Schwartz, D. K.; Medlin, J. W. *J. Am. Chem. Soc.* **2014**, *136*, 520–526.

[10] Kobayashi, H.; Fukuoka, A. *Green Chem.* **2013**, *15*, 1740–1763.

[11] Lee, I.; Zaera, F. *Top. Catal.* **2013**, *56*, 1284–1298.

[12] Lew, W.; Crowe, M. C.; Karp, E.; Campbell, C. T. *J. Phys. Chem. C* **2011**, *115*, 9164.

[13] Liu, S.-S.; Sun, K.-Q.; Xu, B.-Q. *Acs Catalysis* **2014**, *4*, 2226–2230.

[14] McManus, I.; Daly, H.; Thompson, J. M.; Connor, E.; Hardacre, C.; Wilkinson, S. K.; Bonab, N. S.; ten Dam, J.; Simmons, M. J. H.; Stitt, E. H.; D'Agostino, C.; McGregor, J.; Gladden, L. F.; Delgado, J. J. *J. Catal.* **2015**, *330*, 344–353.

[15] Medlin, J. W. *ACS Catal.* **2011**, *1*, 1284–1297.

[16] Norskov, J. K.; Bligaard, T.; Rossmeisl, J.; Christensen, C. H. *Nat. Chem.* **2009**, *1*, 37–46.

[17] Pang, S. H.; Schoenbaum, C. A.; Schwartz, D. K.; Medlin, J. W. *Nat. Comm.* **2013**, *4*, 2448.

[18] Rodriguez, A. A.; Williams, C. T.; Monnier, J. R. *Catalysis Letters* **2015**, *145*, 750–756.

[19] Ruppert, A. M.; Weinberg, K.; Palkovits, R. *Angew. Chem. Int. Ed.* **2012**, *51*, 2564–2601.

[20] Van Santen, R. A. *Acc. Chem. Res.* **2009**, *42*, 57–66.

[21] Wan, H. J.; Vitter, A.; Chaudhari, R. V.; Subramaniam, B. *J. Catal.* **2014**, *309*, 174–184.

[22] Wright, W. R. H.; Palkovits, R. *ChemSusChem* **2012**, *5*, 1657–1667.

[23] Zhou, C. H.; Zhao, H.; Tong, D. S.; Wu, L. M.; Yu, W. H. *Catal. Rev. - Sci. Eng.* **2013**, *55*, 369–453.

[24] Ait Atmane, K.; Michel, C.; Piquemal, J.-Y.; Sautet, P.; Beaunier, P.; Giraud, M.; Sicard, M.; Nowak, S.; Losno, R.; Viau, G. *Nanoscale* **2014**, *6*, 2682–2692, .

[25] Auneau, F.; Michel, C.; Delbecq, F.; Pinel, C.; Sautet, P. *Chemistry-a European Journal* **2011**, *17*, 14288–14299, .

[26] Auneau, F.; Sadr Arani, L.; Besson, M.; Djakovitch, L.; Michel, C.; Delbecq, F.; Sautet, P.; Pinel, C. *Topics in Catalysis* **2012**, *55*, 474–479, .

[27] Chibani, S.; Michel, C.; Delbecq, F.; Pinel, C.; Besson, M. *Catalysis Science and Technology* **2012**, *3*, 339–350 .

[28] Loffreda, D.; Michel, C.; Delbecq, F.; Sautet, P. *Journal of Catalysis* **2013**, *308*, 374–385 .

[29] Michel, C.; Auneau, F.; Delbecq, F.; Sautet, P. *ACS Catalysis* **2011**, *1*, 1430–1440 .

[30] Michel, C.; Göltl, F.; Sautet, P. *Physical Chemistry Chemical Physics* **2012**, *14*, 15286–15290 .

[31] Michel, C.; Gallezot, P. *ACS Catalysis* **2015**, *5*, 4130–4132 .

[32] Michel, C.; Zaffran, J.; Ruppert, A. M.; Matras-Michalska, J.; Jedrzejczyk, M.; Grams, J.; Sautet, P. *Chemical Communications* **2014**, *50*, 12450–12453 .

[33] Ruppert, A. M.; Jedrzejczyk, M.; Sneka-Platek, O.; Keller, N.; Dumon, A. S.; Michel, C.; Sautet, P.; Grams, J. *Green Chemistry* **2016**, –.

[34] Zaffran, J.; Michel, C.; Auneau, F.; Delbecq, F.; Sautet, P. *ACS Catalysis* **2014**, *4*, 464–468, .

[35] Zaffran, J.; Michel, C.; Delbecq, F.; Sautet, P. *Journal of Physical Chemistry C* **2015**, *119*, 12988–12998, .

CHEMISTRY
A EUROPEAN JOURNAL

DOI: 10.1002/chem.201101318

Unravelling the Mechanism of Glycerol Hydrogenolysis over Rhodium Catalyst through Combined Experimental–Theoretical Investigations

Florian Auneau,[a, b] Carine Michel,[b] Françoise Delbecq,*[b] Catherine Pinel,*[a] and Philippe Sautet[b]

Abstract: We report herein a detailed and accurate study of the mechanism of rhodium-catalysed conversion of glycerol into 1,2-propanediol and lactic acid. The first step of the reaction is particularly debated, as it can be either dehydration or dehydrogenation. It is expected that these elementary reactions can be influenced by pH variations and by the nature of the gas phase. These parameters were consequently investigated experimentally. On the other hand, there was a lack of knowledge about the behaviour of glycerol at the surface of the metallic catalyst. A theoretical approach on a model Rh(111) surface was thus implemented in the framework of density functional theory (DFT) to describe the above-mentioned elementary reactions and to calculate the corresponding transition states. The combination of experiment and theory shows that the dehydrogenation into glyceraldehyde is the first step for the glycerol transformation on the Rh/C catalyst in basic media under He or H_2 atmosphere.

Keywords: density functional calculations · lactic acid · propanediol · reaction mechanisms · rhodium

Introduction

In the actual context of shortage of petroleum resources, biomass is considered a renewable alternative for fuels and chemical substitution. More importantly, the chemical transformation of bio-resources has a reduced impact on greenhouse gas emissions compared to petroleum-dependent industrial processes. Glycerol, obtained as a co-product of the transesterification of vegetable oils to produce bio-diesel, is a potential building block to be processed in bio-refineries.[1,2] The valorisation of this abundant C_3-platform molecule has been intensively implemented experimentally along several routes.[3–5] Its heterogeneously catalysed transformation into important value-added products such as acrolein through dehydration,[6] glycerol esters or ethers through esterification or etherification,[7] 1,2-propanediol (12-PDO)[8] or 1,3-propanediol (13-PDO)[9–12] through hydrogenolysis and oxidation products such as glyceric acid or dihydroxyacetone[13–15] has been targeted over recent years. Due to its availability, glycerol has also been envisaged as a potential source of renewable fuels through, for instance, aqueous-phase reforming.[16]

Glycerol hydrogenolysis in the presence of metallic catalysts has always been challenging because of selectivity considerations under the moderate to high hydrogen pressures usually employed (0.1 to more than 100 bar). PDO-selective formation is usually the aim, and it is consequently necessary to avoid C–C bond ruptures, which lead to undesired C1 and C2 cracking products such as ethylene glycol, ethanol, methane, methanol and carbon dioxide. Historically, first attempts with Co, Ni Raney, Cu Raney, Cu, Ru, Rh, Ir and Pt catalysts were conducted by Montassier et al.[17,18] The addition of a second metal was proven to be useful to enhance the selectivity into 12-PDO, for instance, in the case of Cu–chromite,[8] Cu–Ag,[19] Ru–Cu[20] or Ru–Pt.[21] More recently, important works allowed significant improvements in the selective hydrogenolysis into 13-PDO with Ir–Re[9] or Pt–Re.[10]

The glycerol transformation into PDO is formally a dehydration coupled to a hydrogenation: glycerol+H_2→PDO+H_2O. Dehydration is known to be strongly sensitive to the pH medium, whereas hydrogenation is expected to be dependent on the gas-phase atmosphere composition as well as on the nature of the catalyst. Thus, both the pH solution and the atmosphere composition may be key parameters to control the selectivity of the glycerol conversion into PDO in the presence of a metallic catalyst.

Indeed, the pH of the solution influences the activities of various metal catalysts. On the one hand, acidic co-catalysts have shown good abilities to accelerate reaction rates and obtain at the same time good selectivity into 12-PDO, as

[a] F. Auneau, Dr. C. Pinel
Université de Lyon, Institut de Recherches
sur la Catalyse et l'Environnement de Lyon
IRCELYON, Université Lyon I, CNRS, UMR5256
2, Avenue Albert Einstein
69626 Villeurbanne Cedex (France)
Fax: (+33) 4-72-44-53-99
E-mail: catherine.pinel@ircelyon.univ-lyon1.fr

[b] F. Auneau, Dr. C. Michel, Dr. F. Delbecq, Dr. P. Sautet
Université de Lyon, CNRS, Institut de Chimie de Lyon
ENS Lyon, Laboratoire de Chimie, UMR CNRS 5182
46 Allée d'Italie, 69364 Lyon Cedex 07 (France)
Fax: (+33) 4-72-72-88-60
E-mail: francoise.delbecq@ens-lyon.fr

Supporting information for this article is available on the WWW under http://dx.doi.org/10.1002/chem.201101318.

evidenced by the group of Tomishige et al.[22–25] On the other hand, as initially reported by Montassier et al., the Cu Raney activity is increased in alkaline conditions.[17] However, the distribution of the products is strongly affected with the appearance of lactic acid (LA) and the decreased yield for cracking products such as ethylene glycol (EG) compared to neutral pH. These trends were confirmed for other catalytic systems, namely, carbon-supported Pt, Ru, PtRu and AuRu catalysts.[26,27] In addition, the formation of formic acid (FA) and gaseous species was reported. The appearance of oxidation products such as LA and FA under reductive conditions raises questions about the underlying mechanism.

As expected, the role of the gas-phase atmosphere is also debated. Recently, glycerol conversion toward 12-PDO (together with EG) was carried out by D'Hondt et al. in the absence of added hydrogen with a Pt/NaY catalyst.[28] Montassier's group had originally mentioned for a Cu Raney catalyst that the reaction rate of glycerol transformation into 12-PDO and EG at neutral pH was poorly affected by the presence or absence of hydrogen, whereas LA was only formed in low amounts in both cases (<1%).[17] These reports are astonishing at first sight: they demonstrate the feasibility of the hydrodeoxygenation of glycerol under inert atmosphere, whereas, as said before, glycerol conversion into PDO should require the presence of hydrogen. This raises again questions about the mechanism. The hydrodeoxygenation of glycerol under inert atmosphere has not been investigated systematically since these results, though some studies have dealt with this interesting issue.[8,21,29–32]

All these parameters (second metal, pH and gas-phase composition) have a pronounced influence on the reactivity. The simple picture of a hydrogenation coupled to dehydration is not sufficient to understand all the experimental results. In particular, the first step of the reaction is still under debate. It has been proposed to be a dehydration, or more surprisingly, under H_2 atmosphere a dehydrogenation (Scheme 1). The dehydration has been proposed for copper-based[33] catalysts, including copper–zinc[34] and copper–chromite[8] catalysts. Noble metals are also concerned with this dehydration mechanism, as shown with ruthenium carbon-based catalysts in the presence of an acidic co-catalyst.[22–25,32] However, the mechanism originally suggested by Montassier et al.[17] puts forward the dehydrogenation as the first step of the reaction in neutral water and alkaline conditions with a copper Raney catalyst. It was also supported by Hawley et al.[35] and reported for carbon-based Ru, Pt, PtRu and AuRu catalysts in alkaline conditions.[26,27] Nevertheless, the exact mechanism still remains in question, as dehydration and dehydrogenation can occur simultaneously, for instance, with platinum supported on alumina catalysts together with reforming processes.[30] For this kind of catalyst, not only the support but also the platinum metal is shown to play a role in the dehydration of glycerol.[29] Recently, it was demonstrated that even for copper–zinc catalysts, traditionally associated with the dehydration mechanism, dehydrogenation takes place on the metallic copper.[31] Concerning rhodium, this metal has often been associated with the dehydration mechanism in past studies either in association with an acidic co-catalyst[36] or with the assistance of rhenium.[37]

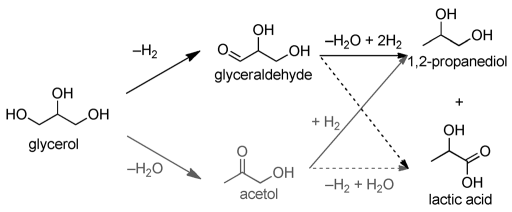

Scheme 1. Glycerol transformation into 12-PDO and LA.

The interpretation of this complex system would benefit from a better comprehension of surface phenomena from a fundamental point of view. For this aim, theoretical modelling appears as a useful complementary tool to experiments. Some of us have already investigated from density functional theory (DFT) calculations the adsorption of glycerol and its dehydration intermediates at the surfaces of Ni(111), Rh(111) and Pd(111) to identify the key points that control the selectivity of the hydrogenolysis reaction.[38] The adsorption and reactivity of other small oxygenated compounds such as methanol[39–45] (MeOH) or ethanol[46–56] (EtOH) on the model surfaces of transition metals can also provide helpful clues. Despite the tremendous number of works realised until now, only a few have performed a mixed experimental and theoretical approach (using DFT) to gain further insights into the reactivity of glycerol. This is the case for Davis, Neurock and their co-workers[57] who have considered the oxidation mechanism of glycerol in alkaline aqueous conditions by using Au, Pd and Pt catalysts on various supports (TiO_2 and C). The theoretical part focused on the oxidation of ethanol into acetic acid on Au(111) and Pt(111) assisted by surface-bonded hydroxide species in liquid water. In the direct line of our experimental investigations on glycerol hydrogenolysis into PDO,[12,58] we focus here on the glycerol hydrogenolysis over an Rh/C catalyst in alkaline solution. We report in detail the behaviour of this catalyst as a function of various reaction parameters. In particular, we have observed the concomitant formation of hydrogenolysis (12-PDO) and oxidation (LA) products under both reductive and inert atmospheres. This raises the question: Is this process really a hydrogenolysis? To arrive at an answer, we aim at a better comprehension of the elementary steps of the reaction. The first step is of particular interest, as it can be either dehydration or dehydrogenation. We have focused on the energy profiles of these two competitive first steps, dehydrogenation and dehydration with theoretical DFT calculations performed on a model rhodium Rh(111) surface. We gather here our experimental results together with the theoretical results to gain a better insight into the unexpected processes that occur during the glycerol conversion and to provide a unified picture of the reaction mechanism.

CHEMISTRY
A EUROPEAN JOURNAL

Experimental Results

First, we detail the behaviour of the 0.7% Rh/C catalyst we have prepared as a function of various reaction parameters such as solution pH and gas-atmosphere composition. We focus in particular on their influence on the products distribution and the kinetics. Then we provide the gas-phase analysis and check the stability of the reaction products.

Catalytic tests: Table 1 shows how the pH of the solution can impact the conversion and the product distribution in the presence of rhodium-based catalyst. At neutral pH under hydrogen atmosphere, almost no glycerol was converted (<2%) in 12 h, and only some traces of 12-PDO (< 1% yield) were analysed. The reaction rate increases with the alkalinity of the glycerol solution to give 12-PDO but also LA as the major products. The best conversion reached is nonetheless still low (23% after 12 h). Moreover, glyceraldehyde (GAL) was observed (together with glyceric acid) at neutral pH, whereas acetol was not observed regardless of the pH (Scheme 1).

Table 1. Influence of the pH on the reactivity.[a]

Entry	Solvent	Conv. [%]	Mass balance [%][b]	Yield [%] 12-PDO	LA	Others[c]
1	H_2O	2	100	<1	0	ε
2	NaOH 0.1 M	11	96	4	5	2
3	NaOH 1 M	23	100	9	9	5

[a] Conditions: glycerol (6 mL, 5 wt%) in solvent, SPR16, 50 bar H_2, 453 K, 12 h. [b] TOC analysis. [c] Others including EG, 13-PDO, formic acid (FA), EtOH, MeOH, acetol, acetic acid (AA).

Interestingly, a catalytic transformation of glycerol also happens in the absence of hydrogen when glycerol comes into contact with the metallic catalyst at basic pH (Table 2). The conversion is even surprisingly higher under He (55%) than under H_2 (22%). Moreover, the product distribution is strongly modified upon atmospheric change. Whereas 12-PDO is the major product under H_2, LA becomes the major product under inert He atmosphere (its yield is multiplied by 5). However, it is striking that 12-PDO, which is the product of the hydrogenolysis reaction (hence requiring H atoms to be formed), is still produced under He (with a yield reduced by 50% relative to the reaction under H_2). In addition, when performing the reaction in water at neutral pH under He, the conversion of glycerol was less than 1% after 12 h and traces of GAL (together with glyceric acid), pyruvaldehyde, acetol and 12-PDO were detected.

Table 2. Gas-phase influence on reactivity of glycerol in alkaline conditions.[a]

Entry	Gas	Conv. [%]	Mass balance [%][b]	Yield [%] 12-PDO	LA	Others[c]
1	He	55	94	4	25	26
2	H_2	22	100	9	5	8

[a] Conditions: glycerol (100 mL, 5 wt%) in NaOH 1 M, Hastelloy autoclave equipped with a Teflon pot, 50 bar H_2/30 bar He, 453 K, 8 h. [b] TOC analysis after 24 h reaction. [c] Others including EG, 1,3-PDO, FA, EtOH, MeOH, acetol, AA.

Kinetic study: A kinetic study was implemented to analyse the evolution of the reaction. The glycerol conversion profile (Figure 1) is very different under He or H_2 atmosphere. Glycerol reacts indeed faster under He than under H_2, and after 24 h reaction, the glycerol is almost totally converted under He (91%), whereas half (49%) of the initial glycerol is still present under H_2. The initial activity of the reaction is 0.8 mol min^{-1} mol_{Rh}^{-1} under hydrogen and 3.3 mol min^{-1} mol_{Rh}^{-1} under helium (hence larger by a factor of 4). The evolution of the yields as a function of the conversion provides information about product formation, stability and reactivity. From the beginning, the product yield increases linearly along the conversion for 12-PDO and LA, regardless of the type of atmosphere (Figure 2). This indicates that LA and 12-PDO are the primary products of the reaction.

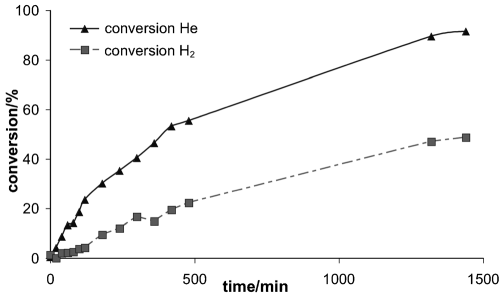

Figure 1. Glycerol conversion over reaction time: glycerol (100 mL, 5 wt%) in NaOH 1 M, Hastelloy autoclave equipped with a Teflon pot, 50 bar H_2/30 bar He, 453 K.

Data can be extracted from the kinetic study to compare the distribution of products at similar glycerol conversion (Table 3). After 24 h, 49% conversion is obtained under 50 bar H_2, thus yielding 22% 12-PDO and 15% LA. Under He, similar conversion (46%) is achieved after 6 h. LA is clearly the major product with a 20% yield; the 12-PDO production reaches only 3% yield.

Gas-phase analysis: Gas-phase analysis has been motivated by the increase of the pressure in the reactor along time at constant temperature under inert atmosphere (Figure 3). The pressure rises rapidly at the very beginning of the reaction but evolves more gradually after 100 min. There is therefore generation of gaseous species, and it is important to identify these compounds. Under hydrogen atmosphere, the initial increase in pressure is interestingly slower than under helium, and rapidly (20 min) the pressure starts to decrease, thereby indicating hydrogen consumption. The final gas-phase composition reflects the observed pressure evolu-

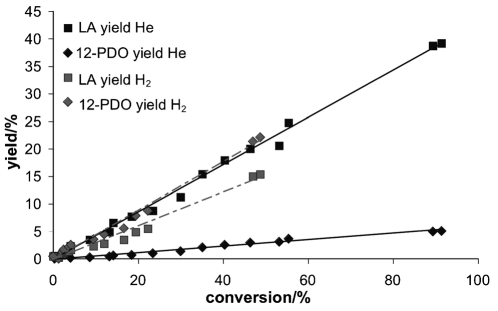

Figure 2. Evolution of the product yields as a function of the conversion of glycerol (linear regression): glycerol (100 mL, 5 wt%) in NaOH 1 M, Hastelloy autoclave equipped with a Teflon pot, 50 bar H_2/30 bar He, 453 K.

Table 3. Products distribution at glycerol isoconversion.[a]

Entry	Gas	t [h]	Conv. [%]	Yield [%]		
				12-PDO	LA	Others[b]
1	He	6	46	3	20	23
2	H_2	24	49	22	15	12

[a] Conditions: glycerol (100 mL, 5 wt%) in NaOH 1 M, Hastelloy autoclave equipped with a Teflon pot, 50 bar H_2/30 bar He, 453 K. [b] Others including EG, 1,3-PDO, FA, EtOH, MeOH, acetol, AA.

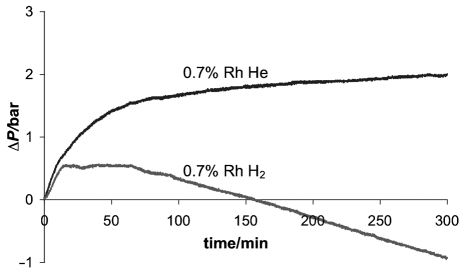

Figure 3. Continuous pressure acquisitions as a function of reaction time under He or H_2 pressure: glycerol (6 mL, 5 wt%) in NaOH 1 M, 30 bar He or 50 bar H_2, 453 K.

tion along the reaction (Table 4). Under hydrogen only trace amounts of water, propane and propene were analysed. Under helium, analysis of the gas phase after 24 h reveals the presence of a large fraction of hydrogen, the origin of which is to be discussed, together with traces of carbon monoxide water.

Aqueous-phase reforming (APR) of oxygenated compounds is a well-known reaction to produce H_2 and other fuels from biomass.[59–61] For glycerol, APR into synthesis gas is usually performed at 498–573 K.[62] Our reactions were performed at a lower temperature of 453 K. Moreover, gas-phase analysis only showed traces of CO under helium and

Table 4. Gas-phase analysis.[a]

Entry	Initial gas phase	Final gas phase			
		He [%]	H_2 [%]	CO [%]	Others
1	He	81	18	0.5	H_2O
2	H_2	0	>99	ε	propane, propene, H_2O

[a] Conditions: glycerol (100 mL, 5 wt%) in NaOH 1 M, Hastelloy autoclave equipped with a Teflon pot, 50 bar H_2/30 bar He, 453 K, 24 h. Helium, hydrogen and carbon monoxide percentages refer to a volumic percentage. Products not quantified were only detected in traces amount.

a small content of C_3 alkane (propane) and alkene (propene) under hydrogen. In both cases, the only gaseous product in any significant amount is hydrogen. It is supposed to be responsible for the small pressure increase noticed under hydrogen at the beginning of the reaction, and for the continuous pressure increase all over the reaction observed under helium. If APR were occurring, other gases such as methane, carbon monoxide and carbon dioxide would have been detected in significant amounts. Furthermore, all the mass balances of the organic soluble products were in the range of 94–100%. We can consequently exclude APR from playing a key role in the pressure augmentation and the H_2 production observed.

Product stability: The stability of LA and 12-PDO has been evaluated under the reaction conditions (5 wt% of product in NaOH 1 M with Rh/C catalyst). LA does not show any conversion after 12 h at 453 K either under He or under H_2. On the contrary, 12-PDO is found to be reactive, especially under inert atmosphere, and yields mainly LA, formic acid (FA), and degradation products (Table 5).

Table 5. Reactivity of the reaction products, 12-PDO and LA, under reaction conditions.[a]

Entry	Substrate	Gas	Conv. [%]	Mass balance[b] [%]	Yield [%]	
					LA	Others[c]
1	12-PDO	He	62	100	13	10
2	12-PDO	H_2	8	100	2	3
3	LA	He	0	100	–	ε
4	LA	H_2	0	100	–	ε

[a] Substrate (6 mL, 5 wt%) in NaOH 1 M, SPR16, 50 bar H_2/30 bar He, 453 K, 12 h. [b] TOC analysis. [c] Others including EG, 1,3-PDO, FA, EtOH, MeOH, acetol, AA.

Theoretical Calculations

In this part, we report the theoretical study on the relative stabilities of glycerol, the products and the potential intermediates when adsorbed on the Rh(111) surface. Then we focus on the first elementary steps of the catalytic reaction and provide energy barriers. The (111) face was chosen because it is the main face of Rh particles.

Glycerol adsorption: Glycerol is a C3 polyalcohol with three hydroxyl groups on terminal (positions 1 and 3 of the alkyl chain) and central (position 2) carbon atoms. Those hydrox-

CHEMISTRY
A EUROPEAN JOURNAL

yl groups will be respectively designated as terminal and central hydroxyl groups in the following. Glycerol exhibits numerous stable conformations in the gas phase.[63,64] The most stable one has been re-optimised with our method to give the lowest conformation in energy represented in Figure 4 (left panel) and to show two internal hydrogen

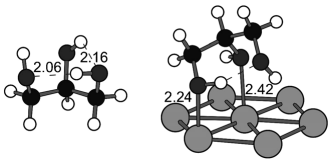

Figure 4. Most stable conformations of glycerol in the gas phase and on the Rh(111) surface. Black, white, dark grey and light grey spheres correspond to C, H, O and Rh atoms, respectively. Hydrogen bonds are represented in dashed dark grey lines. Bond lengths are expressed in Å. Colour version of the figure is available in the Supporting Information (Figure S3).

bonds. Glycerol can adopt several adsorption modes on the Rh(111) surface.[38] The optimal structure (Figure 4, right panel) shows two oxygen atoms adsorbed atop sites of Rh and one hydrogen bond from the adsorbed terminal hydroxyl group to the other terminal hydroxyl, farther from the surface. The corresponding adsorption energy is $E_{ads} = -0.60$ eV. It is higher than the typical adsorption energy of monoalcohols (≈ -0.40 eV).[51]

Stability of products and intermediates on the Rh(111) surface: Experimentally, glycerol can be converted into two products: 1,2-propanediol (12-PDO) and lactic acid (LA). In the gas phase, the corresponding reactions can be formally written [Eqs. (1) and (2)]:

$$\text{Glycerol} + H_2 \rightarrow \text{12-PDO} + H_2O \quad (1)$$

$$\text{Glycerol} \rightarrow \text{LA} + H_2 \quad (2)$$

From a thermodynamic point of view, the first reaction is exothermic ($\Delta E_{react}(1) = -1.00$ eV), whereas the second one is almost athermic ($\Delta E_{react}(2) = 0.03$ eV). On the surface, the situation is reversed. Indeed, the previous chemical reactions can be rewritten in the following manner, taking into account the dissociated character of H_2 and H_2O on Rh(111) [Eqs. (3) and (4)]:

$$\text{Glycerol} + 2\,H \rightarrow \text{12-PDO} + H + OH \quad (3)$$

$$\text{Glycerol} \rightarrow \text{LA} + 2\,H \quad (4)$$

When considering each species being adsorbed on Rh(111) at low coverage, both reactions are exothermic but the formation of LA is strongly favoured by 0.71 eV ($\Delta E_{react}(3) = -0.16$ eV and $\Delta E_{react}(4) = -0.87$ eV, Figure 5).

Two pathways are plausible to convert glycerol into these products. They differ by the first step that can consist of

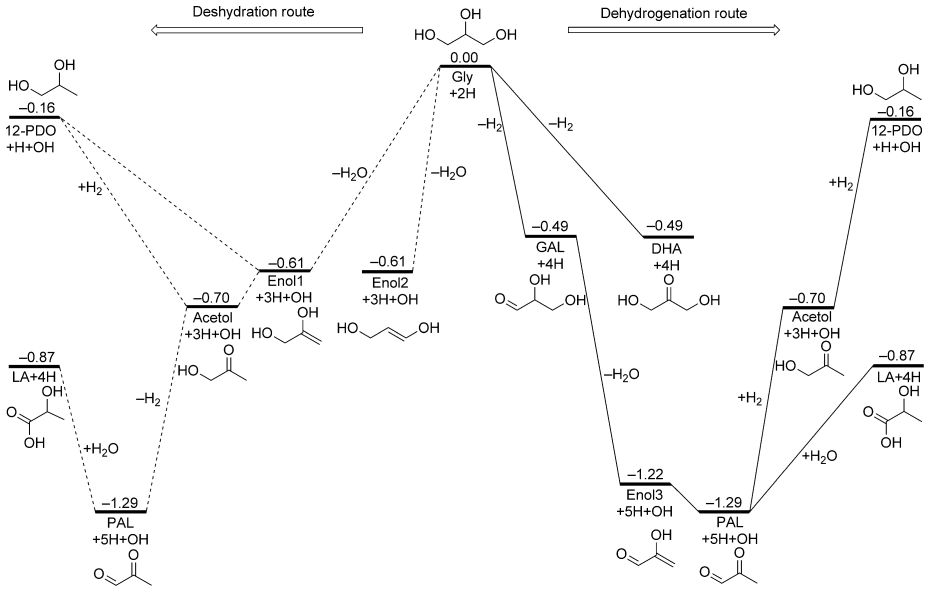

Figure 5. Relative stabilities of intermediates and reaction products adsorbed onto the Rh(111) surface. Dashed lines and continuous lines stand for dehydration and dehydrogenation paths. All the products and atoms considered are adsorbed on the slab. Energies are given in eV. The reference energy taken here is the glycerol adsorbed at the Rh(111) surface plus two isolated hydrogen adsorbed at the Rh(111) surface.

either dehydration or dehydrogenation. We report in Figure 5 the relative stability of the reaction intermediates when adsorbed onto the Rh(111) surface.

Through the dehydration path, glycerol can first lead to two different enols almost isoenergetic on Rh(111): 1) the propene-2,3-diol, namely, Enol 1; or 2) the propene-1,3-diol, namely, Enol 2. On Rh(111) the C=C bond is coordinated in a π mode and a terminal hydroxyl group is bound to the surface (Figure 6). The conversion of Enol 2 into 13-PDO

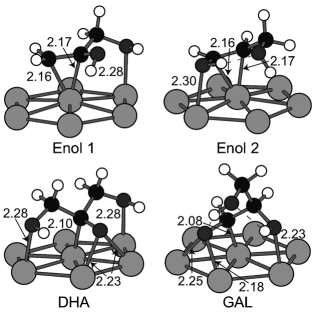

Figure 6. Structures of Enol 1 (propene-2,3-diol), Enol 2 (propene-1,3-diol), DHA and GAL chemisorbed onto the Rh(111) surface. Black, white, dark grey and light grey spheres correspond to C, H, O and Rh atoms, respectively. Dashed dark grey lines represent hydrogen bonds. Colour version of the figure is available in the Supporting Information (Figure S4).

through hydroxypropanaldehyde has not been considered, since 13-PDO is not seen in the experiment. Enol 1 can be rearranged further in acetol ($\Delta E = -0.09$ eV) and then acetol can be hydrogenated into 12-PDO ($\Delta E = 0.54$ eV). Acetol can also be dehydrogenated toward pyruvaldehyde (PAL) ($\Delta E = -0.59$ eV), finally giving LA by an intramolecular Cannizzaro reaction under basic conditions ($\Delta E = 0.42$ eV).

Considering the dehydrogenation path, glycerol leads first to dihydroxyacetone (DHA) or glyceraldehyde (GAL). In the gas phase, DHA is more stable than GAL by 0.17 eV but those two compounds are almost isoenergetic once adsorbed at an Rh(111) slab. Both molecules are adsorbed with a lateral interaction of the C=O bond with the surface (Figure 6). Whereas DHA cannot easily undergo a further dehydration step, GAL can be dehydrated into an enol (Enol 3, with a very exothermic reaction, $\Delta E = -0.73$ eV) that rearranges into PAL (Figure 5). Then LA is reached by an intramolecular Cannizzaro reaction, whereas 12-PDO results from a double hydrogenation through acetol.

Thus, the main difference between the two routes lies in the nature of the first step. Dehydration, dehydrogenation and enol rearrangements into ketone or aldehyde are exothermic on the surface. On the contrary, C=O bonds hydrogenation steps and LA formation are endothermic.

Glycerol dehydrogenation path: The two possible products GAL and DHA result from successive C–H and O–H bond ruptures on the Rh surface. We describe first the structures of the four mono-dehydrogenated intermediates and the eight transition-state (TS) structures. Then we report the four possible reaction paths.

Intermediate and transition-state structures: The first X–H bond scission can take place at the central (CHc) or terminal (CHt) carbon atom, or at the central (OHc) or terminal (OHt) oxygen atom that leads to alkyl intermediates (Int_{CHc}, Int_{CHt}) and alkoxy intermediates (Int_{OHc} and Int_{OHt}), respectively (Figure 7). Both alkyl intermediates are bound to the

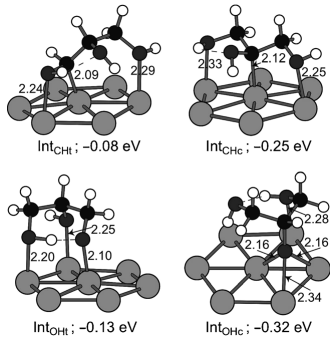

Figure 7. Structure of mono-dehydrogenated intermediates on Rh(111). Black, white, dark grey and light grey spheres correspond to C, H, O and Rh atoms respectively. Dashed dark grey lines represent hydrogen bonds. Int_{CHt}, Int_{CHc}, Int_{OHt} and Int_{OHc} are the mono-dehydrogenated intermediates that resulting respectively from terminal C–H (CHt), central C–H (CHc), terminal O–H (OHt) and central O–H (OHc) bond ruptures in glycerol. The displayed structures are the ones after hydrogen diffusion away from the intermediate, that is without the co-adsorbed hydrogen atom. Energies are in eV. The reference energy taken here is the glycerol adsorbed at the Rh(111) surface. Bond lengths are expressed in Å. Colour version of the figure is available in the Supporting Information (Figure S5).

Rh atoms through the mono-dehydrogenated carbon atom and both the terminal hydroxyl groups. The Int_{CHc} intermediate is more stable than the Int_{CHt} by 0.17 eV, which is in agreement with the greater stability of secondary carbon radicals relative to primary ones. Conversely, alkoxy intermediates structures differ: in Int_{OHc}, the alkoxy in adsorbed in a ternary site, whereas it is adsorbed at a top site in Int_{OHt}. This can explain the greater stability of Int_{OHc} (by 0.19 eV) since methoxy is preferentially adsorbed at a ternary site rather than at a top site by 0.39 eV. For Int_{OHt}, the adsorption of the hydroxyl group and the position of the internal hydrogen bonds constrain the alkoxy to be in its less-stable position. The structures of the transition states for the first and the second dehydrogenation steps are shown in Figure 8 and Figure 9, respectively. The label of the TS for the second hydrogenation is built by concatenating the

CHEMISTRY
A EUROPEAN JOURNAL

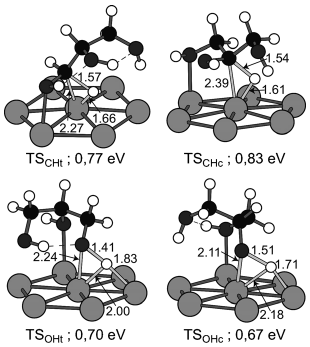

Figure 8. Structure of the transition states for the first step of glycerol dehydrogenation on Rh(111). Black, white, dark grey and light grey spheres correspond to C, H, O and Rh atoms, respectively. Dashed dark grey lines represent hydrogen bonds. Bonds implicated in the TS are represented in light grey. Energies are in eV. The reference energy taken here is the glycerol adsorbed at the Rh(111) surface. Bond lengths are expressed in Å. Colour version of the figure is available in the Supporting Information (Figure S6).

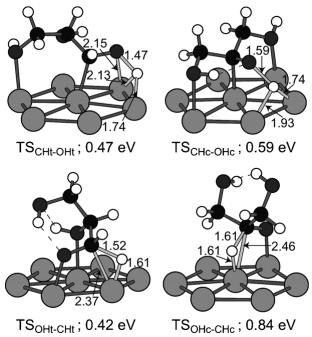

Figure 9. Structure of the transition states for the second step of glycerol dehydrogenation on Rh(111). Black, white, dark grey and light grey spheres correspond to C, H, O and Rh atoms. Dashed dark grey lines represent hydrogen bonds. Bonds implied in the TS are represented in light grey. Energies are in eV. The reference energy taken here is the glycerol adsorbed at the Rh(111) surface. Bond lengths are expressed in Å. Colour version of the figure is available in the Supporting Information (Figure S7).

name of bonds dissociated in the first step and in the second step. TS structures can be divided into two categories: 1) TS of the C–H bond rupture are characterised by a triangle configuration Rh/C/H, the bond being broken onto an atop site 2) TS of the O–H bond rupture are characterised by a oxygen at a top site and a hydrogen atom in a neighbouring bridge position.

Reaction paths: Figure 10 illustrates the glycerol dehydrogenation pathways to GAL and DHA. The reference is the energy of adsorbed glycerol. GAL results from the successive C–H and O–H bond scissions at the terminal position of glycerol. Depending on the order of those two dissociations, two pathways are possible: 1) the alkoxy path starts with the terminal O–H bond scission to lead to Int_{OHt} and continues with the terminal C–H bond scission or 2) the alkyl path starts with the terminal C–H bond scission to lead to Int_{CHt} and continues with the terminal OH bond scission. Similarly, two routes yield DHA through glycerol dehydrogenation at the central position: 1) the alkoxy path through Int_{OHc} and 2) the alkyl path through Int_{CHc}. The two intermediates dehydrogenated at the central position are more stable on the surface than the corresponding terminal ones by around 0.2 eV. Int_{OHc} is even the most stable one (−0.32 eV). In addition, the O–H bond scission at the central position has the lowest activation barrier (E_{act} = 0.67 eV) among the four possible initial dissociations, thereby making Int_{OHc} the most probable intermediate. However, from

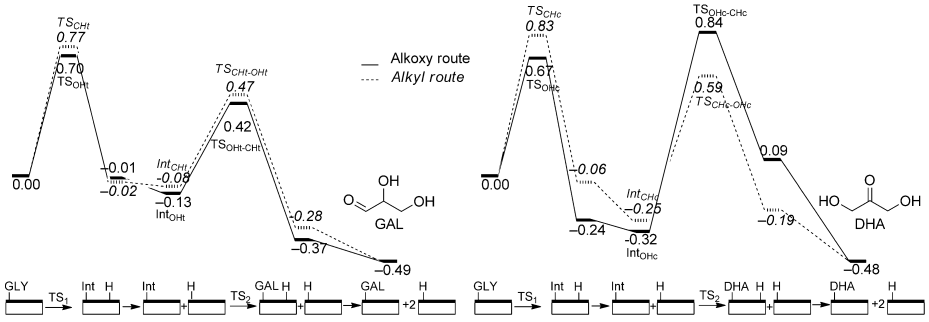

Figure 10. Energy profiles [eV] for the dehydrogenation reaction paths of glycerol toward glyceraldehyde (GAL) and dihydroxyacetone (DHA) formation. The reference energy taken here is the glycerol adsorbed at the Rh(111) surface (Figure 4). GAL and DHA structures on the surface can be seen in Figure 6. The straight line is the alkoxy route along which the mono-dehydrogenated intermediates are Int_{OHt} and Int_{OHc} (Figure 7). The dashed line is the alkyl route along which the mono-dehydrogenated intermediates are Int_{CHt} and Int_{CHc} (Figure 7). Structures of transition states of first and second steps are displayed Figure 8 and Figure 9, respectively.

Int_{OHc}, the following C–H bond dissociation is unfavourable, the central C–H bond being oriented towards the vacuum (Figure 7). To take advantage of the metal catalyst activation, an Rh–Ot bond (2.28 Å) has to be broken and the central oxygen has to switch from a stabilising hollow site to a top site (see Int_{OHc} in Figure 7 and $TS_{OHc-CHc}$ in Figure 9). The associated energy barrier is the highest computed for C–H and O–H bond dissociations in glycerol ($E_{act}=1.16$ eV, Figure 10). Consequently, the alkoxy route that leads to DHA is kinetically slow. Given the lower stability of the terminal intermediates, the OH bond rupture at the terminal position is surprisingly the second-lowest activation barrier ($E_{act}=0.70$ eV). Then it is easily followed by the CHt bond scission with a low energy barrier ($E_{act}=0.55$ eV, Figure 10). Thus, the alkoxy route that leads to GAL is the most favourable route kinetically. Moreover, the alkyl route that leads to GAL is also competitive: the CHt barrier is only 0.07 eV higher than the OHt barrier and the second dissociation transition state CHt–OHt is only 0.05 eV lower in energy than OHt–CHt. Besides, the alkyl route that leads to DHA requires the crossing of higher barriers and is less probable. To conclude, GAL is the major dehydrogenation product and it is mainly obtained through the alkoxy route.

Glycerol dehydration path: The dehydration of an alcohol catalysed by a metallic surface is a two-step process: C–H bond scission followed or preceded by the adjacent C–O bond scission. Wang et al. have shown that the C–H dissociation comes first when dehydrating ethanol at a Rh(111) surface.[50] According to their work, the initial C–O bond rupture is reported to be difficult ($E_{act}=1.76$ eV), whereas the initial C–H bond rupture is accessible ($E_{act}=0.52$ eV). Conversely, the C–O bond rupture as a second step from the mono-dehydrogenated CH_3CHOH species is easy ($E_{act}=$ 0.42 eV). Thus, we have considered the dehydration of glycerol by adopting the following route: C–H scission followed by C–O scission.

Intermediates and transition-state structures: This process shares the first step with the alkyl routes of the dehydrogenation process (see above). The TS structures of the CO rupture are provided in Figure 11. The dissociating hydroxyl group is adsorbed onto a top site of the surface, and is already distant from the forming enol, as the CO bond length is 2.11 Å in both TS structures.

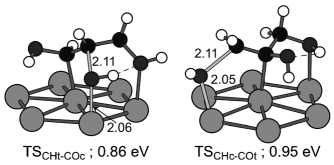

Figure 11. Structure of the transition states for the second step of glycerol dehydration (C–O bond cleavage) on Rh(111). Black, white, dark grey and light grey spheres correspond to C, H, O and Rh atoms. Dashed dark grey lines represent hydrogen bonds. Bonds implied in the TS are represented in light grey. Bond lengths are expressed in Å. Colour version of the figure is available in the Supporting Information (Figure S8).

Reaction paths: As already said, the glycerol dehydration can lead to two different enols: 1) Enol 1 (central C–H bond followed by terminal CO scission) or 2) Enol 2 (terminal C–H bond followed by central CO scission). Figure 12 shows the corresponding reaction pathways. The TS of the CO scission are rather high in energy: 0.95 eV at the terminal position, 0.86 eV at the central position with respect to adsorbed glycerol. Consequently, the main dehydration route is CHt–COc for which both barriers are lower, thus leading to Enol 2.

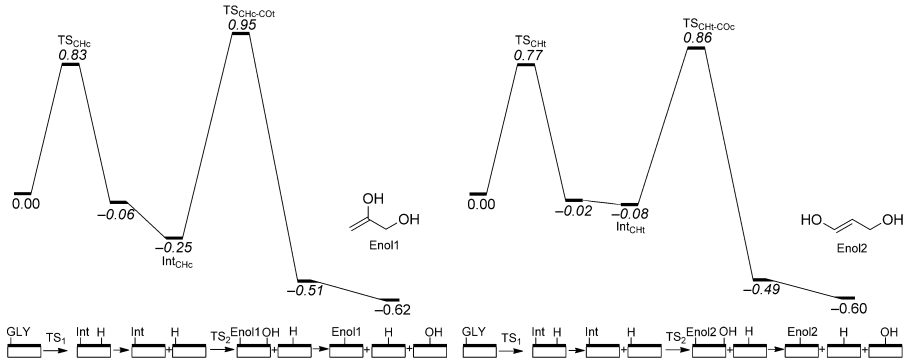

Figure 12. Energy profiles [eV] for the dehydration reaction path of glycerol toward Enol 1 and Enol 2 formation. Enol 1 and Enol 2 structures can be seen in Figure 6. The reference energy taken here is the glycerol adsorbed at the Rh(111) surface (Figure 4). The mono-dehydrogenated intermediates are Int_{CHt} and Int_{CHc}, which are displayed in Figure 7. Structures of transition states of first and second steps are shown in Figure 8 and Figure 11, respectively.

CHEMISTRY
A EUROPEAN JOURNAL

Discussion

The glycerol transformation into propanediols (PDOs) is generally performed in basic or acidic media in the presence of a metal catalyst under hydrogenolysis conditions: 12-PDO is usually the main product. This transformation is formally a dehydration coupled to a hydrogenation reaction. Consequently, dehydration is commonly envisaged as the first step of the reaction. The corresponding mechanism is represented in Scheme 2 in black. The glycerol dehydration yields an enol (Enol 1, propen-1,2-diol) in equilibrium with acetol. Then this ketone is hydrogenated at the metal catalyst into 12-PDO.

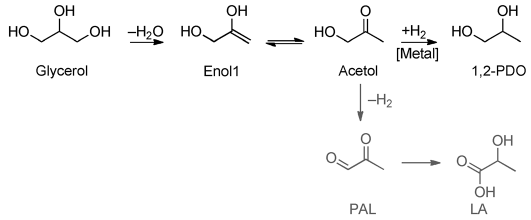

Scheme 2. Dehydration mechanism usually proposed for the glycerol conversion into 1,2-propanediol (12-PDO). In grey, an extension can be easily proposed from acetol to lead to the lactic acid (LA).

As seen in the Results Section, glycerol yields the expected 12-PDO in the presence of an Rh/C catalyst at basic pH under hydrogenolysis conditions ($P(H_2) = 50$ bar) but it also yields an oxidation product, the lactic acid (LA) with a slightly lower yield (Table 2, entry 2). This product could be obtained by the dehydrogenation of acetol into pyruvaldehyde (PAL), followed by a Cannizzaro reaction into LA (Scheme 2, additional path in grey). Moreover, when changing the atmosphere from reductive to inert, both products are still obtained but with a reversed selectivity (Table 2, entry 1). Thus, even in absence of H_2, 12-PDO can be produced. This questions the mechanism of glycerol hydrogenolysis previously described.

In the literature, an alternative mechanism has been proposed by Montassier et al.,[17] starting with a dehydrogenation step, unfamiliar under hydrogenolysis conditions. This alternative route is represented in Scheme 3 in the particular case of Rh/C catalyst in basic media. The glyceraldehyde (GAL) formed by the dehydrogenation of glycerol is dehydrated into PAL. Finally, this intermediate is successively hydrogenated into acetol and 12-PDO. LA can be easily obtained by a Cannizzaro reaction from PAL. Dihydroxyacetone is often reported as another dehydrogenation product of glycerol, but dehydration is difficult in this case because of the absence of adjacent carbons that bear H and OH groups.

Gathering experimental and theoretical results, we will first discuss the nature of the first step, dehydrogenation versus dehydration. Then we will focus on the product selectivity (LA and 12-PDO) depending on the nature of the atmosphere.

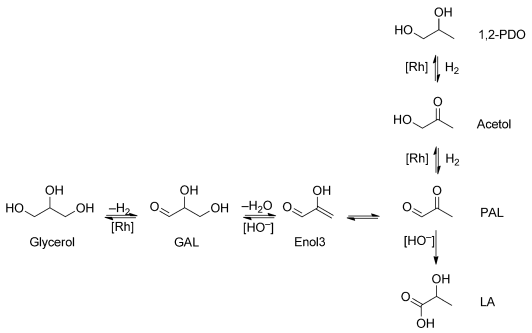

Scheme 3. Proposed mechanism of glycerol conversion into lactic acid (LA) and 1,2-propanediol (12-PDO) starting with a dehydrogenation step.

Dehydration versus dehydrogenation: The glycerol conversion and the pH increase together, and this is often associated with a dehydration mechanism. However, one should note that the basic media is essential in both mechanisms we examine here at different steps: the Cannizzaro reaction that leads to LA from PAL in both routes, the initial glycerol dehydration step in the dehydration mechanism and the dehydration of GAL into Enol 3 in the dehydrogenation mechanism.

To test the feasibility of the glycerol dehydration, glycerol was introduced in sodium hydroxide under He without catalyst. No conversion is observed after 24 h. This means that if the dehydration occurs, the metal catalyst and sodium hydroxide are both required and that there would be an assistance of the metal.[38]

The key intermediates, GAL, PAL and acetol, are not stable in a molar solution of sodium hydroxide at room temperature. Their detection requires performing the experiments in neutral or acidic solution. When reacting glycerol in water (pH 6.5) in the presence of the Rh/C catalyst, a very low glycerol conversion is reached and traces of 12-PDO are observed, whatever the atmosphere. Under H_2 atmosphere, traces of GAL (together with glyceric acid) are seen, whereas acetol is not detected. Under helium atmosphere, traces of GAL (together with glyceric acid), PAL and acetol are detected. GAL is a key intermediate in the dehydrogenation route only, whereas PAL and acetol are expected to be key intermediates in both routes. Following those experiments, dehydrogenation seems to be the first step of glycerol deoxygenation into 12-PDO and LA. But one should wonder whether these findings could be extrapolated to the reaction in alkaline conditions.

In the operating conditions, we observed an initial increase of pressure (Figure 3) whatever the atmosphere. However, under hydrogen atmosphere, a decreasing pres-

sure follows. Analysis of the gas phase indicates that the only gas produced in significant amount is H_2. It is consequently reasonable to attribute the pressure variations to H_2 production and consumption. Since APR is excluded under our conditions, there is necessarily a dehydrogenation step that occurs. Now there is a potential H_2 source in both mechanisms. H_2 is obviously produced from glycerol if dehydrogenation is the first step. If the dehydration is the first step, acetol can be another possible source of H_2 by dehydrogenation into PAL (Scheme 2), which is thermodynamically favoured (Figure 5). However, under hydrogen atmosphere, the pressure increases and then decreases and the main product is 12-PDO. According to the dehydrogenation mechanism (Scheme 3), the first step produces one equivalent of GAL and of H_2. Later, the formation of 12-PDO involves the consumption of two equivalents of H_2, which leads to the further decrease in the pressure. Along the alternative dehydration route (Scheme 2), H_2 production and consumption steps are not sequential as in the previous discussion, but are parallel and initiate from acetol. Consequently, the initial increase of hydrogen pressure would be observed only if LA is the main product. Now, under hydrogen, the hydrogenation product, 12-PDO, is the dominant one at all stages of the reaction. Thus, the dehydration mechanism appears incompatible with the transient formation of H_2.

The influence of the atmosphere on the conversion rate has also to be pointed out. The glycerol hydrodeoxygenation is actually found to be significantly faster under helium than under hydrogen-gas pressure: the catalyst is initially almost four times more active (Figure 1). According to the dehydrogenation mechanism, this can be explained by the reversibility of the initial dehydrogenation step. Under H_2 atmosphere, the high H_2 pressure inhibits the glycerol dehydrogenation. On the contrary, under He atmosphere, the equilibrium is inverted, thereby favouring a faster glycerol conversion. If we consider now the alternative mechanism that is initiated by a dehydration step, the production of the key intermediate acetol should not depend on the H_2 pressure. Hence the rate of transformation of glycerol should not decrease under H_2 compared to He, but only the selectivity should be modified, with more 12-PDO and less LA produced under H_2. Hence, the dehydration mechanism seems to be again incompatible with the experimental results.

Let us now look at the conclusions from the DFT calculations. The glycerol dehydration on model Rh(111) surface leads to two enols, Enol 1 and Enol 2, to yield 12-PDO and 13-PDO, respectively, after isomerisation and hydrogenation steps (Figure 5). Those two enol intermediates are isoenergetic on the metal catalyst and more stabilised than the dehydrogenation intermediates, GAL and DHA. Thermodynamically, dehydration is hence favoured over dehydrogenation on the surface. If we now look at the reaction barriers, the formation of Enol 1 goes through transition states of higher energies (0.83, 0.95 eV, Figure 12) than the reaction path to Enol 2 (0.77, 0.86 eV, Figure 12). Thus, Enol 2 is the kinetically favoured intermediate on the dehydration route. It would lead by hydrogenation to 13-PDO, in contradiction with the experimental selectivity. Alternatively, the dehydrogenation path can be considered. Two routes are possible, the alkyl route and the alkoxy route, depending on the first bond rupture, C–H or O–H. Obviously, the first dehydrogenation step of the alkyl routes (C–H rupture) is common with the dehydration. However, the C–H bond ruptures have higher barriers (0.83, 0.77 eV) than the alternative O–H bond ruptures (0.67, 0.70 eV). In addition, when starting with the terminal hydroxyl scission (OHt–CHt route), the first dissociation is the rate-limiting step (Figure 10). Consequently, the dehydrogenation (overall barrier of 0.70 eV) is favoured kinetically compared with dehydration (overall barrier of 0.86 eV) and leads to GAL by means of an OHt–CHt route.

To sum up, the combination of experiment and theory shows that dehydrogenation into GAL is the first step for the glycerol transformation on the Rh/C catalyst in basic media under He or H_2 atmosphere.

LA and 12-PDO selectivity: The proposed mechanism is summarised in Scheme 3. Glycerol is dehydrogenated into GAL. Then, its subsequent dehydration into Enol 3 is thermodynamically favoured on the surface ($E_{reac} = -0.73$ eV), as shown from DFT calculations. The isomerisation of Enol 3 into PAL is straightforward, and then a double hydrogenation into 12-PDO or a Cannizzaro reaction to yield LA can occur. From our experimental results, PAL conversion into LA is irreversible, whereas PAL hydrogenation into 12-PDO is an equilibrium. Indeed, LA is stable under our experimental conditions (Table 5, entries 3 and 4), whereas 12-PDO is mainly converted into LA under He. Those final steps control the product selectivity depending on the atmosphere.

Under a hydrogen atmosphere, the main product is the 12-PDO since the equilibrium is displaced towards the hydrogenation direction (Table 5, entry 2). Moreover, the PAL hydrogenation into acetol and then 12-PDO is probably faster than the Cannizzaro reaction into LA under H_2 pressure, hence the 12-PDO being the main product.

Under helium atmosphere, the pressure increases continuously, thereby leading to a significant concentration of hydrogen in the gas phase at the end of the reaction. As already noted, hydrogen production is ensured by the glycerol dehydrogenation. However, the H_2 partial pressure is much lower than under H_2 atmosphere. Therefore, all the hydrogenation/dehydrogenation equilibria are displaced towards dehydrogenation. This contributes to the H_2 pressure increase but also to the diminution of the 12-PDO yield and to the increase of the LA yield (Table 5). Since the formation of LA is irreversible under the reaction conditions, this is the main product under He atmosphere.

In a nutshell, the product distribution is controlled by the hydrogenation/dehydrogenation equilibria, and hence by the nature of the atmosphere. Under H_2, the hydrogenation of the intermediates into 12-PDO is favoured, whereas under neutral atmosphere, the transformation of PAL into LA by

CHEMISTRY
A EUROPEAN JOURNAL

a Canizzaro reaction is the main path since 12-PDO is potentially dehydrogenated.

Conclusion

The association of the experimental and theoretical points of view has provided a deep insight into the rhodium-catalysed transformation of glycerol into 1,2-propanediol (12-PDO) and lactic acid (LA). We have particularly focused on the determination of the first step of the reaction, as there was a need to decide between the dehydration and the dehydrogenation mechanisms. Although the conversion and the pH increase together, which could be tentatively associated with a dehydration mechanism, some clues appeared experimentally in favour of the dehydrogenation route. We established that switching the nature of the gas phase from a reductive to an inert atmosphere increased the reaction rate. It must be underlined that under inert atmosphere, although the products distribution was sharply impacted in favour of LA formation, a significant amount of 12-PDO was obtained together with the production of hydrogen. The theoretical investigations on glycerol dehydrogenation and dehydration at a model Rh(111) surface with density functional theory allowed us to distinguish between the two reaction paths. Dehydrogenation was found to be kinetically favoured at the surface over dehydration. In addition, glyceraldehyde (GAL) was found to be the favoured intermediate over dihydroxyacetone (DHA). The dehydrogenation of glycerol into GAL has thus been evidenced as the major phenomenon that initiates the hydrodeoxygenation mechanism on rhodium catalyst. Furthermore, key experimental results such as the transient production of H_2 in the gas phase and the influence of the nature of the atmosphere (H_2 or He) on the reaction rate are fully explained by the proposed mechanism, whereas they cannot be explained from the alternative route initiated by a dehydration step. We have hence revisited Montassier's dehydrogenation mechanism by highlighting the surface phenomena and by showing from the mixed experimental and theoretical study that dehydrogenation and not dehydration is the first step of the reaction.

Experimental Section

Catalyst preparation and characterisation: The rhodium catalyst supported on carbon was prepared by cationic exchange (see the Supporting Information). The effective Rh weight loading determined by ICP analysis was 0.7 wt%. XRD analysis furnished little information, given the amorphous nature of the carbon support. The absence of intense Rh peaks led us to think that Rh particles are well dispersed (Figure S1 in the Supporting Information). TEM analysis confirmed this forecast; the pictures could be seen (Figure S2 in the Supporting Information): the Rh/C catalyst shows small, well-dispersed nanoparticles (2–3 nm).

Catalytic tests and analysis: Initial screening of catalysts was conducted using a Slurry Phase Reactor 16 (AMTEC) for 12 h with glycerol (6 mL, 5 wt%) in solvent (H_2O or NaOH 1 M), 30 mg catalyst, 1000 rpm. The reactors were purged three times with 20 bar helium, heated at 453 K (unless another temperature is specified) and pressurised at 30 bar if the reaction was performed under helium. If the reaction was run under hydrogen, the pressure was adjusted to 50 bar. For the kinetic study, the reaction was performed in a 200 mL stainless steel autoclave equipped with a graphite-stabilised Teflon container. Samples of the reaction medium were taken out regularly and analysed by HPLC using a CarboSep 107H column (0.5 mL min^{-1} of 0.005 N H_2SO_4, $T=40$ °C). 13-PDO, 12-PDO, ethylene glycol, 1-propanol, 2-propanol, ethanol, methanol, acetol, lactic acid, formic acid, acetic acid, glyceraldehyde and glyceric acid were analysed. Total organic carbon (TOC) was also measured using a Shimadzu TOC-5050A analyser. The difference between TOC measured and TOC concentration introduced into the reactor gave an estimation of gaseous products (CO, CO_2, H_2 and so on) formed during the reaction. Gas phase was collected in a gas bag at the end of the reaction and analysed using a GC-MS (Agilent Technologies, 5975C) instrument equipped with Alumina, Poraplot U and 5 Å molecular sieve columns and thermal-conductivity detectors. Backflush injectors were used for Poraplot U and 5 Å molecular sieve columns.

Computational details: Periodic density functional theory (DFT) calculations have been carried out using the Vienna Ab Initio Simulation Program (VASP).[65] The exchange-correlation energy and potential were calculated within the generalised gradient approximation (Perdew–Wang 91 functional).[66] A tight convergence of the plane-wave expansion was obtained with a cutoff of 400 eV. The electron–ion interactions were described by the projector augmented method (PAW) introduced by Blöch[67] and adapted by Kresse and Joubert.[68] The Rh(111) surface is modelled by a 3×3 surface supercell that contains a slab of four layers and a vacuum of five equivalent metal layers (11.10 Å). A Monkhorst–Pack mesh of $3\times3\times1$ k points was used for the 2D Brillouin zone integration.[69]

The adsorption of the molecules was realised on the upper side of the slab. The two bottom layers of the slab were kept frozen in the bulk positions, whereas the uppermost layers and the molecule were free to relax. The adsorption energy E_{ads} is calculated as the difference between the energy of the adsorption complex and that of the bare surface plus the molecule in the gas phase. A negative energy means a stabilising adsorption. The reaction energy E_{react} is defined as the difference between the energy of the product and the energy of the reactant. A negative energy means that the reaction is exothermic, whereas a positive energy means that the reaction is endothermic. Reactions paths have been studied by combining Nudge Elastic Band (NEB) procedures[70] together with our local reaction path generator OpenPath[71] and the dimer method.[72] Then transition-state structures have been optimised with a quasi-Newton algorithm and characterised by a single imaginary frequency. The activation energy E_{act} is specified as the difference between the energy of the TS and the energy of the reactant. Extended calculations with a 4×4 unit cell, a five-layer slab with a 3×3 unit cell, and taking into account the dipole correction have been performed, without affecting notably the activation barriers values and the TS structures (Table S1 in the Supporting Information), hence validating the model initially chosen.

Acknowledgements

We are indebted to the EU (Topcombi contract no. NMP2-CT2005–515792) for financial support. F.A. acknowledges the French Minister of Research and Education for a PhD grant. Pascale Mascunan and Noëlle Christin, Mimoun Aouine, Françoise Bosselet and Chantal Lorentz are acknowledged for their assistance (ICP analysis, TEM, XRD and gas-phase analysis, respectively). Paul Fleurat-Lessard is acknowledged for providing the OpenPath program. We are grateful to PSMN, to GENCI (CINES/IDRIS, project x2010075609) and to CINECA for computer facilities and helpful assistance.

[1] B. Sels, E. D'Hondt, P. Jacobs in *Catalysis for Renewables: From Feed Stock to Energy Production* (Eds.: G. Centi, R. A. van Santen), Wiley-VCH, Weinhem, **2007**, p. 223.
[2] M. Pagliaro, M. Rossi *The Future of Glycerol: New Uses of a Versatile Raw Material*, RSC Publishing, Cambridge, **2008**.
[3] C.-H. Zhou, J. N. Beltramini, Y.-X. Fan, G. Q. Lu, *Chem. Soc., Rev.* **2008**, *37*, 527–549.
[4] A. Behr, J. Eilting, K. Irawadi, J. Leschinski, F. Lindner, *Green Chem.* **2008**, *10*, 13–30.
[5] M. Pagliaro, R. Ciriminna, H. Kimura, M. Rossi, C. Della Pina, *Angew. Chem.* **2007**, *119*, 4516–4522; *Angew. Chem. Int. Ed.* **2007**, *46*, 4434–4440.
[6] B. Katryniok, S. Paul, V. Belliere-Baca, P. Rey, F. Dumeignil, *Green Chem.* **2010**, *12*, 1922–1925.
[7] J. Barrault, F. Jerome, *Eur. J. Lipid Sci. Technol.* **2008**, *110*, 825–830.
[8] M. A. Dasari, P.-P. Kiatsimkul, W. R. Sutterlin, G. J. Suppes, *Appl. Catal. A* **2005**, *281*, 225–231.
[9] Y. Nakagawa, Y. Shinmi, S. Koso, K. Tomishige, *J. Catal.* **2010**, *272*, 191–194.
[10] O. M. Daniel, A. DeLaRiva, E. L. Kunkes, A. K. Datye, J. A. Dumesic, R. J. Davis, *ChemCatChem* **2010**, *2*, 1107–1114.
[11] L.-Z. Qin, M.-J. Song, C.-L. Chen, *Greem Chem.* **2010**, *12*, 1466–1472.
[12] J. Chaminand, L. Djakovitch, P. Gallezot, P. Marion, C. Pinel, C. Rosier, *Green Chem.* **2004**, *6*, 359–361.
[13] Y. Shen, S. Zhang, H. Li, Y. Ren, H. Liu, *Chem. Eur. J.* **2010**, *16*, 7368–7371.
[14] W. C. Ketchie, M. Murayama, R. J. Davis, *J. Catal.* **2007**, *250*, 264–273.
[15] R. Garcia, M. Besson, P. Gallezot, *Appl. Catal. A* **1995**, *127*, 165–176.
[16] R. R. Davda, J. W. Shabaker, G. W. Huber, R. D. Cortright, J. A. Dumesic, *Appl. Catal. B* **2005**, *56*, 171–186.
[17] C. Montassier, D. Giraud, J. Barbier, J.-P. Boitiaux, *Bull. Soc. Chim. Fr.* **1989**, *2*, 148–155.
[18] C. Montassier, J. C. Ménézo, L. C. Hoang, C. Renaud, J. Barbier, *J. Mol. Catal.* **1991**, *70*, 99–110.
[19] J. Zhou, L. Guo, X. Guo, J. Mao, S. Zhang, *Green Chem.* **2010**, *12*, 1835–1843.
[20] T. Jiang, Y. Zhou, S. Liang, H. Liu, B. Han, *Green Chem.* **2009**, *11*, 1000–1006.
[21] D. Roy, B. Subramaniam, R. V. Chaudhari, *Catal. Today* **2010**, *156*, 31–37.
[22] Y. Kusunoki, T. Miyazawa, K. Kunimori, K. Tomishige, *Catal. Commun.* **2005**, *6*, 645–649.
[23] T. Miyazawa, Y. Kusunoki, K. Kunimori, K. Tomishige, *J. Catal.* **2006**, *240*, 213–221.
[24] T. Miyazawa, S. Koso, K. Kunimori, K. Tomishige, *Appl. Catal. A* **2007**, *318*, 244–251.
[25] T. Miyazawa, S. Koso, K. Kunimori, K. Tomishige, *Appl. Catal. A* **2007**, *329*, 30–35.
[26] E. P. Maris, R. J. Davis, *J. Catal.* **2007**, *249*, 328–337.
[27] E. P. Maris, W. C. Ketchie, M. Murayama, R. J. Davis, *J. Catal.* **2007**, *251*, 281–294.
[28] E. D'Hondt, S. Van de Vyver, B. F. Sels, P. A. Jacobs, *Chem. Commun.* **2008**, 6011–6012.
[29] I. Gandarias, P. L. Arias, J. Requies, M. B. Güemez, J. L. G. Fierro, *Appl. Catal. B* **2010**, *97*, 248–256.
[30] A. Wawrzetz, B. Peng, A. Hrabar, A. Jentys, A. A. Lemonidou, J. A. Lercher, *J. Catal.* **2010**, *269*, 411–420.
[31] S. Wang, Y. Zhang, H. Liu, *Chem. Asian J.* **2010**, *5*, 1100–1111.
[32] S. Bolado, R. E. Treviño, M. T. García-Cubero, G. González-Benito, *Catal. Commun.* **2010**, *12*, 122–126.
[33] Z. Huang, F. Cui, H. Kang, J. Chen, X. Zhang, C. Xia, *Chem. Mater.* **2008**, *20*, 5090–5099.
[34] S. Wang, H. Liu, *Catal. Lett.* **2007**, *117*, 62–67.
[35] K. Wang, M. C. Hawley, T. D. Furney, *Ind. Eng. Chem. Res.* **1995**, *34*, 3766–3770.
[36] I. Furikado, T. Miyazawa, S. Koso, A. Shimao, K. Kunimori, K. Tomishige, *Green Chem.* **2007**, *9*, 582–588.
[37] Y. Shinmi, S. Koso, T. Kubota, Y. Nakagawa, K. Tomishige, *Appl. Catal. B* **2010**, *94*, 318–326.
[38] D. Coll, F. Delbecq, Y. Aray, P. Sautet, *Phys. Chem. Chem. Phys.* **2011**, *13*, 1448–1456.
[39] G.-C. Wang, Y.-H. Zhou, Y. Morikawa, J. Nakamura, Z.-S. Cai, X.-Z. Zhao, *J. Phys. Chem. B* **2005**, *109*, 12431–12442.
[40] I. N. Remediakis, F. Abild-Pedersen, J. K. Nørskov, *J. Phys. Chem. B* **2004**, *108*, 14535–14540.
[41] Y.-H. Zhou, P.-H. Lv, G.-C. Wang, *J. Mol. Catal. A* **2006**, *258*, 203–215.
[42] C. J. Zhang, P. Hu, *J. Chem. Phys.* **2001**, *115*, 7182–7186.
[43] G. C. Wang, Y. H. Zhou, J. Nakamura, *J. Chem. Phys.* **2005**, *122*, 044707–1–044707–8.
[44] D. Cao, G. Q. Lu, A. Wieckowski, S. A. Wasileski, M. Neurock, *J. Phys. Chem. B* **2005**, *109*, 11622–11633.
[45] S. Sakong, C. Sendner, A. Gross, *J. Mol. Struct.* **2006**, *771*, 117–122.
[46] P. Ferrin, D. Simonetti, S. Kandoi, E. Kunkes, J. A. Dumesic, J. K. Nørskov, M. Mavrikakis, *J. Am. Chem. Soc.* **2009**, *131*, 5809–5815.
[47] Y. Choi, P. Liu, *J. Am. Chem. Soc.* **2009**, *131*, 13054–13061.
[48] H.-F. Wang, Z.-P. Liu, *J. Am. Chem. Soc.* **2008**, *130*, 10996–11004.
[49] H.-F. Wang, Z.-P. Liu, *J. Phys. Chem. C* **2007**, *111*, 12157–12160.
[50] J.-H. Wang, C. S. Lee, M. C. Lin, *J. Phys. Chem. C* **2009**, *113*, 6681–6688.
[51] M.-M. Yang, X.-H. Bao, W.-X. Li, *J. Phys. Chem. C* **2007**, *111*, 7403–7410.
[52] R. Alcalá, M. Mavrikakis, J. A. Dumesic, *J. Catal.* **2003**, *218*, 178–190.
[53] Y.-W. Chen, J.-J. Ho, *J. Phys. Chem. C* **2009**, *113*, 6132–6139.
[54] H.-L. Chen, S.-H. Liu, J.-J. Ho, *J. Phys. Chem. B* **2006**, *110*, 14816–14823.
[55] V. Pallassana, M. Neurock, *J. Catal.* **2002**, *209*, 289–305.
[56] E. Vesselli, A. Baraldi, G. Comelli, S. Lizzit, R. Rosei, *ChemPhysChem* **2004**, *5*, 1133–1140.
[57] B. N. Zope, D. D. Hibbitts, M. Neurock, R. J. Davis, *Science* **2010**, *330*, 74–78.
[58] M. Besson, L. Djakovitch, P. Gallezot, C. Pinel, A. Salameh, M. Vospernik in *Catalysis of Organic Reactions*, (Ed.: M. L. Prunier), Chemical Industries, Boca Raton, **2009**, p. 313.
[59] R. D. Cortright, R. R. Davda, J. A. Dumesic, *Nature* **2002**, *418*, 964–967.
[60] G. W. Huber, J. A. Dumesic, *Catal. Today* **2006**, *111*, 119–132.
[61] G. W. Huber, R. D. Cortright, J. A. Dumesic, *Angew. Chem.* **2004**, *116*, 1575–1577; *Angew. Chem. Int. Ed.* **2004**, *43*, 1549–1551.
[62] R. Soares, D. Simonetti, J. A. Dumesic, *Angew. Chem.* **2006**, *118*, 4086–4089; *Angew. Chem. Int. Ed.* **2006**, *45*, 3982–3985.
[63] R. Chelli, F. L. Gervasio, C. Gellini, P. Procacci, G. Cardini, V. Schettino, *J. Phys. Chem. A* **2000**, *104*, 11220–11222.
[64] C. S. Callam, S. J. Singer, T. L. Lowary, C. M. Hadad, *J. Am. Chem. Soc.* **2001**, *123*, 11743–11754.
[65] G. Kresse, J. Hafner, *Phys. Rev. B* **1993**, *47*, 558–561.
[66] J. P. Perdew, Y. Wang, *Phys. Rev. B* **1992**, *45*, 13244–13249.
[67] P. E. Blöchl, *Phys. Rev. B* **1994**, *50*, 17953–17979.
[68] G. Kresse, D. Joubert, *Phys. Rev. B* **1999**, *59*, 1758–1775.
[69] H. J. Monkhorst, J. D. Pack, *Phys. Rev. B* **1976**, *13*, 5188–5192.
[70] D. Sheppard, R. Terrell, G. Henkelman, *J. Chem. Phys.* **2008**, *128*, 134106–1–134106–10.
[71] P. Fleurat-Lessard, P. Dayal, *A chemist view on reaction path determination*, to be published. Freely available at: http://forge.cpb.ens-lyon.fr/redmine/projects/openpath/wiki/WikiEnglish.
[72] G. Henkelman, H. Jonsson, *J. Chem. Phys.* **1999**, *111*, 7010–7022.

Received: April 29, 2011
Revised: August 18, 2011
Published online: November 8, 2011

ACS Catalysis

Letter

pubs.acs.org/acscatalysis

Linear Energy Relations As Predictive Tools for Polyalcohol Catalytic Reactivity

Jérémie Zaffran, Carine Michel, Florian Auneau, Françoise Delbecq, and Philippe Sautet*

Université de Lyon, CNRS and Ecole Normale Supérieure of Lyon, 46 Allée d'Italie, 69364 Lyon Cedex 07, France

Supporting Information

ABSTRACT: Molecules extracted from biomass can be complex, and computing their reactivity on a catalyst is a real challenge for theoretical chemistry. We present herein a method to predict polyalcohol reactivity in heterogeneous catalysis. We start from a set of simple alcohol molecules, and we show that an accurate linear energy relationship can be constructed from DFT calculations for the O−H and C−H dehydrogenation reactions. We then show that this relation can then be used for a fast prediction of the reactivity of glycerol. Compared with pure DFT calculations, our method provides results of good accuracy with a systematic deviation of ∼0.1 eV. We were able to prove that this deviation is caused mainly by intramolecular effects occurring in glycerol and not in simpler molecules.

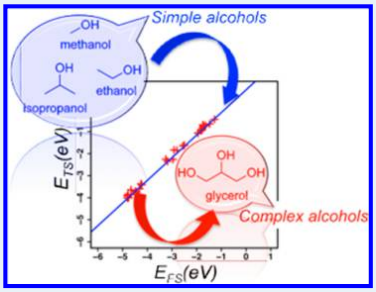

KEYWORDS: *Brønsted−Evans−Polanyi type relationships, glycerol, polyols, biomass, monoalcohols, dehydrogenation, DFT*

Molecules extracted from biomass set new challenges for heterogeneous catalysis and require the design of improved catalysts.[1,2] The cellulosic fraction of biomass is constituted of polyalcohols, which can be transformed to valuable products (chemicals or fuels) by various types of chemical reactions (dehydrogenation, hydrogenolysis, dehydration, ...).[3] These polyalcohols are associated with a large space of geometric configurations, and they can be involved in a complex network of serial or parallel reactions, which render the study of their reactivity with a solid catalyst complex and tedious. The calculation of their reactions at metal surfaces requires quantum chemical methods to properly describe bond-breaking and bond-forming steps, but these methods are too heavy for a fast exploration of complex reaction networks. It is hence of utmost importance to design methods that are of similar accuracy to quantum chemical approaches but can allow a fast screening of multiple elementary steps.

In this work, we show that transition state energies and reaction barriers for polyalcohols can be efficiently predicted from linear relationships of Brønsted−Evans−Polanyi (BEP) type, linking the desired kinetics quantities with more easily accessible adsorption energy or reaction energy data, which are established here using a set of monoalcohol molecules. Here, we use glycerol as a prototype polyalcohol, and we focus on dehydrogenation reactions on a Rh catalyst, hence involving the C−H and O−H bond-breaking processes. Indeed, it has been demonstrated that dehydrogenation is the first step for glycerol transformation on a Rh catalyst, under H_2 gas pressure or under He.[4] Even if one restrains the reactivity of glycerol to dehydrogenation processes, many pathways are possible by a combination of elementary acts dealing with CH/OH groups in central/terminal positions. In addition, glycerol can adopt a very large number of configurations in the gas phase[5] and on a surface.[6] It is unclear if the most stable configuration will be the most reactive one, and probing all configurations/pathways with first principle approaches such as DFT is, hence, a very tedious and computer-intensive task.

The idea of simple and fast evaluation of activation barriers from reaction thermodynamic data traces back to the pioneering work of Brønsted,[7] Bell,[8] Evans, and Polanyi,[9] as detailed in a recent review.[10] These correlations were initially used to compare molecular reactivity and, in a later stage, to model the kinetics of chemical reactions. They have been applied to heterogeneous catalysis reactions by several authors; however, two alternative methods were considered. Although some authors correlated activation energy with reaction energy,[11−14] in a traditional BEP style, others proposed to correlate the transition state energy with the energy of the initial or the final state of the reaction, a method later referred to as transition state scaling (TSS).[15−19] Only a few papers compare the merits of both correlation methods.[20,21] The situation remains confused on this point because for a single type of correlation, different definitions were used. In this paper, we will explore both TSS (with eight possible definitions) and BEP (with four definitions) correlations to clarify their comparison.

A general catalytic elementary step is shown in Scheme 1. The step starts from the initial state minimum, IS; progresses through the transition state, TS; and finishes at the final state

Received: November 11, 2013
Revised: December 17, 2013

Scheme 1. General Scheme of a Surface Catalytic Elementary Step[a]

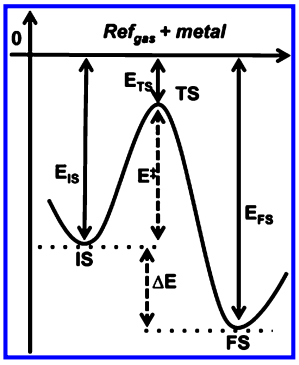

[a] E_{TS}, E_{IS}, and E_{FS} are energies of the transition state, the initial state, and the final state, respectively. $E^{\ddagger}$ and ΔE are activation and reaction energies, respectively.

minimum, FS. The principle of the BEP analysis is to explore the correlation behavior when plotting the activation (or the TS) energy versus the reaction (or FS) energy for a given sample of such reaction steps. The definition of IS and FS is not absolute because it depends on the direction chosen for the reaction. In our case, one can define the direction from the reaction itself, bond dissociation (diss), or association (assoc). Another possibility is to select the direction on an energy criterion, such as for each step choosing the endothermic (endo) or exothermic (exo) direction. This defines four types of BEP analysis, expressing the correlation between the activation energy, $E^{\ddagger} = E_{TS} - E_{IS}$, and the reaction energy, $\Delta E = E_{FS} - E_{IS}$. TSS relations correlate intrinsic TS and FS energies so that a reference energy is needed. We use as a reference a state in which all surface fragments are considered in gas phase, and the most stable spin state was chosen in the case of radicals. A TSS relation is, hence, defined by a direction (diss/assoc or exo/endo), a choice of thermodynamic state (either IS or FS), and a choice for the energy reference (again IS or FS). Our general notation is diss.IS/IS, where the last symbol defines the energy reference. Clearly, diss.IS/IS and assoc.FS/FS are identical definitions, such as exo.FS/FS and endo.IS/IS, so that only diss and exo directions will be kept. Eight types of TSS are then defined.

The existence and the quality of the correlation will be studied on a sample of simple alcohol molecules that are displayed in Scheme 2. Six molecules have been chosen with several substitution levels and a mixture of primary and secondary alcohols. For each of them, OH and CH bond dissociations have been considered, with a further distinction between CH bonds in the α or β position with respect to the OH. First and second dehydrogenation reactions have been considered so that a set of dehydrogenated products is formed of various chemical natures (radicals, carbonyls, enols). In total, the sampling set contains 29 bond activations (12 CHα, 7 CHβ, and 10 OH, see the Supporting Information (SI)).

Scheme 2. Sample of Molecules Used to Establish the BEP Type Relationships[a]

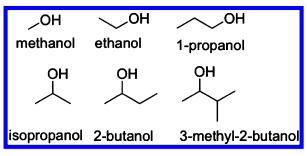

[a] Here are depicted the six monoalcohol molecules generating the 29 elementary CH and OH dissociation steps included for the construction of the linear relations.

If we first select the diss.FS/FS, exo.FS/IS, and BEP.diss forms of correlation, which have been previously used in the literature,[11−21] the 29 points E_{TS}/E_{FS} or $E^{\ddagger}/\Delta E$ are displayed in Figure 1. A clear and high-quality linear relation is seen. The statistical analysis of the deviations between DFT values and linear relation values are shown for each correlation as box plots on the inserts of Figure 1. We also report the mean absolute error (MAE) and the maximum error (MAX). Error is defined as "DFT value − linear relation value". The three chosen correlation definitions give very similar error distributions for the three subsets CHα/CHβ/OH, in a range from ∼−0.1 to +0.1 eV. This attests to the good quality of these relationships, which is confirmed by a MAE on the order of 0.05 eV (see Table 1) in each case. Note that the range of data is smaller for the BEP definition, giving a less visually appealing correlation (and a larger confidence interval for the slope of the linear relation; see the SI) for a similar distribution of errors. Let us highlight in addition that splitting the sample into three subsets considerably lowers the errors of the linear model, as shown by the MAE/MAX analysis, which is almost divided by 2. Furthermore, predicting CHα/CHβ/OH by a model established with all the points together leads to nonnegligible systematic errors (see SI Figure S2), significantly degrading the prediction.

From this analysis of the sampling set, the three selected types of correlations are of equivalent and high quality, and the error values after a separation in the three types of bonds is small (MAE ∼ 0.05 eV), which is very encouraging for a use of these correlations in predicting reactivity. A similar result was obtained for all 12 types of correlations considered, as seen in Figure 2. When taking all bonds together, only small variations are seen in the MAE between the methods, and hence, all 12 should be evaluated as being of the same general quality (error ∼ 0.08 eV). Separation of the set in each type of dissociated bond (CHα/CHβ/OH) again lowers the error, showing fluctuations around 0.05 eV for the various methods. None, however, is consistently better than the other ones, even if for the specific case of CHβ dissociation BEP are more accurate than TSS (for box plots, see SI Figure S3). The main point here is to clearly stress that TSS and BEP type relations have a similar (and high) merit,[19] at least for Rh catalysts and the chosen family of monoalcohol molecules.

Our results also show that the choice of the direction of the reaction (either on a chemical or energy base) or of the reference (for TSS modes) is not determinant for the result. This is, of course, reassuring for the robustness of the correlation concept and its usage for a wide range of systems and reactions. The BEP formulation has some practical advantages because the correlated quantities are more directly linked with reaction thermodynamics and kinetics so that trends can more clearly be caught and so that the slope (also called the transfer coefficient) has a simple interpretation in terms of early or late character of the transition state.

dx.doi.org/10.1021/cs4010503 | ACS Catal. 2014, 4, 464−468

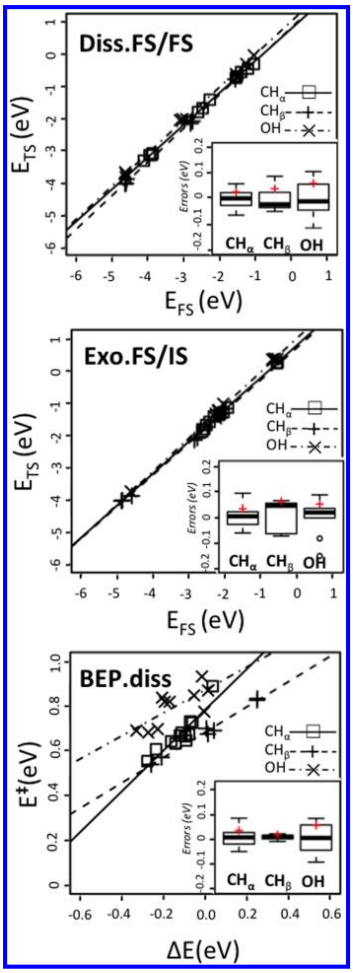

Figure 1. Linear relations constructed from first and second dehydrogenation steps of the six monoalcohol molecules of Scheme 1 on Rh(111). Three definitions of the correlation are considered: □, ×, and + are the DFT calculated values for CHα, CHβ, and OH respectively; and full, dashed, and mixed lines are the corresponding linear relations. At the bottom right corner of each graph, the box plots depict the corresponding error distribution. Red crosses signal mean absolute errors (MAE).

Now that we have established these correlations on the monoalcohol sample set, we turn to the central question: Can we use them to predict the reactivity of glycerol, chosen as a prototype polyalcohol? We have considered all first and second C−H and OH bond dissociations of glycerol on Rh(111). Note that in the case of glycerol, all CH bonds are in α of an OH group. For simplicity, we focus here on only the three correlation modes already selected for Figure 3 (diss.FS/FS, exo.FS/IS, and BEP.diss), but a complete analysis is provided in the SI (see Figure S4). We calculated the most stable initial and final states for first and second hydrogenation processes on

Table 1. Error Analysis for Monoalcohol BEP Type Relationships[a]

	TSS-diss.FS/FS		TSS-exo.FS/IS		BEP.diss	
	MAE	MAX	MAE	MAX	MAE	MAX
all	0.09	0.23	0.08	0.17	0.07	0.18
CH_α	0.03	0.06	0.03	0.09	0.03	0.07
CH_β	0.04	0.09	0.06	0.07	0.01	0.02
OH	0.06	0.11	0.05	0.15	0.05	0.10

[a]Here is presented the error analysis (mean absolute error, MAE; maximal absolute error, MAX) for the 29 CH and OH dissociation elementary steps of the considered monoalcohols family on Rh(111). The correlation can be established from the global sample (all), or subfamilies can be considered for each type of chemical bond activated (CHα, CHβ, OH).

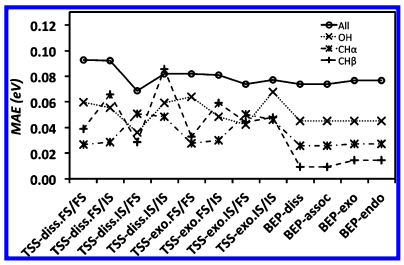

Figure 2. Comparison of the 12 considered definitions for the correlations (grouped into 8 TSS and 4 BEP types). MAE is given for the linear relation considering the 3 subsets (CHα/CHβ/OH) separately and the whole set ("All") of monoalcohol dehydrogenation reactions.

glycerol on Rh(111) and determined the TS linking them. Note that for some reaction steps, we included several TS and their corresponding reactants and products (associated with different conformations of glycerol) to improve the reliability of our statistical analysis (see glycerol structures in the SI and Figure S5).

The 31 (18 C−H and 13 O−H dissociations) points for glycerol are shown in Figure 3, together with their associated linear relation in black and with the correlation lines previously established for the monoalcohol family (in red). This graph clearly shows that the correlation established with the monoalcohol family is already a good model to predict the transition state energy or the activation energy for glycerol. The analysis of the deviation between the points for glycerol and the (red) line from the monoalcohol family quantifies this result (see box plots in Figure 3 and Table 2).

Notice that in this case, we also present the mean signed error (MSE), which is nonzero here because the linear relation is not associated with the sample considered for glycerol. One can clearly notice a systematic deviation, the prediction line underestimating the activation energy (on average, by 0.1 eV) for the CH bonds and overestimating it (by 0.1 eV) for the OH bonds. We will see the consequence of this systematic error on the predictive potential of the method later. The MAE is very close to this MSE and, hence, remains small (~0.1 eV for all three definitions). The error is, hence, reasonably increased with respect to the sampling set, and this gives predictive power to the approach. Points corresponding to metastable configurations of glycerol follow the linear relation within given statistical errors, although the most stable thermodynamic state

dx.doi.org/10.1021/cs4010503 | ACS Catal. 2014, 4, 464−468

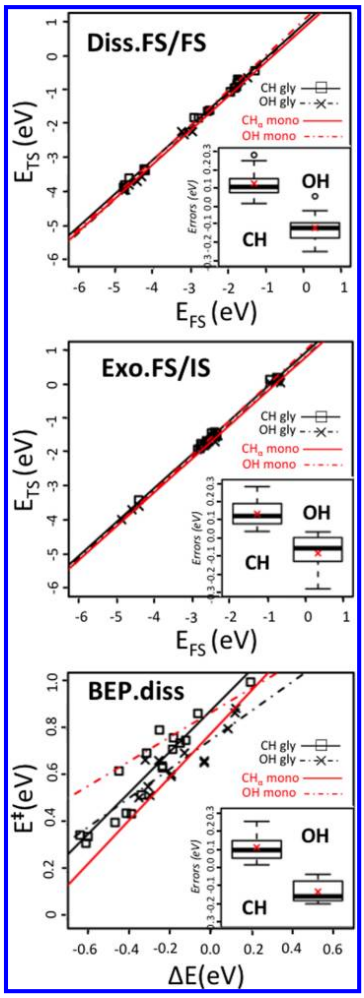

Figure 3. Linear relations constructed from first and second dehydrogenation steps of glycerol on Rh(111). Three definitions of the correlation are considered: □ and × are the DFT calculated values for CH and OH bonds, respectively, and full and mixed lines are the corresponding linear relations. In red are recalled the linear relations obtained in the case of the monoalcohol set for the CHα (full line) and the OH (mixed line) bonds. At the bottom right corner of each graph, the box plots depict the corresponding error distributions between the data points and the (red) monoalcohol linear relations. Red crosses signal mean signed errors.

is not always strictly associated with the most stable TS (see Figure S5 in the SI). Again, the two TSS and the BEP approaches have a very similar performance in terms of error. This can be generalized to all 12 correlation types considered in this paper, as shown in Figure S4 in the SI. All definitions give a similar error distribution, with an especially narrow range for the BEP case for OH dissociation and a larger error for the TSS involving the initial state as variable for the CH activation.

The capability to reasonably predict the catalytic reactivity of glycerol from that of simple alcohols is not a straightforward result, and it opens several perspectives. Generally speaking, to our knowledge, the use of BEP-type relations on simple molecules to predict multifunctional ones has not been demonstrated. It has been proposed, however, to predict the influence of substituents in the case of the hydrogenation of unsaturated aldehydes.[22] There are many reasons why glycerol reactivity might be different from that of simple alcohols. The presence of terminal and central OH/CH is equivalent to primary and secondary alcohols, both of which are in the sampling set. One key difference, however, is the presence in glycerol of intramolecular hydrogen bonds that assist the OH dissociation for the H bond acceptor OH.[23] The DFT-calculated TS energy will, hence, be lower for glycerol than for the monoalcohol sample, hence explaining the ∼-0.1 eV systematic error. This effect appears clearly if one considers some water-assisted reactions in the case of dehydrogenation of monoalcohols.

As a simpler H-bonded system, we considered ethanol, interacting with a chemisorbed water molecule through a H-bond, ethanol being the H-bond acceptor.[22] In this configuration, the OH bond scission in ethanol is modified, and the corresponding points are shifted toward the glycerol line in the BEP plots (see Figure S6 in the SI). In contrast, the positive systematic error seen for the CH bond dissociation is not related to the H bond effect. It stems from the constraints that neighboring OH groups in glycerol exert on glycerol. By interacting with the metal surface, they make the adsorbed molecule more rigid; hence, hindering the formation of the optimal C−H transition structure and increasing its energy with respect to the freer situation of monoalcohol sample. However, these effects are not very marked, and on average, the predictive potential remains good.

In the following, we will consider some examples of glycerol dehydrogenation elementary steps focusing on selectivity issues, that is, on the comparison of the barriers between different paths from a given intermediate. This is a severe test in situations for which DFT barriers are close and will highlight the cases in which a prediction is valid and those for which the accuracy might be insufficient. Scheme 3 presents two examples for glycerol or its hydrogenated intermediate on a Rh(111) surface and compares DFT calculated barriers (below arrow) with those predicted by three correlations built from the monoalcohol family (above arrows). The comparison between CH and OH dissociation (first line) is especially difficult because the systematic deviation in the prediction is different, with an overestimation for OH and an underestimation for CH, and because here, the DFT barrier difference is small. The method is, hence, not able to correctly grasp the preferred reaction.

The second elementary reaction starts from dehydrogenated glycerol at the terminal carbon and compares two further OH dissociation steps. The systematic deviation is eliminated because similar reactions are compared and the random error remains, which is inherent to any statistical model. Errors range now between ∼-0.1 and ∼+0.1 eV, which is similar to the results obtained for simple alcohols. In addition, the difference between barriers obtained from the correlations (0.13−0.22 eV) being large enough to safely predict that the reaction on the right, forming glyceraldehyde, is favored.

We, hence, showed that linear energy relations established for a sample of monoalcohol molecules on Rh can efficiently be

dx.doi.org/10.1021/cs4010503 | ACS Catal. 2014, 4, 464−468

Table 2. Error Analysis for the Prediction of Glycerol Reactivity[a]

	TSS-diss.FS/FS			TSS-exo.FS/IS			BEP.diss		
	MSE	MAE	MAX	MSE	MAE	MAX	MSE	MAE	MAX
CH	+0.13	0.13	0.28	+0.13	0.13	0.29	+0.11	0.13	0.25
OH	−0.11	0.12	0.24	−0.09	0.10	0.28	−0.13	0.13	0.20

[a]Here is presented the error analysis for predicting glycerol reactivity on Rh(111) from the monoalcohol linear energy relationship using the three main definitions: MSE, mean signed error; MAE, mean absolute error; and MAX, maximal absolute error.

Scheme 3. Prediction of Activation Energies for Glycerol Dehydrogenation[a]

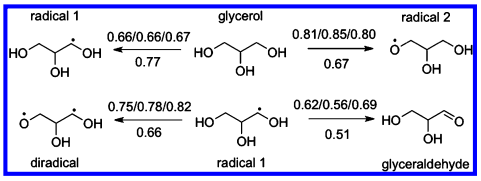

[a]The first line describes two possible paths for the first dissociation starting from glycerol, and the second line describes two probable routes for the second step starting from "radical 1". The value below each arrow is the activation energy predicted by DFT, and the three values above are the activation energies predicted from three definitions of the monoalcohol linear energy relationship (TSS-diss.FS/FS, TSS-exo.FS/IS, BEP.diss).

applied to the prediction of reaction barriers for polyalcohol molecules, such as glycerol with a statistical mean absolute error of ∼0.1 eV. Coupled with other approaches that simplify the evaluation of the adsorption energy of large molecules, as group additivity[24] or scaling relations,[25] this opens a fast and powerful exploration of the complex mechanisms and of the kinetics for the catalytic transformation of molecules extracted from biomass. Small deviations occur from the presence of intramolecular H bonds in the polyalcohol molecule, underestimating (respectively overestimating) the barrier for CH (respectively OH) and, hence, favoring CH dissociation versus OH in the predicted values. It would be certainly important to develop methods to estimate this systematic deviation between the set of CH or OH dissociation steps for glycerol versus monoalcohols because this would allow us to implement a correction on the data and to improve the prediction when comparing dehydrogenation at CH and OH on the polyalcohol. Although this analysis has been performed on a Rh(111) surface, the conclusions should not be specific to that system and extend to other faces or metal, as already proposed for other reaction steps.[18,20] Immediate perspectives aim at generalizing this behavior to other bond cleavages, such as C−C or C−O; other metals; and other types of molecular systems extracted from biomass, such as lignin.

■ ASSOCIATED CONTENT

Supporting Information

Computational methods and elements of statistics, additional tables and schemes, list of reactions and their corresponding structures used to get the relationships. This material is available free of charge via the Internet at http://pubs.acs.org.

■ AUTHOR INFORMATION

Corresponding Author

*E-mail: philippe.sautet@ens-lyon.fr.

Notes

The authors declare no competing financial interest.

■ ACKNOWLEDGMENTS

We thank PSMN at ENS Lyon, IDRIS-CNRS, and CINES for computational resources. We also acknowledge the support of ANR through the GALAC Project (ANR-10-CD2I-011).

■ REFERENCES

(1) Huber, G. W.; Chheda, J. N.; Barrett, C. J.; Dumesic, J. A. *Science* **2005**, *308*, 1446−1450.
(2) Chheda, J. N.; Huber, G. W.; Dumesic, J. A. *Angew. Chem., Int. Ed.* **2007**, *46*, 7164−7183.
(3) Ruppert, A.; Weinberg, K.; Palkovits, R. *Angew. Chem., Int. Ed.* **2012**, *51*, 2564−2601.
(4) Auneau, F.; Michel, C.; Delbecq, F.; Pinel, C.; Sautet, P. *Chem.—Eur. J.* **2011**, *17*, 14288−14299.
(5) Callam, C. S.; Singer, S. J.; Lowary, T. L.; Hadad, C. M. *J. Am. Chem. Soc.* **2001**, *123*, 11743−11754.
(6) Coll, D.; Delbecq, F.; Aray, Y.; Sautet, P. *Phys. Chem. Chem. Phys.* **2011**, *13*, 1448−1456.
(7) Brønsted, J. N. *Chem. Rev.* **1928**, *5*, 231−338.
(8) Bell, R. P. *Proc. R. Soc. London, Ser. A* **1936**, *154*, 414−429.
(9) Evans, M. G.; Polanyi, M. *Trans. Faraday Soc.* **1938**, *34*, 11−23.
(10) Van Santen, R. A.; Neurock, M.; Shetty, S. G. *Chem. Rev.* **2010**, *110*, 2005−2048.
(11) Pallassana, V.; Neurock, M. *J. Catal.* **2000**, *191*, 301−317.
(12) Liu, Z. P.; Hu, P. *J. Chem. Phys.* **2001**, *115*, 4977−4980.
(13) Michaelides, A.; Liu, Z. P.; Zhang, C. J.; Alavi, A.; King, D. A.; Hu, P. *J. Am. Chem. Soc.* **2003**, *125*, 3704−3705.
(14) Wang, H. F.; Liu, Z. P. *J. Am. Chem. Soc.* **2008**, *130*, 10996−11004.
(15) Logadottir, A.; Rod, T.; Nørskov, J. K.; Hammer, B.; Dahl, S.; Jacobsen, C. J. H. *J . Catal.* **2001**, *197*, 229−231.
(16) Alcala, R.; Mavrikakis, M.; Dumesic, J. A. *J. Catal.* **2003**, *218*, 178−190.
(17) Loffreda, D.; Delbecq, F.; Vigné, F.; Sautet, P. *Angew. Chem., Int. Ed.* **2009**, *48*, 8978−8980.
(18) Chen, Y.; Vlachos, D. G. *J. Phys. Chem. C* **2010**, *114*, 4973−4982.
(19) Liu, B.; Greeley, J. *J. Phys. Chem. C* **2011**, *115*, 19702−19709.
(20) Wang, S.; Petzold, V.; Tripkovic, V.; Kleis, J.; Howalt, J. G.; Slulason, E.; Fernandez, E. M.; Hvolbaek, B.; Jones, G.; Toftelund, A.; Falsig, H.; Björketun, M.; Studt, F.; Abild-Pedersen, F.; Rossmeisl, J.; Nørskov, J. K.; Bligaard, T. *Phys. Chem. Chem. Phys.* **2011**, *13*, 20760−20765.
(21) Sutton, J. E.; Vlachos, D. G. *ACS Catal.* **2012**, *2*, 1624−1634.
(22) Laref, S.; Delbecq, F.; Loffreda, D. *J. Catal.* **2009**, *265*, 35−42.
(23) Michel, C.; Auneau, F.; Delbecq, F.; Sautet, P. *ACS Catal.* **2011**, *1*, 1430−1440.
(24) Salciccioli, M.; Chen, Y.; Vlachos, D. G. *J. Phys. Chem. C* **2010**, *114*, 20155−20166.
(25) Abild-Pedersen, F.; Greeley, J.; Studt, F.; Rossmeisl, J.; Munter, T. R.; Moses, P. G.; Skulason, E.; Bligaard, T.; Nørskov, J. K. *Phys. Rev. Lett.* **2007**, *99*, 016105.

View Online / Journal Homepage
Dynamic Article Links

Catalysis
Science & Technology

Cite this: DOI: 10.1039/c2cy20363d

www.rsc.org/catalysis

PAPER

On the key role of hydroxyl groups in platinum-catalysed alcohol oxidation in aqueous medium†

Siwar Chibani,‡[a] Carine Michel,*[a] Françoise Delbecq,[a] Catherine Pinel[b] and Michèle Besson*[b]

Received (in CYZUR) 29th May 2012, Accepted 10th August 2012
DOI: 10.1039/c2cy20363d

In the aerobic selective oxidation of alcohols in aqueous medium in a batch reactor, it was observed that the addition of water to dioxane solvent (10–50 vol%) substantially increased the activity of a Pt/C catalyst. Periodic density functional theory (DFT) calculations were carried out to compare the reactivity of alcohols on the bare Pt(111) surface and in the presence of adsorbed water or hydroxyl groups, to explain the effect of water. The calculations indicate that the presence of adsorbed hydroxyl groups promotes the catalytic activity by participating directly in the catalytic pathways and reducing the activation barrier. Good agreement was found between the experiments in aqueous phase and these calculations. Further, decarbonylation of the aldehyde may be involved in the deactivation during oxidation of a primary alcohol.

1. Introduction

The selective oxidation of alcohols into the corresponding aldehydes, carboxylic acids and/or carbonyl compounds is one of the most important and useful reactions in the fine chemical, pharmaceutical and agrochemical sectors.[1–3] Classical oxidants (stoichiometric quantities of inorganic oxidants such as permanganates, chromates, hypochlorites, or HNO_3),[4] the Dess–Martin periodinane,[5] or the Swern reagent,[6] are often used for commercial applications. However, they may be toxic and release large amounts of waste. An attractive clean method known for a long time,[7] and which has received considerable attention over the years, is aerobic oxidation with a cheap oxidant such as molecular oxygen using metal catalysts. These catalysts can efficiently oxidize alcohols, using oxygen or air to generate only water as a by-product under mild conditions (40–100 °C), atmospheric or a low pressure, and pH 7–10. Several supported metallic systems (particularly palladium, platinum, ruthenium, and recently gold) on various supporting materials have been an area of intense interest and have emerged as efficient catalysts as described in reviews.[8–11]

From a practical point of view, the first studies have mostly concentrated on the use of water as the solvent for oxidation of carbohydrates over Pt or Pd catalysts.[12] However, the poor solubility in aqueous solution of weakly polar alcohols is a crucial issue for the generalization of this reaction. Though the use of detergents,[13] organic solvents,[14] $scCO_2$,[15,16] or amphiphilic resin-supported particles of Pd or Pt,[17,18] has been proposed to overcome the difficulty, the choice of the solvent remains crucial. Several studies have indicated a promoting effect of water on the activity in aerobic oxidation of alcohols on metallic catalysts. For instance, we have investigated the oxidation of primary and secondary alcohols which are poorly soluble in water, and dioxane was used as additional solvent. 1- and 2-Octanol were chosen, since, moreover, aliphatic alcohols have been reported as being particularly difficult to oxidize compared with aromatic and allylic alcohols.[19] Upon reacting the alcohol in dioxane solvent, only a slow oxidation took place. In comparison to the dioxane solvent, a significant enhancement in catalytic activity of a Pt/C catalyst was observed for both alcohols, by addition of increasing amounts of water to the solvent. The higher the water content, the higher the activity is. A promoting effect of water was also revealed in the oxidation of 1-phenylethanol and α-substituted pyridinemethanol derivatives over Pt/C and PtBi/C,[20] of benzyl alcohol over Pd confined in SBA-16,[21] Au/TiO_2 in xylene,[22] or carbon nanotube supported Ru catalysts in toluene.[23] The solvent composition also modified the activity of Au–Pd and Au–Pt catalysts in oxidation of *n*-octyl, cinnamyl or benzylic alcohols.[24,25]

Another major problem in alcohol oxidation is the possible catalyst deactivation. Upon comparing 1-octanol and 2-octanol, we noted different reaction profiles with reaction time.[19] A severe

[a] *Université de Lyon, CNRS, École Normale Supérieure de Lyon, 46 allée d'Italie, F-69364 Lyon Cedex 07, France. E-mail: carine.michel@ens-lyon.fr*
[b] *Université de Lyon, CNRS, IRCELYON, 2 avenue A. Einstein, F-69626 Villeurbanne, France. E-mail: michele.besson@ircelyon.univ-lyon1.fr; Fax: +33 (0)472445399*
† Electronic supplementary information (ESI) available. See DOI: 10.1039/c2cy20363d
‡ Present address: Laboratoire CEISAM - UMR CNRS 6230, Université de Nantes, 2 rue de la Houssiniére, BP 92208, 44322 Nantes Cedex 3, France.

deactivation was observed during 1-octanol oxidation and complete conversion was not achieved at 100 °C. In the 2-octanol oxidation, full conversion could be attained with total selectivity to 2-octanone. One reason might be decarbonylation of the produced aldehyde resulting in site-blocking by chemisorbed CO and carbonaceous fragments under anaerobic conditions. Spectroscopic studies have shown that the aldehydes formed from primary alcohols (1-octanol, cinnamyl alcohol) were decarbonylated, while the ketones (in particular 2-octanone) were stable.[26] Decarbonylation of crotonaldehyde was demonstrated by synchrotron XPS combined with temperature-programmed desorption during oxidation of crotyl alcohol.[27] Strongly adsorbed CO could be removed by air.[28,29]

The exact reaction sequence through which a dehydrogenation mechanism occurs during selective oxidation of alcohols over noble metal catalysts is still debated. There are still discussions concerning the oxidation state of the active metallic sites, the elementary steps, and the involvement of oxygen or water in the reaction mechanism, the reason for the catalyst deactivation.[8–11] The generally accepted mechanism for Pt group metals involves a dehydrogenation step of the adsorbed alcohol molecule on the metallic sites forming the carbonyl compound. The adsorbed hydrogen becomes oxidized by dissociatively adsorbed oxygen to liberate the metallic sites. This was supported by kinetic modelling,[30] by the observation that oxygen can be replaced by an H-acceptor,[31] or by the fact that the metal catalyst is in a reduced state both in the presence and absence of molecular oxygen by measurements of electrode potential,[32] or *in situ* X-ray absorption spectroscopy (XAS).[33] The direct interaction of surface oxygen species with the adsorbed alcohol (or its partially dehydrogenated intermediate) has also been proposed, supported by XAS studies that indicate partial oxygen coverage on the metal surface,[34] and some kinetic studies revealing a Langmuir–Hinshelwood-type mechanism.[35] The major role of oxygen has also been shown to be the removal of impurities from the aldehyde degradation on the surface sites.[28,29]

Clearly, the oxide species and chemisorbed oxygen species at the surface of the platinum (O_2, –OH, H_2O) should play an important role during the oxidation reactions. There are few data on how the presence of water at the catalyst–liquid solution interface can influence the kinetics of the catalytic reaction.[36–38] Investigating the reactions at the solid–liquid interface in the complex solvent environment becomes essential to improve the heterogeneous process and to understand the mechanism. Computational studies using the density functional theory (DFT) have been undertaken for many years to shed light on the mechanisms of alcohols oxidation *i.e.* dehydrogenation and decomposition on surfaces, in particular of methanol[39–45] and ethanol[46–49] on Pt(111). Recently, 1- and 2-propanol have been also considered.[50] Nowadays the experimental conditions begin to be taken into account in the calculations, particularly the solvent[51] and co-adsorbates on the surface.[52–55] To our knowledge, none of the previous works studied systematically the influence of the presence of hydroxyl groups or water on the energy of the intermediates on the Pt surface.

The aim of the present study is a further understanding of the promotion of the oxidation reaction by water and the possible poisoning of the active sites:

(i) To further assess the general use of aqueous phase promotion, the study was extended to some other alcohols in dioxane–water solvent, such as sterically hindered menthol and borneol.

(ii) To gain insight into the nature of the interactions of adsorbates with the platinum surface in the solvent environment, DFT calculations have been performed. We tried to elucidate the rate-determining step in different environments, including water molecules and co-adsorbates in the calculations to show whether they can enhance the activity of the catalyst by providing a low energy route for dehydrogenation.

We also examined the possible deactivation attributed to subsequent decarbonylation of the produced aldehyde in the case of primary alcohols.

2. Experimental details

Pt catalysts supported on a synthetic carbon catalyst (2.8–4.7 wt% Pt) were prepared by impregnation with an aqueous solution of H_2PtCl_6, followed by liquid phase reduction with formaldehyde in alkaline medium, as described previously.[19] The carbon was prepared by carbonization at 1073 K of a porous polymeric phenolic resin, washing and activation with CO_2 at 1123 K with 30% burn-off.[56]

The oxidation reactions were performed in a 300 mL autoclave reactor made of Hastelloy C with a magnetically driven stirrer. The reactor was loaded with the feed solution (150 mL, 35–100 mmol L^{-1}) and an appropriate amount of catalyst, then sealed, purged with Ar and heated to the desired temperature. Air was introduced up to the pressure of 10 bar and the reaction started upon applying efficient stirring. Liquid samples were periodically withdrawn from the reactor *via* a sample diptube, and analyzed *via* gas chromatography (GC) equipped with a flame ionization detector (FID) and a HP5 column (30 m × 0.25 mm, 0.25 μm film thickness).

3. Computational details

Periodic density Functional Theory (DFT) calculations have been carried out using the Vienna Ab Initio Simulation Program (VASP).[57] The exchange-correlation energy and potential were calculated within the generalized gradient approximation (Perdew-Wang 91 functional).[58] A tight convergence of the plane-wave expansion was obtained with a cut-off of 400 eV. The electron–ions interactions were described by the projector augmented method (PAW) introduced by Blöchl[59] and adapted by Kresse and Joubert.[60] The supported platinum catalyst has been modelled by a Pt(111) surface using a 3 × 3 supercell of a periodic slab of four layers and a vacuum of five equivalent metal layers. A Monkhorst–Pack mesh of 3 × 3 × 1 *k* points was used for the 2D Brillouin zone integration.[61] Molecules have been adsorbed at the upper side of the slab. The adsorbates and the two upper layers were free to relax while the two bottom layers have been kept frozen in the bulk position (Pt–Pt distance = 2.82 Å). Geometries were converged up to reach forces less than 0.01 eV $Å^{-1}$.

Reaction paths have been studied combining Nudged Elastic Band (NEB) procedures[62,63] together with our local reaction path generator OpenPath[64] and the dimer method.[65,66] Then, transition

state (TS) structures have been optimized with a quasi-Newton algorithm and characterized by a single imaginary frequency.

The reaction energy ΔE of the bond scissions is the difference between the adsorbed reactant and the two products considered at infinite distance. The activation energy $\Delta E^{\ddagger}$ is specified as the difference between the energy of the TS and the energy of the reactant. The adsorption energy, E_{ads}, is the difference between the energy of the whole system and the energies of the reactant in gas phase and of the considered surface (Pt, H_2O@Pt or OH@Pt). A negative value means stabilization.

The HREEL spectra have been simulated by calculation of the vibration frequencies, following a previous procedure.[67] The technique used is based on the numerical calculation of the second derivatives of the potential energy surface within the harmonic approach. The force constant matrix is built with finite differences of the first derivatives of the total energy by geometrical perturbations of the optimized Cartesian coordinates of the system. The diagonalization of this matrix provides the harmonic molecular frequencies and the associated harmonic normal vibration modes. The intensities of the HREELS spectra are estimated by applying the formula given in ref. 67 where the intensities are proportional to the square of the dynamic dipole moments (derivatives of the dipole moments with respect to a given normal mode), to a function depending on experimental parameters and to the inverse of the frequencies.

4. Results and discussion

4.1. Water effects

Experimental results. Previous experiments on oxidation of 1- and 2-octanol showed the positive influence of water; with increasing water contents in dioxane–water solvent, a large enhancement of the initial reaction rate was observed, as illustrated in Fig. 1.[19]

In the oxidation of 2-octanol, whereas the catalyst was poorly active in dioxane, addition of water to the solvent greatly enhanced the reaction rate to attain total conversion to 2-octanone within one hour in dioxane–water 50/50 vol%. The initial reaction rate in 1-octanol oxidation was also greatly enhanced even by addition of a low amount of water (dioxane–water 90/10 vol%). Further addition of water (dioxane–water 50/50 vol%) did not significantly improve the performances. However, in contrast to the observations with 2-octanol, none of the reactions could attain completion; after a high initial reaction rate, a severe inhibition was clearly observed and conversion was rapidly limited to *ca.* 70–75% after 1 h reaction. In dioxane the major product was 1-octanal, while in dioxane–water solvent octanoic acid concentration was the higher.

We further explored the oxidation of some secondary alcohols. Fig. 2 shows the reaction of menthol and borneol in dioxane and different dioxane–water mixtures to the corresponding ketone.

In the reactions with these secondary alcohols, the activity of the catalyst was also improved by increasing the water concentration. Conversion attained rapidly completion, and no inhibition of the reaction was observed. The selectivity to the ketone was >95%.

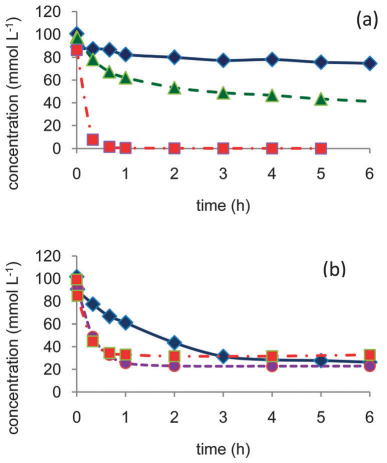

Fig. 1 Role of water in the aerobic oxidation of 1- and 2-octanol: (a) 2-octanol in dioxane (◆) or dioxane–water 80/20 vol% (▲) or dioxane–water 50/50 vol% (■), (b) 1-octanol in dioxane (◆), dioxane–water 90/10 vol% (●), or dioxane–water 50/50 vol% (■). Reaction conditions: 150 mL 0.1 mol L^{-1} alcohol, 373 K, 10 bar air, substrate/Pt molar ratio = 100.

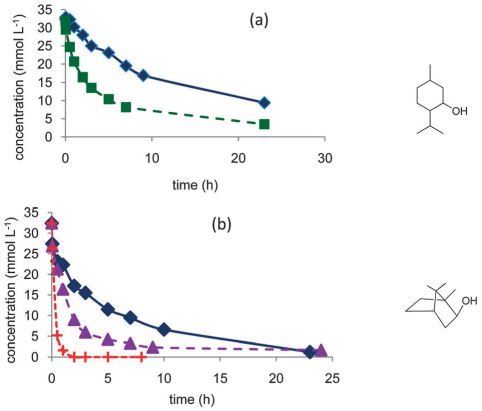

Fig. 2 Evidence of the role of water in the aerobic oxidation of secondary alcohols to the ketone: (a) menthol in dioxane (◆) or dioxane–water 80/20 vol% (■), (b) borneol in dioxane (◆), dioxane–water 70/30 vol% (▲), or dioxane–water 50/50 vol% (+). Reaction conditions: 150 mL 0.035 mol L^{-1} alcohol, 373 K, 10 bar air, substrate/Pt molar ratio = 100.

Theoretical results. The target of this theoretical part will be essentially a better understanding of the role of water in promoting the reaction according to the experimental results. As alcohol models, primary alcohols are represented by ethanol (EtOH) while secondary alcohols are represented by isopropanol (iPrOH). As a reference, the reactivity of alcohols at the bare platinum surface will be provided first. Then, the effect of the co-adsorption of an oxygen atom will be studied

to analyse the effect of the O_2 atmosphere. Similarly, the effect of the water in the liquid phase will be mimicked by the co-adsorption of a water molecule at the platinum surface. To end, as the reaction $O + H_2O \rightarrow 2OH$ is known to occur easily on Pt(111),[68–70] the influence of a co-adsorbed hydroxyl will be also analysed. Finally, in the case of primary alcohols the decarbonylation of the resulting aldehyde will be also considered.

The transformation of the primary alcohol into the aldehyde and of a secondary alcohol into the ketone corresponds to the scission of two bonds: an O–H bond and a C–H bond. Depending on which breaking occurs first, two routes are possible: (i) route O starting with the O–H bond dissociation and followed by the α-CH bond breaking of the alkoxy, (ii) route C starting with the C–H bond dissociation and then the O–H bond breaking. In the following paragraphs, the influence of the environment (bare surface, adsorbed H_2O and OH) on these two paths will be discussed for EtOH and then iPrOH. For the first step, the transition states (TSs) are labelled after the bond breaking (TS_{OH} and TS_{CH}), and so does the subsequent intermediate (Int_{OH} and Int_{CH}). For the second step, the TS label is built by concatenating the name of bonds dissociated in the first step and in the second step: for instance, $TS_{OH–CH}$ corresponds to the CH scission as a second step (route O).

Ethanol

Adsorption. The adsorption of the ethanol molecule at a Pt(111) surface follows the general mode of alcohols on this surface: EtOH interacts with the metallic surface through an oxygen lone pair and is consequently adsorbed at a top position. The adsorption energy is −0.34 eV (33 kJ mol^{-1}) with our calculation parameters, slightly higher than the one calculated previously, 27 kJ mol^{-1},[48] but smaller than the experimental value determined from TPD experiments, 50 kJ mol^{-1},[71] which indicates a weak adsorption.

Let us now consider a modified platinum surface. When one oxygen atom is already adsorbed at the surface, the adsorption energy of ethanol adsorbed at a vicinal site is reduced to −0.15 eV and its adsorption geometry is not modified. In other words, an ethanol molecule prefers to adsorb at the bare platinum surface or far from an oxygen atom of the oxygenated one. Thus, the influence of oxygen on alcohol reactivity at the Pt(111) surface will not be considered further.

When one water molecule is already chemisorbed at the Pt(111) surface, the adsorption energy is increased to −0.61 eV which means that the presence of chemisorbed water promotes the ethanol adsorption. In addition, the adsorption geometry is strongly modified. The ethanol molecule does not interact directly with the surface through an oxygen lone pair. However, it interacts with the pre-adsorbed water molecule through a H-bond (H···O = 1.61 Å), the water molecule being the H-bond donor and the ethanol being the H-bond acceptor (Fig. 3). This configuration has been found 0.32 eV more stable than the co-chemisorption of the two molecules, each one on a top position on a Pt atom. Thus, an ethanol molecule prefers to interact with the pre-adsorbed water molecule than to be chemisorbed on the Pt(111) surface. This strongly stabilizing

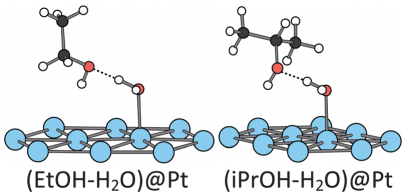

Fig. 3 Structures of the adsorbed alcohols in the presence of water. E_{ads} = −0.61 eV for both.

co-adsorption mode has already been described and analysed on Rh(111).[54]

The hydroxylated surface has an even more surprising reactivity towards ethanol adsorption. The hydroxyl is considered to be adsorbed at a top position (only 0.05 eV higher than the bridge position). On such a modified platinum surface, the ethanol is strongly adsorbed (−0.89 eV). It interacts with a neighbour platinum atom (Pt–O = 2.07 Å) and its hydroxyl hydrogen is transferred to the pre-adsorbed hydroxyl group along the adsorption path, leading to the H_2O–EtO structure represented in Fig. 4 (O–H = 1.39 and 1.09 Å between ethanol and OH, respectively). It is worth noting that EtOH is already partially oxidized by the pre-adsorbed hydroxyl. While our work was in progress, similar results have been published.[52] The same transfer has also been calculated in the case of phenylethanol on a gold catalyst.[53]

Reaction paths. The co-adsorbed species affects not only the adsorption process but also the reaction paths followed by the target molecule. As already mentioned, the oxidation of ethanol into acetaldehyde can follow two routes, route O and route C depending on which bond is broken first (OH or CH, respectively).

The stationary points along these two routes have been fully characterized in three cases: (i) bare Pt(111) surface, (ii) H_2O@Pt(111) surface and (iii) OH@Pt(111) surface. At the bare surface, the TS structure of route C exhibits a classical triangular shape for the first scission (TS_{CH}) while the first TS of route O involves four atoms (Fig. 5 and Table 1 for the main geometrical characteristics). The resulting intermediates Int_{CH} and Int_{OH} are bonded top to a platinum atom through the C and O atom, respectively. The next dissociation leads to the formation of a C=O bond. The $TS_{OH–CH}$ is a five-centres transition state: two platinum atoms plus the C, O and H atoms are directly involved in the TS (Fig. 5) and the resulting acetaldehyde is adsorbed at a top configuration (Pt–O = 2.0 Å, the C=O bond

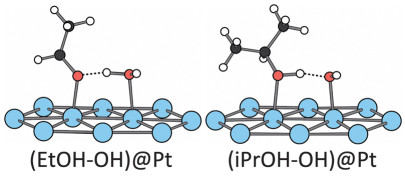

Fig. 4 Structures obtained after adsorption of ethanol and isopropanol in the presence of an adsorbed hydroxyl (E_{ads} = −0.89 eV in both cases).

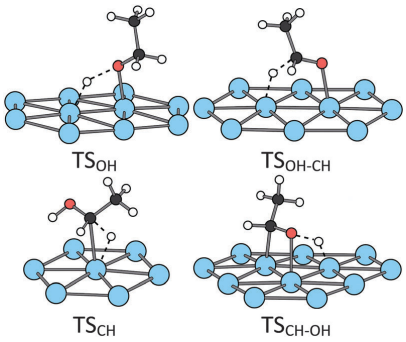

Fig. 5 Transition states structures of the ethanol oxidation at a bare Pt(111) surface.

Table 1 Energetic and main geometrical characteristics of the transition state structures for the ethanol oxidation at the bare platinum surface (Pt(111)), at the hydrated platinum surface (H_2O@Pt(111)) and at the hydroxylated surface (OH@Pt(111)). The CH step is the first step of route C. The CH–OH step is the second step of route C. The OH step is the first step of route O. The OH–CH step is the second step of route O. The reaction energy ΔE and the activation energy $\Delta E^{\ddagger}$ of each step are provided in eV. The transition state structures are characterized by the number of involved atoms (N). The main distances are given in Å: X–H is the breaking bond; Pt–Y corresponds to the Pt–C (resp. Pt–O) bond for the CH bond scissions (resp. OH bond scissions). In the case of reaction at the hydrated and hydroxylated surfaces, C or O is not adsorbed in the final product. H···O corresponds to the hydrogen bonds

	ΔE	$\Delta E^{\ddagger}$	N	X–H	Pt–Y	Pt–H	H···O
OH							
Pt(111)	0.67	0.88	4	1.70	2.06	1.63	
H_2O@Pt(111)	0.53	0.84	4	1.58	2.18	1.65	1.62
OH–CH							
Pt(111)	−0.48	0.08	5	1.45	2.95	1.70	
H_2O@Pt(111)	−0.21	0.43	5	1.55	3.10	1.67	1.76
OH@Pt(111)	−0.17	0.33	5	1.55	3.05	1.66	1.67
CH							
Pt(111)	−0.14	0.67	3	1.63	2.52	1.64	
H_2O@Pt(111)	−0.02	0.90	3	1.61	2.40	1.63	1.79
CH–OH							
Pt(111)	0.45	0.81	4	1.56	2.23	1.64	
H_2O@Pt(111)	0.34	0.68	6	1.62	3.13	1.62	1.51

being almost perpendicular to the surface). The adsorption energy is −0.32 eV, in agreement with previous calculations.[47] On the other route, the $TS_{CH–OH}$ is a four-centres transition state (Fig. 5). The resulting acetaldehyde is adsorbed in a less stable di-sigma mode (E_{ads} = 0.21 eV), the C═O bond being almost parallel to the surface.

When adsorbed at the hydrated surface, the ethanol molecule does not interact directly with the surface. However, the first dissociation is also promoted by the platinum surface, the corresponding TS being close to the ones obtained at the bare surface (Fig. 6 and Table 1). The second scission is more affected. The $TS_{OH–CH}$ keeps a five-centres structure, but the $TS_{CH–OH}$ is a six-centres one, involving the water molecule (Fig. 6 and Table 1). Both TS lead to an acetaldehyde molecule, non-adsorbed at the surface but H-bonded with the water molecule, the C═O bond being almost parallel to the surface, but farther than in the absence of water (Fig. 7).

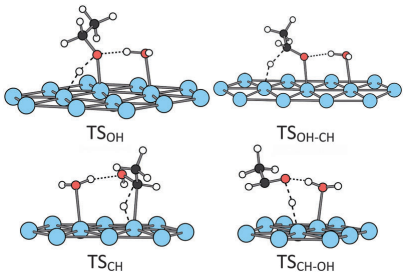

Fig. 6 Transition states structures of the ethanol oxidation at a H_2O@Pt(111) surface.

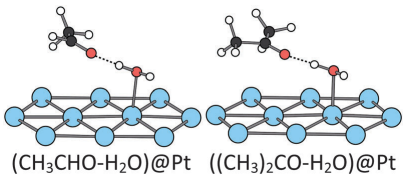

Fig. 7 Final state structures of ethanol and isopropanol oxidation at a H_2O@Pt(111) surface.

The hydroxylated platinum surface is the last case under consideration. It differs from the two previous cases, as the first OH scission is concomitant with the adsorption process (see above). The following CH dissociation is promoted by the platinum surface through a five-centres transition state. This TS is similar to $TS_{OH–CH}$ at the hydrated surface (Fig. 6).

The presence of co-adsorbed species modifies also strongly the energetics of the reaction paths. The two possible reaction paths for ethanol oxidation are represented in Fig. 8 for each case: (i) bare Pt(111), (ii) H_2O@Pt(111) and (iii) OH@Pt(111). At the bare platinum surface, the main reaction path is clearly route C compared with route O. On this route C, both steps are equally demanding energetically. In the presence of co-adsorbed water, the OH scissions are slightly facilitated while the CH bond scissions are inhibited: $\Delta E^{\ddagger}(TS_{CH})$ = 0.67 eV at the bare Pt(111) while $\Delta E^{\ddagger}(TS_{CH})$ = 0.90 eV at the hydrated surface for instance. The same phenomenon has been observed and explained in the case of Rh.[54] This shift up in energy for the CH dissociation makes those dissociations the rate-limiting step in both routes (*i.e.* the first step of route C and the second step of route O) at the hydrated surface. Another consequence is that route O becomes competitive with route C: the main route cannot be easily identified. However, both of them are more demanding energetically than route C at the bare surface. In other words, the hydrated platinum surface is less active than the bare surface.

Once again, the hydroxylated surface presents a completely different behaviour. Only one step is activated and its barrier is low ($\Delta E^{\ddagger}(TS_{OH–CH})$ = 0.33 eV, half the CH bond breaking at the bare surface). Thus, this surface is strongly activated compared with the bare surface and the hydrated surface and will promote easily the ethanol dehydrogenation into acetaldehyde.

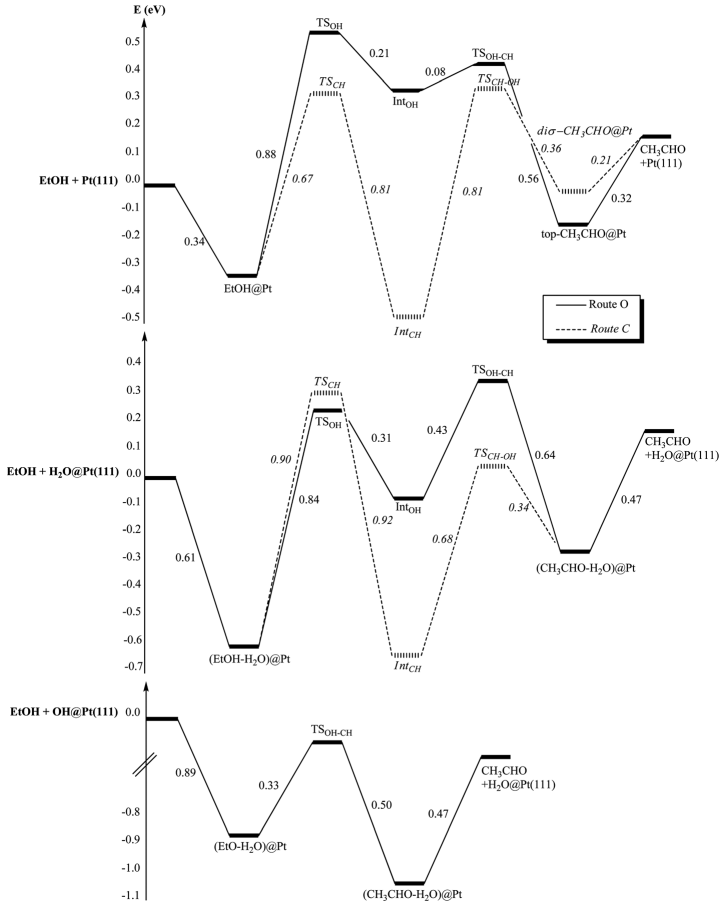

Fig. 8 Reaction paths of EtOH oxidation into acetaldehyde (CH_3CHO): (i) at the bare platinum surface Pt(111), (ii) at the hydrated platinum surface H_2O@Pt(111) and (iii) at the hydroxylated surface OH@Pt(111). Energies are in eV. The reference energy is the isolated EtOH and (i) the bare platinum surface, (ii) H_2O@Pt(111), (iii) OH@Pt(111).

Isopropanol

Adsorption. On the bare surface and the hydrated surface, the adsorption of iPrOH is similar to that of ethanol, both geometrically (Fig. 3) and energetically: $E_{ads} = -0.35$ eV for the bare surface, $E_{ads} = -0.61$ eV for the hydrated surface. The adsorption energy of this secondary alcohol at the hydroxylated surface is close to the one of ethanol (−0.89 eV). But the geometry differs: the pre-adsorbed OH does not abstract the hydroxyl hydrogen of iPrOH and isopropanol adsorbs molecularly, making only a hydrogen bond with OH (see Fig. 4, the O–H distances being 1.07 and 1.42 Å with iPrO and OH, respectively). So, adsorbed on a platinum surface, iPrOH is less acidic than EtOH.

Reaction paths. The transition states for the different elementary steps of the isopropanol oxidation are very similar to the ones of ethanol oxidation. They are represented in Fig. S1, S2 and S3 (ESI†). The reaction energy, the activation energy and the main geometrical characteristics of the TS of each step are collected in Table S1 (ESI†). The transition state structures are similar to those of ethanol but with longer C–H and Pt–C distances due to the steric hindrance, in the case of the first CH breaking. In the other cases, second CH dissociation or hydrated surface, the bond lengths are not modified because the $C(CH_3)_2$ group is farther from the surface. At the bare surface, the final product (acetone) is preferentially adsorbed on-top and the di-σ adsorption mode is 0.6 eV less stable. At the hydrated surface, acetone is adsorbed through a H-bond with the water molecule, similarly to acetaldehyde (Fig. 7).

The reaction paths for the isopropanol oxidation are shown in Fig. 9. At the bare surface, route C is the easiest one and conversely, route O is preferred at the hydrated surface. In both cases, the two steps are equally energetically demanding. The corresponding transition states energies are lower for the

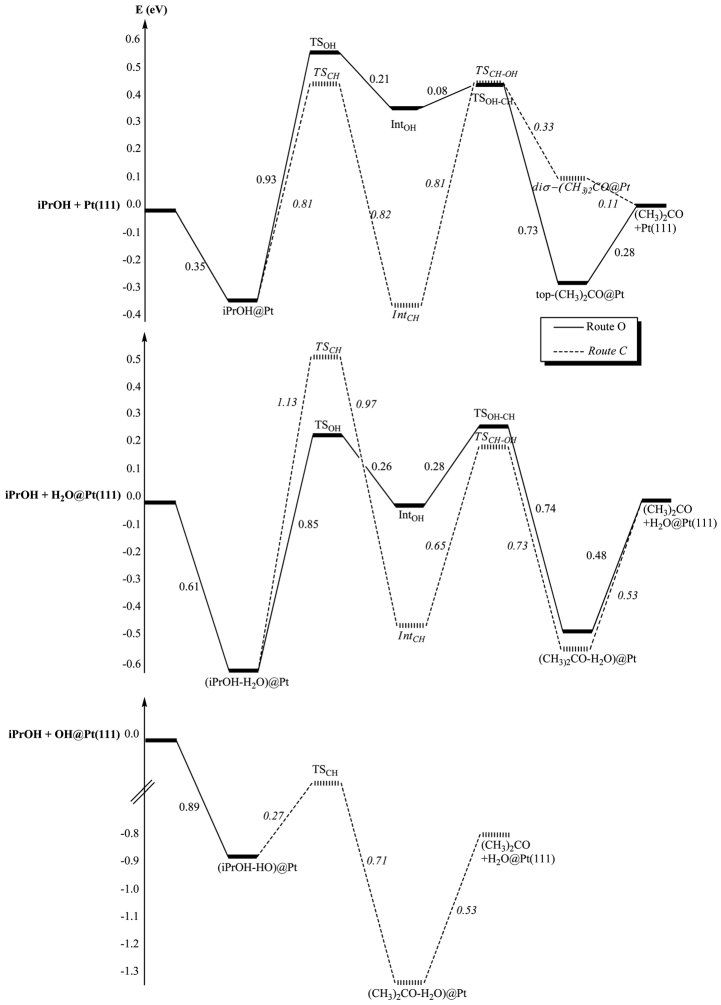

Fig. 9 Reaction paths of the iPrOH oxidation into acetone $(CH_3)_2CHO$: (i) at the bare platinum surface Pt(111), (ii) at the hydrated platinum surface H_2O@Pt(111) and (iii) at the hydroxylated surface OH@Pt(111). Energies are in eV. The reference energy is the isolated iPrOH and (i) the bare platinum surface, (ii) H_2O@Pt(111), (iii) OH@Pt(111).

bare surface than for the hydrated one. Once again, the hydroxylated surface is completely different from the bare and hydrated ones. As seen in the previous paragraph, isopropanol does not undergo OH dissociation when co-adsorbed with a hydroxyl. In addition, even if one tries to enforce a iPrO–H_2O configuration, the system turns back spontaneously to a iPrOH–OH configuration. This means that route O is not possible for isopropanol at a hydroxylated surface. However, route C is feasible. The activation energy of the CH scission is only 0.27 eV, the lowest activation energy found in this complete study. Moreover, the OH bond breaking occurs simultaneously with the CH scission and acetone, not adsorbed at the surface but making a hydrogen bond with H_2O, is obtained directly. In other words, here again the oxidation of the alcohol at the hydroxylated platinum surface requires only one activated step.

Comparison of primary/secondary alcohols. Let us compare now the isopropanol and ethanol reaction paths. The first observation, when Fig. 8 and 9 are compared, is that the global oxidation reaction is endothermic for both alcohols, as well in the gas phase as on the surface, except in the presence of a hydroxyl group. Nevertheless, the endothermicity is less important in the case of isopropanol. If the Hammond principle is valid, this would mean that isopropanol should be more reactive. However, the reaction is multistep and the kinetics can give different results.

Ethanol and isopropanol only differ by an extra methyl group adjacent to the C–O bond. This group increases the bulkiness of the C atom that undergoes the C–H dissociation and also the stability of the resulting radical, secondary *vs.* primary. The two effects are opposite. In the case of the first step of route C, where the carbon must approach the surface, the strong steric effect prevails over the electronic one and an increase of the barrier by 0.14 and 0.28 eV is observed, compared to ethanol, in the case of the bare and hydrated surface, respectively. In the case of the second CH scission ($TS_{OH–CH}$), the carbon atom is farther from the surface and the electronic effect prevails, leading to a decrease of the barrier by 0.15 eV, compared to ethanol in the case of the hydrated surface. In the case of the hydroxylated surface, the carbon atom is also farther from the surface since the final product is directly a non-bonded acetone molecule, and the same effect is observed: a decrease of the barrier by 0.06 eV. The OH scission is much less affected by the substitution: the activation energies $\Delta E^{\ddagger}$(OH) and $\Delta E^{\ddagger}$(CH–OH) are close to the ones for ethanol (±0.05 eV).

Depending on the surface under consideration, the conclusions are different. At the bare surface, route C is preferred for both alcohols. In the case of isopropanol, the barriers are higher than in the case of ethanol. Hence, the secondary alcohol is less reactive than the primary one, in agreement with the experimental results observed in pure dioxane (without water).

In the case of the hydrated surface, route O becomes the most favourable route for isopropanol. In addition, isopropanol appears being more reactive than ethanol, since the barrier of the second step is smaller, which agrees with the experimental observations (Fig. 1). However, if the bare and the hydrated surfaces are compared, the latter appears being less reactive towards both alcohols (higher barriers), which is in contradiction with the experimental observations. Therefore, these results do not explain the role of water in enhancing the reactivity of the alcohols on the catalyst.

Now, as mentioned previously, it has been shown experimentally that the adsorption of water at a Pt surface, precovered with oxygen, leads to the easy formation of OH groups adsorbed at the surface.[68–70] The barrier for the reaction $O + H_2O \rightarrow 2OH$ has been calculated at 0.25 eV.[74] At the hydroxylated surface, we have already noted that the unique activation energy along the reaction path is the lowest one for both alcohols. Not only this surface is promoting the alcohol oxidation, but also it seems to be slightly more reactive towards isopropanol than towards ethanol: $\Delta E^{\ddagger}$(ethanol) = 0.33 eV and $\Delta E^{\ddagger}$(isopropanol) = 0.27 eV. These results are in agreement with the experimental results: the addition of water increases the rate of the reaction and more for 2-octanol than for 1-octanol.

Our results show that the role of water in enhancing the reactivity of the platinum surface during the oxidation of alcohols is an indirect one: the hydroxyl groups, formed by reaction of H_2O with O atoms at the surface, are indeed the promoters of the reaction. The role of OH groups has indeed been observed experimentally on Au and Pt catalysts.[51]

4.2. Deactivation by decarbonylation

The experimental results described above for 1-octanol oxidation at 373 K (Fig. 1) showed that the oxidation reaction could be strongly inhibited. However, performing the reaction at 333 K in dioxane–water 50/50 vol% solvent made slightly alkaline (0.03 eq. NaOH) instead of 373 K allowed the reaction to be complete to the acid, without any deceleration of the reaction rate, though, as expected, the reaction rate was lower.[19]

The aldehyde obtained after oxidation of the primary alcohol can be further oxidized in solution into a carboxylic acid thanks to the presence of water, through the formation of the gemdiol. It can also be decomposed at the platinum surface, as observed for acetaldehyde.[72,73] In that case, the final product is CO, showing that there is a decarbonylation. Some theoretical works have already dealt with the decomposition scheme of acetaldehyde on Pt(111).[46–48,52] In these works, the possible bond breakings (C–H, C–C, C–O) were calculated. The conclusion was that breaking the C–H bond of the aldehydic group is the easiest reaction. Then the C–C bond is broken more easily than the C–O one but the barrier is high. We have revisited the C–H and C–C bond breaking of acetaldehyde and of the subsequent species with the present surface model and method in order to be consistent and able to compare with the previous energy diagrams.

The C–H dissociation of the aldehyde hydrogen is exothermic by −0.76 eV and needs a small energy barrier of 0.26 eV (Table 2), higher than the one calculated in ref. 43 and 44, but in the same range as the one extracted from kinetics measurements (0.21 eV). The corresponding transition state is a four-centers TS, rather early along the path with a C–H bond of 1.33 Å (21% elongation) and a Pt–H bond of 1.77 Å. The resulting acetyl intermediate CH_3CO is adsorbed by the carbon atom in a top geometry (Pt–O = 2.02 Å). The di-σ geometry where both the carbon and the oxygen are bound to the surface (with a long Pt–O bond of 2.42 Å) is only slightly less stable than the first one. This step presents the lowest barrier we have found in the transformation of ethanol (see Fig. 8). It is even lower than the desorption energy of acetaldehyde. Hence, this intermediate can be easily obtained. In addition, the reverse barrier is rather high (1.02 eV) preventing the system from going back to acetaldehyde.

The following step can be either a C–C or a C–H bond breaking. The C–C bond breaking is slightly exothermic (−0.16 eV) and the energy barrier is high (1.44 eV), in agreement with the values found previously.[48,49] In the TS, the C–C bond is elongated to 1.99 Å and the Pt–C bond is almost formed (2.27 Å, 9% elongation). This TS can be considered as late in relation with the high barrier. A secondary agostic interaction takes place between a H of the methyl group and a Pt atom (Pt–H = 1.94 Å), which elongates the

Table 2 Energetics and main geometrical characteristics of the transition state structures for the decomposition steps of acetaldehyde at the bare platinum surface Pt(111). The reaction energy ΔE and the activation energy $\Delta E^{\ddagger}$ of each step are provided in eV. The main distances are given in Å

Reaction	ΔE	$\Delta E^{\ddagger}$	C–H	C–C	Pt–H	Pt–C(CO)
$CH_3CHO \rightarrow CH_3CO + H$	−0.76	0.26	1.33		1.77	
$CH_3CO \rightarrow CH_2CO + H$	0.08	1.06	1.52		1.62	
$CH_3CO \rightarrow CH_3 + CO$	−0.16	1.44		1.99		1.94
$CH_2CO \rightarrow CHCO + H$	0.10	0.87	1.53		1.63	

C–H bond to 1.15 Å. This agostic interaction is broken in the final state. Except the latter interaction that was not mentioned, the present TS looks very similar to the one previously reported. The products are a methyl group and a C═O group chemisorbed at top vicinal positions (Pt–C = 2.08 Å and 1.86 Å, respectively and C–O = 1.16 Å). The C–H bond breaking leads to a ketene molecule, adsorbed in a di-σ CC geometry (Pt–C = 2.08 and 2.03 Å, C–C = 1.50 Å, CO = 1.20 Å). The reaction is slightly endothermic by 0.08 eV and the barrier is also relatively high at 1.06 eV (compared to 0.96 eV[49]). The TS is a relatively late three-centres TS with C–H and Pt–H distances of 1.52 and 1.62 Å, respectively. The barriers of the C–C and C–H bond breakings are both high, the C–H bond rupture being the smallest. Hence at low temperature (333 K), CH_3CO is likely the acetaldehyde decomposition species. In the presence of OH groups, it can be hydroxylated to acetic acid. The barrier for this step is low (0.31 eV[46]).

At higher temperature (373 K), a barrier of 1 eV is likely to be overcome. Hence for such temperatures, the C–H bond rupture could take place and ketene be obtained. Alcala *et al.* have shown that the barrier to break the C–C bond in ketene is higher than in the case of acetyl CH_3CO (1.38 eV) but that the corresponding barrier in the ketenyl CHCO is much smaller (0.96 eV). However, the transformation of ketene into ketenyl had not been studied. Hence, we have considered the C–H breaking in ketene leading to ketenyl. The reaction is slightly endothermic (0.10 eV) and the barrier is 0.87 eV far lower than the one for the C–C bond breaking calculated previously. The TS is an usual three-centers TS with C–H and Pt–H distances of 1.53 and 1.63 Å, respectively. Hence, in ketene, as in acetyl, it is preferable to break first the C–H bond to obtain CHCO; then the C–C bond breaks more easily. The transition states structures can be found in Fig. 10.

The acetaldehyde decomposition on Pt(111) has been followed by temperature-programmed desorption (TPD) experiments associated with high-resolution electron-energy loss spectroscopy (HREELS).[72,73] The HREEL experimental spectrum collected following adsorption at 120 K corresponds to a monolayer of adsorbed acetaldehyde (see Fig. 11). During the heating, the νCO peak of CH_3CHO at 1663 cm^{-1} almost disappears as well as the bands between 1360 and 1427 cm^{-1}. Meanwhile, a high peak grows at 620 cm^{-1}. At 350 K, the characteristic peak of on-top bonded CO dominates (2089 cm^{-1}) accompanied by the corresponding peak at 474 cm^{-1}. A small peak assigned to bridge bonded CO exists also at 1819 cm^{-1}. This evidences that decarbonylation takes place from this temperature. In the region of the νCH vibrations, the peak at 3008 cm^{-1}, present at low temperature, disappears when the temperature increases and a new peak appears at 2981 cm^{-1} at 350 K.

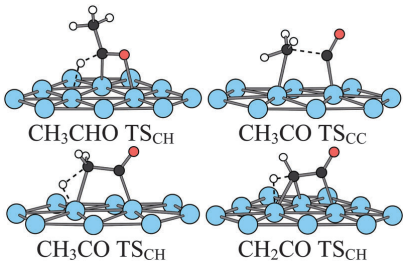

Fig. 10 Transition states structures of the acetaldehyde decomposition at a bare Pt(111) surface.

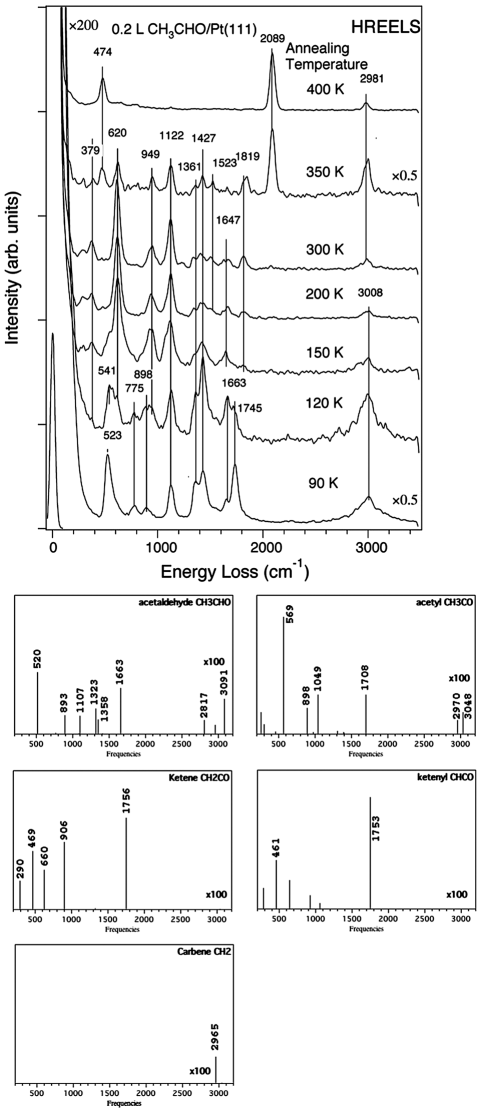

Fig. 11 Experimental HREELS spectra of adsorbed acetaldehyde on Pt(111) after heating at various temperatures (reprinted with permission from ref. 72). Simulated spectra of CH_3CHO, CH_3CO, CH_2CO, CHCO, CH_2. All calculated spectra have the same scale.

To characterize adsorbed surface species during the desorption experiment, we have simulated the vibrational spectra of CH_3CHO, CH_3CO, CH_2CO, CHCO, and CH_2 and compared them to the experimental ones. CH_3 has not been considered since its formation is unlikely owing to the high barrier (Table 2). The simulated spectrum for CH_3CHO has been already published[75] but is redone here for the sake of consistency. This calculated spectrum exhibits two main peaks at 1663 and 520 cm^{-1}, corresponding to νCO and νPtO, respectively, and found experimentally at 1663–1745 and 523–541 cm^{-1}. There are also features at 893, 1107 and 1323–1358 cm^{-1}. All these peaks are found in the experimental spectrum (898, 1122, 1362–1427 cm^{-1}). Finally high νCH peaks are obtained between 2817 and 3091 cm^{-1}. They correspond to the large band observed in the experimental spectrum taken after heating at 120 K. The simulated spectrum of CH_3CO shows significant differences both in intensity and in position of the peaks. The peaks centred around 1300 cm^{-1} no longer exist and the spectrum is dominated by the νPtC mode at 569 cm^{-1}, corresponding to the experimental peak at 620 cm^{-1} observed above 150 K. The other peaks are also slightly shifted. The νCH peaks are also less intense. Hence, between 150 and 300 K, the appearance in the experimental spectra of a peak at 620 cm^{-1} and the disappearance of the peaks at 1361–1427 cm^{-1} indicates that, in this temperature range, the main species is CH_3CO.

At 350 K, CO is obviously already present and a small quantity of CH_3CO remains. However the high intensity νCH peak at 2981 cm^{-1} shows the existence of hydrocarbons. In fact, we have shown before that CH_3CO decomposes likely into CH_2CO and CHCO before the C–C bond is broken. The calculated spectra of ketene CH_2CO and ketenyl CHCO are dominated by an intense peak at 1756 and 1753 cm^{-1}, respectively. Such peaks do not exist in the experimental spectrum at 350 K. Hence ketene and ketenyl are transient intermediates and therefore species like adsorbed CH_2 or CH are likely present. These species give intense νCH vibrations as illustrated for the carbene, which could explain the high peak at 2981 cm^{-1} appearing with CO at 350 K. Ketene can also be at the origin of acetic acid production by hydration.

This analysis of the TPD experiment allows us to confirm that the first step of acetaldehyde decomposition is the C–H breaking of the aldehydic group. It occurs at temperature as low as 150 K in agreement with the low calculated barrier. The subsequent C–H and C–C breakings are more energy demanding and occur at higher temperature so that CH_3CO remains the main species over a large range of temperatures. At high temperature, the final result of acetaldehyde decomposition is decarbonylation.

To summarize, the above study of acetaldehyde decomposition allows us to shed light on some experimental details. In the case of primary alcohols, at the temperature of the reaction (373 K), the product resulting from the removal of the aldehydic hydrogen (corresponding to acetyl) can easily be hydroxylated to carboxylic acid or decomposed further into CO and carbonaceous residues, poisoning the surface, which could explain the limitation of the conversion. At lower temperature, the decomposition is less easy and the reaction can go to completion with production of large amounts of acid as observed experimentally.

The C–C bond breakings are more difficult than the C–H ones and become feasible after the removal of almost all hydrogens. In acetone, the absence of H on the C=O group prevents decomposition from taking place. This could be the reason why the catalyst is not poisoned in the case of secondary alcohols.

5. Conclusion

The combination of experimental results on the oxidation reaction of alcohols on Pt catalysts and of DFT calculations has allowed the understanding of the different behaviour of primary and secondary alcohols. In particular, it has been shown that the higher activity of secondary alcohols compared with the primary alcohols in the presence of water is due to a balance between steric and electronic effects of the substituents. The present study has also shed light on the role of water in these reactions. The main new conclusion is that the rate enhancement in the presence of water is not due to water itself but to hydroxyl groups formed by reaction of water with dissociated oxygen at the surface of the catalyst. The most energetically favorable pathway is then facilitated by the presence of adsorbed OH, which reduces the overall barrier. Decarbonylation of acetaldehyde at 373 K is likely to be the cause of deactivation of the catalyst.

Acknowledgements

The calculations have been performed using the local HPC resources of PSMN at ENS-Lyon and of GENCI (CINES/IDRIS), project x2010075105.

Notes and references

1 J. I. Kroschwitz, in *Kirk-Othmer Encyclopedia of Chemical Technology*, Wiley-Intersciences, New York, 4th edn, 1992, vol. 4.
2 R. A. Sheldon, I. W. C. E. Arends, G. T. Brink and A. Dijksman, *Acc. Chem. Res.*, 2002, **35**, 774.
3 J. Muzart, *Tetrahedron*, 2003, **59**, 5789.
4 J. March, in *Advanced Organic Chemistry: Reactions*, Wiley, New York, 1992.
5 D. B. Dess and J. C. Martin, *J. Org. Chem.*, 1983, **48**, 4155.
6 A. J. Mancuso, S. L. Huang and D. Swern, *J. Org. Chem.*, 1978, **43**, 2480.
7 O. Dolmer and H. Heyns, *US Pat.* 2 190 377, 1940.
8 M. Besson and P. Gallezot, *Catal. Today*, 2000, **57**, 127.
9 T. Mallat and A. Baiker, *Chem. Rev.*, 2000, **104**, 3037.
10 C. Della Pina, E. Falletta, L. Prati and M. Rossi, *Chem. Soc. Rev.*, 2008, **37**, 2077.
11 C. P. Vinod, K. Wilson and A. F. Lee, *J. Chem. Technol. Biotechnol.*, 2011, **86**, 161.
12 H. van Bekkum, in *Carbohydrate as Organic Raw Materials*, ed. F. W. Lichtenthaler, Wiley VCH, Weinheim, 1990, p. 289.
13 G. Jenzer, M. S. Schneider, R. Wandeler, T. Mallat and A. Baiker, *J. Catal.*, 2001, **199**, 141.
14 A. M. Steele, J. Zhu and S. C. Tsang, *Catal. Lett.*, 2001, **73**, 9.
15 G. Jenzer, D. Sueur, T. Mallat and A. Baiker, *Chem. Commun.*, 2000, 2247.
16 Z. S. Hou, N. Theyssen and W. Leitner, *Green Chem.*, 2007, **9**, 127.
17 Y. Uozumi and R. Nakao, *Angew. Chem., Int. Ed.*, 2003, **42**, 194.
18 Y. M. A. Yamada, T. Arakawa, H. Hocke and Y. Uozumi, *Angew. Chem., Int. Ed.*, 2007, **46**, 704.
19 A. Frassoldati, C. Pinel and M. Besson, *Catal. Today*, 2011, **173**, 81.
20 A. Frassoldati, C. Pinel and M. Besson, *Catal. Today*, 2012, DOI: 10.1016/j.cattod.2012.01.012.

21 Z. Ma, H. Yang, Y. Qin, Y. Hao and G. Li, *J. Mol. Catal. A: Chem.*, 2010, **331**, 78.
22 X. Yang, X. Wang, C. Liang, W. Su, C. Wang, Z. Feng, C. Li and J. Qiu, *Catal. Commun.*, 2008, **9**, 2278.
23 X. Yang, X. Wang and J. Qiu, *Appl. Catal., A*, 2010, **382**, 131.
24 A. Villa, D. Wang, N. Dimitros, D. Su, V. Trevisan and L. Prati, *Catal. Today*, 2010, **150**, 8.
25 A. Villa, M. Plebani, M. Schiavoni, C. Milone, E. Piperopoulos, S. Galvagno and L. Prati, *Catal. Today*, 2012, **186**, 76.
26 C. Keresszegi, D. Ferri, T. Mallat and A. Baiker, *J. Catal.*, 2005, **234**, 64.
27 A. F. Lee, Z. Chang, P. Ellis, S. F. J. Hackett and K. Wilson, *J. Phys. Chem. C*, 2007, **111**, 18844.
28 C. Keresszegi, T. Bürgi, T. Mallat and A. Baiker, *J. Catal.*, 2002, **211**, 244.
29 D. M. Meier, A. Urakawa and A. Baiker, *J. Phys. Chem. C*, 2009, **113**, 21849.
30 H. G. J. de Wilt and H. S. van der Baan, *Ind. Eng. Chem. Prod. Res. Dev.*, 1972, **11**, 374.
31 C. Keresszegi, T. Mallat and A. Baiker, *New J. Chem.*, 2001, **25**, 1163.
32 R. Di Cosimo and G. M. Whitesides, *J. Phys. Chem.*, 1989, **93**, 768.
33 C. Keresszegi, J. D. Grunwaldt, T. Mallat and A. Baiker, *Chem. Commun.*, 2003, 2304.
34 J. D. Grunwaldt, C. Keresszegi, T. Mallat and A. Baiker, *J. Catal.*, 2003, **213**, 291.
35 A. P. Markusse, B. F. M. Kuster and J. C. Schouten, *Catal. Today*, 2001, **66**, 191.
36 X. Yang, X. Wang, C. Liang, W. Su, C. Wang, Z. Feng, C. Li and J. Qiu, *Catal. Commun.*, 2008, **9**, 2278.
37 X. Yang, X. Wang and J. Qiu, *Appl. Catal., A*, 2010, **382**, 131.
38 A. Villa, M. Plebani, M. Schiavoni, C. Milone, E. Piperopoulos, S. Galvagno and L. Prati, *Catal. Today*, 2012, **186**, 76.
39 S. K. Desai, M. Neurock and K. Kourtakis, *J. Phys. Chem. B*, 2002, **106**, 2559.
40 J. Greeley and M. Mavrikakis, *J. Am. Chem. Soc.*, 2002, **124**, 7193.
41 J. Greeley and M. Mavrikakis, *J. Am. Chem. Soc.*, 2004, **126**, 3910.
42 C. Hartnig and E. Spohr, *Chem. Phys.*, 2005, **319**, 185.
43 D. Cao, G.-Q. Lu, A. Wieckowski, S. A. Wasileski and M. Neurock, *J. Phys. Chem. B*, 2005, **109**, 11622.
44 S. Kandoi, J. Greeley, M. A. Sanchez-Castillo, S. T. Evans, A. A. Gokhale, J. A. Dumesic and M. Mavrikakis, *Top. Catal.*, 2006, **37**, 17.
45 C.-Y. Niu, J. Jiao, B. Xing, G.-C. Wang and X.-H. Bu, *J. Comput. Chem.*, 2010, **31**, 2023.
46 H.-F. Wang and Z.-P. Liu, *J. Am. Chem. Soc.*, 2008, **130**, 10996.
47 K. I. Gursahani, R. Alcala, R. D. Cortright and J. A. Dumesic, *Appl. Catal., A*, 2001, **222**, 369.
48 R. Alcala, M. Mavrikakis and J. A. Dumesic, *J. Catal.*, 2003, **218**, 178.
49 J.-H. Wang, C. S. Lee and M. C. Lin, *J. Phys. Chem. C*, 2009, **113**, 6681.
50 D. Basaran, A. Genest and N. Rösch, *J. Catal.*, 2012, **287**, 210.
51 B. N. Zope, D. D. Hibbitts, M. Neurock and R. J. Davis, *Science*, 2010, **330**, 74.
52 R. Kavanagh, X. Cao, W.-F. Lin, C. Hardacre and P. Hu, *J. Phys. Chem. C*, 2012, **116**, 7185.
53 C. Shang and Z.-P. Liu, *J. Am. Chem. Soc.*, 2011, **133**, 9938.
54 C. Michel, F. Auneau, F. Delbecq and P. Sautet, *ACS Catal.*, 2011, **1**, 1430.
55 X. Q. Qi, Z. D. Wei, L. L. Li, L. Li, M. B. Ji, Y. Zhang, M. R. Xia and X. L. Ma, *J. Mol. Struct.*, 2010, **980**, 208.
56 P. Korovchenko, C. Donze, P. Gallezot and M. Besson, *Catal. Today*, 2007, **121**, 13.
57 G. Kresse and J. Hafner, *Phys. Rev. B: Condens. Matter Mater. Phys.*, 1993, **47**, 558.
58 J. P. Perdew and Y. Wang, *Phys. Rev. B: Condens. Matter Mater. Phys.*, 1992, **45**, 13244.
59 P. E. Blöchl, *Phys. Rev. B: Condens. Matter Mater. Phys.*, 1994, **50**, 17953.
60 G. Kresse and D. Joubert, *Phys. Rev. B: Condens. Matter Mater. Phys.*, 1999, **59**, 1758.
61 H. J. Monkhorst and J. D. Pack, *Phys. Rev. B: Solid State*, 1976, **13**, 5188.
62 G. Henkelman, B. P. Uberuaga and H. Jonsson, *J. Chem. Phys.*, 2000, **113**, 9901.
63 D. Sheppard, R. Terrell and G. Henkelman, *J. Chem. Phys.*, 2008, **128**, 134106.
64 P. Dayal and P. Fleurat-Lessard, A chemist view on reaction path determination, to be published. Available at http://perso.ens-lyon.fr/paul.fleurat-lessard/ReactionPath.html.
65 G. Henkelman and H. Jonsson, *J. Chem. Phys.*, 1999, **111**, 7010.
66 J. Kastner and P. Sherwood, *J. Chem. Phys.*, 2008, **128**, 014106.
67 D. Loffreda, Y. Jugnet, F. Delbecq, J. C. Bertolini and P. Sautet, *J. Phys. Chem. B*, 2004, **108**, 9085.
68 S. Völkening, K. Bedürfig, K. Jacobi, J. Wintterlin and G. Ertl, *Phys. Rev. Lett.*, 1999, **83**, 2672.
69 C. Clay, S. Haq and A. Hodgson, *Phys. Rev. Lett.*, 2004, **92**, 046102.
70 W. Lew, M. C. Crowe, E. Karp and C. T. Campbell, *J. Phys. Chem. C*, 2011, **115**, 9164.
71 C. Panja, N. Saliba and B. E. Koel, *Surf. Sci.*, 1998, **395**, 248.
72 H. Zhao, J. Kim and B. E. Koel, *Surf. Sci.*, 2003, **538**, 147.
73 A. F. Lee, D. E. Gawthrope, N. J. Hart and K. Wilson, *Surf. Sci.*, 2004, **548**, 200.
74 R. Ferreira de Morais, PhD thesis, ENS Lyon, Ecole Doctorale de Chime de Lyon ED206, France, 2011.
75 F. Delbecq and F. Vigné, *J. Phys. Chem. B*, 2005, **109**, 10797.

Volume 50 | Number 83 | 25 October 2014 | Pages 12403–12580

ChemComm

Chemical Communications

www.rsc.org/chemcomm

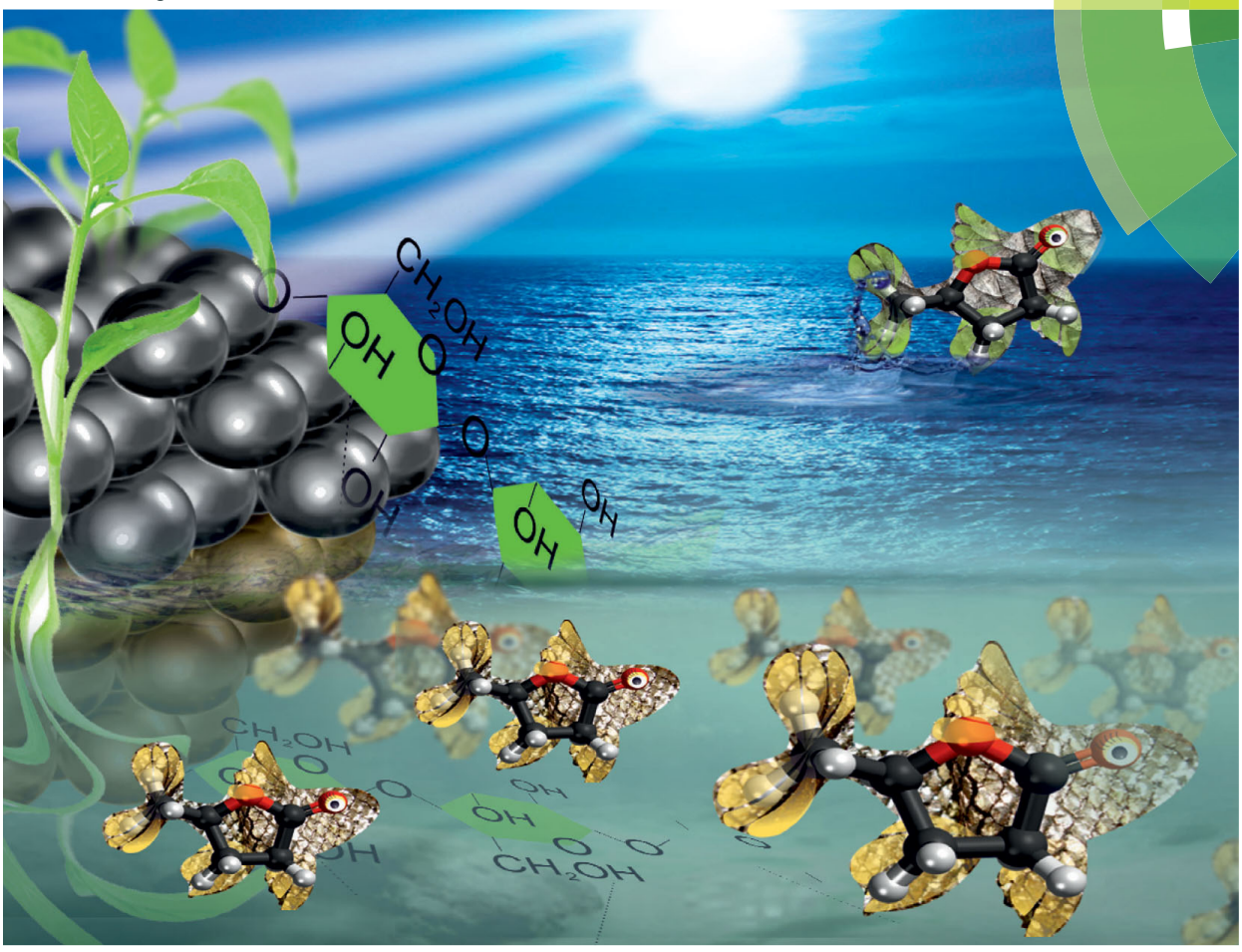

ISSN 1359-7345

ROYAL SOCIETY OF CHEMISTRY

COMMUNICATION

Carine Michel, Agnieszka M. Ruppert *et al.*

Role of water in metal catalyst performance for ketone hydrogenation: a joint experimental and theoretical study on levulinic acid conversion into gamma-valerolactone

ChemComm

COMMUNICATION

Role of water in metal catalyst performance for ketone hydrogenation: a joint experimental and theoretical study on levulinic acid conversion into gamma-valerolactone†

Cite this: *Chem. Commun.*, 2014, **50**, 12450

Received 9th June 2014,
Accepted 18th June 2014

DOI: 10.1039/c4cc04401k

www.rsc.org/chemcomm

Carine Michel,*[a] Jérémie Zaffran,[a] Agnieszka M. Ruppert,*[b] Joanna Matras-Michalska,[b] Marcin Jędrzejczyk,[b] Jacek Grams[b] and Philippe Sautet[a]

While Ru is a poor hydrogenation catalyst compared to Pt or Pd in the gas phase, it is efficient under aqueous phase conditions in the hydrogenation of ketones such as the conversion of levulinic acid into gamma-valerolactone. Combining DFT calculations and experiments, we demonstrate that water is responsible for the enhanced reactivity of Ru under those conditions.

The swap from hydrocarbon based to biomass based feedstock triggers the development of novel catalysts and processes to transform oxygenates into valuable molecules.[1] Most of the time, those reactions with reactants extracted from biomass are conducted in water to efficiently solubilise reaction intermediates and products. We will show here that water can also play an essential role in the catalytic activity, focusing on the conversion of levulinic acid (LA) into γ-valerolactone (GVL)[2] (see Fig. 1). LA can be obtained *via* cellulose hydrolysis and dehydration of such obtained glucose. GVL is an attractive platform molecule that can be derived from biomass and can be converted to a variety of chemicals, including biofuel additives.[3–5]

Galletti *et al.*[6] have established that with supported metal catalysts LA hydrogenation to GVL follows the scheme presented in Fig. 1: (i) the metal catalyses the first step, *i.e.* the hydrogenation of the ketone moiety into 4-hydroxy pentanoic acid and (ii) the cyclising esterification easily leads to the GVL.

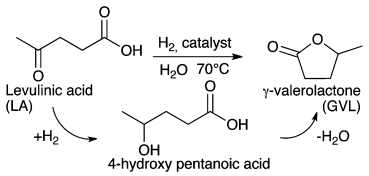

Fig. 1 Conversion of levulinic acid into gamma-valerolactone.

Another route is opened at higher temperatures (>200 °C), starting with the cyclising dehydration of the enolic form of LA.[7–9] The C=C bond of the intermediary angelica lactone is then hydrogenated, leading to GVL. This alternative route is not accessible under our mild conditions.

Under these conditions, it is striking that Ru is usually more active in the conversion of LA to GVL than Pd and Pt in water,[9–12] while Ru is known to be poorly active compared to Pd and Pt in the hydrogenation of ketones under gas phase conditions.[13] Actually, the hydrogenation capability of Ru is strongly modulated by the reaction environment. Rooney *et al.* have shown that the hydrogenation of 2-butanone catalyzed by Ru/SiO_2 is 30 times faster in water than in heptane.[14] Thus, Ru is much more active in aqueous media, even more active than Pt or Pd, so it is frequently used for aqueous phase hydrogenation of various ketones.[15]

This strong dependence of Ru activity upon solvent can also be transferred to our target reaction, the hydrogenation of LA towards GVL. We analysed three noble metal catalysts (Ru, Pt, Pd) supported on titania in two different environments (water and tetrahydrofuran (THF)) under mild conditions (70 °C, 50 bar of hydrogen, details in ESI†). The catalysts were prepared in a way that the particle size effect could be minimized since all metal particles possess a similar size (2.1–3.2 nm). With the same support and particle size, the experiments here provide a consistent case of comparison of two solvents under similar conditions, hence avoiding other effects on the hydrogenation activity. TEM images (ESI†) generally demonstrated a homogeneous distribution of the active phase on the support. The results of the catalytic

[a] *Laboratoire de Chimie UMR5182, University of Lyon, CNRS, Ecole Normale Supérieure de Lyon, 46 allée d'Italie, F-69364 Lyon Cedex 07, Lyon, France. E-mail: carine.michel@ens-lyon.fr; Fax: +33472728080; Tel: +33472728847*
[b] *Institute of General and Ecological Chemistry, Faculty of Chemistry, Łódź University of Technology, ul. Żeromskiego 116, 90-924 Łódź, Poland. E-mail: agnieszka.ruppert@p.lodz.pl; Fax: +48426313128; Tel: +48426313106*

† Electronic supplementary information (ESI) available: Experimental section; TEM images; computational details; energetic span definition; energetic spans of each path and each metal, without and with water; energetic spans of each path with an implicit solvent for Ru(0001); transition state structure for the hydrogenation of the alkoxy on Ru(0001) in the presence of 3 water molecules and in the presence of 11 water molecules; an alternative route to the alkoxy path in the presence of water on Ru(0001); correlation of the energetic span variation for the alkoxy path with the d-band center; all calculated structures together with their absolute energies. See DOI: 10.1039/c4cc04401k

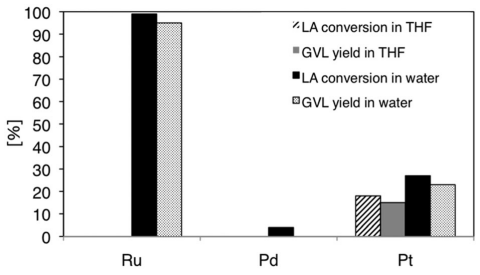

Fig. 2 LA conversion and GVL yield in % for Ru, Pd, Pt catalysts in THF and in water solvent. No conversion was observed for Ru and Pd in THF solvent.

activity are presented in Fig. 2. The Ru catalyst activity is strongly dependent on the reaction media. While it is not active in THF, Ru is the most active in water (99% LA conversion, 95% GVL yield). Pt and Pd activities are not sensitive to the solvent: around 15–20% of GVL yield together with a 20–30% conversion of LA is obtained using Pt and negligible activity is observed using Pd. Note that Pd was active for this reaction but at higher temperatures (190 °C) and with conservation of the same order of reactivity: Ru > Pt > Pd. Finally, the trends of the metal and solvent are similar for the LA conversion into GVL and the ketone hydrogenation, indicating that the first step (*i.e.* the ketone hydrogenation, see Fig. 1) is the rate determining step of this reaction.

To our knowledge, this striking dependence of the relative activity of Ru, Pt and Pd for ketone hydrogenation on the reaction medium is not yet well understood. In this paper, we aim to explain the apparently unique behaviour of Ru in the presence of water using DFT calculations. Several strategies are possible to model solvent effects. Implicit models take into account the dielectric constant and its capability to stabilize charges.[16] Explicit models include solvent molecules increasing the number of atoms and accessible configurations.[17] The increase of activity of Ru in the aqueous phase compared with the organic solvent lies probably in the hydrogen bond effect of liquid water. An implicit model cannot grasp this kind of effect easily. However, an explicit model of liquid water is highly expensive. We propose here the use of a micro-solvation approach, including only the most important solvent molecule, following our previous studies on the influence of water on alcohols dehydrogenation.[18–20] The ketone was modelled by acetone, since both molecules show very similar trends upon metal and solvent changes, implying that the acid group does not affect the hydrogenation of the ketone function.

We start by the elementary steps for acetone hydrogenation on the Ru(0001) surface. We modelled gas phase hydrogenation with a periodic slab approach (see ESI†). The two possible reaction paths are presented in Fig. 3, both starting in the centre of the figure and evolving towards the left, the reference being the Ru(0001) and acetone and hydrogen in the gas phase. In the alkyl path, the chemisorbed acetone (IS*) is hydrogenated on the oxygen first through the transition state TS_{OH}. It leads to an alkyl radical IntC. In the second step, the carbon is hydrogenated (TS_{OH-CH}) resulting in the weakly chemisorbed isopropanol (FS*, E_{ads} = −0.44 eV). This route is disfavoured by high lying transition states (TS) of energy −0.41 eV and −0.28 eV relative to the reference. The second TS is the highest, 1.37 eV higher than chemisorbed acetone. In the alkoxy path, the carbon is hydrogenated first (TS_{CH}), leading to a very stable alkoxy intermediate (IntO, 0.25 eV more stable than the chemisorbed acetone and one chemisorbed H atom). Then, the second step for the O hydrogenation (TS_{CH-OH}) has to overcome a high activation energy barrier (1.40 eV) despite a transition state lying lower than in the alkyl route. Those results are in agreement with the acetone hydrogenation paths on Ru(0001) obtained by Sinha and Neurock.[23]

To compare kinetic rates for the two pathways, we can follow the energetic span analysis introduced by Kozuch and Shaik,

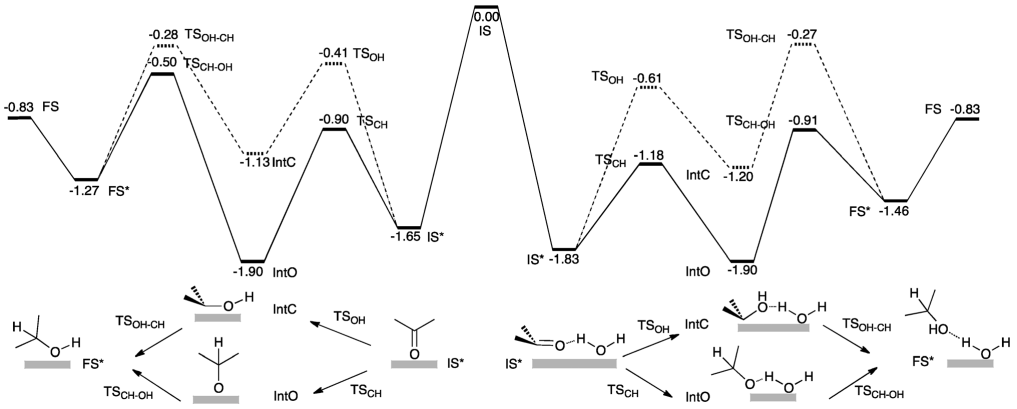

Fig. 3 Reaction paths (in eV) for the hydrogenation of acetone on Ru(0001) in the absence (left) and in the presence of a water molecule (right). The alkyl path is represented in dash line and the alkoxy path in solid line. The reference energy is common and includes the acetone and a H_2 molecule in the gas phase, three bare Ru(0001) slabs and a 'hydrated' slab bearing a chemisorbed water molecule.

by establishing the TOF-determining intermediate (TD-I) and the TOF-determining TS (TD-TS).[24] The energetic span (or effective barrier) is calculated as the energy difference between the TD-TS and the TD-I of a catalytic cycle.

The smaller the energetic span, the higher the rate and the more efficient is the corresponding catalyst. More details on the procedure are given in the Computational details section of the ESI.† This approach shows that the two paths are equally disfavoured with an energetic span of 1.37 eV for the alkyl route and 1.40 eV for the alkoxy one.

To grasp the major effect of the water solvent, we used the simplest possible approach and added a chemisorbed water molecule to our model. The chemisorption of acetone is strongly modified. In the absence of water, acetone exhibits two iso-energetic chemisorbed structures (E_{ads} = −0.47 eV; the C═O bond parallel to the surface or perpendicular to the surface). In the presence of water, the most stable situation for acetone corresponds to the configuration parallel to the surface forming a H-bond with the chemisorbed water molecule (see Fig. 4, left). This configuration is 0.18 eV more stable than the separated adsorption of water and acetone. The co-adsorption of the resulting isopropanol and water is in line with previous studies on Pt(111)[18] and Rh(111):[19,20] the alcohol is H-bonded to the chemisorbed water and shows no direct interaction with the surface. Here again, the two possible hydrogenation paths starting from this configuration are presented in Fig. 3 starting from the centre and going towards the right, the reference being the Ru(0001) slab with water already chemisorbed and acetone and hydrogen in the gas phase. The chemisorbed acetone (IS*) is stabilised by ∼0.2 eV. The TS_{OH} of the alkyl path is also stabilized by ∼0.2 eV. However, the second transition state TS_{OH-CH} is not affected and still remains high in energy (−0.27 eV relative to the reference). Thus, the overall effective barrier is increased by 0.2 eV. The situation is more favourable on the alkoxy path. The two transition states remain lower in energy in the presence of water. In addition, the formation of the alkoxy intermediate is less exothermic, although it remains the TD-I for that path. Altogether, the effective barrier markedly decreases by 0.41 eV (from 1.40 to 0.99 eV). To conclude, the presence of co-adsorbed water slightly inhibits the alkyl path and strongly favours the alkoxy path. The effective activation barrier is diminished by 35%, leading to a strong increase of the predicted activity of Ru(0001).

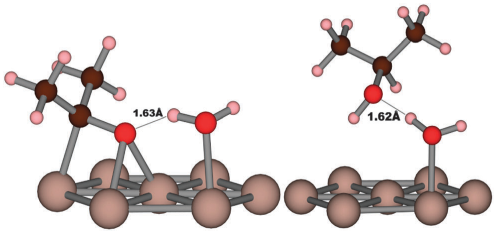

Fig. 4 Co-adsorption structures of acetone and water (left) and isopropanol and water (right) on Ru(0001).

The addition of a single chemisorbed water molecule hence allows us to capture the origin of the enhanced activity of Ru under aqueous conditions observed for the hydrogenation of ketones[14] or for the conversion of LA into GVL as already exposed. To go beyond this initial model, we have refined the most favourable alkoxy route. Adding the surrounding aqueous environment as a continuum model[21] does not change the energetic span significantly (see Tables S2 and S3, ESI†). Then, we increased the number of water molecules to 11 to include the first solvation sphere as suggested by Hu and co-workers.[22] Here again, the energetic span is not strongly affected (Fig. S3, ESI†). A single water molecule is enough to grasp the Ru catalyst activation. An alternative route could involve the dissociation of a water molecule (Fig. S4, ESI†). For instance, the hydrogen-bonded water could dissociate and transfer the proton involved in the hydrogen bond to the alkoxy (second elementary step of the alkoxy route) leading to the isopropanol and a surface hydroxyl. However, surface hydroxyl groups cannot accumulate at the catalyst surface and have to be eliminated. Their hydrogenation is as energy demanding as the hydrogenation of the alkoxy intermediate.

To better understand the periodic trends for the influence of water, the same paths were computed for a larger series of late transition metals (Ru, Co, Rh, Ir, Ni, Pd, Pt, Cu) on the corresponding close-packed surfaces (111) for fcc metals and (0001) for hcp ones. For most of the metals under consideration, the two routes are almost equally probable in the absence of water, with a small preference for the alkyl path (except for Rh and Ir). The energetic span of the most favourable path is provided in the absence and presence of water and for each metal under consideration in Fig. 5 (more details in ESI,† Table S2). At the bare metallic surface, the most active catalysts are Ir, Pt and then Cu and Rh according to their respective energetic span while Ni, Pd, Ru and Co are much less active catalysts. This is in good agreement with experimental observations for gas phase acetone hydrogenation.[13] For the common subset of metals, the experiment gives the activity order Pt > Rh > Pd ∼ Ru > Ni ∼ Co while calculations show Pt > Rh > Ni > Pd ∼ Ru > Co so that only Ni is slightly misplaced. Last, one can notice that the activity for the alkyl paths is mainly controlled by the acetone adsorption (IS*) as the TOF-determining state and the TS for the second

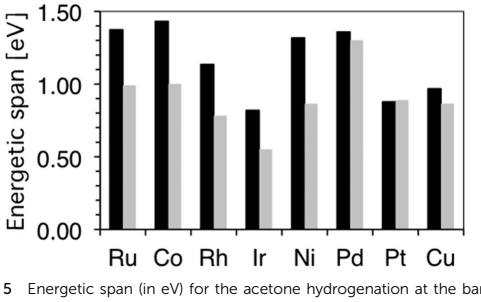

Fig. 5 Energetic span (in eV) for the acetone hydrogenation at the bare metallic surface (in black) and in the presence of one chemisorbed water (in grey) for a series of transition metals.

hydrogenation on the carbon (TS_{OH-CH}) as the TOF-determining-TS while the alkoxy paths are controlled by the oxygen hydrogenation TS (TS_{CH-OH}) and the chemisorbed acetone (IS*) or the alkoxy state (IntO) for more oxophilic metals such as Co, Ni, and Ru.

The presence of one water molecule strongly modifies the energetic span values and the alkoxy route is clearly preferred over the alkyl one for all metals (see ESI,† Table S3). This inversion results from an activation of the alkoxy route with a concomitant deactivation of the alkyl route. The influence of water on the energetic span of the most favourable route is summarized in Fig. 5. We have already seen that the capability of Ru to hydrogenate acetone is strongly enhanced by the presence of a single chemisorbed water. On the other hand, the less-oxophilic metals (Pd and Pt) are barely affected. The promotion of the alkoxy route is not strong enough to facilitate the acetone hydrogenation: Pt is as active as in the absence of water; Pd is still inactive. This is in line with our experimental findings: Pt is active to some extent in both THF and water while Pd is not in both environments under our mild conditions. Calculations clearly show the promotion of Ru *vs.* Pt in the aqueous phase. However, from the intrinsic error bar of DFT-GGA (0.15 eV) it is not possible to determine in absolute value which metal is the most active one under aqueous conditions, since the calculated barriers only differ by 0.1 eV. Other aspects, as the coverage of hydrogen, could also slightly alter the relative energies of the hydrogenation transition states. This goes beyond the scope of this communication.

Our wider screening of transition metals shows in addition that the promotion effect seen for Ru can be generalized to the other oxophilic metals such as Co and Ni. The higher the energy of the d-band centre is, the more oxophilic the metal is. The variation of the energetic span of the alkoxy path upon water assistance nicely correlates with the d-band centre of the metal under consideration (Fig. S5, ESI†). Surface species on those metals are more strongly affected by the co-adsorption of a water molecule. The TD-TS (TS_{CH-OH}) is stabilized while the TD-I (mainly IntO) is often destabilized. Therefore, the energetic span is strongly reduced (up to $\sim$0.4 eV) and those metals become good candidate catalysts for acetone hydrogenation in an aqueous environment. This result clears up the difference in the catalytic reactivity order of metal for acetone hydrogenation in the gas phase[13] and in the aqueous phase.[15] As discussed above, in the gas phase, Ru, Co, Ni and Pd are poorly active.[13] Things change completely in aqueous phase experiments and Ru, Co, Ni become excellent catalysts while Pd remains poor.[15] The calculated assistance of water for oxophilic metals hence shed light on experimental observations.

Ru is widely used to hydrogenate biomass sourced oxygenates such as levulinic acid while this metal is known to be a poor hydrogenation catalyst of acetone in the gas phase. Combining experiments in THF and water together with DFT calculations, we showed that this metal activity is highly sensitive to its environment. The presence of a H-bonded water molecule dramatically reduces the energetic span of the reaction pathway, hence enhancing the catalytic activity. We predict that this activation can be generalized to other oxophilic metals such as Co or Ni while Pt and Pd are insensitive to their aqueous environment.

The authors gratefully acknowledge that this work was done within the framework of Polonium project 2012/2013. A.M.R. acknowledges that part of this work was done within the NCN grant NN 209 75 83 40. J.Z., C.M. and P.S. acknowledge that part of this work was done within the ANR GALAC project (ANR-10-CD2I-011). We thank also PSMN at ENS Lyon, IDRIS-CNRS, and CINES for computational resources. The authors would like to thank Prof. Bert Weckhuysen and his group for help in the GC analysis of the products.

Notes and references

1 D. M. Alonso, J. Q. Bond and J. A. Dumesic, *Green Chem.*, 2010, **12**, 1493.
2 W. R. H. Wright and R. Palkovits, *ChemSusChem*, 2012, **5**, 1657.
3 I. T. Horvath, H. Mehdi, V. Fbos, L. Boda and L. T. Mika, *Green Chem.*, 2008, **10**, 238.
4 D. M. Alonso, S. G. Wettstein and J. A. Dumesic, *Green Chem.*, 2013, **15**, 584.
5 J.-P. Lange, R. Price, P. M. Ayoub, J. Louis, L. Petrus, L. Clarke and H. Gosselink, *Angew. Chem., Int. Ed.*, 2010, **122**, 4581.
6 A. M. Raspolli Galletti, C. Antonetti, V. De Luise and M. Martinelli, *Green Chem.*, 2012, **14**, 688.
7 W. Luo, U. Deka, A. M. Beale, E. R. H. van Eck, P. C. A. Bruijnincx and B. M. Weckhuysen, *J. Catal.*, 2013, **301**, 175.
8 V. Mohan, C. Raghavendra, C. V. Pramod, B. D. Raju and K. S. R. Rao, *RSC Adv.*, 2014, **4**, 9660.
9 P. P. Upare, J.-M. Lee, D. W. Hwang, S. B. Halligudi, Y. K. Hwang and J.-S. Chang, *J. Ind. Eng. Chem.*, 2011, **17**, 287.
10 L. Corbel-Demailly, B.-K. Ly, D.-P. Minh, B. Tapin, C. Especel, F. Epron, A. Cabiac, E. Guillon, M. Besson and C. Pinel, *ChemSusChem*, 2013, **6**, 2388.
11 J. M. Tukacs, R. V. Jones, F. Darvas, G. Dibo, G. Lezsak and L. T. Mika, *RSC Adv.*, 2013, **3**, 16283.
12 L. E. Manzer, *Appl. Catal., A*, 2004, **272**, 249.
13 N. N. Rimar and G. N. Pirogova, *Russ. Chem. Bull.*, 1998, **47**, 398.
14 B. S. Akpa, C. D'Agostino, L. F. Gladden, K. Hindle, H. Manyar, J. McGregor, R. Li, M. Neurock, N. Sinha, E. H. Stitt, D. Weber, J. A. Zeitler and D. W. Rooney, *J. Catal.*, 2012, **289**, 30.
15 J. Lee, Y. Xu and G. W. Huber, *Appl. Catal., B*, 2013, **140**, 98.
16 J. Tomasi, B. Mennucci and R. Cammi, *Chem. Rev.*, 2005, **105**, 2999.
17 C. D. Taylor and M. Neurock, *Curr. Opin. Solid State Mater. Sci.*, 2005, **9**, 49–65.
18 S. Chibani, C. Michel, F. Delbecq, C. Pinel and M. Besson, *Catal. Sci. Technol.*, 2013, **3**, 339.
19 C. Michel, F. Auneau, F. Delbecq and P. Sautet, *ACS Catal.*, 2011, **1**, 1430.
20 D. Loffreda, C. Michel, F. Delbecq and P. Sautet, *J. Catal.*, 2013, **308**, 374.
21 K. Mathew, R. Sundararaman, K. Letchworth-Weaver, T. A. Arias and R. G. Hennig, *J. Chem. Phys.*, 2014, **140**, 084106.
22 J. Liu, X.-M. Cao and P. Hu, *Phys. Chem. Chem. Phys.*, 2014, **16**, 4176.
23 N. K. Sinh and M. Neurock, *J. Catal.*, 2012, **295**, 31.
24 S. Kozuch and S. Shaik, *Acc. Chem. Res.*, 2011, **44**, 101.

4

ELECTROCATALYSIS

Introduction

Electrocatalysis can be seen as a branch of catalysis where the current (generated or utilized) is analogous to the heat in thermal catalysis. Endothermic reactions can be reached using adequate current and potentials while exothermic reactions can produce a current in addition to the targeted product. The choice of the electrode and of the operating conditions are essential, but they can hardly be rationalized based on a molecular understanding of the reactive processes occurring at the electrode/electrolyte interface. They are difficult to characterize also experimentally. While modeling seems like an adequate complementary tool, it also suffers from severe limitations. The direct inclusion of the electrochemical potential is not trivial, even though several methods have been developed in the last decade.[4,6,10,13,15,19] Those methods have been barely used to understand the bond breaking/formation at the metal/electrolyte interface.[7] We have recently used them to understand the electrocatalytic behavior of CO_2 and related compounds such as alkenes and formic acid thanks to the strong investment of S. Steinmann, a post-doc that was first hired on a Solvay contract.[21,22,23] The inclusion of the electrochemical potential can be necessary but is computationally expensive. The computational hydrogen electrode (CHE) is a cheaper approach, based on a basic correction a posteriori on the thermochemistry of the elementary steps.[12] It has been extensively used in

the last decade.[1,3,5,8,11,14,18] We have recently used this simple model in the context of ethanol alkaline fuel cell, in collaboration with E. Baranova and her PhD student E. Monyoncho (Canada, LIA Funcat).

4.1 Computational hydrogen electrode

This approach was proposed in 2004 by Norskov and co-workers.[12] The basic idea is that each electron transfer is coupled with a hydronium ($H^+ + e^-$) and the experimental electrochemical potential of this couple is taken as a reference electrochemical potentiel. For instance, at a given potential U, the reaction energy of the following reaction

$$CH_3CO + H_2O \longrightarrow CH_3COOH + H^+ + e^-$$

is computed as:

$$\Delta G_r(U) = E(CH_3COOH) - [E(CH_3CO) + E(H_2O)] - 0.5\, E(H_2) - U,$$

where we have assumed U to be with respect to the pH insensitive Reversible Hydrogen Electrode and a pH of 0.

The CHE is straightforward in its application since it only requires to add or remove a correction term to the reaction energy. This term depends only on the number of hydrogen that are involved in the elementary step (usually 0 or 1) and the reaction energy is computed in absence of potential or charge, it corresponds to the thermal reaction energy. The simplicity of CHE relies on strong assumptions. We emphasize here the two main ones. First, CHE can be used only in cases where the electron transfert is coupled to a proton (or another cation such as sodium). Second, it implies that the reaction energy obtained in absence of any charge or potential (the 'thermal' reaction energy) corresponds to the U=0 V/RHE situation, whatever the nature of the surface species at the electrochemical interface. This is a strong limitation of the model, since the relation between the charge and the potential is

given by the capacitance of the system and this quantity depends on the interface under consideration.

However, the simplicity of this approach allows to tackle large reaction networks. We recently focused on the ethanol oxidation in alkaline fuel cells in collaboration with E. Baranova and E. Monyoncho from uOttawa, Canada. To reach a high current and efficiency, the oxidation of ethanol needs to be complete, yielding 12 electrons per ethanol. However, the reaction generally stops at the acetate/acetic acid. We studied the whole reaction network of ethanol oxidation to acetate and then CO_2. Combining polarization modulation infrared reflection absorption spectroscopy (PM-IRRAS) and density functional theory (DFT) calculations (see Figure 4.1), we understood why the C−C bond is not broken and the oxidation stops at acetate. As shown in Figure 4.1, acetate is clearly the most stable species of the complete reaction network of the conversion of ethanol into CO_2. In addition, acetate is highly resistant to C−C bond scission. Thus, we focused on the steps that precede the oxidation in acetate and we highlighted the pivotal role of the acetyl CH_3CO intermediate: it can either undergo a C−C bond scission yielding CO and then CO_2 or it can either be oxidized towards acetate. The latter is facilitated by the overpotential but it is a dead end in the reaction scheme towards CO_2 production, since it cannot be easily oxidized nor broken into C1 fragments. CH_3CO is however not the most favored intermediate formed from ethanol electrooxidation on Pd, hence limiting the production of CO_2. This reaction mechanism is sum up in Figure 4.2. Building on this study, we plan to screen catalysts *in silico* to favor the formation of the acetyl and its dissociation.

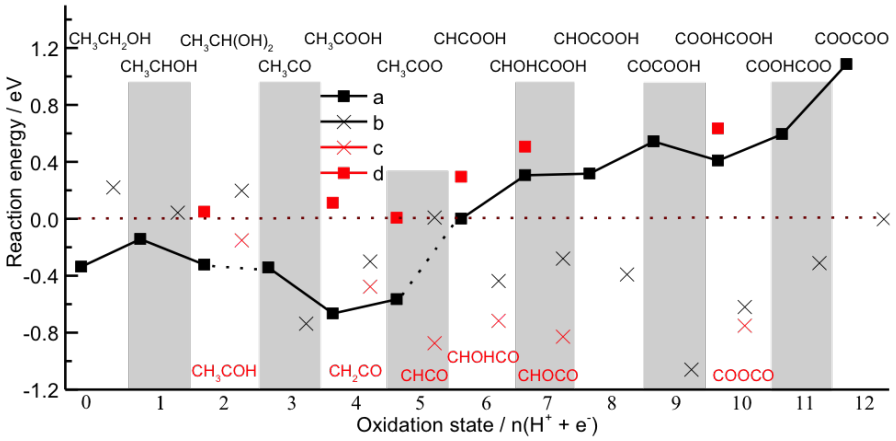

Figure 4.1: Global reaction energy profile of the most stable intermediates during ethanol electrooxidation process on Pd(100) at 0.26 V/RHE. The black squares show the most stable C2 intermediates at each oxidation state (C2 path) whose intermediates are indicated at the top. To guide the eyes, a line has been added, in solid (resp. dotted) when the intermediates are connected (resp. not) from one oxidation state to the next. Legend: (a) Most stable C2 species, (b) C1 fragments generated from the most stable C2, (c) Most stable C1 fragments, and (d) Parent C2 species of the most stable C1 fragments which are shown at the bottom.

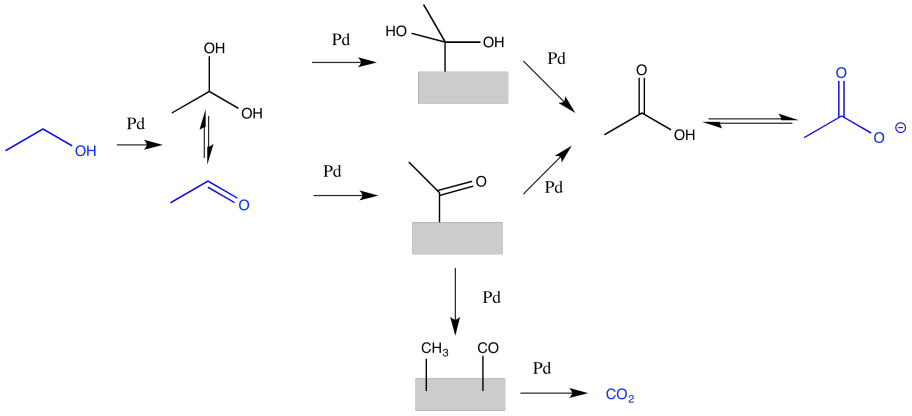

Figure 4.2: General Reaction Scheme based on our DFT results (shown in Figure 4.1. In blue, the experimental evidences. In black, the intermediates as suggested by our DFT simulations. Most of the steps are catalyzed by the Pd electrode (single arrows) while others are solution equilibria (two one-sided arrows).

4.2 Inclusion of the potential

A system of interest for Solvay is the development of novel routes yielding adipic acid. An elegant strategy is to use CO_2 as a C1 building block and couple it to butadiene, using electrocatalysis to perform this endothermic reaction. CO_2 is an inert molecule. It requires a preliminary (partial) reduction to be active and this can be achieved only at highly reductive potentials. To design a proper catalyst able to activate CO_2 with a low overpotential without opening the door to side reactions is a key challenge in the domain of CO_2 electrocatalytic valorisation.

We started to demonstrate that the inclusion of the potential using the method developed by Filhol and Neurock[4] in the simulations of the electrochemical interface requires the inclusion of the solvent, at least as a continuum, to get a realistic capacitance.[22] In addition, we evidenced that non-electrochemical steps could be sensitive to the electrochemical potential such as the CO_2 adsorption or the formate rotation in the HCOOH/CO_2 conversion on Ni.[21] Once the modeled was appropriate, we tackled the targeted reaction. The electrochemical coupling between CO_2 and butadiene on Ni and Pt electrodes is difficult: our simulations are in agreement with the strong overpotential observed experimentally. The C−C bond formation is not sensitive to the electrochemical potential and could be eventually facilitated by a change in the catalyst morphology.[23]

4.3 What's next?

As a natural next step, I would like to compare the electrocatalytic conditions to the thermal catalytic conditions. A potential target is the oxidation of biomass-derived alcohols, where interestingly, the same kind of catalysts are currently used in both domains (namely Au, Pd and Pt and alloys of Au-Pd and Au-Pt).[2,9,16,17,20]

In addition, this domain will greatly benefit of any methodological development to improve the description of the solvent, as we already

discussed in the previous chapter.

Bibliography

[1] Bandarenka, A. S.; Varela, A. S.; Karamad, M.; Calle-Vallejo, F.; Bech, L.; Perez-Alonso, F. J.; Rossmeisl, J.; Stephens, I. E. L.; Chorkendorff, I. *Angew. Chem. Int. Ed.* **2012**, *51*, 11845.

[2] Besson, M.; Gallezot, P.; Pinel, C. *Chem. Rev.* **2014**, *114*, 1827–1870.

[3] Ferrin, P.; Nilekar, A. U.; Greeley, J.; Mavrikakis, M.; Rossmeisl, J. *Surf. Sci.* **2008**, *602*, 3424.

[4] Filhol, J.-S.; Neurock, M. *Angew. Chem. Int. Ed.* **2006**, *45*, 402.

[5] Greeley, J.; I. E. L., S.; Bondarenko, A. S.; Johansson, T. P.; Hansen, H. A.; Jaramillo, T. F.; Rossmeisl, J.; Chorkendorff, I.; Norskov, J. K. *Nat. Chem.* **2009**, *1*, 552.

[6] Hamada, I.; Sugino, O.; Bonnet, N.; Otani, M. *Phys. Rev. B* **2013**, *88*, 155427.

[7] Janik, M. J.; Taylor, C. D.; Neurock, M. *J. Electrochem. Soc.* **2009**, *156*, B126–B135, OH.

[8] Keith, J. A.; Jerkiewicz, G.; Jacob, T. *ChemPhysChem* **2010**, *11*, 2779.

[9] Liu, S.-S.; Sun, K.-Q.; Xu, B.-Q. *Acs Catalysis* **2014**, *4*, 2226–2230.

[10] Mamatkulov, M.; Filhol, J.-S. *Phys. Chem. Chem. Phys.* **2011**, *13*, 7675.

[11] Man, I. C.; Su, H.-Y.; Calle-Vallejo, F.; Hansen, H. A.; Martinez, J. I.; Inoglu, N. G.; Kitchin, J.; Jaramillo, T. F.; Norskov, J. K.; Rossmeisl, J. *ChemCatChem* **2011**, *3*, 1159.

[12] Norskov, J. K.; Rossmeisl, J.; Logadottir, A.; Lindqvist, L.; Kitchin, J. R.; Bligaard, T.; Jonsson, H. *J. Phys. Chem. B* **2004**, *108*, 17886.

[13] Otani, M.; Sugino, O. *Phys. Rev. B* **2006**, *73*, 115407.

[14] Rossmeisl, J.; Qu, Z.-W.; Zhu, H.; Kroes, G.-J.; Norskov, J. *J. Electroanal. Chem.* **2007**, *607*, 83.

[15] Rossmeisl, J.; Skulason, E.; Bjorketun, M. E.; Tripkovic, V.; Norskov, J. K. *Chem. Phys. Lett.* **2008**, *466*, 68–71.

[16] Shi, X.; Simpson, D. E.; Roy, D. *Physical Chemistry Chemical Physics* **2015**, *17*, 11432–11444.

[17] Simoes, M.; Baranton, S.; Coutanceau, C. *ChemSusChem* **2012**, *5*, 2106–2124.

[18] Stamenkovic, V.; Mun, B. S.; Mayrhofer, K. J. J.; Ross, P. N.; Markovic, N. M.; Rossmeisl, J.; Greeley, J.; NÃ¸rskov, J. K. *Angew. Chem. Int. Ed.* **2006**, *45*, 2897.

[19] Taylor, C. D.; Wasileski, S. A.; Filhol, J.-S.; Neurock, M. *Phys. Rev. B* **2006**, *73*, 165402.

[20] Zalineeva, A.; Serov, A.; Padilla, M.; Martinez, U.; Artyushkova, K.; Baranton, S.; Coutanceau, C.; Atanassov, P. B. *J. Am. Chem. Soc.* **2014**, *136*, 3937.

[21] Steinmann, S. N.; Michel, C.; Schwiedernoch, R.; Filhol, J.-S.; Sautet, P. *ChemPhysChem* **2015**, *16*, 2307–2311 .

[22] Steinmann, S. N.; Michel, C.; Schwiedernoch, R.; Sautet, P. *Phys. Chem. Chem. Phys.* **2015**, *17*, 13949–13963 .

[23] Steinmann, S. N.; Michel, C.; Schwiedernoch, R.; Wu, M.; Sautet, P. *J. Catal.* **2016**, –.

PCCP

PAPER

View Article Online
View Journal | View Issue

Cite this: *Phys. Chem. Chem. Phys.*, 2015, **17**, 13949

Impacts of electrode potentials and solvents on the electroreduction of CO_2: a comparison of theoretical approaches†

Stephan N. Steinmann,[a] Carine Michel,[ab] Renate Schwiedernoch[c] and Philippe Sautet*[ab]

Received 13th February 2015,
Accepted 21st April 2015

DOI: 10.1039/c5cp00946d

www.rsc.org/pccp

Since CO_2 is a readily available feedstock throughout the world, the utilization of CO_2 as a C1 building block for the synthesis of valuable chemicals is a highly attractive concept. However, due to its very nature of energy depleted "carbon sink", CO_2 has a very low reactivity. Electrocatalysis offers the most attractive means to activate CO_2 through reduction: the electron is the "cleanest" reducing agent whose energy can be tuned to the thermodynamic optimum. Under protic conditions, the reduction of CO_2 over many metal electrodes results in formic acid. Thus, to open the road to its utilization as a C1 building block, the presence of water should be avoided to allow a more diverse chemistry, in particular for C–C bond formation with alkenes. Under those conditions, the intrinsic reactivity of CO_2 can generate carbonates and oxalates by C–O and C–C bond formation, respectively. On Ni(111), almost exclusively carbonates and carbon monoxide are evidenced experimentally. Despite recent progress in modelling electrocatalytic reactions, determining the actual mechanism and selectivities between competing reaction pathways is still not straight forward. As a simple but important example of the intrinsic reactivity of CO_2 under aprotic conditions, we highlight the shortcomings of the popular linear free energy relationship for electrode potentials (LFER-EP). Going beyond this zeroth order approximation by charging the surface and thus explicitly including the electrochemical potential into the electronic structure computations allows us to access more detailed insights, shedding light on coverage effects and on the influence of counterions.

1 Introduction

Heterogeneous electrocatalysis is at the heart of advanced energy technologies such as hydrogen production[1] and fuel-cells.[2] Furthermore, electrochemistry, in combination with photovoltaic cells, promises access to "green" and "mild" redox chemistry.[3–5] In particular, the electroreduction of CO_2 is a conceptually attractive avenue: electrochemistry activates the intrinsically rather inert green-house gas under mild conditions (*i.e.*, low pressure and temperature), enabling us to utilize CO_2 as a C1 building block in C–C coupling reactions[6–9] or to generate small, energy rich molecules such as CO, methanol or formic acid.[10–13]

In protic media, the reduction of CO_2 competes with H_2 evolution and mixtures of CO + H_2O, formic acid and very small amounts of hydrocarbons are observed in general.[14,15] Hence, the efficient use of CO_2 as a C1 building block precludes the presence of water and protons. For instance the electroreduction of CO_2 in DMF in the presence of a diene over Ni has been reported to yield C–C coupled products, in particular the dicarboxylates.[6,7,16–18] However, the existing procedure is not very efficient in terms of yield and selectivity and the mechanism is poorly understood. In addition, in aprotic solvents, CO_2 has an intrinsic reactivity, potentially yielding oxalate and a combination of CO and carbonate,[11,19] opening additional reaction paths.

Electrocatalysis is carried out in a complex environment, *i.e.*, an electrolyte is required to increase the conductivity of the solution and the interface between the catalyst and the solvent is thin compared to the solution, making experimental characterization challenging.[20–25] Despite considerable efforts, we lack, therefore, a detailed mechanistic understanding at the atomic level, hampering the rational design of novel catalysts. For all these reasons, research and development have still huge

[a] *Université de Lyon, Laboratoire de Chimie, Ecole Normale Supérieure de Lyon 46 allee d'Italie, Lyon, France*
[b] *CNRS, Laboratoire de Chimie, UMR 5182, 46 allee d'Italie, Lyon, France. E-mail: philippe.sautet@ens-lyon.fr; Fax: +334 7272 8080; Tel: +334 7272 8155*
[c] *Eco-Efficient Products and Processes Laboratory (E2P2L), UMI 3464 Solvay/CNRS, Shanghai, P. R. China*

† Electronic supplementary information (ESI) available: Bader charges for selected adsorbates as a function of potential, all geometries optimized at zero-charge in a vacuum and a shell-script to post-process VASP computations according to the correction proposed by Filhol and Neurock. See DOI: 10.1039/c5cp00946d

View Article Online
Paper PCCP

challenges to overcome in order to efficiently use CO_2 as a C1 building block.

Atomic scale modelling is a powerful tool for complementing the experimental effort and providing detailed information under very well controlled conditions (catalyst surface, applied potential). However, computations are usually performed on simplified models and the influences of the electrolyte and of the solvent on the catalyst interfacial properties are rarely considered,[26] although their importance is well known from more empirical approaches.[27,28] The classical description of electrochemical systems typically relies on ''empirical'' or at least drastically simplified equations[29] (*e.g.*, Marcus–Hush for electron transfer, Gouy–Chapman for the double layer properties or the Fokker–Planck equation for mass transport). These mesoscopic equations require system averaged parameters which can either be obtained by fitting to experiment or approximately extracted from first principles data. Although such multi-scale models[30,31] may correctly describe the relevant physics, the fundamental issue is that the central ingredient in electrocatalysis, the electrochemical potential, is far from being straight forward to include explicitly in a first principles approach at the atomic level.

The present study investigates the electroreduction of CO_2 in an aprotic solvent as a prerequisite for further investigations of the CO_2 coupling with alkenes.[6,7,16–18] Oxalate is the major product of CO_2 electrolysis under aprotic conditions on ''inert'' electrodes, in particular over Pb.[32,33] The proposed reaction mechanism, which is in good agreement with the high overpotentials required for this reaction, goes through $CO_2^{\bullet-}$. The radical anion is supposed to be slightly stabilized by the surface at potentials below −1.8 V (*vs.* Ag/AgCl) and then undergo a fast surface assisted coupling.[34] On more reactive electrodes, and in particular over nickel, CO formation is frequently reported.[11,14]

The large majority of simulations of heterogeneous electrocatalysis rely on a simple model proposed in the seminal work reported by Norskov and coworkers under the name of the computational hydrogen electrode (CHE),[35] and its extension to other cations than H^+, *e.g.*, Li^+[36] or Na^+, which we call linear free energy relationship for electrode potentials (LFER-EP). In this model, the electrochemical potential is assumed to affect only the chemical potential of the exchanged electrons and solvent effects are generally neglected. In a nutshell, this approach is an *a posteriori* correction of first principles studies of neutral metal surfaces in a vacuum that are routine computations for some decades.[37] The CHE model leads to highly exploitable results,[38–44] despite its known limitations: the absence of polarisation of adsorbed molecules and electron transfer strictly coupled to cation transfer. This implies, for example, that this method cannot grasp the transient anionic species $CO_2^{\bullet-}$.

The comparison by Rossmeisl *et al.*[45] of the zeroth order approach CHE and the more advanced surface charge (SC) method of Filhol and Neurock[46] (*vide infra*) concluded that for adsorbates with large dipole moments and for kinetic studies the more sophisticated SC method should be applied.[45] However, to go beyond the CHE approach, one needs to explicitly integrate the electrochemical potential into the first principles calculations. Applying an electrochemical potential is equivalent to tune the workfunction, which is simulated by adding or subtracting electrons from the neutral system. Hence, charged systems are necessary to explicitly investigate the effect of an electrochemical potential on surface adsorbed species. Unfortunately, charged systems cannot be simulated under periodic boundary conditions, which most efficiently simulate extended metallic systems: a periodically charged system is infinitely charged and hence the Coulomb potential diverges. Therefore, when changing the number of electrons in periodic computations a countercharge is required. Several schemes have been proposed in the literature.[26,46–53] The technically simplest way to deal with the situation is to include a homogeneous background charge.[46] The technical simplicity leads to a major drawback: the uniform background charge interacts with the system, even within the metallic slab. Filhol and Neurock have proposed a correction, leading to the surface charging (SC) mehod, in order to mitigate the issue.[46,52] The SC model provides, despite the approximations, excellent agreement with experiment when a water bilayer is used to solvate the surfaces, as exemplified by the phase diagram of H_2O over Pt[45,54] and Ni,[55] CO electro-oxidation over Pt[56] and the borohydride oxidation.[57]

In addition to the electrochemical potential, electrochemistry depends critically on the solvent because the dielectric constant of the solvent governs the capability of a system to stabilize and ''store'' charges, *i.e.*, the capacitance of the system. Therefore, solvent effects are especially important for charged systems. So far, the water solvent was modeled using an explicit bilayer of water.[45,54–59] In our case, we aim at modelling an aprotic solvent such as DMF. However, just like including an electrochemical potential into the simulations, accounting for solvent effects in electronic structure computations of extended systems is still in its infancy,[60–63] with implicit solvent models becoming publicly available only very recently.[64] This is in contrast with the situation of molecular chemistry where several solvent models have been developed and applied for many years.[65]

The aim of this study is two-fold. On the one hand, we will provide some insight into the selectivity towards the formation of carbonates upon CO_2 electrolysis over nickel under aprotic conditions. On the other hand, we will elucidate the influence of the applied electrochemical potential on species adsorbed on a metal surface in order to clarify two aspects of the modelling of heterogeneous electrocatalysis: first, the importance to account explicitly for the electrochemical potential, going beyond the simplest consideration of the electrochemical potential and second the role of modelling the solvent.

The following section reminds the reader of the basics of modelling electrochemistry, before discussing the advantages and limitations of the two schemes applied herein: the simple linear free energy relationship for the electron chemical potential (LFER-EP), popularized by Norskov and coworkers and the explicit change of the electrochemical potential through charging the surface and neutralizing the simulation cell with a homogeneous background charge (SC) as developped by Filhol and Neurock. After this methodological discussion, the results for aprotic CO_2 reduction as described by the two approaches are presented to illustrate the influence of the applied electrochemical potential

View Article Online
PCCP Paper

and the solvation effects simultaneously. With the SC method, we investigate the origin of the selectivity of Ni(111) to produce carbon monoxide and carbonates rather than oxalates.

2 Methods

Computational modelling of electrochemistry is hampered by the simple fact that the electrode potential is not a natural variable in quantum chemical computations. Most chemists are used to think in the "constant charge" picture, *i.e.*, the number of electrons is not fluctuating during a reaction. Since each species with a given number of electrons corresponds to a different electrochemical potential, the "constant charge" picture is inadequate for electrochemistry, where all the intermediates should be treated at the same potential. For example, CO_2 adsorbed on a metal surface corresponds to a different potential than CO and O co-adsorbed on the same surface. Hence, to get the correct reaction energy, the charge on the surface for adsorbed CO_2 and CO, O needs to be adapted individually to reach the desired potential. Therefore, an electrochemical half-cell is effectively a grand-canonical ensemble where the number of electrons is adapted according to the electrochemical potential in a different way for different intermediates of an electrochemical reaction. The most realistic approach would be to account for solvent molecules and explicit counterions, but this approach is computationally very demanding, requiring large unit cells together with statistically meaningful sampling of the solvent and counterion positions. To overcome this challenge, more approximate schemes have been developed, where the counter-charge is introduced as some idealized distribution in the unit cell (*vide infra*).

2.1 Basics of electrochemistry

To set the stage, this section gives a brief reminder of the basic text book equations in electrochemistry, starting with the standard Gibbs energy of reaction $\Delta_r G^{\ominus}$

$$\Delta_r G^{\ominus} = -nFU^{\mathrm{SHE},\ominus} \quad (1)$$

where n is the number of electrons transferred, F the Faraday constant and $U^{\mathrm{SHE},\ominus}$ the standard reduction potential referenced to the standard hydrogen electrode (SHE).

The SHE is an ideal electrode which is immersed in an aqueous solution with a H_2 and H^+ activity of unity and a zero overpotential for hydrogen evolution, which corresponds to the following definition

$$2H^+ + 2e^- \rightleftharpoons H_2 \quad \Delta_r G^{\ominus} = 0.0 \text{ at } U^{\mathrm{SHE}} = 0 \text{ V} \quad (2)$$

It is with respect to this idealized electrode reaction that formal "half-cell" potentials are commonly defined.

By definition, the reduction occurs at the cathode and the oxidation at the anode, yielding the cell potential $U^{\ominus}_{\mathrm{cell}}$

$$U^{\ominus}_{\mathrm{cell}} = U^{\ominus}_{\mathrm{cathode}} - U^{\ominus}_{\mathrm{anode}} \quad (3)$$

Away from standard conditions, it is most straight forward to compute first $\Delta_r G$ of the reaction and then convert it back into a potential, also known as electromotive force, using the universal equation

$$U_{\mathrm{cell}} = -\frac{\Delta_r G}{nF} \quad (4)$$

For spontaneous reactions, $\Delta_r G$ is negative and hence U_{cell} is positive.

When applying an electrochemical potential, it is helpful to work with the following equation

$$\Delta_r G(U^{\mathrm{SHE}}) = -nF(U^{\mathrm{SHE},\ominus} - U^{\mathrm{SHE}}) = \Delta G^{\ominus}_r + nFU^{\mathrm{SHE}} \quad (5)$$

where U^{SHE} is the imposed potential and $U^{\mathrm{SHE},\ominus} - U^{\mathrm{SHE}}$ is, in general, the over- or underpotential.

The SHE is inconvenient for computational purposes, as simulating the hydrogen evolution under realistic conditions and measuring potentials relative to this half-cell are extremely cumbersome. Therefore, the common computational reference state is vacuum: on the "vacuum scale", the energy of an electron in vacuum is defined as zero and all the attractive energy comes from interactions with the nuclei. This scale is often called the "absolute" scale for redox potentials; we will stick to the unambiguous term "vacuum scale".[66]

A concept closely related to the electrode potential on the vacuum scale is the workfunction W. The workfunction is the energy required to remove one electron from a surface, *i.e.*, we can understand the workfunction as the ionization energy. For metals, the electron affinity and the ionization energy have the same value with opposite signs. Since the vacuum scale sets the energy of the electron in a vacuum to zero, the chemical potential of the electron (μ_e) in the electrode is equal to minus the workfunction, whereas the workfunction is identical to the electrochemical potential, U^{vac}. Hence we might write

$$W = U^{\mathrm{vac}} = -\mu_e \quad (6)$$

Of course, the "experimental scale", U^{SHE}, and the vacuum scale, U^{vac}, are related. IUPAC recommends[67] to assign a value of $U^{\mathrm{vac}} = 4.44$ V to the standard hydrogen electrode.[70] Accordingly, we easily switch from one scale to the other using $U^{\mathrm{vac}} = U^{\mathrm{SHE}} + 4.44$ V as illustrated in Fig. 1. The remaining question is how a given computation is connected to one or the other scale.

2.2 Linear free energy relationship for electrochemical potentials

The linear free energy relationship for accounting for the electrochemical potential, LFER-EP, is the zeroth order level to treat electrochemical reactions, since it accounts exclusively for the energy of the transferred electron. The premise is that elementary reaction steps can be devided into chemical steps (where the composition of the system remains constant) and electrochemical steps, where the number of electrons changes due to adding/removing an electron and its cation (*e.g.*, $Na^+ + e^- \rightleftharpoons Na_{(s)}$ or the more typical $H^+ + e^- \rightleftharpoons \frac{1}{2}H_2$). The LFER-EP has been introduced by Norskov and coworkers in the formulation of the computational hydrogen electrode (CHE).[35] Throughout this article, we will use LFER-EP for the generalization of the CHE to other cations than the proton.[36] However, in this section,

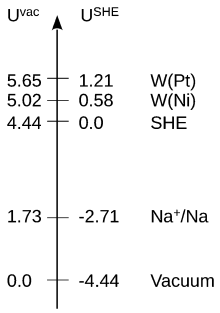

Fig. 1 Scales of the electrochemical potential in volts with respect to the vacuum (left) and to the standard hydrogen electrode (right). The experimental Na/Na^+ redox couple and the computed workfunction of Ni(111) and Pt(111) are given as examples.

the characteristics of the LFER-EP are discussed with the example of the CHE.

The model and assumptions of the CHE are summarized in the following:

1. Electronic energies are only required for electroneutral entities and thus do not depend on the electrochemical potential. When evaluating the potential dependence of reaction energies, these "zero charge" results give the reaction energy at 0 V *vs.* SHE.[71]

2. Electron transfers are always coupled to proton transfers and no charged systems are involved. Therefore, processes that have no direct involvement of counterions (*e.g.*, $Fe^{3+}(cp)_2 + e^- \rightarrow Fe^{2+}(cp)_2$ with cp = cyclopentadienyl) cannot be studied straightforwardly.

3. The applied electrochemical potential only affects the electrochemical steps, *i.e.*, the proton coupled electron transfers.

4. The correction for the applied potential is derived from: $\Delta G_{H^+ + e^-}\left(U^{SHE}\right) = \frac{1}{2}\Delta G^{\ominus}_{H_2} - qU^{SHE}$. In other words, the energy of the electron in the electrode is equal to $-qU^{SHE}$, where q is the fundamental charge involved in the electrochemical step.

5. The choice of the reference electrode and how it is coupled to the system under consideration imply that the solvent is water and that the hydration energy of a proton is neither influenced by the electrochemical potential nor by the electrolyte.

To summarize, the computational hydrogen electrode allows us to account for the nominal potential dependence of an electrochemical reaction, *i.e.*, to account for the last term of eqn (5), *nFU*. However, it disregards any influence of the interaction between species and the electrode itself at a specific potential, *i.e.*, it describes the correct physics for solution phase electrochemistry, but it is an approximation for the elementary reaction steps on an electrified interface where the number of electrons is variable in order to keep the potential constant. Despite these limitations, the LFER-EP is not only extremely simple to apply (being an *a posteriori* correction to "standard" computations), but also the first step in any scheme improving on the LFER-EP.

2.3 Beyond the linear free energy relationship: the surface charging method

Any method aiming to improve over the LFER-EP has to take the specific interactions between adsorbates and the electrified electrode explicitly into account, lifting assumptions 1–3 in the CHE (*vide supra*) by introducing $\Delta G_r^{elec}(U)$. The superscript "elec" indicates that the electronic contribution, originating in polarization and charge-transfer, to the free energy is included. The simplest approach to assess the importance of the applied electrochemical potential on the energies of adsorbates would be to apply an electrical field in the simulation cell.[72–74] However, the surface charge density q_{surf}, needed for obtaining the electrochemical free energy, is tricky to evaluate.[75]

Schemes that account for all relevant free energy changes alter, therefore, the number of electrons in the system explicitly[46,48,49,51–53,76] and work with the grand-canonical energy expression for all the surface adsorbed species. The potential dependent free energy of the surface $G_{surf}(U^{vac})$ is given by

$$\begin{aligned}\Delta G_{surf}(U^{vac}) &= \Delta E^{elec}_{surf}(U^{vac}) - q_{surf}(U^{vac})FU^{vac} \\ &\approx \Delta E^{elec}_{surf}(U_0) - \tfrac{1}{2}C(U^{vac} - U_0^{vac})^2 \end{aligned} \quad (7)$$

with $\Delta E^{elec}_{surf}(U^{vac})$ being the electronic energy at potential U^{vac} and q_{surf} is positive if electrons are removed and negative when electrons are added, *i.e.*, q_{surf} is the surface charge density of the system and U^{vac} is the vacuum scale potential of the electrode. The reasoning behind eqn (7) is that electrons removed from the system are transferred to the electrode which serves as the reservoir of electrons at the potential U^{vac}. Similarly, adding an electron from the electrode is associated with the energetic cost of removing the electron from the reservoir. The approximate equality refers to the quadratic development of the electronic free energy,[76,77] which can serve to introduce the notion of the capacitance C of the surface and simplifies the link between SC and LFER-EP results. Assuming a constant capacitance for a given surface (which is often a reasonable first order approximation[78]) the results of LFER-EP and eqn (7) are identical at the potential which corresponds to the average of the zero charge potentials (U_0), *i.e.*, the workfunctions. Note that in the SC model the capacitance C is not an "external" constant: its value, which corresponds to the curvature of the parabola (*vide infra*), is determined for each system independently and is thus quite different in a vacuum than in implicit DMF. Furthermore, as can be seen in Fig. 6, the capacitance weakly depends on the adsorbate: the binding energy difference between two adsorbates (*e.g.*, $2CO_2$ *vs.* CO, CO_3) is not simply a straight line as would be the case if the capacitances of the implicated systems were equal.

The different surface charging schemes (*e.g.*, neutralization with a homogeneous background-charge as developed by Filhol and Neurock[46,52,76] or Otani's implicit counterelectrode[48,53]) have a different way to obtain the first term of eqn (7), *i.e.*, $\Delta E^{elec}(U^{vac})$, while the second term is, essentially, the same as the one needed for the nominal potential dependence, introduced in the previous section. Here, we will apply the surface charging method in the formulation by Filhol and Neurock which we abreviate by SC.[76]

View Article Online

The two main advantages of these general approaches are (a) Proper potential alignment: since these methods work with the vacuum scale potential, assessed through workfunctions, the potential of all the systems is referenced to vacuum and properly aligned, *i.e.*, changes in the workfunction due to adsorptions and reactions are fully taken into account. (b) Decoupling of electrons and counterion transfer: eqn (7) does not make use of any counterion. Hence a potential dependence of a system where only an electron transfer has occurred is easily accessible. For example, the potential dependence of CO_2 adsorption is readily evaluated with such a scheme, while it is a constant within the LFER-EP framework. To be explicit, the clear distinction between "chemical" and "electrochemical" steps makes place for a "gradual, nuanced" description, where the electrochemical potential fixes an electrode polarization, which requires a specific surface charge density, q_{surf}. Hence, the coupled electron cation transfer, which could be reasonably described by LFER-EP and be a good approximation in the case of covalent bond formation (*e.g.*, C–H), becomes a special case, while in general the surface charge changes by a characteristic value for a given elementary reaction.

The energy of the reactants in the formally electrochemical steps are obtained like in the LFER-EP approach, *i.e.*,

$$\Delta G_{X+e^-}(U^{vac}) = \Delta G_X + q(U_X^{vac,\ominus} - U^{vac}) \quad (8)$$

where, $U_X^{vac,\ominus}$ can be either obtained from the experiment (*e.g.*, 4.44 V for $\frac{1}{2}H_2$) or from the computed workfunction (*e.g.*, 2.74 V for Na(100) in a vacuum). The advantage of the later approach is that the workfunction of an uncharged sodium surface can be computed under the specific computational conditions, *e.g.*, using the same solvent model, giving a "consistent" description. Of course, this standard redox-potential can also be applied in the LFER-EP.

3 Model

The electroreduction of CO_2 under aprotic conditions opens up several reaction channels. Herein, we investigate the C–C coupling of CO_2, leading to oxalates

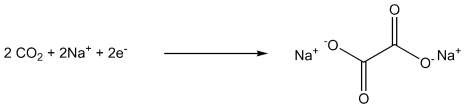

and the dissociation reaction of CO_2 into CO and adsorbed oxygen. Under electrochemical conditions, the surface bound oxygen may further be reduced to carbonate

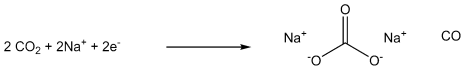

Both products are, in principle, competitors in any reaction where CO_2 is reduced electrochemically, *e.g.*, formic acid or hydrocarbon formation[8,9,11,12,14,15] and are therefore worth studying in order to, subsequently, assess the selectivity of the target reactions. However, under the studied aprotic conditions, no formic acid or hydrocarbons can be formed.

As far as simulations are concerned, the aprotic solvent DMF has the advantage compared to water that it is non-reactive and that no specific interactions (H-bonds) are expected between the solvent and the solute, but the disadvantage that its size is considerably larger, pushing simulations with meaningful explicit layers of DMF beyond our present capabilities. However, the average effect of the solvent, *i.e.*, increased capacitance, might be captured well enough by an implicit solvent model, which avoids the ambiguities in choosing a structure for the static solvent layers as usually proposed when including solvent effects.[46] Therefore, our study investigates the combination of implicit solvent treatment and explicit accounting of the electrochemical potential. Although this model is far from perfect (the double layer is grossly approximated by the homogeneous background charge and there are no explicit solvent molecules), to the best of our knowledge, it is the state of the art that can be done with publicly available, well established, periodic DFT codes.

We model the catalyst surface by the Ni(111) facet and the solvent by a continuum with a relative dielectric constant (ε) of 37.2, characteristic of DMF. The latter is also very close to the one of another typical aprotic solvent for electrochemistry, acetonitrile (ε = 37.7). The results will hence be generally applicable to aprotic solvents with a high dielectric constant. Vlachos and co-workers concluded that the water gas shift reaction, which involves chemisorbed CO_2 and co-adsorbed CO and O, similarly to systems reported herein, yields overall similar results at the Ni(111) surface or the Ni(211) facet.[79] Therefore, we have limited ourselves to the ideal Ni(111) surface. In order to gain a more complete understanding, simulations over different surfaces and the determination of activation barriers should be considered, but these investigations are beyond the scope of this study.

Experimentally, the electroreductive coupling of CO_2 to alkenes is carried out with a sacrifying aluminum or magnesium electrode.[16–18] Computationally, the monovalent sodium cation is more convenient than the di- or trivalent cations and the redox potential is comparable. Therefore, we model the counterion by Na^+. For example, carbonate is simulated as Na_2CO_3 instead of $Al_2(CO_3)_3$. The solvation energy of Na^+ is predicted to be −3.14 eV by the implicit solvation model. At the equilibrium potential, the energy of Na^+ in solution is equal to the energy of Na on the metallic sodium surface, *i.e.*, the solvation energy is roughly compensated by the workfunction. The solvation energy provided by the implicit solvent model is, thus, fairly consistent with the workfunction of sodium metal (2.7 V) but underestimated compared to the 4–4.5 eV expected based on experimental data and cluster-continuum data in a similar solvent.[80] Considering that Na^+ is co-adsorbed on the surface (or embedded in the salt solid) and therefore never "fully solvated" and its energy is obtained from the workfunction of solid sodium, we did not try to improve the description of Na^+ by including explicit solvent molecules. Furthermore, the incurred error has an undetermined sign and magnitude compared to the experimentally relevant Al^{3+} or Mg^{2+}.

View Article Online
Paper PCCP

The salts (Na_2CO_3 and $Na_2C_2O_4$) are modelled as crystals with two chemical formulas per unit cell. These models are derived from experimental crystal structures[81,82] and are fully optimized.

To assess the window of the electrochemical stability of Na^+ under our conditions, there is, on the one hand, a workfunction of sodium ($\sim$2.7 V), which assures the formal stability of Na^+ down to about −1.8 V *vs.* SHE with respect to the formation of solid sodium. On the other hand, Na^+ adsorption on Ni(111) is positive (*i.e.*, unstable) within this potential window (*vide infra*, Fig. 2). Hence, Na^+ is, indeed, the relevant chemical species under the simulated conditions.

4 Computational details

The metal surface is modeled as a symmetric $p(3 \times 3)$ Ni(111) slab with a lattice constant of 3.52 Å and a thickness of 5 layers (the middle layer is frozen in its bulk position), in a periodic box of 37.35 Å. The spin-polarized electronic structure is described at the PBE level,[83] with an energy cut-off of 400 eV for the plane-wave basis set. The electron–ion interactions are described by the PAW formalism.[84,85] All computations are performed with VASP 5.3.3.[86,87] Accounting for solvation effects is achieved by exploiting the implicit solvation model[26,88] as implemented by Hennig and co-workers under the name VASPsol.[64] In this model, the electrostatic interaction with the implicit solvent is computed based on a linear polarization model, where the relative permittivity of the medium is a continuous function of the electron density. A switching function around a specified isodensity value is used to vary the relative permitivity from 1 (well "inside" the surface metal atoms) to the solvent bulk value far away from the surface. This modified Hartree potential is obtained by solving the modified Poisson equation. Hence, the polarization of the system due to the solvent is included self-consistently. In order to get numerically stable results for the potential in empty space, the surface tension was set to zero (no cavitation energy) and the critical density value was reduced to 2.5×10^{-4} e Å^{-3}. The dielectric constant of DMF was set to 37.2. Note that when we started this study, VASPsol was incompatible with non-local van der Waals density functionals and we did therefore not apply them. Since we are mainly comparing two electrochemical approaches, we do not expect to obtain qualitatively different conclusions upon accounting for weak non-bonded interactions. All geometries were optimized to reach a gradient smaller than 0.05 eV Å^{-1} with wave functions converged to 5×10^{-5} eV. The precision setting of VASP is set to "normal" and the automatic optimization of the real-space projection operators is used.

The energy of the sodium cation is obtained according to eqn (7) with the energy of an atom in bulk sodium (ΔG_{Na}) and the workfunction of the Na(100) surface ($U_{Na}^{vac,\ominus}$ is 2.74 V in a vacuum and 2.67 V in implicit DMF).

In the SC method, the system is charged and N_e electrons are present in total instead of the neutral N_0 number. In order to reach an overall neutral cell, a uniform background charge of the opposite sign is applied. This uniform charge is also present in the metal slab itself, where it is screened by the metal. Hence, the "effective" applied charge is reduced and the DFT energy must be corrected accordingly. The correction suggested by Filhol and Neurock[46,52,76] reads

$$G^{elec}(U^{abs}) = E_{DFT}(N_0) + \frac{z_0}{Z}(E_{DFT}(N_e) - E_{DFT}(N_0)) + \frac{z_0}{Z} q \int_{N_0}^{N_e} V_a(N_e) dN_e + U^{abs}(N_e - N_0) \quad (9)$$

where U^{abs} is the workfunction for the system with N_e electrons and N_0 is the number of electrons for the neutral system. Z is the interslab repeat vector of one supercell (z-direction) and z_0 is the segment along this direction not occupied by the metal slab (the radius of the atoms is derived from the lattice constant), therefore $\frac{z_0}{Z}$ (in our setup $\frac{z_0}{Z} = 0.703$) gives the ratio of the space in which the homogeneous back-ground charge is "active", *i.e.*, not screened by the metallicity of the slab. This "screening" concerns $(N_e - N_0)\left(1 - \frac{z_0}{Z}\right)$ electrons. q is the elementary charge and the integral approximates the interaction energy of the homogeneous background with the system in order to remove this spurious interaction. The interaction is estimated from the electrostatic potential V_a, in the middle between the two symmetric surfaces, which is taken to be the energy of the "vacuum", *i.e.*, it is also used to compute the workfunction. Note that even though we are using the symbol G for the free energy (to emphasize that the free energy change due to electron transfer is taken into account) eqn (9) would need to be supplemented by the standard terms accounting for translational, rotational and vibrational degrees of freedom in order to be a "proper" Gibbs energy. When discussing the results, we will thus refer to "adsorption energies" and not "adsorption free energies", although they are "electronic free energies".

Energies were obtained for at least 5 different charges for each system. Subsequently, a parabolic fit was used for accessing arbitrary potentials. The same procedure is applied to get the effective charge $q_{surf}(U)$ at an arbitrary potential. These data are used to evaluate the charge injection $\Delta^{ads}q(U) = (q_{surf}^{slab}(U) + N^{mol}) - q_{surf}^{system}(U)$ for a given reaction, where N^{mol} is the sum of the electrons in the isolated molecules (the counterion, Na^+, is considered as a charged species) adsorbed on the surface. A script for automating these tasks is available in the supplementary information. Whenever technically possible, the charges were chosen to obtain an interpolating parabola between −2 and 1 V (*vs.* SHE). Depending on the system this was not possible, as in the highly (negatively) charged systems the required electrons are not bound on the surface anymore but spilling out into the "vacuum", filled with the background charge. In these situations, eqn (9) is not applicable anymore, which is seen as strong deviations from the parabolic behavior.

5 Results and discussion

CO_2 electrolysis under aprotic conditions is reported to yield CO and carbonate or the C–C coupling product, oxalate, depending

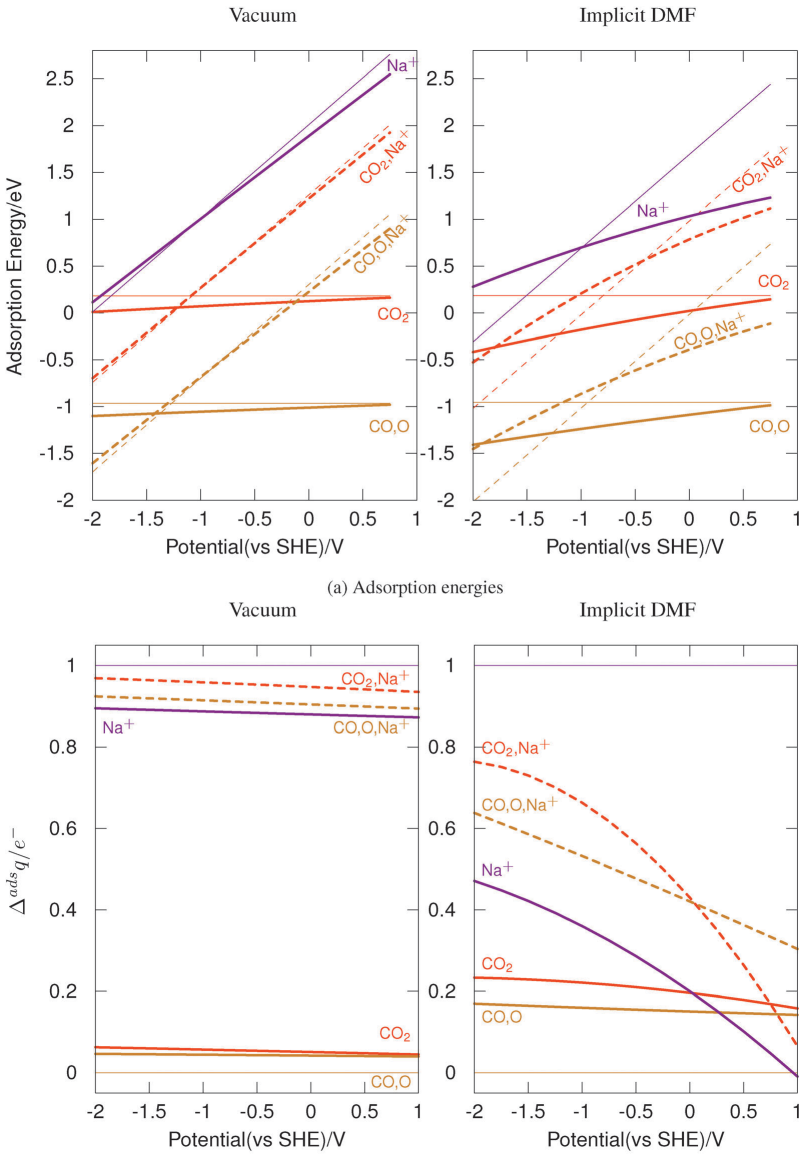

Fig. 2 Adsorption (top) and associated charge injection (bottom) upon adsorption of Na^+(purple) and of CO_2 on Ni(111) as a function of electrochemical potential in a vacuum (left) and implicit DMF (right). Two adsorption modes are compared for CO_2: the intact chemisorption (red) and the dissociative adsorption (*i.e.*, CO and O co-adsorption, brown). Broken lines indicate the co-adsorption with Na^+. The thin lines refer to the LFER-EP, while the thick lines are computed with the SC method.

on the electrode material. We therefore start by investigating the adsorption of the reactant, CO_2, and its dissociation into co-adsorbed CO and O. Then we consider the influence of CO_2 coverage and the formation of oxalate, competing with the one of carbonate and carbon monoxide. Investigating this intrinsic reactivity of CO_2 under aprotic, reductive conditions will not

View Article Online

Paper PCCP

only be helpful to understand the mechanism and selectivity of the carboxylation reaction of alkenes under similar conditions, but serves equally well to determine the level of modelling necessary to conduct such mechanistic studies for reactions where experimental results are scarce.

We compare the simple linear free energy relationship for the electrochemical potential (LFER-EP) to the more advanced surface charging (SC) method. As explained above, LFER-EP does not describe the polarization of the surface and imposes a strict coupling of the Na^+ and e^- transfer. In contrast, the SC model polarizes the surface according the the electrochemical potential and electron transfer occurs also in the absence of a cation transfer. Hence, under strongly reducing conditions SC and LFER-EP may differ significantly and SC is potentially more convenient: the cation (Na^+) has no well defined place in the reduced species (in contrast to the proton which forms regular C–H and O–H bonds), but has to be introduced in LFER-EP, while it might not be necessary in SC.

The adsorption of CO_2 together with the preferred adsorption mode of oxalate on Ni(111) as a function of potential will be used to assess the limitations of LFER-EP in practice and the role of the solvent. Having established the consequences of the improved description of SC compared to LFER-EP, we investigate the coverage effect on CO_2 dissociative adsorption and elucidate the origin of the selectivity of CO and carbonate rather than oxalate formation over Ni(111).

5.1 Comparison of the potential dependence of adsorption energies in a vacuum and an implicit solvent

Fig. 2 shows the energetics and associated charge injection $\Delta^{ads}q$ in the case of CO_2 and Na^+ adsorption on Ni(111) as a function of electrochemical potential in a vacuum (left) and when accounting for solvent effects through an implicit solvent (right). The charge injection is defined as the net charge applied for the considered potential for the chemisorbed system minus that of the bare Ni(111) surface. It hence corresponds to the extra charge that needs to be injected in the presence of adsorbed species to maintain the potential constant. The LFER-EP framework is characterized by the distinction of elementary steps into "chemical" and "electrochemical" steps. The former are rearrangements of nuclear coordinates, while the latter involve addition/substraction of an electron and its counterion, *e.g.*, $Na^+ + e^-$. Since electron and cation transfer are strictly coupled, the injected charge is simply 1 e^- for electrochemical steps and 0 for chemical steps. As a consequence, only the reaction energies of electrochemical steps depend on the potential within the LFER-EP approach. Furthermore, all systems are electroneutral. Within the SC model, however, the number of electrons in the system is individually adapted to every intermediate to tune the work-function to the specified level. Therefore, the chemical and electrochemical steps are no longer formally separated from each other. In the text we will frequently refer to "oxalate" or "carbonate" for species adsorbed on the surface. These adsorbates do not necessarily have the "net" charge of the corresponding solution species: the adsorbate and the electrode form one system and the (surface) charge is a continuous function of the electrochemical potential.

We start the comparison of the two methods for including the electrochemical potential first in a vacuum and only in a second stage when accounting for solvent effects.

As a first example for a chemical step, consider the adsorption of CO_2 in the absence of Na^+ co-adsorption: by construction, LFER-EP yields an adsorption energy which is independent of the potential and the injected charge is strictly 0. However, when co-adsorbing CO_2 with Na^+, we are confronted with an electrochemical step within the LFER-EP framework, since cation and electron transfer are coupled. The adsorption energy as a function of potential has a slope of one, corresponding to the coupled electron transfer. In the case of the SC model, the surface charge adapts to the potential. However, since charges are not well stabilized in a vacuum, the charge variations compared to LFER-EP (strict coupling of electron and cation transfer), obtained with the surface charging method, are almost negligible (Fig. 2b): the maximum difference occurs for Na^+ where the charge injection is $\sim$ 0.9 instead of 1. The number of injected electrons is the main factor determining the potential dependence: according to eqn (5) the slope of $\Delta G(U)$ is, to first order, proportional to the number of electrons injected. The inability of vacuum to stabilize charges implies that minor charge variations change the potential considerably, leading to very small free energy changes due to potential alignment effects. Since at the same time the electrons are only marginally better stabilized in one system than in the other (*e.g.*, on CO_2@Ni(111) compared to the bare surface), the adsorption energies barely change compared to the zero charge (LFER-EP) results. In a vacuum, the systems are thus effectively electroneutral and introducing a counterion is strongly coupled to an electron transfer. Hence, the potential dependence for the more detailed SC method is very similar to the simple LFER-EP method, *i.e.*, adsorptions in the absence of Na^+ are basically horizontal lines, while the reductive Na^+ adsorption or co-adsorption leads to a strong potential dependence with a slope of $\sim$1. Therefore, in a vacuum, where charge accumulation at metals is small, the LFER-EP is a very reliable approximation.

Accounting for solvent effects leads to a very different picture when explicitly tuning the electrode potential, while the LFER-EP lines are quite similar to the ones in a vacuum: on Fig. 2a (right) slopes of the thin lines are unchanged by construction, while intercepts are only affected in the case of Na^+ adsorption where the charge distribution is somewhat stabilized by the polarizable solvent. When applying the surface charging method, the dielectric medium stabilizes charges at the interface, especially in the presence of adsorbates and as a result the injected charge significantly deviates from the ideal values of zero or 1. Equivalently one might say that the dielectric medium increases the capacitance of the system. For chemisorbed CO_2 or CO, O, the injected charge is significantly enhanced by the solvent, up to a value of $\sim 0.2e^-$, and hence the adsorption energy depends on the potential with a marked stabilization at negative potentials, where CO_2 or CO accumulates a negative charge, which is stabilized by the solvent (Bader charges on the

View Article Online

adsorbate as a function of potential and the solvent can be found in the ESI†). Such a potential dependence is obviously absent in the LFER-EP. Hence, the two methods considerably deviate in the presence of a solvent. For example, at $U = -1$ V CO_2 is underbound by 0.4 eV compared to the SC method, which gives an exothermic reaction for CO_2 adsorption below 0 V.

Assuming a constant capacitance (C, see eqn (7)), lines for SC and LFER-EP cross at the average zero charge potential, *i.e.*, at the potential that corresponds to the average of the work-function of the neutral systems. Note that such an assumption is not involved in the SC model, but might be made for interpretative purposes. For example, the workfunction of Ni(111) and CO_2@Ni(111) is 0.58 and 1.39 V *vs.* SHE in implicit DMF, respectively (see ESI†). Hence, the thin and thick full orange-red lines in the graph on the right of Fig. 2a are expected to cross at 0.99 V. Indeed, at 0.75 V (the limit of the x-axis in Fig. 2a), the two lines almost cross. The good agreement between the constant C prediction and the actual crossing point gives credibility to the approximation of constant capacity when comparing similar systems. Furthermore, this observation justifies to call the potential at the crossing point the effective potential to which the LFER-EP results of non-electrochemical steps correspond to. Hence, the LFER-EP results for CO_2 adsorption in the absence of Na^+ co-adsorption correspond to an effective potential of almost 1 V, which is very far from the reducing conditions of interest herein.

The potential dependence of the Na^+ assisted adsorptions is also considerably modified by the solvent. The injected charge is markedly lower than 1 for Na^+ adsorption since the polar solvent stabilizes the partial positive charge on Na. This can be easily explained considering a particular case. Neutral Na@Ni-(111) corresponds to a potential of −2.6 V. At this potential, the bare surface is, however, not neutral, but effectively charged by 0.5 e^- for a $p(3 \times 3)$ super cell. Hence, the injected charge to reach the neutral Na@Ni(111) is only 0.5 e^-. The co-adsorption of Na^+ and CO_2 combines the effects described above and the charge injection (although not complete to −1) reaches $\sim$0.75e^- at strongly reducing potentials. In other words, Na^+ adsorption is not coupled anymore with a full electron transfer and we are dealing with a somehow solvated Na^+ and partially reduced carbon dioxide. Similarly, in the case of CO_2 dissociation, there is only a rather weak potential dependence. Nevertheless, in both competing reactions, we clearly obtain a stronger potential dependence in the presence of the counterion than in its absence, demonstrating the stabilizing capabilities of counterions without imposing counterion-coupled electron transfers, provided that ionic species are stabilized in a dielectric medium. The partially injected charge under realistic solvent conditions and its deviation from the ideal values of 0 or 1 have strong consequences on the slope of the adsorption energy as a function of potential energy, which markedly differs between the two methods as seen on Fig. 2a right. Obviously, in the presence of a high dielectric constant solvent, the LFER-EP is not anymore a reliable approximation to evaluate adsorption energies.

5.2 Preferred surface species and coverage dependence of CO_2 adsorption

In the following section, we will focus more closely on the nature of the preferred surface species as a function of electrochemical potential. Independent of the scheme and conditions, the dissociative adsorption of CO_2 into CO and O is favored by at least 1 eV at low coverage (1/9 ML), motivating us to investigate higher coverages. Increasing the coverage also allows us to model carbonate and oxalate formation since they require at least two CO_2 molecules in the unit cell, which corresponds, in our case to a coverage of 2/9 ML.

As seen in the previous section, SC delivers a more general description of the electrochemical systems than LFER-EP, provided solvation is included. Here, we are discussing the extreme case of dissociative adsorption of CO_2 in the absence of Na^+ co-adsorption as a function of surface coverage. By construction, LFER-EP gives constant adsorption energies for these reactions. Furthermore, CO, O co-adsorption at zero charge has a workfunction of 1.37 V *vs.* SHE. Hence, the LFER-EP results for the dissociative adsorption correspond to an effective potential of about 1 V, just like CO_2@Ni(111) (*vide supra*). This oxidative potential is far from the potentials of interest herein and we will thus not consider LFER-EP any further in this section. In the SC model, we can compute the Bader charges as a function of potential (see ESI†). This analysis reveals that the charge on the surface bound oxygen varies less than the charge on CO when lowering the potential: the oxygen is already negatively charged like in a surface oxide and does not accept significantly more electrons. CO_3 is, on the other hand, a rather powerful electron acceptor and hence the injected charge is significantly higher when a CO_2 is coupled to a surface oxygen atom instead of being dissociated into CO, O (blue compared to brown lines in Fig. 3b). With the solvent taken into account, the charge injection reaches up to 0.5 electrons for carbonate at the highest coverage considered. This significant charge injection goes along with a dramatic stabilization of the species at reducing potentials, not only compared to the LFER-EP results, but also compared to other surface bound species. For example carbonate and CO at high coverages (full, blue line in Fig. 3b) get more stable than dissociated CO_2 at 2/9 ML (broken, brown line) at potentials < -1.2 V.

This comparison shows that solvent effects are crucial for the prediction of relative stabilities under electrochemical conditions and for allowing rather decoupled electron transfers. Hence, for chemical conclusions only SC results with a solvent description are discussed.

Increasing the CO_2 coverage from 1/9 to 3/9 ML (see Fig. 3a) goes along with a reduced tendency (per CO_2 molecule) to dissociate CO_2. Dissociative CO_2 adsorption is even endothermic at a coverage of 3/9 ML for potential > -0.5 V, while at 2/9 ML the CO_2 dissociation is exothermic, but already less than twice the value for 1/9 ML. Comparing the dissociated systems with the ones where carbonate is formed ($CO_2 + O \rightarrow CO_3$), a contrasting picture emerges. At a coverage of 2/9 ML carbonate formation (without counterions) is still disfavored at all potentials considered,

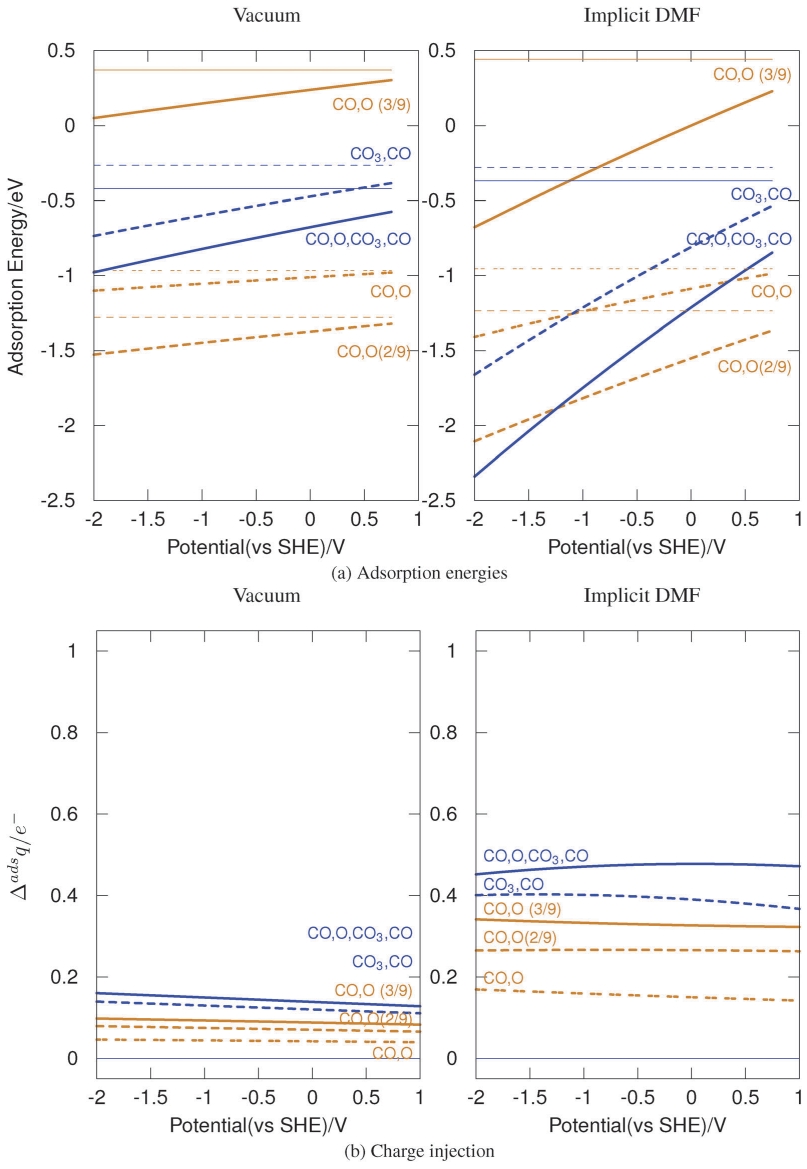

Fig. 3 Total adsorption energies (top) and associated charge injection (bottom) of one, two and three CO_2 on Ni(111) as a function of electrochemical potential. The adsorbed species are derived from dissociated CO_2, *i.e.*, CO and O (in brown), and at higher coverages, CO and CO_3. Three coverages are considered: 1/9 ML (spaced broken lines), 2/9 ML (broken lines) and 3/9 ML (full lines) in a vacuum (left) and implicit DMF (right). The lines in blue correspond to systems where one CO_2 has reacted with a surface adsorbed oxygen atom to give CO_3. Thin lines refer to LFER-EP and thick lines to the SC method.

but if a coverage of 3/9 ML is imposed, carbonate formation is expected even at mildly positive potentials. Furthermore, since the full blue line crosses the broken brown line in Fig. 3a right, the thermodynamically preferred state switches with the potential: from dissociated CO_2 at an intermediate coverage (2/9 ML) for potentials > -1.2 V to carbonate and dissociated CO_2,

yielding higher coverages (3/9 ML), for potentials <-1.2 V. The latter is in fair agreement with the report of carbonate formation starting around -1.5 V.[15,19,89] Nevertheless, even at 3/9 ML coverage, the dissociative adsorption of CO_2 is exothermic at potentials below -0.5 V in solution, suggesting that CO might generally be a relevant intermediate in CO_2 reduction over Ni, *e.g.*, even for C–C bond formation with alkenes.

From a chemical point of view we have learned two lessons: first, CO_2 has a strong thermodynamic tendency to dissociate on Ni(111) at any potential considered. Nevertheless, strongly reducing conditions are required to desorb reduced products (*vide infra*), *i.e.*, the dissociation at anodic potentials is not catalytic but just poisoning the catalyst surface. This tendency to dissociate CO_2 is well in line with the frequently reported CO production during CO_2 electroreduction over Ni[15,19,89] and the use of Ni as a catalyst at the cathode of solid oxide electrolyzers of CO_2.[90] Second, thermodynamically, the surface bound oxygen can be coupled to a second CO_2 molecule yielding carbonates – and carbonate formation is favored at reducing potentials and high surface coverage.

5.2.1 Adsorption mode of oxalate. Above, we have focused on CO_2 dissociation and the formation of a C–O bond. As an alternative, the reductive dimerization, *i.e.*, the C–C bond formation yielding oxalate, has to be considered. When comparing the relative stability of C_2O_4 with CO_3, CO on Ni(111) one finds that oxalates are much higher in energy than carbonates, which is largely due to the important CO adsorption energy. Nevertheless, the adsorption mode of oxalates serves as an example for a switch in the preferred adsorption mode (as opposed to a switch in the preferred surface species) as a function of electrochemical potential. Such a switch is, by definition, absent in the LFER-EP and thus illustrates the truly atomic, detailed understanding which is obtained with the SC method.

Fig. 4 displays the geometries of oxalates either adsorbed "flat", parallel, to the Ni(111) surface or slightly twisted, "perpendicular", creating a strong surface dipole and Fig. 5 shows their adsorption energies. The different magnitude of the surface dipole is also reflected by the workfunction, which is 1.52 and 1.78 V *vs.* SHE for the parallel and perpendicular adsorption mode, respectively. The first observation is that with or without implicit solvent, the parallel adsorption mode is favored in the zero charge picture, which is what would be discussed in the context of the LFER-EP. However, when accounting for the potential dependence of the two adsorption modes, a crossing is obtained: in a vacuum, quite reducing potentials (<-1.1 V) are necessary to stabilize the perpendicular mode. However, when accounting for the solvent, the situation is completely reversed: for potentials as high as 0.5 V the "perpendicular" mode is more stable, as now the charge accumulation "far" from the surface is stabilized by the solvent. In addition, the energy of the adsorbed species is markedly modified. For example, the surface charging method stabilizes oxalate by 0.7 eV at -1 V compared to the zero charge picture.

Unfortunately, this implies that the "zero charge" relative stabilities (here a difference of about 0.2 eV) are not necessarily representative for the relative stabilities under electrochemical conditions. Therefore, even for the "conformational search" the potential dependence would need to be accounted for. However, since this is associated with substantial effort, we have limited ourselves herein to the lowest adsorption energy at zero charge. Further studies will try to establish a rapid prescreening or a "predictive" scheme which exploits the workfunction differences between competing adsorption modes in order to identify the structures for which computing the potential dependence is warranted.

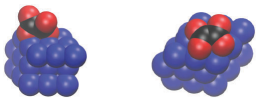

Fig. 4 "Perpendicular" and "parallel" adsorption modes of oxalate (C_2O_4) on Ni(111) on the left and right, respectively.

5.3 Reaction energies for carbonate and oxalate formation

Carbonates are possibly formed at high coverages, even in the absence of counterions. On the other hand, the simplest C–C coupling product, oxalate, seems to lie at considerably higher energy. These findings raise the question: with the possibility of stabilizing counterions, would carbonate form quantitatively or could oxalate be dramatically stabilized?

To start with, we consider the reaction energy of the overall reactions starting from CO_2 in the gas-phase

$$2CO_2(g) + 2(Na^+ + e^-) \rightarrow Na_2CO_3(s) + CO(g)$$

$$2CO_2(g) + 2(Na^+ + e^-) \rightarrow Na_2C_2O_4(s)$$

yielding the $Na_2CO_3(s)$ and $Na_2C_2O_4(s)$ salts, which are, for computational efficiency, modelled by perfect periodic crystals (see section Models). These salts are dissolved by high dielectric solvents such as DMF. Hence, their true energy (*e.g.*, as ion pairs in solution) is lower than assumed herein. These reaction energies are given as a function of potential in thin broken lines in Fig. 6. For the sake of consistency with the adsorption energies discussed above, reaction energies are "electronic" energies, *i.e.*, neglecting zero-point and thermal corrections.

If the overall reaction is uphill at potential U, then the reaction is unlikely to proceed at room temperature. Hence, we first investigate the overall thermodynamics of the quantitative formation of crystalline sodium carbonate and sodium oxalate starting from CO_2, Na^+ and electrons at a potential U that is sufficiently reductive (see broken lines in Fig. 6). In the case of carbonates, the side product is carbon monoxide, which has to be desorbed from the surface in order to close the catalytic cycle. This step is endothermic by about 1.9 eV and therefore the formation of crystalline sodium carbonate requires a minimal potential of -1.25 V for the combined reaction to be exothermic, in reasonable agreement with the reported onset potential around -1.5 V.[15] Oxalate formation, on the other hand, is thermodynamically much more accessible: already at potentials lower than -0.6 V, the formation of sodium oxalate is thermodynamically feasible.

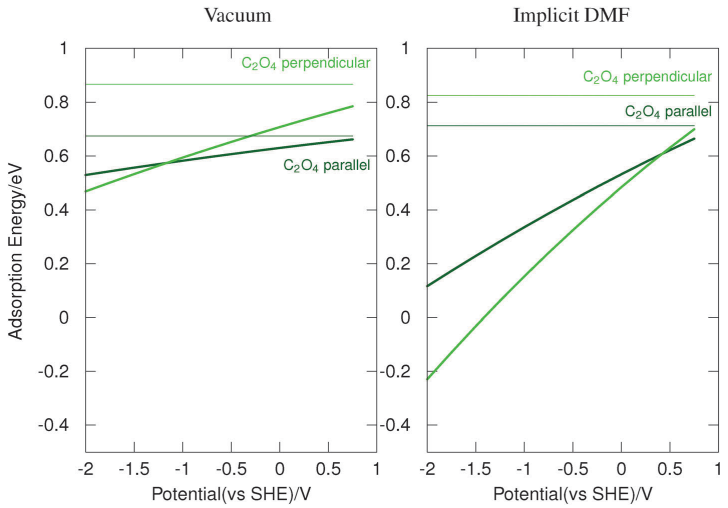

Fig. 5 Adsorption energies of two CO_2 molecules, in the form of oxalate as a function of electrochemical potential. The oxalate can be adsorbed "parallel" to the nickel surface (dark green) or perpendicular (green). Thin lines refer to the zero charge picture while broken lines refer to the surface charging method. The graph on the left and right corresponds to vacuum and implicit DMF, respectively.

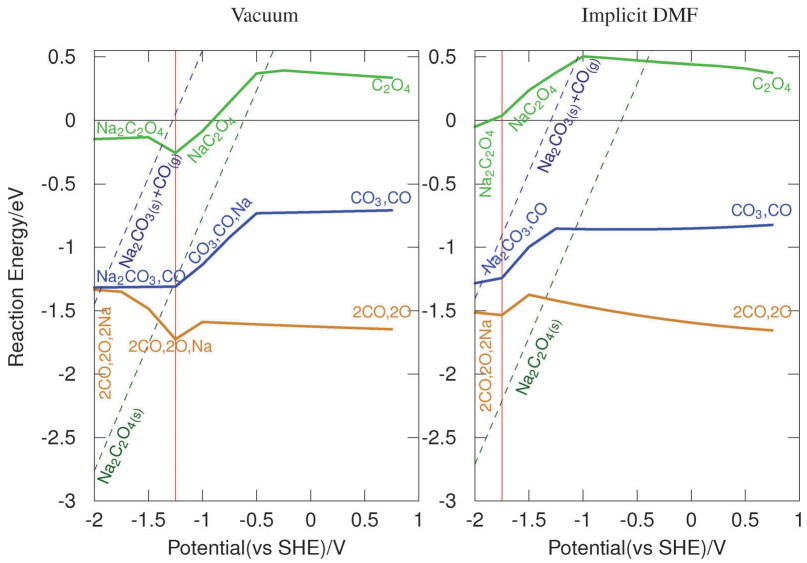

Fig. 6 Reaction energies of two CO_2 as a function of electrochemical potential in a vacuum (left) and implicit DMF (right). Thick lines refer to reactions starting from chemisorbed CO_2 yielding adsorbed products, *e.g.*, CO_3, CO (blue): $2CO_2^{ads} \rightarrow CO, CO_3^{ads}$, with the number of co-adsorbed Na^+ adapted according to the potential. Thin lines refer to the overall reaction: isolated CO_2 reacts with electrons and counterions to yield precipitated salts, *e.g.*, $Na_2C_2O_{4(s)}$ (dark-green): $2CO_2(g) + 2Na^+ + 2\,e^- \rightarrow Na_2C_2O_{4(s)}$. The vertical red lines indicate the point where the reactant changes from CO_2, Na@Ni(111) to CO_2@Ni(111).

Since both carbonate and oxalate formation are surface assisted processes, the second relevant question is if these reactions are feasible on the surface. Hence, we investigate the transformation of chemisorbed CO_2 into adsorbed products. Depending on the potential, the reactant and/or the products are co-adsorbed with Na^+ and the corresponding SC

reaction energies are represented in thick lines in Fig. 6. Concerning the reactant, the co-adsorption of CO_2 with Na^+ is favored at stronlgy reducing potentials. This change in the energy reference leads to a discontinuity in the reaction energies and is indicated by a vertical line. Similarly, for each segment, the most stable product is indicated in Fig. 6 at the given coverage (*i.e.* 2/9 ML): the number of co-adsorbed Na^+ increases with more and more reducing (more negative) potentials. These changes in the number of cations lead to the other discontinuities in the reaction energy. Since we are considering reaction energies, the reference energy is different from that of the preceding figures, which modifies the aspect of the potential dependence. The potential dependence of relative energies is directly related to workfunction differences. The change in workfunction (potential of zero charge) is often larger for an adsorption process than for a surface reaction. Therefore, the potential dependence of reaction energies is often less pronounced than for adsorption energies. Nevertheless, since the workfunction still changes during a reaction, the SC method delivers more reliable results in general and we are only showing and discussing these results.

The oxalate formation is shown as a green line in Fig. 6: at potentials >-0.5 V, Na^+ does neither co-adsorb with the reactant nor with the product in vacuum and the formation of oxalate on the surface is endothermic. For lower potentials, one counterion is co-adsorbed with oxalate, but not with CO_2, giving rise to the noticeable potential dependence of the reaction energy. Furthermore, at potentials lower than -0.9 V, the surface catalyzed reaction could take place at a reasonable rate since it is exothermic, provided that there is chemisorbed CO_2 available and not only CO and O. At potentials lower than -1.25 V, the reactant is CO_2, co-adsorbed with Na^+ that yields surface adsorbed sodium oxalate ($Na_2C_2O_4$). However, the potential dependence of the elementary reaction is almost negligible in the absence of Na^+ co-adsorption, *i.e.*, the capacitance and workfunction of C_2O_4@Ni(111) are not significantly larger than those of CO_2@Ni(111). The situation for carbonate formation is similar to that for oxalate formation, except that thermodynamically it is much more accessible on the surface, not the least because of the CO@Ni(111) byproduct. Hence, carbonate formation is preferred over oxalate formation on the Ni(111) surface, although the overall reaction energy is less favorable. Nevertheless, the dominating surface species down to -1.75 V is CO, O, which itself might react with additional CO_2 to yield carbonate, but is not expected to form oxalates.

Na^+ co-adsorption provides less stability under solvent conditions than in a vacuum. For instance, surface adsorbed oxalate is stabilized by Na^+ at potentials below -0.5 V in vacuum, but only below -1.0 V in implicit DMF. As a consequence, the surface reaction forming C_2O_4 is isoenergetic at ~-0.9 V in a vacuum, but it takes -1.9 V when solvating the systems. Hence, oxalate formation on Ni(111) is even less expected under solvent conditions than in a vacuum. Furthermore, adsorbed oxalate is more compact and thus less accessible to the solvent than two chemisorbed CO_2 molecules, resulting in a loss of solvation energy for oxalate formation. Although similar remarks apply to carbonate formation, the details differ slightly, mostly because the solvent effect is enhanced for carbonate compared to oxalate. Finally, the relative stability of CO, O (2/9 ML) compared to carbonate in solvent varies less with the potential than in vacuum. Nevertheless, at very reducing potentials carbonate formation becomes competitive with the poisoning of the catalyst by the CO, O surface layer, just like in vacuum. Hence, the combination of unfavorable oxalate formation on the surface with the overwhelming competition of CO_2 dissociation and carbonate formation makes oxalate formation unlikely over a nickel catalyst despite a favorable overall reaction energy. In contrast, carbonate and carbon monoxide formation is likely at low potentials. This selectivity between the two possible products of CO_2 electroreduction under aprotic conditions over Ni is in excellent agreement with experimental observations: oxalate formation accounts for less than 10% of the current density, while CO formation is the major product observed under aprotic conditions.[11,14,15]

6 Conclusion

Investigating by first principles the intrinsic reactivity of CO_2 on Ni(111) under electrochemically reducing conditions in aprotic media, we have compared two approaches that take the electrochemical potential into account. Furthermore, the comparison exploits a recently implemented implicit solvent model[64] to move towards more realistic conditions than vacuum.

The present study evidences that the zeroth order method for including the electrochemical potential (LFER-EP) is a valuable tool for quickly assessing the thermodynamic aspects of electrocatalysis in vacuum, which often gives a good indication of the processes under more realistic conditions. For example, this highly efficient approach correctly identifies the dissociative adsorption of CO_2 yielding CO and O as exothermic at all relevant potentials and predicts the formation of carbonates, rather than oxalates, over Ni(111). This preference is due to an insufficiently stabilizing interaction of oxalate with the surface. The surface charging method (SC) allows us to vary the charge on the adsorbates as a function of potential. Therefore, in contrast to the LFER-EP, which is limitted to cation coupled electron transfers, the SC method stabilizes the chemisorption of CO_2 at reducing potentials even in the absence of counterions. While the LFER-EP results are insensitive to the inclusion of an implicit solvent description, the situation is dramatically modified when explicitly accounting for the electrochemical potential by charging the electrode. The solvent strongly increases the capacitance of the surface and hence the surface charge for a given bias potential. Even the rather simplistic solvation model applied herein gives rise to marked changes in electrochemical reactivity compared to vacuum. Most strikingly, the charge injection is system dependent and differs significantly from the ideal values of 0 and 1. As a consequence, adsorption energies are potential dependent when accounting for solvent effects. This results, even in the absence of counterion co-adsorption, in a potential dependence of the most stable surface species, *e.g.*, the formation of carbonates rather than

just CO and O for coverages above 2/9 ML, and the preferred adsorption mode of oxalate, while such a dependency is inherently absent in LFER-EP. In summary, the SC method coupled with an implicit solvent model gives access to a wealth of detailed information beyond the LFER-EP. Therefore, we recommend this more advanced, but still quite efficient, model when seeking an understanding of the fundamental processes in an electrochemical interfacial system.

Acknowledgements

The authors acknowledge Solvay for financial support. J.-S. Filhol and N. Lespes are thanked for help in setting up the surface charging method and for fruitful discussions in the early stage of composing the manuscript. The authors acknowledge computational resources generously provided by the mesocenter PSMN. This work was granted access to the HPC resources of CINES and IDRIS under the allocation 2014-080609 made by GENCI.

References

1 K. S. Joya, Y. F. Joya, K. Ocakoglu and R. van de Krol, *Angew. Chem., Int. Ed.*, 2013, **52**, 10426.
2 A. J. Appleby, *Catal. Rev.*, 1971, **4**, 221.
3 J. Bockris, *Int. J. Hydrogen Energy*, 1999, **24**, 1.
4 N. S. Lewis and D. G. Nocera, *Proc. Natl. Acad. Sci. U. S. A.*, 2006, **103**, 15729.
5 J. O. Bockris, *Int. J. Hydrogen Energy*, 2008, **33**, 2129.
6 D. Pletcher and J. Girault, *J. Appl. Electrochem.*, 1986, **16**, 791.
7 J. Bringmann and E. Dinjus, *Appl. Organomet. Chem.*, 2001, **15**, 135.
8 M. Gattrell, N. Gupta and A. Co, *J. Electroanal. Chem.*, 2006, **594**, 1.
9 Y. Hori, *Modern Aspects of Electrochemistry*, Springer, New York, Gaithersburg MD, 2008, ch. 3, p. 89.
10 D. Canfield and K. W. Frese, *J. Electrochem. Soc.*, 1983, **130**, 1772.
11 S. Ikeda, T. Takagi and K. Ito, *Bull. Chem. Soc. Jpn.*, 1987, **60**, 2517.
12 D. T. Whipple and P. J. A. Kenis, *J. Phys. Chem. Lett.*, 2010, **1**, 3451.
13 I. Ganesh, *Renewable Sustainable Energy Rev.*, 2014, **31**, 221.
14 M. Jitaru, D. Lowy, M. Toma, B. Toma and L. Oniciu, *J. Appl. Electrochem.*, 1997, **27**, 875.
15 J.-P. Jones, G. K. S. Prakash and G. A. Olah, *Isr. J. Chem.*, 2014, **54**, 1451.
16 G.-Q. Yuan, H.-F. Jiang, C. Lin and S.-J. Liao, *Electrochim. Acta*, 2008, **53**, 2170.
17 C.-H. Li, G.-Q. Yuan, X.-C. Ji, X.-J. Wang, J.-S. Ye and H.-F. Jiang, *Electrochim. Acta*, 2011, **56**, 1529.
18 R. Matthessen, J. Fransaer, K. Binnemans and D. E. D. Vos, *RSC Adv.*, 2013, **3**, 4634.
19 T. Yamamoto, D. A. Tryk, K. Hashimoto, A. Fujishima and M. Okawa, *J. Electrochem. Soc.*, 2000, **147**, 3393.
20 O. M. Magnussen, J. Hotlos, R. J. Nichols, D. M. Kolb and R. J. Behm, *Phys. Rev. Lett.*, 1990, **64**, 2929.
21 T. Iwasita and F. Nart, *Prog. Surf. Sci.*, 1997, **55**, 271.
22 K. Jambunathan and A. C. Hillier, *J. Electrochem. Soc.*, 2003, **150**, E312.
23 K. Jambunathan, S. Jayaraman and A. C. Hillier, *Langmuir*, 2004, **20**, 1856.
24 Y. X. Chen, M. Heinen, Z. Jusys and R. J. Behm, *Angew. Chem., Int. Ed.*, 2006, **45**, 981.
25 Y. Gorlin, B. Lassalle-Kaiser, J. D. Benck, S. Gul, S. M. Webb, V. K. Yachandra, J. Yano and T. F. Jaramillo, *J. Am. Chem. Soc.*, 2013, **135**, 8525.
26 K. Letchworth-Weaver and T. A. Arias, *Phys. Rev. B: Condens. Matter Mater. Phys.*, 2012, **86**, 075140.
27 J. I. Siepmann and M. Sprik, *J. Chem. Phys.*, 1995, **102**, 511.
28 S. Tazi, M. Salanne, C. Simon, P. Turq, M. Pounds and P. A. Madden, *J. Phys. Chem. B*, 2010, **114**, 8453.
29 D. M. Bernardi and M. W. Verbrugge, *J. Electrochem. Soc.*, 1992, **139**, 2477.
30 W. Goddard, B. Merinov, A. van Duin, T. Jacob, M. Blanco, V. Molinero, S. Jang and Y. Jang, *Mol. Simul.*, 2006, **32**, 251.
31 R. Ferreira de Morais, P. Sautet, D. Loffreda and A. A. Franco, *Electrochim. Acta*, 2011, **56**, 10842.
32 K. Ito, S. Ikeda, N. Yamauchi, T. Iida and T. Takagi, *Bull. Chem. Soc. Jpn.*, 1985, **58**, 3027.
33 L. Sun, G. K. Ramesha, P. V. Kamat and J. F. Brennecke, *Langmuir*, 2014, **30**, 6302.
34 B. Eneau-Innocent, D. Pasquier, F. Ropital, J.-M. Leger and K. B. Kokoh, *Appl. Catal., B*, 2010, **98**, 65.
35 J. K. Norskov, J. Rossmeisl, A. Logadottir, L. Lindqvist, J. R. Kitchin, T. Bligaard and H. Jonsson, *J. Phys. Chem. B*, 2004, **108**, 17886.
36 J. S. Hummelshoj, J. Blomqvist, S. Datta, T. Vegge, J. Rossmeisl, K. S. Thygesen, A. C. Luntz, K. W. Jacobsen and J. K. Norskov, *J. Chem. Phys.*, 2010, **132**, 071101.
37 J. Greeley, J. K. Norskov and M. Mavrikakis, *Annu. Rev. Phys. Chem.*, 2002, **53**, 319.
38 V. Stamenkovic, B. S. Mun, K. J. J. Mayrhofer, P. N. Ross, N. M. Markovic, J. Rossmeisl, J. Greeley and J. K. Norskov, *Angew. Chem., Int. Ed.*, 2006, **45**, 2897.
39 J. Rossmeisl, Z.-W. Qu, H. Zhu, G.-J. Kroes and J. Norskov, *J. Electroanal. Chem.*, 2007, **607**, 83.
40 P. Ferrin, A. U. Nilekar, J. Greeley, M. Mavrikakis and J. Rossmeisl, *Surf. Sci.*, 2008, **602**, 3424.
41 J. Greeley, I. E. Stephens, A. S. Bondarenko, T. P. Johansson, H. A. Hansen, T. F. Jaramillo, J. Rossmeisl, I. Chorkendorff and J. K. Norskov, *Nat. Chem.*, 2009, **1**, 552.
42 J. A. Keith, G. Jerkiewicz and T. Jacob, *ChemPhysChem*, 2010, **11**, 2779.
43 I. C. Man, H.-Y. Su, F. Calle-Vallejo, H. A. Hansen, J. I. Martinez, N. G. Inoglu, J. Kitchin, T. F. Jaramillo, J. K. Norskov and J. Rossmeisl, *ChemCatChem*, 2011, **3**, 1159.
44 A. S. Bandarenka, A. S. Varela, M. Karamad, F. Calle-Vallejo, L. Bech, F. J. Perez-Alonso, J. Rossmeisl, I. E. L. Stephens and I. Chorkendorff, *Angew. Chem., Int. Ed.*, 2012, **51**, 11845.

45 J. Rossmeisl, J. K. Norskov, C. D. Taylor, M. J. Janik and M. Neurock, *J. Phys. Chem. B*, 2006, **110**, 21833.
46 C. D. Taylor, S. A. Wasileski, J.-S. Filhol and M. Neurock, *Phys. Rev. B: Condens. Matter Mater. Phys.*, 2006, **73**, 165402.
47 A. Y. Lozovoi and A. Alavi, *Phys. Rev. B: Condens. Matter Mater. Phys.*, 2003, **68**, 245416.
48 M. Otani and O. Sugino, *Phys. Rev. B: Condens. Matter Mater. Phys.*, 2006, **73**, 115407.
49 R. Jinnouchi and A. B. Anderson, *Phys. Rev. B: Condens. Matter Mater. Phys.*, 2008, **77**, 245417.
50 I. Dabo, B. Kozinsky, N. E. Singh-Miller and N. Marzari, *Phys. Rev. B: Condens. Matter Mater. Phys.*, 2008, **77**, 115139.
51 Y.-H. Fang and Z.-P. Liu, *J. Phys. Chem. C*, 2009, **113**, 9765.
52 M. Mamatkulov and J.-S. Filhol, *Phys. Chem. Chem. Phys.*, 2011, **13**, 7675.
53 I. Hamada, O. Sugino, N. Bonnet and M. Otani, *Phys. Rev. B: Condens. Matter Mater. Phys.*, 2013, **88**, 155427.
54 J.-S. Filhol and M. Neurock, *Angew. Chem., Int. Ed.*, 2006, **45**, 402.
55 C. Taylor, R. G. Kelly and M. Neurock, *J. Electrochem. Soc.*, 2006, **153**, E207.
56 M. J. Janik and M. Neurock, *Electrochim. Acta*, 2007, **52**, 5517.
57 G. Rostamikia and M. J. Janik, *Energy Environ. Sci.*, 2010, **3**, 1262.
58 S. A. Wasileski and M. J. Janik, *Phys. Chem. Chem. Phys.*, 2008, **10**, 3613.
59 K.-Y. Yeh and M. J. Janik, *J. Comput. Chem.*, 2011, **32**, 3399.
60 J.-L. Fattebert and F. Gygi, *Int. J. Quantum Chem.*, 2003, **93**, 139.
61 S. A. Petrosyan, A. A. Rigos and T. A. Arias, *J. Phys. Chem. B*, 2005, **109**, 15436.
62 Y.-H. Fang and Z.-P. Liu, *J. Am. Chem. Soc.*, 2010, **132**, 18214.
63 O. Andreussi, I. Dabo and N. Marzari, *J. Chem. Phys.*, 2012, **136**, 064102.
64 K. Mathew, R. Sundararaman, K. Letchworth-Weaver, T. A. Arias and R. G. Hennig, *J. Chem. Phys.*, 2014, **140**, 084106.
65 C. J. Cramer and D. G. Truhlar, *Chem. Rev.*, 1999, **99**, 2161.
66 J. O. Bockris, A. K. N. Reddy and M. Gamboa-Aldeco, *Modern Electrochemistry 2A, Fundamental of Electrodics*, Kluwer Academic Publishers, New York, 2002.
67 *GoldBook*, Standard Hydrogen electrode, http://goldbook.iupac.org/S05917.html.
68 C. P. Kelly, C. J. Cramer and D. G. Truhlar, *J. Phys. Chem. B*, 2006, **110**, 16066.
69 Y. P. Zhang, C. H. Cheng, J. T. Kim, J. Stanojevic and E. E. Eyler, *Phys. Rev. Lett.*, 2004, **92**, 203003.
70 If we use $2H^+ + 2e^- \rightarrow H_2$ to estimate the energy of H_2 at standard conditions, we need the energy of the solvated proton and the energy of the electrons. The hydration free energy of the proton is estimated to be about −11.5 eV.[68] Together with the electron potential of −4.44 V *vs.* vacuum, we get −31.88 eV, which is in good agreement with the "quantum chemical estimate" of 2 × −13.6 eV (energy of a hydrogen atom) + −4.5 eV (binding energy of the hydrogen molecule[69]) = −31.7 eV.
71 In the generalization of the CHE to an arbitrary reference couple (see ref. 36) the severeness of this approximation is most clearly visible: the zero charge energy of a system always corresponds to the reversible potential of the reference redox couple. For example the zero charge energy of CO_2@Ni corresponds to 0 V, if we consider a hydrogenation, but to −2.7 V if we consider a reduction with sodium.
72 S. A. Wasileski, M. T. M. Koper and M. J. Weaver, *J. Am. Chem. Soc.*, 2002, **124**, 2796.
73 A. Panchenko, M. T. M. Koper, T. E. Shubina, S. J. Mitchell and E. Roduner, *J. Electrochem. Soc.*, 2004, **151**, A2016.
74 M. P. Hyman and J. W. Medlin, *J. Phys. Chem. B*, 2005, **109**, 6304.
75 S. A. Wasileski and M. J. Weaver, *J. Phys. Chem. B*, 2002, **106**, 4782.
76 J.-S. Filhol and M.-L. Doublet, *Catal. Today*, 2013, **202**, 87.
77 J.-S. Filhol and M.-L. Doublet, *J. Phys. Chem. C*, 2014, **118**, 19023.
78 Y.-H. Fang, G.-F. Wei and Z.-P. Liu, *J. Phys. Chem. C*, 2014, **118**, 3629.
79 R. C. Catapan, A. A. M. Oliveira, Y. Chen and D. G. Vlachos, *J. Phys. Chem. C*, 2012, **116**, 20281.
80 E. Westphal and J. R. Pliego, *J. Chem. Phys.*, 2005, **123**, 074508.
81 M. Dusek, G. Chapuis, M. Meyer and V. Petricek, *Acta Crystallogr., Sect. B: Struct. Sci.*, 2003, **59**, 337.
82 D. A. Reed and M. M. Olmstead, *Acta Crystallogr., Sect. B: Struct. Crystallogr. Cryst. Chem.*, 1981, **37**, 938.
83 J. P. Perdew, K. Burke and M. Ernzerhof, *Phys. Rev. Lett.*, 1996, **77**, 3865.
84 P. E. Blochl, *Phys. Rev. B: Condens. Matter Mater. Phys.*, 1994, **50**, 17953.
85 G. Kresse and D. Joubert, *Phys. Rev. B: Condens. Matter Mater. Phys.*, 1999, **59**, 1758.
86 G. Kresse and J. Hafner, *Phys. Rev. B: Condens. Matter Mater. Phys.*, 1993, **47**, 558.
87 G. Kresse and J. Furthmuller, *Phys. Rev. B: Condens. Matter Mater. Phys.*, 1996, **54**, 11169.
88 D. Gunceler, K. Letchworth-Weaver, R. Sundararaman, K. A. Schwarz and T. A. Arias, *Modell. Simul. Mater. Sci. Eng.*, 2013, **21**, 074005.
89 K. Hara, A. Kudo and T. Sakata, *J. Electroanal. Chem.*, 1995, **391**, 141.
90 R. J. Lim, M. Xie, M. A. Sk, J.-M. Lee, A. Fisher, X. Wang and K. H. Lim, *Catal. Today*, 2014, **233**, 169.

ChemPubSoc Europe

DOI: 10.1002/cphc.201500187

CHEMPHYSCHEM Communications

Modeling the $HCOOH/CO_2$ Electrocatalytic Reaction: When Details Are Key

Stephan N. Steinmann,[a] Carine Michel,[a, b] Renate Schwiedernoch,[c] Jean-Sebastien Filhol,[d] and Philippe Sautet*[a, b]

Our first principles simulations of the electrooxidation of formic acid over nickel identify the reorientation of the formate intermediate and the desorption of CO_2 as the rate-limiting steps. Although they are not associated with an electron transfer, these barriers are strongly modified when the electrochemical potential is explicitly accounted for and when modeling the influence of the solvent. Hence, such a level of modeling is key to understand the kinetic limitations that penalize the reaction.

Formic acid is an attractive fuel for direct fuel cells, avoiding the delicate storage and transportation of hydrogen and ideally even yielding 0.2 V higher cell potentials.[1,2] To be a carbon neutral fuel, formic acid could be generated from CO_2, which can either be achieved chemically through hydrogenation,[3,4] or by the reasonably efficient electroreduction of CO_2, which can benefit from temporary excesses in wind or solar power.[5,6] From a chemical point of view, the electrochemical transformation of CO_2 into formic acid and vice versa has the unique advantage that the CO_2 skeleton does not need to be broken or formed, which limits the byproducts compared to the transformation of CO_2 into less oxygenated compounds. Hence, developing efficient processes for those two electrochemical reactions is a timely challenge.

Atomic scale modeling complements the experimental effort to understand and improve the efficiency of catalysis. In particular, first principles studies are key to give credibility to experimental hypotheses in electrochemistry, where in situ characterizations are extremely challenging. For example, the debate about the active intermediates of the electrooxidation of formic acid over platinum is still ongoing, despite significant progress in both experimental and theoretical understanding.[7] In particular, earlier claims about the negligible reactivity of formate[8] have been challenged by the identification of the double role of (solution) formate: first, formate is weakly adsorbed and then it is oxidized (decoupled electron proton transfer).[9] Second, co-adsorption of formate with itself, like the co-adsorption of formate with other anions, is proposed to stabilize the C–H down adsorption mode (orientation **5** in Figure 1, see below), which is the active intermediate that undergoes oxidation to CO_2.[10,11]

In the present study, we investigate the activity of earth abundant and cheap nickel catalysts for the electrooxidation of formic acid and the electroreduction of CO_2 to formic acid. Nickel is commonly used in heterogeneous catalysts for the hydrogenation of carbon dioxide to methane,[12] for dry reforming,[13] solid oxide electrolyzers for the conversion of CO_2 into CO,[14] and solid oxide fuel cells,[15] which can be fed with formic acid.[16] Although pure nickel is not very active for the electrooxidation of formic acid, that is, the kinetics are slow at an onset potential of about 0.3 V versus SHE,[17] nickel alloys are highly active electrocatalysts for the oxidation of formic acid.[17–20] Nevertheless, theoretical electrochemical studies for the electrooxidation of formic acid have, so far, focused on platinum.[7,21–23] Hence, the investigation of nickel is overdue as a next step towards understanding the improved activity of alloys of Ni with Pt and Pd. Note that Ni surfaces are likely to be passivated by NiO layers under oxidizing, acidic conditions.[24] However, one might expect that Ni alloys with the noble Pt and Pd metals will not suffer from this deactivation. Therefore, we investigate metallic Ni rather than NiO in this model study on the influence of the electrochemical potential.

The major challenge for the description of electrochemistry at the periodic density functional theory (DFT) level is the incorporation of the electrochemical potential. The computational hydrogen electrode[25] (CHE) is the first successful model[26–29] to allow a link to be made between routine computations in vacuum and electrochemical experiments. The stunning simplicity of the CHE comes with two major drawbacks: first, proton- and electron-transfer are strictly coupled, and second, the use of CHE implies that computed barriers of elementary reactions are not affected by the electrochemical potential. To overcome these drawbacks, several advanced and computationally more involved models have been proposed.[30–38]

Here, we investigate the reaction mechanism of the decomposition of formic acid into CO_2 at a Ni(111) model surface. As the reverse reaction is also of considerable interest, we also

[a] Dr. S. N. Steinmann, Dr. C. Michel, Dr. P. Sautet
Université de Lyon, Ecole Normale Supérieure de Lyon
Laboratoire de Chimie, 46 allee d'Italie, Lyon (France)
E-mail: philippe.sautet@ens-lyon.fr

[b] Dr. C. Michel, Dr. P. Sautet
CNRS, Laboratoire de Chimie, UMR 5182
46 allee d'Italie, Lyon (France)

[c] Dr. R. Schwiedernoch
Eco-Efficient Products and Processes Laboratory (E2P2L)
UMI 3464 Solvay/CNRS
Shanghai (PR China)

[d] Dr. J.-S. Filhol
CTMM, Institut Charles Gerhardt Montpellier UMR 5253
Universite Montpellier 2
Place E Bataillon, Montpellier (France)

Supporting Information for this article is available on the WWW under http://dx.doi.org/10.1002/cphc.201500187.

ChemPubSoc Europe

CHEMPHYSCHEM Communications

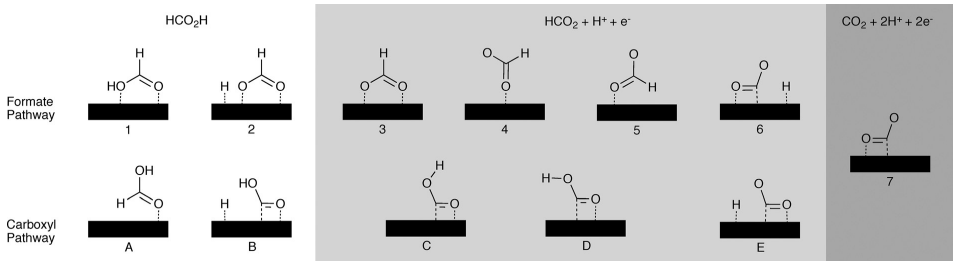

Figure 1. Schematic representation of formic acid electrooxidation over nickel along the formate (top) and carboxylate (bottom) pathway. Depictions of the geometries and their coordinates can be found in the Supporting Information.

briefly consider the electroreduction of CO_2. We compare the results of CHE to the more general and detailed, but still quite stable and efficient surface charging (SC) method, in which the surface charge applied to tune the electrochemical potential is neutralized by a homogeneous background charge.[33,39] Introduction of a homogeneous background charge is the simplest approach to neutralize the simulation cell. The spurious interactions with the system are corrected for,[33,39] leading to a robust approach that has been shown to compare well to experiments.[40–43] Through using the SC model, we investigate the mechanism in detail and address the following questions: 1) Are proton and electron transfer strictly coupled when they occur on the catalyst surface? 2) Are activation barriers dependent on the electrochemical potential?

Although the influence of solvent and electrolytes is highly relevant according to experiment and empirical models,[44,45] the associated complexity is prohibitive for routine DFT computations and is, thus, largely neglected or drastically simplified. To capture the bulk-solvent effect, an implicit description of the water solvent is included (see the Supporting Information for further details).[46,47,48] We have already applied this methodology to the intrinsic reactivity of CO_2 under aprotic conditions (DMF solvent) over a Ni(111) catalyst.[49] The use of an implicit solvent model is computationally efficient and does not require the (somewhat) arbitrary placement of the adsorbate within the water layers, which together significantly simplify the transition-state search. In addition, the implicit solvent model screens the electrostatic interactions between the homogeneous background charge and the metal surface, leading to robust results that essentially do not depend on the vacuum (i.e. solvent) size and thus reducing one of the typical limitations of the SC model.

The two competing pathways in formic acid electrocatalytic oxidation were investigated (see Figure 1) and the associated free-energy profiles are shown in Figure 2 (top). Starting from the adsorption of formic acid, the path branches either to the left (carboxyl) or to the right (formate). Note that we did not consider indirect pathways, in which the CO_2 framework is broken to form CO, which is subsequently re-oxidized. The C–O bond breaking requires a high activation free energy and is, thus, unlikely to occur at room temperature.[22] Additionally, experimental studies suggest that the decomposition of formic acid over nickel gives mainly carbon dioxide and dihydrogen.[50] The nevertheless observed CO is ascribed to the dissociation of CO_2, not of formic acid itself,[51] a process that we have studied previously under aprotic (DMF) conditions.[49] As $2e^-$ processes have rarely been observed,[52] we did not consider the concerted liberation of two protons either.

The pathways are given for three potential values: −0.25 V, where the electrochemical cell is operating slightly above the maximum spontaneous potential (−0.2 V); 0 V, where a small overpotential is applied; and +0.25 V, where the oxidation is artificially accelerated by a substantial overpotential (see Table S1 in the Supporting Information for the thermodynamic overpotential). In the CHE framework the potential only changes the relative energies when a proton and an electron are removed (indicated by a change in the background color in Figures 1 and 2), whereas the SC method applies a certain charge to each structure (intermediate and TS) to maintain the potential at the imposed value. This difference of surface charge is called charge injection and is given in the bottom panel of Figure 2. We will discuss the charge injection after the analysis of the free energy profile. In contrast to SC, the CHE works at zero charge, that is, the injected charge strictly follows the number of protons in the system.

Despite the intrinsic limitations of CHE, most of the key aspects of the reaction mechanism hold for both models and all considered potentials. Firstly, the carboxyl pathway (left pathway in Figure 2) shows transition states with higher energy than the formate one, both for O–H and C–H bond scissions. Although only marginally, the CHE results thus prefer the formate path over the carboxyl path, in agreement with experimental evidence and the results presented here from the SC approach. Furthermore, the most probable species initially formed from formic acid is formate (**3**), both kinetically and thermodynamically and this species will, thus, be the dominant rate-limiting intermediate, which is in good agreement with experimental conclusions.[9,10,11]

Hence, we focus our discussion on the formate pathway (right pathway in Figure 2). The proposed reaction pathway is straightforward: Formic acid adsorbs and the O–H bond is broken to create the formate intermediate **3** and release ($H^+ + e^-$). To break the C–H bond, formate **3** needs to reorient to reach the correct precursor state (**5**). This reorientation occurs

ChemPubSoc Europe

CHEMPHYSCHEM Communications

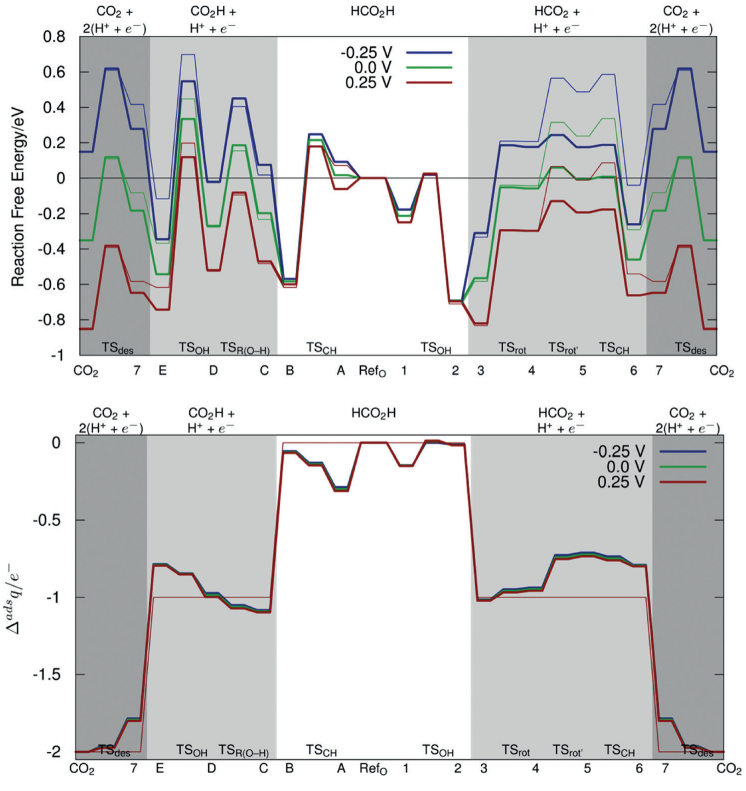

Figure 2. Top) Free energy profile for formic acid electrooxidation relative to the reference for oxidation [Ref_O; formic acid and a slab of Ni(111)] according to the CHE (thin lines) and SC (thick lines) approach at three different electrochemical potentials (vs. SHE): 0 V, +0.25 V (where the oxidation is artificially accelerated) and −0.25 V (where the electrochemical cell is operating slightly above the maximum spontaneous potential). The path to the right goes through formate and the alternative carboxyl path is shown on the left. Note that until the first proton-coupled electron transfer occurs (change from white to gray background) all the CHE lines overlap by construction. The second formally electrochemical step is indicated by a background color change from light to dark gray. Bottom) Charge injection along the paths. Charge injection in the CHE approach is strictly coupled to proton transfer, and thus, does not depend on the potential.

in two steps (from **3** to **4** then to **5**) and is associated with a high energy barrier, which originates from the substantial stabilization of the bidentate binding mode of formate to metal surfaces, as extensively discussed previously for Pt.[21,22] After reorientation, the C–H bond breaks easily, producing chemisorbed CO_2 (**7**), which then has to desorb. The rate-limiting TS, which, together with the low-lying formate intermediate **3**, defines the energetic span of the reaction,[53] depends on the potential: at positive potentials, it is associated with the reorientation of formate ($\mathbf{TS_{rot'}}$), whereas at the ideal potential of −0.2 V, it is found to be the TS for CO_2 desorption ($\mathbf{TS_{des}}$).

CO_2 desorption is particularly crucial when considering the reverse process. Indeed, to perform the electrochemical reduction of CO_2 into formic acid, the working potential needs to be negative to compensate for the endothermicity of the reaction. Under these conditions, the situation is relatively simple (see the Supporting Information for the corresponding reaction energy profile): the limiting transition state is the chemisorption of CO_2 and formate is the limiting intermediate. Unfortunately, the chemisorption barrier is essentially independent of the potential, and thus, responsible for a significant kinetic limitation on the Ni(111) surface. Hence, to find more active electrocatalysts for CO_2 reduction, the initial adsorption barrier needs to be lowered. Analysis of the Fukui function might provide further insights for designing improved catalysts,[54] for example, by alloying, which is also the most promising strategy to destabilize the formate intermediate.

We now analyze the main steps for formic acid oxidation in more detail. In broad terms, the SC and CHE results are consistent. However, the SC results provide a more nuanced picture of the formate oxidation path, in particular for the chemical steps, such as the CO_2 desorption and the formate reorientation.

The CO_2 chemisorption is an endothermic process and we find a barrier of almost 0.5 eV at zero charge. The importance of this barrier for CO_2 adsorption has not been underlined in the literature to our knowledge. In the desorption direction, the barrier is smaller (0.2 eV) and, as no coupled proton–electron transfer is involved in this process, the CHE results suggest that the situation is identical under electrochemical conditions. However, according to the SC method, chemisorbed CO_2 is stabilized by 0.1 eV at −0.25 V, which increases this potential-dependent desorption barrier by 50% compared to the CHE results. The reorientation of formate is the other chemical step that is sensitive to the inclusion of the electrochemical potential. If the energy profiles for the CHE (thin lines; Figue 2) and SC (thick lines) method are similar until species **4**, the constant potential mode of SC stabilizes the TS for formate reorientation by 0.3 eV ($\mathbf{TS_{rot'}}$). The difference between the two methods is maximal at $\mathbf{TS_{CH}}$ and disappears, by construction, upon CO_2 desorption. As a consequence, the potential at which the limiting transition state becomes CO_2 desorption is predicted to be less negative within the SC than the CHE framework.

ChemPubSoc Europe

CHEMPHYSCHEM Communications

We next analyze the varying surface charge. CHE assumes that electrons are released abruptly in electrochemical steps, with 1 e^- released when entering the light gray zone and a second one in the dark gray zone of the bottom panel of Figure 2. The SC method mostly follows these steps in charge injection, but with notable deviations by up to 0.25 e^-. The charge injection ($\Delta^{ads}q$) gives the charge injected into a system with respect to the metal surface at the same potential, and aligns the Fermi level of the systems, thus keeping the potential constant. As the capacitances of all involved systems, including the reference Ni surface, are similar, the $\Delta^{ads}q$ values barely depend on the electrochemical potential. In our case, rotating and oxidizing bidentately bound formate **3**, that is, breaking the C–H bond, also requires a counterintuitive charge injection (i.e. a partial reduction) of about 0.2 e^-. Chemisorbed CO_2 requires a charge injection of about 0.2 e^-, which can be easily explained:[55,56] both the bent geometry (see the Supporting Information) and the analysis of the electronic structure[55] provide evidence that the metal surface donates electron density to CO_2, forming a formal CO_2^- ion that interacts with the surface. Indeed, bending CO_2 becomes energetically favorable upon reduction, creating a dipole moment and lifting the degeneracy of the LUMO orbital of CO_2. This state crossing requires significant electronic reorganization from the highly polar chemisorbed CO_2 state to the apolar solvated CO_2 state. Thus, the large deformation energy in the transition state is not compensated by the incipient electron transfer, resulting in the observed activated adsorption/desorption process. Note that the implicit solvent does not accurately capture the large solvent reorganization energy upon desorption and the presented barrier might, therefore, be under estimated.

Some models that go beyond the simplest application of CHE to obtain potential dependent barriers, assume that the barriers of the nominally electrochemical step are dependent on the potential.[57,28] In the present case, those steps are the breaking of the C–H and O–H bonds, leading to the release of the couple (H^+, e^-). Considering Figure 2, the situation is not that clear cut. In the formate pathway (on the right), according to the SC model, the potential has the largest influence on the "chemical step": the transition state of the reorientation of formate **$TS_{rot'}$** is lowered by 0.3 eV, compared with CHE, at 0 V versus SHE. This reorientation causes a change in the surface dipole, and thus, in the workfunction (Figure 3, see below). The accompanying charge injection of 0.25 e^- reflects the partial negative charging of monodentately bound formate **5**, in agreement with the postulated importance of weakly bound formate.[10,11] As explained above, this charge injection is retained after CO_2 formation, to stabilize its bent form.

As seen in the preceding discussion, the potential dependence of elementary steps does not seem to be only related to H^+-formation steps, that is, the breaking of the C–H or O–H bond. However, what is at the origin of the potential dependence? Liu and co-workers have proposed[58] that the potential dependence of an elementary reaction is directly related to the difference in the workfunction (ΔW) of the involved species at zero charge. Figure 3 traces the potential of zero charge (i.e. the workfunction) along the reaction path. Indeed, the largest jumps in the workfunction occur for adsorption/desorption processes, for **$TS_{rot'}$**, and for **TS_{OH}**, which correspond to the steps that are sensitive to the potential. More precisely, ΔW is linearly correlated to the derivative with respect to the potential of the difference between SC and CHE, whereas the difference between SC and CHE is a quadratic function of ΔW (see the Supporting Information, Figures S3–S5). Furthermore, the workfunction changes (ΔW) are, as expected,[59] roughly anticorrelated to the dipole moment of the (neutral) adsorbates (see Figure 3). Although not quantitative, monitoring the surface dipole allows the quick identification of the elementary steps when CHE might not be a good approximation.

In summary, we presented potential-dependent reaction barriers for the conversion of formic acid over nickel in implicit water, comparing the popular CHE method (zero charge) with the more detailed SC model (constant potential). The key points of the mechanism are consistent between the two methods: formate is the main intermediate and the reaction requires a certain overpotential to proceed. The most important barriers, which explain the low activity of Ni at its onset potential, are found for "chemical steps" that are also the most sensitive steps towards the electrochemical potential, that is, the desorption of CO_2, together with the energetically unfavorable reorientation of formate, which is associated with a dramatic change in the surface dipole moment.

Hence, explicitly accounting for the electrode potential emphasizes the complexity of heterogeneous electrocatalysis and our results highlight the benefit of going beyond the CHE when seeking a detailed and realistic description of electrochemistry on metal electrodes. Monitoring the surface dipole allows the quick identification of elementary steps, for which the CHE might not be a good approximation, and opens the way to using a combination of the CHE model, to quickly screen the reaction network, and the SC model to refine the key steps.

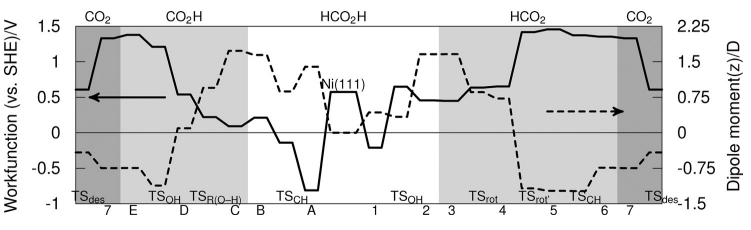

Figure 3. Evolution of the potential of zero charge, that is, the workfunction (left axis, full lines), and of the dipole moment of the adsorbate (right axis, broken lines) along the electrooxidation pathway of formic acid. The formate pathway is shown on the right and the alternative carboxyl path is shown on the left.

ChemPubSoc Europe

CHEMPHYSCHEM Communications

Acknowledgements

The authors acknowledge Solvay for financial support. Computational resources generously provided by the mesocenter PSMN (Pôle Scientifique de Modélisation Numérique). This work was granted access to the HPC resources of CINES (Centre Informatique National de l'Enseignement Supérieur) and IDRIS (Institut du développement et des ressources en informatique scientifique) under the allocation 2014-080609 made by GENCI (Grand équipement national de calcul intensif).

Keywords: density functional calculations · electrocatalysis · electrochemistry · formic acid · heterogeneous catalysis

[1] C. Rice, S. Ha, R. Masel, P. Waszczuk, A. Wieckowski, T. Barnard, *J. Power Sources* **2002**, *111*, 83.
[2] X. Yu, P. G. Pickup, *J. Power Sources* **2008**, *182*, 124.
[3] S. Enthaler, J. von Langermann, T. Schmidt, *Energy Environ. Sci.* **2010**, *3*, 1207.
[4] B. Loges, A. Boddien, F. Gartner, H. Junge, M. Beller, *Top. Catal.* **2010**, *53*, 902.
[5] D. T. Whipple, P. J. A. Kenis, *J. Phys. Chem. Lett.* **2010**, *1*, 3451.
[6] A. S. Agarwal, Y. Zhai, D. Hill, N. Sridhar, *ChemSusChem* **2011**, *4*, 1301.
[7] W. Gao, E. H. Song, Q. Jiang, T. Jacob, *Chem. Eur. J.* **2014**, *20*, 11005.
[8] Y. X. Chen, M. Heinen, Z. Jusys, R. J. Behm, *Angew. Chem. Int. Ed.* **2006**, *45*, 981; *Angew. Chem.* **2006**, *118*, 995.
[9] A. Cuesta, G. Cabello, M. Osawa, C. Gutirrez, *ACS Catal.* **2012**, *2*, 728.
[10] J. Joo, T. Uchida, A. Cuesta, M. T. M. Koper, M. Osawa, *J. Am. Chem. Soc.* **2013**, *135*, 9991.
[11] J. V. Perales-Rondón, E. Herrero, J. M. Feliu, *Electrochim. Acta* **2014**, *140*, 511.
[12] W. Wang, S. Wang, X. Ma, J. Gong, *Chem. Soc. Rev.* **2011**, *40*, 3703.
[13] M. Mikkelsen, M. Jorgensen, F. C. Krebs, *Energy Environ. Sci.* **2010**, *3*, 43.
[14] R. J. Lim, M. Xie, M. A. Sk, J.-M. Lee, A. Fisher, X. Wang, K. H. Lim, *Catal. Today* **2014**, *233*, 169.
[15] B. C. H. Steele, A. Heinzel, *Nature* **2001**, *414*, 345.
[16] Y. Chen, C. Su, T. Zheng, Z. Shao, *J. Power Sources* **2012**, *220*, 147.
[17] C. Du, M. Chen, W. Wang, G. Yin, P. Shi, *Electrochem. Commun.* **2010**, *12*, 843.
[18] R. F. Wang, H. Wang, H. Q. Feng, S. Ji, *Int. J. Electrochem. Sci.* **2013**, *8*, 6068.
[19] L. Shen, H. Li, L. Lu, Y. Luo, Y. Tang, Y. Chen, T. Lu, *Electrochim. Acta* **2013**, *89*, 497.
[20] B. T. Sneed, A. P. Young, D. Jalalpoor, M. C. Golden, S. Mao, Y. Jiang, Y. Wang, C.-K. Tsung, *ACS Nano* **2014**, *8*, 7239.
[21] M. Neurock, M. Janik, A. Wieckowski, *Faraday Discuss.* **2009**, *140*, 363.
[22] W. Gao, J. A. Keith, J. Anton, T. Jacob, *J. Am. Chem. Soc.* **2010**, *132*, 18377.
[23] A. B. Anderson, H. A. Asiri, *Phys. Chem. Chem. Phys.* **2014**, *16*, 10587.
[24] J. Scherer, B. Ocko, O. Magnussen, *Electrochim. Acta* **2003**, *48*, 1169.
[25] J. K. Nørskov, J. Rossmeisl, A. Logadottir, L. Lindqvist, J. R. Kitchin, T. Bligaard, H. Jonsson, *J. Phys. Chem. B* **2004**, *108*, 17886.
[26] V. Stamenkovic, B. S. Mun, K. J. J. Mayrhofer, P. N. Ross, N. M. Markovic, J. Rossmeisl, J. Greeley, J. K. Norskov, *Angew. Chem. Int. Ed.* **2006**, *45*, 2897; *Angew. Chem.* **2006**, *118*, 2963.
[27] J. Greeley, I. E. L. Stephens, A. S. Bondarenko, T. P. Johansson, H. A. Hansen, T. F. Jaramillo, J. Rossmeisl, I. Chorkendorff, J. K. Nørskov, *Nat. Chem.* **2009**, *1*, 552.
[28] J. A. Keith, G. Jerkiewicz, T. Jacob, *ChemPhysChem* **2010**, *11*, 2779.
[29] A. S. Bandarenka, A. S. Varela, M. Karamad, F. Calle-Vallejo, L. Bech, F. J. Perez-Alonso, J. Rossmeisl, I. E. L. Stephens, I. Chorkendorff, *Angew. Chem. Int. Ed.* **2012**, *51*, 11845; *Angew. Chem.* **2012**, *124*, 12015.
[30] A. B. Anderson, T. V. Albu, *J. Am. Chem. Soc.* **1999**, *121*, 11855.
[31] A. Y. Lozovoi, A. Alavi, *Phys. Rev. B* **2003**, *68*, 245416.
[32] M. Otani, O. Sugino, *Phys. Rev. B* **2006**, *73*, 115407.
[33] C. D. Taylor, S. A. Wasileski, J.-S. Filhol, M. Neurock, *Phys. Rev. B* **2006**, *73*, 165402.
[34] E. Skúlason, G. S. Karlberg, J. Rossmeisl, T. Bligaard, J. Greeley, H. Jónsson, J. K. Norskov, *Phys. Chem. Chem. Phys.* **2007**, *9*, 3241.
[35] Y.-H. Fang, Z.-P. Liu, *J. Phys. Chem. C* **2009**, *113*, 9765.
[36] S. Schnur, A. Gross, *Catal. Today* **2011**, *165*, 129.
[37] J.-S. Filhol, M.-L. Doublet, *Catal. Today* **2013**, *202*, 87.
[38] N. Bonnet, I. Dabo, N. Marzari, *Electrochim. Acta* **2014**, *121*, 210.
[39] M. Mamatkulov, J.-S. Filhol, *Phys. Chem. Chem. Phys.* **2011**, *13*, 7675.
[40] J.-S. Filhol, M. Neurock, *Angew. Chem. Int. Ed.* **2006**, *45*, 402; *Angew. Chem.* **2006**, *118*, 416.
[41] J. Rossmeisl, J. K. Norskov, C. D. Taylor, M. J. Janik, M. Neurock, *J. Phys. Chem. B* **2006**, *110*, 21833.
[42] M. J. Janik, M. Neurock, *Electrochim. Acta* **2007**, *52*, 5517.
[43] G. Rostamikia, M. J. Janik, *Energy Environ. Sci.* **2010**, *3*, 1262.
[44] J. I. Siepmann, M. Sprik, *J. Chem. Phys.* **1995**, *102*, 511.
[45] S. Tazi, M. Salanne, C. Simon, P. Turq, M. Pounds, P. A. Madden, *J. Phys. Chem. B* **2010**, *114*, 8453.
[46] K. Letchworth-Weaver, T. A. Arias, *Phys. Rev. B* **2012**, *86*, 075140.
[47] D. Gunceler, K. Letchworth-Weaver, R. Sundararaman, K. A. Schwarz, T. A. Arias, *Modell. Simul. Mater. Sci. Eng.* **2013**, *21*, 074005.
[48] K. Mathew, R. Sundararaman, K. Letchworth-Weaver, T. A. Arias, R. G. Hennig, *J. Chem. Phys.* **2014**, *140*, 084106.
[49] S. N. Steinmann, C. Michel, R. Schwiedernoch, P. Sautet, *Phys. Chem. Chem. Phys.* **2015**, *17*, 13949 – 13963.
[50] R. J. Ruka, L. O. Brockway, J. E. Boggs, *J. Am. Chem. Soc.* **1959**, *81*, 2930.
[51] J. B. Benziqer, G. R. Schoofs, *J. Phys. Chem.* **1984**, *88*, 4439.
[52] M. T. Koper, *J. Electroanal. Chem.* **2011**, *660*, 254.
[53] S. Kozuch, S. Shaik, *Acc. Chem. Res.* **2011**, *44*, 101.
[54] J.-S. Filhol, M.-L. Doublet, *J. Phys. Chem. C* **2014**, *118*, 19023.
[55] H.-J. Freund, R. Messmer, *Surf. Sci.* **1986**, *172*, 1.
[56] S.-G. Wang, X.-Y. Liao, D.-B. Cao, C.-F. Huo, Y.-W. Li, J. Wang, H. Jiao, *J. Phys. Chem. C* **2007**, *111*, 16934.
[57] X. Nie, M. R. Esopi, M. J. Janik, A. Asthagiri, *Angew. Chem. Int. Ed.* **2013**, *52*, 2459; *Angew. Chem.* **2013**, *125*, 2519.
[58] Y.-H. Fang, G.-F. Wei, Z.-P. Liu, *J. Phys. Chem. C* **2014**, *118*, 3629.
[59] H. P. Bonzel, G. Pirug, J. E. Muller, *Phys. Rev. Lett.* **1987**, *58*, 2138.

Received: March 3, 2015
Revised: April 29, 2015
Published online on June 10, 2015

5

PERSPECTIVES

The short term perspectives are obviously dictated by my on-going projects. With **Mascat**, I will join my expertise in homogeneous catalysis with the one gained in heterogeneous catalysis for the characterization and the development of novel supported metathesis catalysts in collaboration with Pr. Ch. Copéret and Dr. O. Safonova from Zurich. **Shapes** is dedicated to the amination of alcohols using an H-transfer strategy. On this typical example of hydrogen transfer reactions in heterogenous catalysis, we will develop a screening *in silico* of catalysts based on a descriptor-based approach coupled with a micro-kinetic model. This strategy is built on the current PhD work of A. Dumon and will be highly valuable for Solvay, our industrial partner. **Music** will develop the methodological framework to tackle the challenging study of the reactivity of polyols at the metal/water interface. Last, **Tanopol** will target two major challenges in metal supported catalysis: (i) understanding the processes underlying the synthesis of the nanoparticles (ii) rationalizing the structure/activity relationships.

In those on-going projects are en-rooted my research perspectives on a longer term. For the selective conversion of cellulosic biomass, water is the solvent of choice. It is ideal as a green solvent, that perfectly solubilises the oxygenates derived from cellulose. However, water can also strongly modify the catalytic activity and stability of the heterogeneous catalysts traditionally used for the upgrade of the petroleum feedstock. In addition, the pH can also play a role: for instance, the

oxidation of alcohols into carboxylic acid is generally performed using metallic supported catalysts such as Au, Pt or Pd, and require the addition of a strong base such as NaOH, generating a carboxylate salt. This salt is then hydrolyzed yielding carboxylic acid and one equivalent of inert salt. For a greener process with a better atom economy, this salt generation should be avoided. Despite a constant effort in the domain, no catalyst can avoid the usage of a base keeping a reasonable conversion and yield. Accordingly, the electro-oxidation of polyols is mostly based on the same metal supported catalysts (Au, Pd, Pt and combination of those three metals in bimetallic or alloys catalysts). Based on the development foreseen in the **Music** project, we will tackle the reactivity at the metal/water interface, hopefully including pH and potential effects in the simulations. Those studies should open the door to a more rational development of oxidation catalysts for cellulosic biomass upgrade, the simulations being at the intercrossing between heterogeneous catalysis and electro-catalysis.

In parallel to the development of solvatation models for heterogeneous interfaces, I would like also to address the key challenge of a constant improvement of the quality of the model of the catalyst in its steady state. Surface species – spectator or not – can tune the catalytic activity of heterogeneous catalysts. Similarly, reactant, product or counter ions can modify the coordination sphere of the catalytic site in a single site catalyst. The inclusion of those influences can be key in understanding the physics underlying the catalytic activity. Fro instance, during the PhD project of A. Dumon, we have recently demonstrated that one needs to include chemisorbed ammonia to appropriately describe the hydrogen transfer process from alcohol to the intermediate imine. We expect that the ligands used to shape the metallic nanocatalysts in **Tanopol** could also affect the catalytic activity, opening the door to new strategies to design catalysts. Not only ligands but also species generated in the transient regime can impact the steady state (formate in the hydrogen transfer from formic acid, etc.). To identify those species, we will couple DFT studies with micro-kinetics or even

kinetic Monte Carlo simulations: the efficient self-consistent coupling of several scales of simulations will be highly challenging and valuable for the incoming years in the domain of catalysts modeling.

Curriculum Vitae

Education

2004–2007 Doctorate in Theoretical Chemistry

Theoretical Studies of chemical reactivity: from static methods to metadynamics, under the supervision of Pr. Anne MILET, defended the 27/06/2007, Université Joseph Fourier, Grenoble, France ; financed by the Ministry of Education.

2000–2004 Élève normalienne de l'ENS de Lyon

Recruited on the first competitive exam in Physics/Chemistry

2004 Master in Molecular and Structural Physical Chemistry

Université Joseph Fourier - Grenoble 1

2004 Agrégation de Sciences Physiques, option chimie

2002 Maîtrise in Physical Chemistry

ENS de Lyon/Université Claude Bernard - Lyon 1

2001 Licence in Physical Chemistry

ENS de Lyon/Université Claude Bernard - Lyon 1

1998–2000 Classes Préparatoires aux Grandes Écoles (PCSI/PC*)

Lycée Berthollet, Annecy (74).

1998 Baccalauréat, série S, option Physique-Chimie

Research Positions

Oct 2009 - Chargée de Recherche CNRS , Lyon, France
Computational Studies across catalysis
Laboratoire de Chimie, ENS de Lyon, Lyon, France

Sep. 2008 -Oct. 2009 Agrégée préparateur , Lyon, France
Reactivity of alcohols at metallic surfaces
Laboratoire de Chimie, ENS de Lyon, Lyon, France.

Sep. 2007– Aug. 2008 PostDoc , Amsterdam, Pays-Bas
Electronic structure and catalysis
Pr. E.J. Baerends, Vrieje Universiteit, Amsterdam, The Netherlands

Sep. 2004 – Aug. 2007 PhD in Theoretical Chemistry , Grenoble, France
Theoretical Studies of chemical reactivity: from static methods to metadynamics
under the supervision of Pr. A. Milet, Département de Chimie Moléculaire, Grenoble, France.

R&D projects funded through competitive calls

ANR Contracts

GALAC 2011-2014 co-PI
From glycerol to acrylic acid via lactic acid

SHAPes 2013-2017 co-PI
Novel Selective Heterogeneous Amination Processes for the Synthesis of Bio-based Monomers

MASCAT 2014-2018 French PI, in collaboration with Switzerland
Metathesis Supported Catalysis

MUSIC 2014-2018 French co-PI, in collaboration with USA
Multiscale Simulations of Bifunctional Catalysis ? Application to the Hydrodeoxygenation of Molecules Extracted From Biomass

International Collaborations

PHC Polonium 2012-2014 Agnieszka Ruppert, Łódź, Poland
One-pot GVL production from sugars

PHC De Staël 2014-2016 Marcella Iannuzzi, Zurich, Switzerland
Reactivity at the solid/liquid interface: Better simulation for a better comprehension.

LIA Funcat 2013-2017 Pr. Tom Baker, Pr. Javier Giorgi, Pr. Elena Baranova, Ottawa, Canada.
Fundamental catalysis for green chemistry: From well-defined active sites to mechanistic explorations

PHC Polonium 2015-2017 Agnieszka Ruppert, Łódź, Poland
Hydrogen transfer reactions

Industrial Contracts

Rhodia 2012 -2013 18 months PostDoc
Mechanisms in catalytic oxidation

Solvay 2013-2014 12 months PostDoc
Electrochemical valorisation of CO_2

CNRS-Solvay 2013/16 1 PhD
Selective amination of alcohols

Responsibilities

Seminars Co-organisation of weekly seminars since 2013

Conseil du Laboratoire Member since 2016.

Website of the Theoretical Chemistry group since 2013

PhD Comitee Member : Florian Auneau (2011) ; Jijin Wang (2013) ; Jérémie Zaffran (2014) ; Kim Larmier (2015) ; Sarah Gautier (2015).

Referee

- Journals: ChemSusChem, ACS Catalysis, Journal of Physical Chemistry, Journal Of Molecular Modeling, etc.
- Price: Europacat Young award
- Conferences: ECOSS 2016 panel

Organisation and Scientific Committee Member

- "Catalysis training course", 28/08/13-31/08/13, Lyon ; 80 participants internationaux
- "Computational Studies across catalysis", 13/03/2016 – 17/03/2016, Symposium at the 251th ACS Meeting
- "Rencontres des Chimistes Théoriciens Francophones 2016", 27/06/2016 - 01/07/2016

Distinctions

2015 Médaille de Bronze du CNRS 2015

Experience supervising doctoral thesis and/or final year projects

Doctoral theses

Florian Auneau (20%), Ministry od Education, defended 17/10/11

Jérémie Zaffran, (50%), ANR GALAC, defended 20/04/14

Alexandre Dumon, (80%), BDI CNRS-Solvay, defense scheduled in September 2016

Romain Réocreux, (100%), Ministry of Education (LIA Funcat), defense scheduled in June 2017

Benjamin Schweitzer, (100%), ANR MUSIC, defense scheduled in September 2018

Evans Monyoncho (10%) PhD, uOttawa, Canada

Post-doctorates

Prokopis Andrikopoulos, CNRS-Rhodia, 18 months, 2012-2013

Stephan Steinmann, ENSL-Solvay, 36 months, 2013-2014

Rodrigo Ferreira De Morais, ANR, 12 months, 2015-2016

Tao Wang, ANR, 18 months, 2015-2017

Undergraduates and Experimental PhD

Lise Morlet, L3, Ecole Normale Supérieure de Lyon, 2 months, 2009

Leila Sadr Arani, M2, Université Claude Bernard, 5 months, 2010

Siwar Shibani, M2, Université Claude Bernard, 5 months, 2011

Kahina Aitatmane, PhD, Université Paris Diderot, 1 month, 2011

Sarah Saadek, L2, uOttawa, Canada, 2 months, 2012

Mathilde Iachella, M1, Université Paris Diderot, 3 months, 2012

Joanna Matras, PhD, Łódź Technical University, Poland, 2 months, 2012

Thomas Konincks, M1, Université de Toulouse, 3 months, 2013

Alexandra Anghel, L2, uOttawa, Canada, 2 months, 2013

Romain Réocreux, M2, ENS de Lyon, 6 months, 2014

Joshua Pocher, PhD, Marburg University, Allemagne, 1 month, 2014

Minh Huynh, L3, uOttawa, Canada, 3 months, 2014

Ahmad Galuta, L3, uOttawa, Canada, 2 months, 2014

Aghiles Ouldhamou, Master, uOttawa, Canada, 2 months, 2014

Kuncheng Li, M2, Université Claude Bernard, 5 months, 2015

Natalia Potrzebowska, Master, Łódź Technical University, Poland, 2 months, 2015

Kamila Kazmierczak, Master, Łódź Technical University, Poland, 2 months, 2015

Quingyi Gu, M2, ENS de Lyon, 6 months, 2016

Teaching

Few hours per year at the ENS de Lyon

Course in a Summer school (2013, 2015)

Popularization

Fête de la Science
Promoting Science and Chemistry using the Foldit Project

Année Mondiale de la Chimie (2011)
Three presentations in High School in the framework "Les chercheurs s'invitent au lycée" organized by the CNRS

High school visitors
I have hosted high school students for a week.

Publication List

37 articles ; H-index=16 ; 660 citations (GoogleScholar data, Researcher id G-3769-2011)

[1] T. J. M. de Bruin, C. Michel, K. Vekey, A. E. Greene, Y. Gimbert, and A. Milet. First C-C bond formation in the Pauson-Khand reaction: Influence of carbon-carbon triple bond polarization on regiochemistry - a density functional theory study. *Journal of Organometallic Chemistry*. **2006**, *691*, 4281–4288. Times Cited: 22.

[2] T. Godet, C. Vaxelaire, C. Michel, A. Milet, and P. Belmont. Silver versus gold catalysis in tandem reactions of carbonyl functions onto alkynes: A versatile access to furoquinoline and pyranoquinoline cores. *Chemistry-a European Journal*. **2007**, *13*, 5632–5641. Times Cited: 99.

[3] C. Michel, T. Godet, M.-L. Dheu-Andries, P. Belmont, and A. Milet. Theoretical study of the cyclization of carbonyl groups on unactivated alkynyl-quinolines in the gas phase and in methanol solution. *Journal of Molecular Structure-Theochem*. **2007**, *811*, 175–182. Times Cited: 2.

[4] C. Michel, A. Laio, F. Mohamed, M. Krack, M. Parrinello, and A. Milet. Free energy ab initio metadynamics: A new tool for the theoretical study of organometallic reactivity? Example of the C-C and C-H reductive eliminations from platinum(IV) complexes. *Organometallics*. **2007**, *26*, 1241–1249. Times Cited: 35.

[5] K. Selmeczi, C. Michel, A. Milet, I. Gautier-Luneau, C. Philouze, J.-L. Pierre, D. Schnieders, A. Rompel, and C. Belle. Structural, kinetic, and theoretical studies on models of the zinc-containing phosphodiesterase active center: Medium-dependent reaction mechanisms. *Chemistry-a European Journal*. **2007**, *13*, 9093–9106. Times Cited: 41.

[6] C. Michel and A. Milet. Free energy calculation of the effects of the fluorinated phosphorus ligands on the C-H and C-C reductive elimination from pt(IV). *Journal of Molecular Structure-Theochem*. **2008**, *852*, 54–61. Times Cited: 6 32nd Congress of Theoretical Chemists of Latin Expression SEP 01-06, 2006 Cotes de Carthage, TUNISIA.

[7] S. Stecko, K. Pasniczek, C. Michel, A. Milet, S. Perez, and M. Chmielewski. A DFT study of 1,3-dipolar cycloaddition reactions of 5-membered cyclic nitrones with alpha,beta-unsaturated lactones and with cyclic vinyl ethers: Part I. *Tetrahedron-Asymmetry*. **2008**, *19*, 1660–1669. Times Cited: 16.

[8] S. Stecko, K. Pasniczek, C. Michel, A. Milet, S. Perez, and M. Chmielewski. A DFT study of 1,3-dipolar cycloadditions of cyclic nitrones to unsaturated lactones. part II. *Tetrahedron-Asymmetry*. **2008**, *19*, 2140–2148. Times Cited: 15.

[9] W. Zeghida, J. Debray, C. Michel, A. Milet, P. Dumy, and M. Demeunynck. Synthesis of N-acridinyl-N '-alkylguanidines: Dramatic influence of amine to guanidine replacement on the physicochemical properties. *Bioorganic & Medicinal Chemistry Letters*. **2008**, *18*, 4779–4782. Times Cited: 3.

[10] C. Michel and E. J. Baerends. What singles out the FeO(2+) moiety? a density-functional theory study of the methane-to-methanol reaction catalyzed by the first row transition-metal ox-

ide dications $MO(H_2O)_p^{2+}$, M = V-Cu. *Inorganic Chemistry*. **2009**, *48*, 3628–3638. Times Cited: 49.

[11] C. Michel, P. Belanzoni, P. Gamez, J. Reedijk, and E. J. Baerends. Activation of the C-H bond by electrophilic attack: Theoretical study of the reaction mechanism of the aerobic oxidation of alcohols to aldehydes by the Cu(bipy)(2+)/2,2,6,6-Tetramethylpiperidinyl-1-oxy cocatalyst system. *Inorganic Chemistry*. **2009**, *48*, 11909–11920. Times Cited: 61.

[12] C. Michel, A. Laio, and A. Milet. Tracing the entropy along a reactive pathway: The energy as a generalized reaction coordinate. *Journal of Chemical Theory and Computation*. **2009**, *5*, 2193–2196. Times Cited: 8.

[13] J. I. Rodriguez, R. F. W. Bader, P. W. Ayers, C. Michel, A. W. Gotz, and C. Bo. A high performance grid-based algorithm for computing QTAIM properties. *Chemical Physics Letters*. **2009**, *472*, 149–152. Times Cited: 46.

[14] R. E. Bulo, H. Van Schoot, D. Rohr, and C. Michel. Bias-exchange metadynamics applied to the study of chemical reactivity. *International Journal of Quantum Chemistry*. **2010**, *110*, 2299–2307. Times Cited: 0 SI 13th International Conference on Application of the Density Functional Theory to Chemistry and Physics AUG 31-SEP 01, 2009 Lyon, FRANCE.

[15] F. Auneau, C. Michel, F. Delbecq, C. Pinel, and P. Sautet. Unravelling the mechanism of glycerol hydrogenolysis over rhodium catalyst through combined experimental-theoretical investigations. *Chemistry-a European Journal*. **2011**, *17*, 14288–14299. Times Cited: 53.

[16] P. Belanzoni, C. Michel, and E. J. Baerends. Cu(bipy)(2+)/TEMPO-catalyzed oxidation of alcohols: Radical

or nonradical mechanism? *Inorganic Chemistry*. **2011**, *50*, 11896–11904. Times Cited: 20.

[17] E. Dumont, C. Michel, and P. Sautet. Unraveling gold(I)-specific action towards peptidic disulfide cleavage: A DFT investigation. *Chemphyschem*. **2011**, *12*, 2596–2603. Times Cited: 2.

[18] C. Michel, F. Auneau, F. Delbecq, and P. Sautet. C-H versus O-H bond dissociation for alcohols on a Rh(111) surface: A strong assistance from hydrogen bonded neighbors. *ACS Catalysis*. **2011**, *1*, 1430–1440. Times Cited: 28.

[19] F. Auneau, L. Sadr Arani, M. Besson, L. Djakovitch, C. Michel, F. Delbecq, P. Sautet, and C. Pinel. Heterogeneous transformation of glycerol to lactic acid. *Topics in Catalysis*. **2012**, *55*, 474–479. Times Cited: 24.

[20] S. Chibani, C. Michel, F. Delbecq, C. Pinel, and M. Besson. On the key role of hydroxyl groups in platinum-catalysed alcohol oxidation in aqueous medium. *Catalysis Science and Technology*. **2012**, *3*, 339–350. Times Cited: 21.

[21] P. Fleurat-Lessard, C. Michel, and R. E. Bulo. Energy extrapolation schemes for adaptive multi-scale molecular dynamics simulations. *Journal of Chemical Physics*. **2012**, *137*, year. Times cited: 6.

[22] C. Michel, F. Göltl, and P. Sautet. Early stages of water/hydroxyl phase generation at transition metal surfaces - synergetic adsorption and O-H bond dissociation assistance. *Physical Chemistry Chemical Physics*. **2012**, *14*, 15286–15290. Times Cited: 16.

[23] R. E. Bulo, C. Michel, P. Fleurat-Lessard, and P. Sautet. Multiscale modeling of chemistry in water: Are we there yet? *Journal of Chemical Theory and Computation*. **2013**, *9*, 5567–5577. Times Cited: 19.

[24] D. Loffreda, C. Michel, F. Delbecq, and P. Sautet. Tuning catalytic reactivity on metal surfaces: Insights from DFT. *Journal of Catalysis*. **2013**, *308*, 374–385. Times Cited: 10.

[25] K. Ait Atmane, C. Michel, J.-Y. Piquemal, P. Sautet, P. Beaunier, M. Giraud, M. Sicard, S. Nowak, R. Losno, and G. Viau. Control of the anisotropic shape of cobalt nanorods in the liquid phase: from experiment to theory... and back. *Nanoscale*. **2014**, *6*, 2682–2692. Times Cited: 6.

[26] W. Guo, C. Michel, R. Schwiedernoch, R. Wischert, X. Xu, and P. Sautet. Formation of acrylates from ethylene and CO_2 on Ni complexes: A mechanistic viewpoint from a hybrid DFT approach. *Organometallics*. **2014**, *33*, 6369–6380. Times Cited: 8.

[27] C. Michel, J. Zaffran, A. M. Ruppert, J. Matras-Michalska, M. Jedrzejczyk, J. Grams, and P. Sautet. Role of water on metal catalyst performance for ketone hydrogenation. a join experimental and theoretical study on levulinic acid conversion into gamma-valerolactone. *Chemical Communications*. **2014**, *50*, 12450–12453. Times Cited: 17.

[28] J. Zaffran, C. Michel, F. Auneau, F. Delbecq, and P. Sautet. Linear energy relations as predictive tools for polyalcohol catalytic reactivity. *ACS Catalysis*. **2014**, *4*, 464–468. Times Cited: 8.

[29] P. C. Andrikopoulos, C. Michel, S. Chouzier, and P. Sautet. In silico screening of iron-oxo catalysts for C-H bond cleavage. *ACS Catalysis*. **2015**, *5*, 2490–2499. Times Cited: 4.

[30] S. Gautier, S. N. Steinmann, C. Michel, P. Fleurat-Lessard, and P. Sautet. Molecular adsorption at Pt(111). how accurate are DFT functionals? *Physical Chemistry Chemical Physics*. **2015**, *17*, 28921–28930. Times Cited: 0.

[31] M. A. Lemes, A. Pialat, S. N. Steinmann, I. Korobkov, C. Michel, and M. Murugesu. Study of a novel hepta-coordinated feiii bimetallic complex with an unusual 1,2,4,5-tetrazine-ring opening. *Polyhedron*. **2015**.

[32] C. Michel and P. Gallezot. Why is ruthenium an efficient catalyst for the aqueous-phase hydrogenation of biosourced carbonyl compounds? *ACS Catalysis*. **2015**, *5*, 4130–4132. Times Cited: 7.

[33] S. N. Steinmann, C. Michel, R. Schwiedernoch, J.-S. Filhol, and P. Sautet. Modeling the HCOOH/CO_2 electrocatalytic reaction: When details are key. *Chemphyschem*. **2015**, *16*, 2307–2311. Times Cited: 5.

[34] S. N. Steinmann, C. Michel, R. Schwiedernoch, and P. Sautet. Impacts of electrode potentials and solvents on the electroreduction of CO_2: a comparison of theoretical approaches. *Physical Chemistry Chemical Physics*. **2015**, *17*, 13949–13963. Times Cited: 5.

[35] J. Zaffran, C. Michel, F. Delbecq, and P. Sautet. Trade-off between accuracy and universality in linear energy relations for alcohol dehydrogenation on transition metals. *Journal of Physical Chemistry C*. **2015**, *119*, 12988–12998. Times Cited: 2.

[36] A. M. Ruppert, M. Jedrzejczyk, O. Sneka-Platek, N. Keller, A. S. Dumon, C. Michel, P. Sautet, and J. Grams. Ru catalysts for levulinic acid hydrogenation with formic acid as a hydrogen source. *Green Chemistry*. **2016**. Times Cited: 1.

[37] S. N. Steinmann, C. Michel, R. Schwiedernoch, M. Wu, and P. Sautet. Electro-carboxylation of butadiene and ethene over Pt and Ni catalysts. *Journal of Catalysis*. **2016**.